EARTH STRUCTURE AND EARTHQUAKE LOCATIONS IN THE COYOTE LAKE AREA, CENTRAL CALIFORNIA

by

Clifford H. Thurber

A.B., Cornell University, Ithaca, New York
(1975)

SUBMITTED IN PARTIAL FULFILLMENT
OF THE REQUIREMENTS FOR THE DEGREE OF
DOCTOR OF PHILOSOPHY
at the

 MASSACHUSETTS INSTITUTE OF TECHNOLOGY
May, 1981

Signature of Author.....
Department of Earth and Planetary Sciences
May 1981

Certified by.....
Thesis Supervisor

Accepted by.....
Chairman, Departmental Committee on Graduate Students

EARTH STRUCTURE AND EARTHQUAKE LOCATIONS IN THE COYOTE LAKE AREA, CENTRAL CALIFORNIA

by

Clifford H. Thurber

Submitted to the Department of Earth and Planetary Sciences on May 9, 1981, in partial fulfillment of the requirements for the degree of Doctor of Philosophy

ABSTRACT

The Coyote Lake, California, earthquake sequence of August, 1979, has provided a rare opportunity for detailed, multidisciplinary study of a moderate-sized earthquake (local magnitude 5.7) and its aftershocks. The sequence occurred within the US Geological Survey Central California Seismic Network, so that good short-period seismological data are available, particularly P-wave arrival times and first motions. In addition, strong motion, teleseismic, geodetic, and magnetic field observations are available. One important step in the process of understanding this event and its aftershocks is an improvement in the knowledge of the crustal structure in this geologically complex, heterogeneous area.

The application of modern geophysical techniques to the study of heterogeneous earth structure has recently become relatively commonplace. Two prominent seismological methods have clearly been demonstrated to be successful, namely teleseismic velocity inversion (e.g. Aki et al., 1977), and reflection profiling (e.g. Oliver, 1980). Refraction studies are also beginning to treat laterally varying structure (e.g. Mooney and Luetgert, 1980).

This study is primarily concerned with the theory and application of a fourth seismological method, simultaneous inversion of local earthquake arrival time data. P (and S) wave arrival times from local earthquakes have the potential of providing the seismologist with information not only

about the locus of the earthquake source itself, but also about the structure of the earth, specifically the variations of the seismic velocity in the earth. Simultaneous inversion is a method for quantitatively treating these two factors in unison.

Previous work on the simultaneous inversion method (e.g. Aki and Lee, 1976; Crosson, 1976a) has been improved and extended to incorporate iterative solution for laterally heterogeneous structure and earthquake locations. Approximate ray tracing and parameter separation are important elements of the improved method. Numerical experiments using artificially generated data illustrate the effectiveness of the method and provide some guidelines for carrying out the inversions and evaluating the solutions.

Application of this method to P-wave arrival time data recorded by stations of the US Geological Survey Central California Network yields two- and three-dimensional models for the velocity structure of the upper crust in an area encompassing the Coyote Lake rupture zone. Improved estimates of the locations of the earthquakes in the area are also determined. The results are supported by evidence from more traditional methods of analysis of travel time data. Very strong correlations with geology, gravity, and magnetic anomalies are also observed.

Examples of specific structural features present in the velocity models include a wedge of strong low velocity located between the San Andreas fault and the southern extension of the Calaveras fault, high velocities southwest of the San Andreas fault in the Gabilan range, low velocity between the San Andreas and Vergeles faults, and high velocities under the southern Santa Cruz mountains, between the Sargent and Calaveras faults. In addition, low velocities are observed at shallow depth in the Santa Clara Valley and the Santa Cruz basin. Each of these features can be related to a corresponding geologic structure and/or geophysical anomaly (i.e. gravity or magnetic).

The low velocity wedge is the most conspicuous feature in the velocity models. It is apparently a northern continuation of the low velocity zone between the San Andreas and San Benito faults in Bear Valley, California, observed by Healy and Peake (1975), Aki and Lee (1976), and others. The combination of seismic, gravity, magnetic, and geologic observations suggests that this wedge consists of fault gouge overlying serpentinite. The pattern of seismic activity in the Coyote Lake area appears to show a relationship to the distribution of serpentinite along the fault zones, a relationship first noted by Allen (1968).

Simultaneous inversion and ray tracing methods have also

been applied to a detailed study of the Coyote Lake earthquake sequence. A three-dimensional velocity model localized around the rupture zone has been determined for the purpose of studying aftershock focal mechanisms and analyzing in detail the aftershock locations. It is found that, for several stations along the Calaveras fault, first motions with apparently reversed polarity can be explained by the lateral refraction of first arrivals. First motion plots derived using ray tracing in the three-dimensional model show far fewer polarity reversals. Focal mechanisms for aftershocks along the main rupture show strike-slip faulting oriented roughly N 25 W and dipping about 75 to the northeast. The relocated main shock and nearby aftershocks are found to lie in a plane with this same orientation, which is also in agreement with the results of Nabelek and Toksoz (1981) based on teleseismic body-wave analysis of the main shock. Thus the orientation of the rupture of the Coyote Lake event is found to be very well constrained.

The general pattern of aftershock locations also appears to be intimately related to the rupture process of the Coyote Lake event. A number of distinct clusters of aftershocks are observed, and each cluster can be associated with a specific discontinuity or complexity in the fault as observed at the surface. These findings are consistent with the results of Bakun (1980), and support the fault failure model of Bakun et al. (1980) developed originally for the San Andreas fault. Moreover, these clusters may be localized at fault barriers (see Das and Aki, 1977) which could have produced detectable effects on strong motion and teleseismic observations of the main shock. In fact, Nabelek and Toksoz (1981) suggest that the Coyote Lake earthquake was a multiple source event, with an initial rupture of about 8 km length. This equals the distance from the main shock hypocenter to a cluster at one of the larger fault offsets. The rupture termination may also correspond to an aftershock cluster and fault bend located at San Felipe Lake. More detailed investigation of strong motion and/or teleseismic observations may reveal a further relationship between the clustering of aftershocks at fault discontinuities and the Coyote Lake rupture.

Thesis Advisor: Keiiti Aki

Title: Professor of Geophysics

ACKNOWLEDGEMENTS

I would like to express my most sincere gratitude to Kei Aki, my thesis advisor, for his guidance throughout the course of this work. His comments and suggestions have always been insightful, and often inspirational. I deeply appreciate the time and effort he has so freely contributed.

I am also grateful for having had the opportunity to work with Nafi Toksöz and Sean Solomon during my formative years at MIT. Their contributions to my education have been enormous.

Special thanks are due to Bill and Nancy Ellsworth and Steve and Heather Taylor. Bill's advice has been invaluable to me, and his and Nancy's friendship and hospitality will never be forgotten. Steve showed me how to finish a thesis in style, and he and Heather in many ways helped me to survive and enjoy my years at MIT.

This thesis could not have been completed without the assistance of Willie Lee and the staff of the US Geological Survey in Menlo Park, California. My thanks to Willie and company for all they have done to help me during my many visits to Menlo Park.

Of all my fellow students at MIT, I would particularly like to thank Steve Roecker, Rob Comer, and Dan Davis. Steve is responsible for introducing me to velocity inversions, but I don't hold that against him. His constant enthusiasm for both life and science has been an

inspiration. Rob has been a never ending source of ideas and advice. I hope we can continue to trace rays and flex lithospheres together in the future. Dan has been vital to my mental and physical well-being. His stories and his love for basketball are deeply appreciated. Thanks also go to Steve Bratt, Roger Buck, Arthur Cheng, Karl Coyner, Lynn Hall, Paul Huang, John Nabelek, Bob Nowack, Dave Olgaard, Steve Park, Scott Phillips, Jay Pulli, Rob Stewart, Gerardo Suarez, Ken Tubman, and Anne Trehu, for being a part of my MIT experience.

I owe thanks to Judy Roos, Sara Brydges, and Debby Gillett for their friendship, support, and assistance. Their administrative wizardry has made vaulting the innumerable hurdles almost a pleasure (well, at least not too painful).

And above all, my most heartfelt thanks to Judy Harackiewicz. Judy kept me going when things looked bleak, and patted me on the back when things went well. I couldn't have made it through without her.

This research was supported by the National Science Foundation grant PFR-8005720.

TABLE OF CONTENTS

CHAPTER 1

INTRODUCTION

Over the past few years, geophysicists have become increasingly aware of the extent of lateral heterogeneity in the earth's crust. Heterogeneity is so widespread that "the old geophysical picture of a simple layered crust should be abandoned," according to Smithson et al. (1977). Two seismological techniques, teleseismic three-dimensional velocity inversion (Aki et al., 1977; Ellsworth and Koyanagi, 1977; Taylor and Toksoz, 1979) and continental reflection profiling (Smithson et al., 1977; Oliver, 1980), have been instrumental in demonstrating the complexity of the continental crust in a number of areas.

Another promising seismological technique for probing crustal structure in seismically active areas is the method of simultaneous inversion of local earthquake arrival-time data (Aki and Lee, 1976). This method addresses the problem of determining crustal velocity structure and the intimately related problem of earthquake location in combination. Simultaneous inversion is the basic analytic tool used in this thesis. The method is applied to P-wave arrival-time data from earthquakes in the vicinity of Coyote Lake, California, to improve the knowledge of crustal structure in that area, and to investigate various characteristics of the August, 1979 Coyote Lake earthquake and its aftershocks.

These results can be combined with information from other studies, for example, refraction, strong motion, and teleseismic body-wave analyses, in order to understand better the rupture process of the Coyote Lake event and its relation to the occurrence and distribution of aftershocks.

The details of the formulation of the simultaneous inversion method are set forth in Chapter 2. The conceptual approach parallels that of Aki and Lee (1976). The fundamental improvement incorporated in this work is the use of three-dimensional ray tracing (primarily in the form of approximate ray tracing) to calculate P-wave travel times. This permits the treatment of laterally varying velocity structures, which in turn allows for the iterative improvement of the solution for earthquake locations and three-dimensional earth structure. An important consequence is the ability to measure directly the model improvement achieved via the inversion (by computing arrival-time residuals after each iteration). An additional practical improvement is the use of parameter separation in the inversion procedure, which permits the inclusion of arbitrarily large amounts of data so as to constrain better the models.

Chapter 3 presents a series of numerical experiments designed to investigate some of the characteristics and limitations of the simultaneous inversion method. The partial derivatives of the P-wave travel time with respect to variations of the hypocenter and velocity model

parameters are examined with two primary objectives in mind. One is to determine the range of parameter perturbations for which the change in travel time is linearly related (to an adequate approximation) to the corresponding change in parameter value. The other is to test the accuracy of the partial derivatives as determined via approximate ray tracing. The remainder of the chapter covers more general aspects of the inversion, including the relative merit of velocity inversion versus simultaneous inversion, the effectiveness of parameter separation, the accuracy of inversion using approximate ray tracing, and the usefulness of measures of resolution and error.

The P-wave velocity structure of the crust in the Coyote Lake area is explored in Chapter 4. First the geological and geophysical features of the study area are described. Next traditional methods of analysis of P-wave arrival-time data (travel time plots and layered velocity models) are used to characterize the seismic velocity and its variations in the region. Finally, the lateral (as well as vertical) variations in structure are directly investigated, using the methods and techniques of simultaneous inversion described in Chapter 2. These results are combined with other geophysical and geological information to infer the structure of the crust at depth. Concurrently, improved estimates of the locations of earthquakes in the study area are derived, resulting in generally improved correspondence between the location of

earthquake epicenters and the mapped surface traces of the local faults.

In Chapter 5, three-dimensional ray tracing and simultaneous inversion methods are applied to a study of the Coyote Lake earthquake sequence of 1979. Aftershock locations and focal mechanisms are derived, taking into account the complex velocity structure of the area. These results are synthesized with information from strong motion and teleseismic observations to deduce a first-order model of the rupture process of the Coyote Lake earthquake.

Finally, Chapter 6 contains a summary of the methods and principal results of the thesis, and some topics for future study are suggested.

CHAPTER 2

METHOD AND TECHNIQUES FOR SIMULTANEOUS INVERSION

Simultaneous inversion is a method for determining the locations of earthquakes and the seismic velocity structure of the earth beneath a seismic array. The data source used for the modeling in this thesis is the times of first P arrivals from local earthquakes and explosions, all of which lie within the volume of the earth being studied. This fact distinguishes the simultaneous inversion method from the three-dimensional velocity inversions using teleseismic data (for example Aki et al., 1977), and also results in added complexity of the problem.

The simultaneous inversion problem has been approached from several different points of view. The principle distinction among these approaches is the nature of the representation of the earth's velocity structure. Crosson (1976a,b) chose to use constant velocity layers; Aki and Lee (1976) chose to use a large number of constant-velocity blocks (in three dimensions); Spencer and Gubbins (1980) chose to use a three-dimensional analytic function defined by a small number of parameters; Chou and Booker (1979) chose to use variable sized "ideal averaging volumes." All but Chou and Booker (1979) formulated the problem as overdetermined. Each approach has its advantages and disadvantages.

The method described in this chapter is similar in some ways to that of Aki and Lee (1976). The inverse problem is formulated to be overdetermined, and the earth structure is represented in three dimensions by the velocity defined at a large number of discrete points (instead of within a large number of blocks). Here the similarity ends. Parameter separation based on the method of Pavlis and Booker (1980) is employed to keep the inverse problem at a tractable size for arbitrarily large amounts of data. The incorporation of three-dimensional ray tracing (and also approximate ray tracing) permits the solution to be determined iteratively. An important consequence is that the variance reduction achieved at each iteration step can be directly computed, rather than merely estimated as in the case of Aki and Lee (1976).

The two following sections provide the conceptual and mathematical basis for simultaneous inversion. The next four sections of the chapter consist of more detailed explanations of some of the important topics, tools, and techniques which underlie our formulation of the method. The final section presents the algorithm constructed for solving the local earthquake simultaneous inversion problem.

2.1 HEURISTIC DESCRIPTION

2.1.1 EARTHQUAKE LOCATION

The method of simultaneous inversion can be thought of as an extension of Geiger's method of determining the location of an earthquake (Aki and Lee, 1976). The formulation of Geiger's method appropriate for local earthquake location using first P arrival time data involves the following steps:

a) assume a model for the P-wave velocity structure of the earth appropriate for the area being investigated;

b) make an initial estimate of the earthquake location and origin time (hypocentral parameters);

c) calculate theoretical P-wave travel times from the estimated location to observing stations, and compute the corresponding arrival time residuals;

d) calculate partial derivatives of the travel times with respect to variations in the earthquake location and origin time;

e) solve a system of linearized equations using inverse theory to find adjustments to the hypocentral parameters which will minimize the arrival time residuals, thus obtaining a new location estimate.

Steps c) to e) generally are repeated until convergence is achieved, that is until a stable solution for the location with small residuals is found. This procedure is basically an application of the Gauss-Newton method for minimization (Lee and Stewart, 1981).

2.1.2 EXTENSION TO SIMULTANEOUS INVERSION

In practice the earth's velocity structure (in step a) is

never completely known. Thus systematic biases can be introduced into the earthquake locations if the assumed velocity structure differs significantly from the "true" earth structure (see for example Engdahl and Lee, 1976). In such a case it would be desirable to be able to use the first P arrival times to try to extract information about the earth's structure in order to improve the locations of the earthquakes. In other situations the velocity structure of the earth may itself be the subject of interest, so that the arrival time data may be viewed as a tool for probing the earth's crustal structure. These two problems, the location of earthquakes and the determination of earth structure, should in many cases be properly dealt with in unison.

Combining these two problems via the simultaneous inversion approach entails treating the velocity structure as an unknown function (see Chou and Booker, 1979) or as a set of unknown parameters in a manner similar to the hypocentral parameters (see Aki and Lee, 1976; Crosson, 1976a; Spencer and Gubbins, 1980). The latter approach is adopted here primarily for the sake of practicality and tractability. These parameters are included in the inversion by modifying steps d) and e) as follows:

> d) calculate partial derivatives of the travel times with respect to variations in the earthquake location and origin time (hypocentral parameters) and with respect to variations in the velocity structure parameters;

e) for a set of earthquakes, solve a system of linearized equations using inverse theory to find adjustments to both the hypocentral and velocity parameters which will minimize the arrival time residuals, obtaining a new estimate of the earthquake locations and the velocity structure.

As before, steps c) to e) should be done iteratively since this is not a linear problem. The following section formally presents the mathematical outline of this simultaneous inversion problem, and introduces some of the tools and techniques used in its solution.

2.2 MATHEMATICAL FORMULATION

The preceding section describes some of the motivation for the simultaneous inversion method and sketches the procedure for its implimentation. In this section the mathematics of the inversion procedure are presented in more detail.

2.2.1 DERIVATION OF THE BASIC EQUATION OF SIMULTANEOUS INVERSION - THE FORWARD PROBLEM

Given initial estimates of the local crustal velocity structure (some finite set of parameters defining the velocity as a function of Cartesian coordinates x,y,z) and the hypocentral parameters (Cartesian coordinates and origin time of each earthquake), theoretical first P arrival times (t_{cal}) are calculated using some form of ray tracing. The

residual r for a given observation is defined by

$$r = t_{obs} - t_{cal} \qquad (2.1)$$

where t_{obs} is the observed arrival time. The goal is to simultaneously perturb the velocity and hypocentral parameters to produce a change in the calculated arrival time Δt_{cal} which satisfies

$$t_{obs} - (t_{cal} + \Delta t_{cal}) = 0 \quad (+ \text{ error}) \qquad (2.2)$$

for each observation of all the events considered. This is a nonlinear problem, so that a single iteration will not be able to satisfy equation 2.2. In addition the presence of data error essentially guarantees that this equation will never be satisfied identically. Combining equations 2.1 and 2.2 we note that

$$r = \Delta t_{cal} \quad (+ \text{ error}) \qquad (2.3)$$

Now the calculated arrival time consists of two parts, the origin time of the event (t_o) and the theoretical P-wave travel time (t):

$$t_{cal} = t_o + t$$

so clearly

$$\Delta t_{cal} = \Delta t_o + \Delta t \qquad (2.4)$$

Using a first order Taylor expansion in all the parameters (hypocenter and velocity), the change in theoretical travel

time can be related to changes in the parameters by

$$\Delta t \simeq \frac{\partial t}{\partial x_e} \Delta x_e + \frac{\partial t}{\partial y_e} \Delta y_e + \frac{\partial t}{\partial z_e} \Delta z_e + \sum_{j=1}^{N} \frac{\partial t}{\partial v_j} \Delta v_j \quad (2.5)$$

where $\frac{\partial t}{\partial x_e}$, $\frac{\partial t}{\partial y_e}$, and $\frac{\partial t}{\partial z_e}$ are partial derivatives of the travel time with respect to the coordinates of the earthquake, Δx_e, Δy_e, and Δz_e are the desired changes in the hypocentral coordinates, $\partial t/\partial v_j$ is the partial derivative of the travel time with respect to the j'th velocity parameter, and Δv_j is the desired change in the j'th velocity parameter (N is the total number of velocity parameters). Combining equations 2.3, 2.4 and 2.5 we find that the system of equations to be solved has the form

$$r = \Delta t_o + \frac{\partial t}{\partial x_e} \Delta x_e + \frac{\partial t}{\partial y_e} \Delta y_e + \frac{\partial t}{\partial z_e} \Delta z_e + \sum_{j=1}^{N} \frac{\partial t}{\partial v_j} \Delta v_j \quad (2.6)$$

with one such equation for each observed P arrival.

2.2.2 EVALUATION OF THE PARTIAL DERIVATIVES

The partial derivatives in equation 2.6 can be easily calculated given the velocity model and the ray path from the earthquake to the observing station. The hypocentral partial derivatives can be shown via either a geometrical or variational argument to satisfy

$$\partial t/\partial x_e = -1/V_e \; dx/ds$$
$$\partial t/\partial y_e = -1/V_e \; dy/ds \qquad (2.7)$$
$$\partial t/\partial z_e = -1/V_e \; dz/ds$$

where V_e is the velocity at the earthquake source (hypocenter) and dx/ds, dy/ds and dz/ds are direction cosines of the vector tangent to the ray path at the hypocenter and pointing in the direction of ray propagation.

The exact form of the velocity partial derivatives depends on the way in which the velocity model is parameterized. The travel time is given by the integral

$$t = \int_{\text{event}}^{\text{station}} \frac{1}{V(x,y,z)} \, ds$$

where s is the parameter of path length. The partial derivative of the travel time with respect to the i'th velocity parameter can be written as

$$\frac{\partial t}{\partial v_i} = \int_{\text{event}}^{\text{station}} \frac{-1}{(V(x,y,z))^2} \frac{\partial V(x,y,z)}{\partial v_i} \, ds \qquad (2.8)$$

The velocity V is explicitly a function of the spatial coordinates x, y and z, but obviously it is also implicitly a function of the velocity parameter values

$$V = F(x, y, z; v_j, j=1,N)$$

The factor $\partial V/\partial v_i$ in equation 2.8 reflects the nature of the velocity representation or interpolation function F used. Once the velocity interpolation function is chosen, the form of $\partial V/\partial v_i$ is uniquely determined. Thus from equations 2.7 and 2.8 we see that the hypocentral derivatives explicitly depend upon the velocity at the source and the initial direction of the ray path, while the velocity partial derivatives explicitly depend upon the ray path and the velocity along it, making calculation of the quantities needed for equation 2.6 a straightforward matter.

As an example of the way in which the form of the velocity partial derivatives is controlled by the type of interpolation, suppose the velocity model is assumed to be a set of constant velocity cubical volumes of dimension L. Then we can represent the velocity function as

$$V(x,y,z) = \sum_j \Pi(x-x_j, y-y_j, z-z_j)\ V_j$$

where

$$\Pi = \begin{cases} +1 \text{ for } |x-x_j|<L/2,\ |y-y_j|<L/2, \text{ and } |z-z_j|<L/2 \\ +\tfrac{1}{2} \text{ for } |x-x_j|=L/2,\ |y-y_j|=L/2, \text{ and } |z-z_j|=L/2 \\ 0 \text{ otherwise} \end{cases}$$

It immediately follows that

$$\frac{\partial V(x,y,z)}{\partial v_i} = \Pi(x-x_i, y-y_i, z-z_i)$$

which is a unit size three-dimensional boxcar coincident with the cubical volume corresponding to the parameter v_i.

2.2.3 THE INVERSE PROBLEM

After the entire set of equations 2.6 has been constructed (the forward problem) one is faced with solving the inverse problem. This is expressed in matrix notation as starting with the relation

$$\underline{\underline{A}}\ \underline{x} = \underline{r} \qquad (2.9)$$

where $\underline{\underline{A}}$ is the known matrix of partial derivatives, $\underline{r}$ is the known vector of residuals, and $\underline{x}$ is the unknown vector of parameter adjustments. From equation 2.9 we must derive a solution

$$\underline{x} = \underline{\underline{a}}^{-1}\ \underline{r}$$

where $\underline{\underline{a}}^{-1}$ is some generalized form of the "inverse" of the original matrix $\underline{\underline{A}}$. Lee and Stewart (1981) discuss many aspects of this inversion problem in detail. We solve the inverse problem in a three step process using the parameter separation method (see Pavlis and Booker, 1980, or Spencer and Gubbins, 1980). The steps involved are

a) separating the velocity parameters from the hypocentral parameters in equation 2.9 utilizing the QR decomposition to form the hypocenter-independent velocity (or medium) partial derivative matrix $\underline{\underline{M}}'$ and data vector $\underline{r}'$;

b) forming $M'^{T}M'$ and $M'^{T}r'$ and solving for the velocity parameter changes using damped least squares;

c) relocating the earthquakes individually in the adjusted velocity model.

The primary advantage of this procedure is that it allows one to replace a very large system of equations (of size 4 times the number of events plus the number of velocity parameters by the number of observations) with an essentially equivalent pair of systems of equations, one containing just velocity parameters (of size number of velocity parameters by number of velocity parameters) and one containing just hypocentral parameters (of size 4 by the number of observations). The entire procedure is done iteratively since this simultaneous inversion problem is in general not a linear one.

Parameter separation is one of several recent innovations which have been incorporated in this work. Section 2.6 contains further discussion of this method. One fundamental requirement for the ability to properly treat laterally heterogeneous earth structure in an iterative solution is three-dimensional ray tracing. Section 2.3 covers the basic elements of the two common approaches to ray tracing, known as shooting and bending. In addition, section 2.4 presents two methods for approximate ray tracing - computing travel times via the determination of an approximation to the true ray path. In section 2.5 the expressions for the hypocentral and velocity partial derivatives are derived and

discussed. Finally section 2.7 covers some aspects of the inversion and iteration procedure.

2.3 THREE-DIMENSIONAL RAY TRACING

The desire to do more than a single step solution to the simultaneous inversion problem in a heterogeneous medium requires the use of three dimensional ray tracing. Crosson (1976a,b) incorporated iterative solutions in his inversion but treated only flat-lying constant velocity layers. Aki and Lee (1976) permitted lateral variations in velocity, but could only compute a single-step solution. Both these approaches are not entirely satisfactory. Crosson (1976b) was forced to include station corrections in his model for the Puget Sound, Washington, region in an attempt to account for lateral heterogeneity. The fairly large station corrections found suggest that inhomogeneities may be important even for an area such as Puget Sound. Aki and Lee (1976) specifically modeled the situation of a laterally heterogeneous earth. However their single step solution gave no direct information on residual reduction achieved by the inversion - the improvement could only be estimated. In addition, although the teleseismic three-dimensional inversion for velocity structure is thought to be linear to a good approximation (Ellsworth, 1977), the problem of earthquake location certainly is not (see for example Lee and Stewart, 1981), so that the simultaneous inversion

problem can not justifiably be assumed to be linear and solvable in a single step. Thus three-dimensional ray tracing is a vital part of simultaneous inversion.

2.3.1 ORIGIN OF THE RAY EQUATIONS

The problem at hand is as follows: given some function V = V(x,y,z) which describes the (estimated) P-wave velocity as a function of position in the earth, and given two points P1=(x1,y1,z1) and P2=(x2,y2,z2), determine the path of minimum travel time between P1 and P2. Mathematically this is known as a two-point boundary value problem. To solve this problem it is necessary to begin with the equations which govern the propagation of an elastic wave in a heterogeneous medium. With appropriate assumptions about the nature of the medium, one can then derive the ray equations, written in vector form as

$$\frac{d}{ds}\left(\frac{1}{V(\underline{r})}\frac{d\underline{r}}{ds}\right) - \nabla\left(\frac{1}{V(\underline{r})}\right) = 0 \qquad (2.10)$$

where s is arc length along the ray and V is the velocity as a function of position $\underline{r}$ (see Appendix A for further discussion).

2.3.2 APPROACHES FOR SOLUTION

Numerous authors have studied the three-dimensional ray tracing problem, including Jacob (1970), Julian (1970),

Wesson (1971), Julian and Gubbins (1977), and Pereyra et al. (1980). Two basic ray tracing techniques have been developed; they are commonly known as the shooting and bending methods. The shooting approach involves the specification of the starting point and initial direction of a ray (an initial value problem) and the propagation of that ray up to the surface. The initial direction of the ray is then modified until the ray path reaches the surface at the position of the receiver. For the bending method the end points of the ray path are specified (a boundary value problem). Some initial path connecting the fixed endpoints is then mathematically perturbed or "bent" until it converges to a true ray path.

This work has made use of two modern computer programs for three-dimensional ray tracing. One is the bending routine of Pereyra et al. (1980), and the other is the shooting routine of Luk et al. (1981). The basic elements of these two programs are discussed briefly.

2.3.3 THE BENDING METHOD

The ray equations 2.10 can be rewritten as

$$\begin{aligned} \ddot{x} &= V(\underline{r})\ (-G(\underline{r})\ \dot{x} + \partial u/\partial x) \\ \ddot{y} &= V(\underline{r})\ (-G(\underline{r})\ \dot{y} + \partial u/\partial y) \\ \ddot{z} &= V(r)\ (-G(r)\ \dot{z} + \partial u/\partial z) \end{aligned} \qquad (2.11)$$

where $\underline{r}=(x,y,z)$, a dot denotes differentiation with respect to arc length s, u is slowness (i.e. $u=1/V(\underline{r})$), and G is defined as

$$G(\underline{r}) = \frac{\partial u}{\partial x}\dot{x} + \frac{\partial u}{\partial y}\dot{y} + \frac{\partial u}{\partial z}\dot{z}$$

In their bending routine, Pereyra et al. (1980) solve the set of equations 2.11, subject to appropriate boundary conditions, by reducing this second order system of differential equations to a larger first order system. The first order system is then solved using an adaptive finite-difference computer program developed by Lentini and Pereyra (1977). This first order system is written as

$$\begin{aligned}
\frac{dw_1}{dt} &= w_8\, w_2 \\
\frac{dw_2}{dt} &= w_8\, V\, (-G\, w_2 + \partial u/\partial x) \\
\frac{dw_3}{dt} &= w_8\, w_4 \\
\frac{dw_4}{dt} &= w_8\, V\, (-G\, w_4 + \partial u/\partial y) \\
\frac{dw_5}{dt} &= w_8\, w_6
\end{aligned} \qquad (2.12)$$

$$\frac{dw_6}{dt} = w_8 \, V \, (-G \, w_6 + \partial u/\partial z)$$

$$\frac{dw_7}{dt} = w_8 \, u$$

$$\frac{dw_8}{dt} = 0$$

where t is defined as s/S, S is total path length, and the variables w are given by $[x,\dot{x},y,\dot{y},z,\dot{z},T(s),S]$ with T(s) representing partial travel time.

The first order differential equation solver of Lentini and Pereyra (1977) uses a finite difference approximation to equations 2.12 on a mesh of points. This mesh is permitted to be nonuniform, so that the solver can automatically adapt the mesh to increase resolution in regions in which the solution is varying rapidly. Given an initial trajectory, convergence is achieved using a modification of Newton's method. A procedure known as Armijo's step control combined with the requirement of descent for each iteration enhances the convergence properties of the usual Newton's method. For a more detailed description, the interested reader is referred to Pereyra et al. (1980).

2.3.4 THE SHOOTING METHOD

The shooting method is a two part iterative process - one step tracing a ray, and a second step attempting to converge to the desired endpoint. There are of course a number of methods for numerically treating each of these two steps. Julian and Gubbins (1977) discuss two iterative methods for solving step two, Newton's method and the method of false position. Possible approaches for solving step one include Euler's method, the Runge-Kutta method, Adams methods, and extrapolation methods.

The computer routine for shooting which we have chosen to use has been developed by Luk et al. (1981). The actual ray tracing (step one) is accomplished using an ordinary differential equation integrator written by Shampine and Gordon (1975). The integrator uses a variable order, variable step size version of the Adams method (see Shampine and Gordon, 1975, for a detailed explanation). Luk et al. (1981) utilize the same formulation of the ray equations (equations 2.12) as do Pereyra et al. (1980). Convergence (step two) is achieved using a non-linear equation solver written by Powell (1968). This solver uses a combination of Newton's method and the method of steepest descent.

2.3.5 ALTERNATIVE FORM OF THE RAY EQUATIONS

As first noted by R. Comer (personal communication, 1980), there is a simpler alternative way of expressing the ray equations in a form similar to equations 2.12. Consider

the x-component of the ray equations from equation 2.10:

$$\frac{d}{ds}[\ 1/V\ dx/ds\ ] - \frac{\partial}{\partial x}(1/V) = 0 \qquad (2.13)$$

If we introduce the definition $\gamma_x = \frac{1}{V}\ \frac{dx}{ds}$, then equation 2.13 can be rewritten as two equivalent first-order equations

$$\frac{dx}{ds} = V\ \gamma_x$$

$$\frac{d}{ds}\gamma_x = \frac{\partial}{\partial x}(1/V)$$

In this way equations 2.12 can be written more simply as

$$dw_1/ds = V\ w_2$$
$$dw_2/ds = -1\ \gamma^2\ \partial V/\partial x$$
$$dw_3/ds = V\ w_4$$
$$dw_4/ds = -1\ \gamma^2\ \partial V/\partial y$$
$$dw_5/ds = V\ w_6$$
$$dw_6/ds = -1\ \gamma^2\ \partial V/\partial z$$

where s is the parameter of path length, and the variables w are given by $[x,\gamma_x,y,\gamma_y,z,\gamma_z,T(s),S]$. This representation preserves the clear symmetry of the ray equations and is more efficient computationally than equations 2.12.

2.3.6 INTERPOLATION: THREE-DIMENSIONAL CUBIC SPLINE

An important element of both of these ray tracing computer programs (and most three-dimensional ray tracers in general) is the need for an effective interpolater. Since the velocity will only be specified at a finite number of points $v_i(x_i,y_i,z_i)$, i=1,N, the velocity at any other point must be determined by interpolation. The shooting method requires that the velocity and its first spatial derivatives be continuous, while for the bending method the second derivatives must be continuous as well. To satisfy these requirements, and to maintain a smoothly varying velocity function, a three-dimensional cubic spline under tension interpolation routine developed by A.K. Cline (written communication, 1979) has been utilized.

The cubic spline is simple to define in one dimension. Consider a mesh of N points π given on an interval $x \in [a,b]$

$$\pi: \quad a=x_1<x_2<x_3 \cdots <x_N=b$$

and the corresponding set of ordinate values O

$$O: \quad y_1, y_2, y_3, \cdots, y_N$$

Then the cubic spline S on the mesh π has the following properties:

a) $S(x_i) = y_i$, i=1,N

b) S, S', and S'' are continuous on the interval [a,b]

c) S is given by a cubic polynomial on each subinterval (x_j, x_{j+1})

(Ahlberg et al.,1967). The spline S will always exist, but additional constraints are necessary to define it uniquely (e.g. end conditions at a and b). "Tension" is introduced to help eliminate extraneous points of inflection in the interpolated curve (Cline,1974).

The generalization of the cubic spline to two dimensions is straightforward (Ahlberg et al.,1967). Only recently has the extension to higher dimensions been considered, however. The approach adopted by Cline (written communication, 1979) for his three-dimensional interpolation routine involves the computation of three bicubic splines, fitting surfaces on the x-y, y-z, and x-z rectangular grids. The actual interpolation requires forming the tensor product of these three bicubic splines.

2.3.7 RAY PATH INITIALIZATION

An important step in any ray tracing scheme is the selection of an appropriate initial guess. For a bending routine, that means an estimate of the ray path, while for a shooting routine it means an estimate of the initial ray direction. An estimate which is close to the true ray path (or initial direction) will generally lead to more rapid convergence. On the other hand, a poor initial estimate

could either drastically slow convergence or result in convergence to an undesirable answer, for example a local minimum in travel time instead of the desired global minimum. The ray initializer of Thurber and Ellsworth (1980), which was originally developed to determine initial estimates of ray paths for use with a bending ray tracing routine, can be used to provide reasonable estimates of initial ray directions as well. In the next section we discuss this application of approximate ray tracing (i.e. the ray initializer method), along with its use as a replacement in some situations for truly three-dimensional ray tracing.

2.4 APPROXIMATE RAY TRACING (ART)

Three-dimensional ray tracing is currently a very costly time-consuming procedure. Any device which can improve the efficiency of a ray tracing routine, or perhaps replace it entirely, is of significant value. Approximate ray tracing (henceforth ART) is such a device. In one form ART can be used to provide a starting guess for a ray tracing routine, either bending or shooting. More importantly, in many situations an ART routine is sufficiently accurate in terms of its path and travel time calculations that it can supplant three-dimensional ray tracing completely. Horie (1980) independently has developed a similar method and applied it to a study of the velocity structure under Japan.

In this section two schemes for ART are described and evaluated, and some simple examples of their application are presented.

2.4.1 ART BY LATERALLY AVERAGING THE VELOCITY STRUCTURE

Thurber and Ellsworth (1980) demonstrate a method for deriving approximate solutions for ray paths and travel times in laterally heterogeneous media. Their strategy is first to approximate the medium between a given event and an observing station by a one-dimensional, laterally averaged, layered velocity model. The averaging can be done in a number of ways. The key is to produce a reasonable estimate of the velocity structure seen by rays propagating from the event to the station, and to represent that structure with horizontal constant-velocity layers (see Figure 2.1).

The next step is to determine the minimum time (first arrival) ray path in this one-dimensional averaged structure using standard techniques for ray tracing in a horizontally layered medium (see for example Lee and Lahr, 1975). The direct and all possible refracted arrivals are considered, and low velocity layers are permitted. The direct ray is determined using the method of false position (Acton, 1970). The false position algorithm starts with two points straddling the desired solution (in our case two rays hitting the surface, one on the near and one on the far side of the station), and iterative interpolation is used to

reach the answer (i.e. the correct take-off angle and the resulting ray path). Refracted rays are handled using time terms (Officer, 1958; Lee and Lahr, 1975). The refracted ray travel times are particularly simple to calculate since the take-off angle can only have certain specific values (those which produce critical refractions at layer boundaries below the source). This fact permits the explicit determination of the time spent by a particular ray in each layer (the time terms), which are then summed to give the total travel time> These techniques are extremely efficient and inexpensive. The travel time along the direct ray is compared to that along the possible refracted rays to select the desired minimum time path. This path will in general be a reasonable approximation to the true first arrival ray path.

The ray path estimate can now provide an initial guess for a three-dimensional ray tracing routine (ray initialization). For the bending method the estimated path itself is used as the initial guess, while for the shooting method the starting direction of the estimated path is used. In general this can result in a significant reduction in the number of computational steps needed to arrive at a solution, compared to using the standard first guess of the straight line connecting the event to the seismic station.

2.4.2 LOCAL MINIMUM PROBLEM

A second aspect of the ray path initialization procedure is also of some importance. It is quite possible that a ray tracing algorithm may converge to a ray path that is not the path of minimum travel time. The reason is that local extrema in travel time generally exist for inhomogeneous velocity structures, so that a ray path corresponding to a secondary arrival may be determined by a ray tracing routine. A simple example of the local minimum problem is presented to illustrate the need for care in the selection of the initial ray path estimate.

Consider a velocity model given by

$$V(z) = 4.75 + 0.75 \arctan[\, 2(z-7.5) \,]$$

where z is depth in km and V is velocity in km/sec (see Figure 2.2a). Let there be a source at 6.0 km depth and a receiver located at an epicentral distance of 24.0 km. Suppose a straight line is selected as the initial guess of the ray path. Then the bending ray tracing routine used (Pereyra et al., 1980) converges to an upgoing path (path 1) with a travel time of 6.75 sec and a path length of 24.8 km (Figure 2.2b). If instead the initial path guess used is the path determined via the described ray initialization procedure, the ray tracer converges to a refracted type path (path 2) with a travel time of 6.23 sec and a path length of 27.5 km (Figure 2.2c).

Path 1 is a true ray path. However it corresponds to a

local minimum in travel time, i.e. a secondary arrival. The ray tracing routine would never find path 2, the global minimum, starting from a straight-line initial path. Ray initialization provides an efficient algorithm for exploring the travel time surface to find the region of the global minimum. Of course it is not certain that this method will always result in finding the first-arrival path, but it is definitely an improvement over a simple straight-line guess.

2.4.3 ACCURACY OF TRAVEL TIMES FROM ART

Approximate ray tracing can also be used to take the place of costly three-dimensional ray tracing in some circumstances. According to Fermat's principle the travel time along a ray path is a stationary quantity, so that small perturbations in the path do not alter the travel time significantly. Thus if the estimated path is sufficiently close to the actual ray path, one can obtain a reasonable estimate of the true travel time by computing the travel time along the estimated path (now using the true velocity structure instead of the one-dimensional averaged structure).

To do this, the estimated path is divided into N segments all of length Δs. The travel time integral

$$T = \int_{\text{path}} \frac{1}{V}\, ds$$

can then be approximated by the sum

$$T = \sum_{j=1}^{N} 1/V(x_j,y_j,z_j)\ \Delta S$$

where (x_i,y_i,z_i) are the coordinates of the midpoint of the j'th segment. Alternatively the trapezoidal rule or Simpson's rule for numerical integration may be used. It is found that the travel time estimate calculated in this manner is a good approximation to the true travel time. The following representative tests illustrate the satisfactory results which can be achieved when a three-dimensional ray tracer is replaced by an ART routine.

An obvious way to determine the relative accuracy of travel times computed using ART is by making a direct comparison to travel times computed with three-dimensional ray tracing, using a laterally heterogeneous velocity structure. The velocity structure chosen for this comparison is an analytical three-dimensional model for Bear Valley, California, developed by Wesson (1971) and given by

$$V(x,y,z) = C_o + C_1 z + \frac{A(x-x_o)}{e^2+|x-x_o|} + \frac{C_p}{1+a(x-x_o)^2+b(y-y_o)^2+d(z-z_o)^2}$$

Parameter values are listed in Table 2.1, and a representative cross section is shown in Figure 2.3a. The model has a sharp velocity gradient along the San Andreas fault (at x=0), with generally higher velocities to the southwest (x>0) and a shallow low-velocity trough just northeast of the fault. Wesson derived this semi-empirical model from a study of P-wave travel times from a 1967

explosion in Bickmore Canyon.

In order to estimate the typical travel-time error resulting from the use of ART, travel times to the 13 stations shown in Figure 2.3b were calculated using both the three-dimensional ray tracer of Pereyra et al. (1980) and the ART routine for a set of hypothetical sources distributed through the area. A histogram of the difference in calculated travel time between the two methods, grouped in 0.01-sec intervals, is shown in Figure 2.4a. The mean error of ART is -0.02 sec with a standard deviation of 0.02 sec. Thus the ART arrivals tend to be late, but only by a per cent or so. For comparison a similar histogram is shown in Figure 2.4b with travel times calculated in a one-dimensional layered velocity model (see Table 2.2) using standard techniques. The mean error for this method is -0.18 sec and the standard deviation is 0.43 sec. Clearly ART provides a much improved estimate of the travel times, and at little more expense than the one-dimensional method.

2.4.4 EARTHQUAKE LOCATION USING ART

As a final test of the ART method, this routine is used to relocate the 1967 Bickmore Canyon shot (treating it as if it were an earthquake). The final location is compared to the true location, the location determined using three-dimensional ray tracing, and the location determined using the one-dimensional layered velocity model given in

Table 2.2. The results of these relocations are shown in Table 2.3. The three-dimensional ray tracer produces a solution essentially identical to that of Wesson (1971), who used the same data and velocity model but a different ray tracing technique. Remarkably, the relocation using ART is nearly the same as well, but it required fully 99 per cent less computer time. In contrast, the relocation using the layered model yields a strongly biased location and origin time with large arrival-time residuals.

These results could be anticipated to some extent. In section 2.4.4 it was shown that the ART routine could estimate travel times to roughly 0.02 sec in the velocity model used. Since this error is within the reading accuracy of the arrival-time readings, no increase in rms residual should be expected, and this is the case. In addition the travel times were consistently overestimated by 0.02 sec. Thus one would predict a change in the ART solution origin time of about 0.02 sec earlier than the ray tracing solution, and again this is the case. One final point is the fact that, in addition to the travel times, the hypocentral partial derivatives used in relocating the shot are only approximate. This probably results in the introduction of some additional bias into the final solution for the location (see Chapter 3).

2.4.5 ART BY DIRECT SEARCH

The ART routine just described has as its basis two assumptions. The first is that in general a ray path does not deviate substantially from a vertical plane. The second is that the path determined using ART will be sufficiently close (in the "Fermat" sense) to the true ray path. When these assumptions break down an alternative way of approximately determining ray paths and travel times is needed. Some reflection on Fermat's principle leads to a different simple approach for ART, which will be dubbed ART2. The only underlying assumption for ART2 is that the true ray path can be adequately approximated by an arc of a circle.

The scheme for ART2 involves the construction of a substantial number of arcs or circular paths connecting the source and the receiver, and the computation of the travel times along all of those paths. Arcuate paths of varying radii of curvature are examined (see Figure 2.5a), and the dip of the plane containing the arcs is varied systematically (Figure 2.5b) in order to adequately sample the relevant volume. From this large set of paths the estimate of the true minimum travel time path is selected on the basis of having the smallest travel time. If the actual minimum-time path is not severely contorted, ART2 should produce a good estimate of the path and the corresponding travel time.

The accuracy of ART2 can be assessed in an identical manner to that used for the first ART routine. The travel

times from the ficticious sources to the stations in Figure 2.3b are compared to those computed using three-dimensional ray tracing. The results are shown in a histogram in Figure 2.6. The mean error of ART2 is -0.01 sec with a standard deviation of 0.01 sec, clearly superior to the performance of the original ART routine. This doubling of accuracy is done at the cost of about a 50 per cent increase in computer time, but ART2 still remains far more economical than three-dimensional ray tracing.

2.4.6 SUMMARY

In summary, two independent means of deriving approximations to ray paths and travel times have been discussed. The original motivation for ART was to provide an initial guess of the ray path (for bending) or the initial ray direction (for shooting) for a three-dimensional ray tracing routine. However ART has proven to be quite useful for other purposes as well.

The travel time accuracy of both methods (ART and ART2), when compared with an actual three-dimensional ray tracer, is within the normal reading error for P-wave arrival times. As a result these routines are useful for determining earthquakes locations in three-dimensional velocity structures to a reasonable accuracy and at extremely low cost. In Chapter 3 we explore the usefulness of approximate ray tracing for the total simultaneous inversion problem.

2.5 PARTIAL DERIVATIVES

Sections 2.3 and 2.4 discuss techniques for computing P-wave travel times in a heterogeneous medium. These travel times are used to compute the arrival time residuals for equation 2.6, the basic equation of the simultaneous inversion method. The other quantities needed for the construction of this equation are the partial derivatives of the arrival (or travel) time with respect to each parameter of the model. These parameters are the x, y and z coordinates of the earthquake source, the source origin time, and the velocity parameters. In this section expressions for these partial derivatives are formally derived.

2.5.1 HYPOCENTRAL PARTIAL DERIVATIVES

The origin time partial derivative is by far the simplest to evaluate. The calculated arrival time t_{cal} is given by

$$t_{cal} = t_o + t$$

where t_o is the origin time and t is the travel time. So obviously

$$\frac{\partial t_{cal}}{\partial t_o} = +1$$

The other partial derivatives are rather less trivial to

derive.

The partial derivatives of the arrival time (or equivalently the travel time) with respect to the source coordinates can be obtained from a simple geometrical argument. An example for a homogeneous velocity model is illustrative.

Let there be a source at $\underline{P1}=(x1,y1,z1)$ and a receiver at $\underline{P2}=(x2,y2,z2)$, and let the velocity be given by $V(x,y,z)=V_o$. Then the travel time from $\underline{P1}$ to $\underline{P2}$ is given by

$$t = || \underline{P2} - \underline{P1} ||/V_o$$

or simply

$$t = \frac{1}{V_o} \sqrt{(x2-x1)^2+(y1-y2)^2+(z2-z1)^2} \qquad (2.14)$$

From equation 2.14 it is easy to show that

$$\partial t/\partial x1 = -1/V_o \; dx/ds$$
$$\partial t/\partial y1 = -1/V_o \; dy/ds$$
$$\partial t/\partial z1 = -1/V_o \; dz/ds$$

where dx/ds, dy/ds and dz/ds are the direction cosines of the ray path. If we define the ray vector

$$\underline{r} = (dx/ds, \; dy/ds, \; dz/ds)$$

and an infinitesimal source displacement vector

$$\underline{d} = (\delta x1, \; \delta y1, \; \delta z1)$$

(see Figure 2.7) then the change in travel time due to the displacement is given by

$$\delta t = -1/V_o \ (\underline{r} \cdot \underline{d}) \qquad (2.15)$$

Inspection of equation 2.15 reveals that travel time changes will be greatest for source displacements close to the direction of the ray vector, but will vanish for displacement normal to the ray vector. Thus the Cartesian directions (x, y or z) for which the ray vector has a relatively large component have the largest corresponding partial derivatives, and displacement along such a direction produces the maximal change in the travel time.

These simple arguments can be extended to a medium which is heterogeneous. As before, let there be a source at P1 and a receiver at P2, $\underline{r}$ is the ray vector (at P1), and $\underline{d}$ is the infinitesimal displacement vector (see Figure 2.8a). It is claimed that, to first order, the change in travel time resulting from the displacement $\underline{d}$ is due only to the infinitesimal change in the length of the path. To see that this is the case, consider the ray path from P0 to P2 which passes through point P1 (call it C) and the path (not necessarily a raypath) from P0 to P1 which passes through the point P1 + $\underline{d}$ (call it C'; see Figure 2.8b). According to Fermat's principle, the travel time along C and C' are essentially the same. Obviously there is some point P1' along C' such that the travel time from P1' to P2 is the same as that from P1 to P2. Since the displacement $\underline{d}$ is

infinitesimal, from geometry this point P1' is at the intersection of the normal to the ray vector $\underline{r}$ at P1 with the curve C' (see Figure 2.8c).

Since the travel time from P1' to P2 equals that from P1 to P2, the travel time from P1 + $\underline{d}$ to P2 will differ by an amount

$$|\delta t| = 1/V(\underline{P1}) \quad |\delta s| \tag{2.16}$$

From Figure 2.8c it is clear that

$$\delta s = \underline{r} \cdot \underline{d} \tag{2.17}$$

Combining equations 2.16 and 2.17, and noting that if δs is positive (the new ray path is shorter) then δt should be negative (the travel time will decrease) we find

$$\delta t = -1/V(\underline{P1}) \quad (\underline{r} \cdot \underline{d})$$

which replicates equation 2.15 for a homogeneous medium. Recalling the definitions of $\underline{r}$ and $\underline{d}$ we find

$$\delta t = -1/V(\underline{P1}) \; [dx/ds \; \delta x1 + dy/ds \; \delta y1 + dz/ds \; \delta z1]$$

so that we arrive at the expressions for the partial derivatives with respect to the hypocenter coordinates:

$$\begin{aligned} \partial t/\partial x1 &= -1/V \quad dx/ds \\ \partial t/\partial y1 &= -1/V \quad dy/ds \\ \partial t/\partial z1 &= -1/V \quad dz/ds \end{aligned} \tag{2.18}$$

where the velocity V and the ray vector components dx/ds, dy/ds and dz/ds are all evaluated at the hypocenter P1.

An elegant mathematical derivation of equations 2.18 due to R. Comer (written communication, 1979) is based on the calculus of variations. Returning to Figure 2.8a, consider the travel time integrals for the paths from P1 to P2 and P1 + d to P2. Parameterize both paths in terms of the parameter q which varies from the fixed values of q1 to q2:

$$\underline{P1} \text{ to } \underline{P2}: \quad \text{path } \underline{P}(q),\ q = q1 \text{ to } q2$$

$$\underline{P1} + \underline{d} \text{ to } \underline{P2}: \quad \text{path } \underline{P}(q)+\delta P(q),\ q = q1 \text{ to } q2$$

and write the path integral as

$$t = \int_{q1}^{q2} W(x,\dot{x},y,\dot{y},z,\dot{z})\ dq$$

where the dot indicates differentiation with respect to q and

$$W = (\dot{x}^2+\dot{y}^2+\dot{z}^2)^{\frac{1}{2}}/V(x,y,z)$$

The variation in travel time δt between the two paths is given by

$$t = \int_{q1}^{q2} \delta W\ dq$$

$$= \int_{q1}^{q2} \left(\frac{\partial W}{\partial x}\delta x + \frac{\partial W}{\partial y}\delta y + \frac{\partial W}{\partial z}\delta z + \frac{\partial W}{\partial \dot{x}}\delta \dot{x} + \frac{\partial W}{\partial \dot{y}}\delta \dot{y} + \frac{\partial W}{\partial \dot{z}}\delta \dot{z}\right) dq$$

Integrating the last three terms by parts yields

$$\delta t = [\partial W/\partial \dot{x}\ \delta x + \partial W/\partial \dot{y}\ \delta y + \partial W/\partial \dot{z}\ \delta z]_{q1}^{q2} - \int_{q1}^{q2} \left(\frac{d}{dq}\frac{\partial W}{\partial \dot{x}} - \frac{\partial W}{\partial x}\right)\delta x\, dq - \int_{q1}^{q2} \left(\frac{d}{dq}\frac{\partial W}{\partial \dot{y}} - \frac{\partial W}{\partial y}\right)\delta y\, dq - \int_{q1}^{q2} \left(\frac{d}{dq}\frac{\partial W}{\partial \dot{z}} - \frac{\partial W}{\partial z}\right)\delta z\, dq \qquad (2.19)$$

The integrands in equation 2.19 are Euler's equations, which vanish along a ray path. Additionally, the end point P2 is fixed, so that

$$\delta x(q2) = \delta y(q2) = \delta z(q2) = 0$$

We are left with

$$\delta t = -\left[\frac{\partial W}{\partial \dot{x}}\,\delta x + \frac{\partial W}{\partial \dot{y}}\,\delta y + \frac{\partial W}{\partial \dot{z}}\,\delta z\right]_{q=q1}$$

or

$$\delta t = -\frac{\partial W}{\partial \dot{x}}\Big|_{q1}\delta x1 - \frac{\partial W}{\partial \dot{y}}\Big|_{q1}\delta y1 - \frac{\partial W}{\partial \dot{z}}\Big|_{q1}\delta z1 \qquad (2.20)$$

Returning to the definition of W, we have

$$\frac{\partial W}{\partial \dot{x}} = \frac{\partial}{\partial \dot{x}}\left[(\dot{x}^2 + \dot{y}^2 + \dot{z}^2)^{1/2}/V\right]$$

$$\frac{\partial W}{\partial \dot{x}} = \frac{1}{V}\frac{dx}{ds} \qquad (2.21)$$

with similar equations for the y and z components. Finally,

combining Equations 2.20 and 2.21

$$\frac{\partial t}{\partial xl} = -\frac{1}{V}\frac{dx}{ds}$$

$$\frac{\partial t}{\partial yl} = -\frac{1}{V}\frac{dy}{ds}$$

$$\frac{\partial t}{\partial zl} = -\frac{1}{V}\frac{dz}{ds}$$

replicating equations 2.18.

2.5.2 VELOCITY PARAMETER PARTIAL DERIVATIVES

The partial derivative of the travel time with respect to a velocity parameter is much more difficult to fully grasp intuitively. It is obvious that the travel time between two points depends on the values of the velocity parameters, but this dependence in turn depends explicitly on the route of the ray path and implicitly on the nature of the velocity parameterization. The general expression for the partial derivative for the i'th parameter illustrates this dependence:

$$\frac{\partial t}{\partial v_i} = -\int_{path} (V(x,y,z))^{-2} \frac{\partial V(x,y,z)}{\partial v_i}\, ds$$

The term $\partial V/\partial v_i$ is tied to the representation or parameterization of the velocity model.

In section 2.2.2 an example of a simple block-type parameterization was discussed. As another example,

consider the case of a velocity model defined by values specified at grid points (nodes) with an interpolation function used between points. The travel time integral can be approximately represented by a discrete sum

$$t = \sum_{i=1}^{N} \Delta s_i / V(x_i, y_i, z_i) \qquad (2.22)$$

where, for example, the path is broken up into N segments and the velocity is evaluated at the segment midpoint (see Figure 2.9a). In this case the velocity is computed as a weighted sum of velocity values specified at nodes (grid points):

$$V(x_i, y_i, z_i) = \sum_{j=1}^{M} w_j \, v_j$$

where v_j is the velocity at the j'th node and w_j is the interpolation weight for that node (see Figure 2.9b). Thus equation 2.22 becomes

$$t = \sum_{i=1}^{N} \frac{\Delta s_i}{\sum_j w_j \, v_j}$$

The partial derivative of the travel time with respect to the velocity at the k'th node is then

$$\frac{\partial t}{\partial v_k} = \sum_{i=1}^{N} -\Delta s_i \, V(x_i, y_i, z_i)^{-2} \, \frac{\partial}{\partial v_k} \left[\sum_{j=1}^{M} w_j \, v_j \right]$$

or

$$\frac{\partial t}{\partial v_k} = \sum_{i=1}^{N} -\Delta s_i \, V(x_i, y_i, z_i)^{-2} \sum_{j=1}^{M} w_j \, \delta_{jk} \qquad (2.23)$$

where δ_{jk} is the Kronecker delta. This formulation of the velocity partial derivative is generally applicable to almost any interpolation scheme.

The tools and techniques presented in this and the previous two sections are sufficient for constructing the set of equations needed for the simultaneous inversion problem, that is Equation 2.6. The final two sections of this chapter discuss methods for carrying out the inverse problem - iteratively solving the system of equations like 2.6 to derive a solution for the earthquake locations and the earth's velocity structure.

2.6 PARAMETER SEPARATION

For the earthquake location problem it is never necessary to invert an untractably large matrix to arrive at a solution. The reason is that there are only four hypocentral parameters involved, so the matrix will be (at most) of size 4 x number of observations. However for the simultaneous inversion problem matrix size is an important issue. First, many observations are usually required to resolve the velocity structure, and second, the addition of each earthquake adds four more parameters to the number of

unknowns, which includes all the velocity parameters as well. A typical three-dimensional inversion might have 100 velocity parameters, 100 earthquakes, and 2000 observations, resulting in a matrix of size 500 x 2000! Even the use of least squares can only reduce the size of this system to 500 x 500, far too large to be economically inverted in the usual fashion.

Fortunately two similar methods for dealing with the size of the simultaneous inversion problem have recently been developed, one by Pavlis and Booker (1980) and one by Spencer and Gubbins (1980). Both methods take advantage of the fact that the portion of the matrix containing the hypocentral partial derivatives is extremely sparse, and also that the hypocentral parameters (4 for each event) are in principle overdetermined by the data. (Note that the entire problem is overdetermined in the Spencer and Gubbins approach, as it is in this work). These two approaches to this technique, which we term the parameter separation method, are outlined here.

2.6.1 METHOD OF PAVLIS AND BOOKER

Pavlis and Booker (1980) consider the mixed discrete-continuous inverse problem, whereby the hypocenters are represented as usual by four discrete parameters each, but the velocity structure is represented by a continuous function (essentially an infinite number of parameters).

However their separation procedure is directly applicable to the formulation of simultaneous inversion adopted in section 2.2 in which the velocity is represented by a finite number of parameters.

In general, the simultaneous inversion problem can be expressed mathematically as the solution of a linearized matrix equation

$$\underline{\underline{A}}\ \underline{x} = \underline{r}$$

where $\underline{\underline{A}}$ is the matrix of hypocentral and medium (i.e. velocity) partial derivatives, $\underline{x}$ is the column vector of unknown perturbations of hypocentral and medium parameters, and $\underline{r}$ is the column vector of arrival time residuals. The structure of the matrix $\underline{\underline{A}}$ is

$$\underline{\underline{A}} = \left|\begin{array}{ccccc|c} H_1 & & & & & \\ & H_2 & & & & \\ & & \ddots & & & M \\ & & & \ddots & & \\ & & & & H_n & \end{array}\right|$$

where $\underline{\underline{H}}_i$ is the matrix of hypocentral partial derivatives for the i'th event, and $\underline{\underline{M}}$ is the matrix of medium partial derivatives. Clearly the residuals of one event are coupled to those of another event through the medium matrix $\underline{\underline{M}}$ only.

Consider the equations corresponding to a single event. Then we have

$$\underline{\underline{A}}_i\ \underline{x}_i = \underline{r}_i \qquad (2.24)$$

where $\underline{A}_i = [\ H_i\ M_i\ ]$, and let $\underline{r}_i$ be D x 1. Pavlis and Booker (1980) have shown that if D is greater than 4 (the number of hypocentral parameters) then equation 2.24 can be operated upon to construct a matrix equation which contains only the medium parameters. Their technique is summarized here, modified to correspond to the finite parameterization approach.

Rewrite equation 2.24 as

$$\underline{H}_i\ \underline{\Delta h} + \underline{M}_i\ \underline{\Delta m} = \underline{r}_i \qquad (2.25)$$

where $\underline{\Delta h}$ and $\underline{\Delta m}$ are vectors of adjustments to the hypocentral and medium parameters respectively. If we have D>4, then the unknown vector $\underline{\Delta h}$ will be overdetermined. The matrix $\underline{H}_i$ can be decomposed as

$$\underline{H}_i = \underline{U}\ \underline{S}\ \underline{V}^T \qquad (2.26)$$

where $\underline{U}$ and $\underline{V}$ are square orthogonal matrices, $\underline{S}$ is a diagonal matrix, $\underline{H}_i$ is D x 4, $\underline{U}$ is D x D, $\underline{V}$ is 4 x 4, and $\underline{S}$ is D x 4 (Lanczos, 1961). Furthermore $\underline{U}$ can be written as

$$\underline{U} = [\ U_p\ U_o\ ]$$

where $\underline{U}_p$ is D x 4. The matrix $\underline{U}_o$ (D x D-4) has the property that

$$\underline{U}_o^T\ \underline{H}_i = 0$$

so that operating on equation 2.25 with $\underline{U}_o^T$ results in

$$\underline{M}_i' \, \underline{\Delta m} \equiv \underline{U}_o^T \, \underline{M}_i \, \underline{\Delta m} = \underline{U}_o^T \, \underline{r}_i \equiv \underline{r}_i'$$

which contains only medium parameters.

Why does $\underline{U}_o^T$ annihilate $\underline{H}_i$? To see that this is the case, write out equation 2.26 as

$$\underline{H}_i = [\, U_p \; U_o \,] \begin{vmatrix} S_1 & & & 0 \\ & S_2 & & \\ & & S_3 & \\ 0 & & & S_4 \\ - & - & - & - \\ & & 0 & \end{vmatrix} [\, V^T \,] \qquad (2.27)$$

$\underline{U}$ is orthogonal, so equation 2.27 can be rewritten as

$$\begin{vmatrix} U_p^T \\ U_o^T \end{vmatrix} \underline{H}_i = \begin{vmatrix} S_1 & & & 0 \\ & S_2 & & \\ & & S_3 & \\ 0 & & & S_4 \\ - & - & - & - \\ & & 0 & \end{vmatrix} [\, V^T \,] \qquad (2.28)$$

From equation 2.28 it is clear that $\underline{U}_o^T \, \underline{H}_i = 0$.

The matrix $\underline{U}_o$ can be computed using the singular value decomposition, but unless the singular values are specifically desired it is more sensible (i.e. less costly) to determine $\underline{U}_o$ via the QR decomposition. See Appendix B.1 for the definition of a Householder transformation and a description of QR decomposition.

The value of this separation procedure is that for each earthquake the hypocenter part of the inversion can be separated from the medium part, reducing the overall size of the linear system to be solved. As each event is treated

the hypocentral parameters are decoupled and the new rows of the separated medium partial derivative matrix $\underline{\underline{M}}'$ are formed. Once all events have been processed, the relatively small system

$$\underline{\underline{M}}' \ \underline{\Delta m} = \underline{r}' \qquad (2.29)$$

can be solved using standard inverse techniques. We note that to include explosion data in the inversion, one need only add rows to $\underline{\underline{M}}'$ and $\underline{r}'$ corresponding to medium partial derivatives along explosion-to-station ray paths and the computed arrival time residuals. It is also simple to include quarry blasts for the case when the position of the blast is accurately known but the origin time is not.

The parameter separation approach has other desirable features. First it is important to emphasize that this procedure does not by itself alter the final solution. In principle you will get the same answer by carrying out the parameter separation and then solving the system as you would by directly solving the entire system in one step. See Appendix B.3 for an illustration.

A second valuable property described by Pavlis and Booker (1980) is that the solution for the velocity parameters is "locally independent" of the initial estimates of the hypocenters. This means that if the hypocenter estimates lie close to the true hypocenters then the "separated" data are not biased by the actual hypocenter estimates used. Unfortunately it is not clear what "close" really means, but

a necessary condition is clearly that the hypocenters are well constrained.

2.6.2 METHOD OF SPENCER AND GUBBINS

Spencer and Gubbins (1980) describe a similar method for parameter separation based on a finite parameterization for the velocity structure. Starting with the simultaneous inversion matrix equation

$$\underline{H}\ \underline{\Delta h} + \underline{M}\ \underline{\Delta m} = \underline{r} \qquad (2.30)$$

the normal equations corresponding to the least squares solution to equation 2.30 can be written in two distinct parts

$$\underline{H}^T\ \underline{H}\ \underline{\Delta h} + \underline{H}^T\ \underline{M}\ \underline{\Delta m} = \underline{H}^T\ \underline{r} \qquad (2.31a)$$

$$\underline{M}^T\ \underline{H}\ \underline{\Delta h} + \underline{M}^T\ \underline{M}\ \underline{\Delta m} = \underline{M}^T\ \underline{r} \qquad (2.31b)$$

Solving equation 2.31a in terms of $\underline{\Delta h}$ yields

$$\underline{\Delta h} = (\underline{H}^T\ \underline{H})^{-1}\ [\ \underline{H}^T\ \underline{r} - \underline{H}^T\ \underline{M}\ \underline{\Delta m}\ ]$$

which can then be substituted for $\underline{\Delta h}$ in equation 2.31b and solved for $\underline{\Delta m}$ as

$$\underline{\Delta m} = (\underline{O}^T\ \underline{M})^{-1}\ \underline{O}^T\ \underline{r}$$

where

$$\underline{O}^T = \underline{M}^T - \underline{M}^T \underline{H} (\underline{H}^T \underline{H})^{-1} \underline{H}^T$$

Note that $\underline{H}^T\underline{H}$ and $\underline{O}^T\underline{M}$ are square matrices of sizes 4 times the number of earthquakes and the number of velocity parameters, respectively. Furthermore, $\underline{H}^T\underline{H}$ is composed of 4 x 4 submatrices lying along the diagonal with zeros elsewhere, so that its inverse is the matrix composed of submatrices lying along the diagonal which are the inverses of each of the 4 x 4 submatrices of $\underline{H}^T\underline{H}$. The result is that the simultaneous inversion problem formulated in this manner requires the inversion of many 4 x 4 matrices (one for each earthquake) and one square matrix of size number of velocity parameters, a considerable computational savings.

The modified Pavlis and Booker approach (modified to deal with a finitely parameterized velocity structure) was adopted for the major part of the work of this thesis principally because of the timely availability of the method. In section 2.7 the inversion and iteration algorithm is discussed, including the details of the scheme for implimenting the parameter separation procedure.

2.7 INVERSION AND ITERATION

The preceding sections have described the various elements of the simultaneous inversion problem. In this final section these elements are assembled into an iterative algorithm. The points which remain to be discussed include

how to begin the procedure, how to invert equation 2.29 for the velocity model perturbations, how to iterate, and how (or when) to terminate the procedure.

2.7.1 INITIAL MODEL

The requirements for starting the inversion are an initial model for the velocity structure and initial estimates of the hypocenters. The possible choices for the starting velocity model are basically controlled by the availability of independent information on the local crustal structure. In the case where there is an absence of any other data on the structure, it is vital to explore a range of initial models (in fact this is desirable in all situations!). There are many sources of useful information for constructing (or evaluating) velocity models, for example geology combined with laboratory determinations of rock velocities, well-log data, refraction studies, and of course previous earthquake studies.

Given an initial model for the velocity structure, there exists a reasonable choice for the starting hypocenter estimates. As Pavlis and Booker (1980) point out, the hypocenters determined by a standard earthquake location procedure using the initial velocity structure provide a logical starting location. This choice has some inherent advantages. Hypocenter locations have been found to be only weakly dependent on the velocity structure (Peters, 1973).

Therefore this choice is likely to be reasonably close to the true location and thus hopefully within the range of "local independence" for the separation procedure as discussed by Pavlis and Booker (1980) and hopefully close to the range of linearity for the simultaneous inversion problem as a whole (see Chapter 3). In addition, this choice automatically means that the residual vector $\underline{r}$ is as small as possible initially, which should aid the inversion in making cautious stable steps towards a final solution.

The routine for performing the relocations uses approximate ray tracing to compute the theoretical travel times. The error analyses described in section 2.4 suggest that the locations will be sufficiently accurate for our purposes. Moreover, each event generally needs to be relocated using several iterations, so that the cost of three-dimensional ray tracing would be enormous. The routine uses singular value decomposition (SVD; see Appendix B.2) to compute the hypocentral adjustments. SVD is moderately expensive compared to, say, solving the normal equations. However the singular values give important information regarding how well constrained the solution is. In particular poor depth control, which is quite undesirable, can be detected and those events removed from the inversion. These relocations are done after each velocity inversion step (as well as initially) yielding a stable algoritm which has been found to converge smoothly and strongly in every modeling attempt to date.

2.7.2 THE FORWARD PROBLEM - CHOICE OF RAY TRACING METHOD

The choice of ray tracing method is the principle option available in the forward problem for simultaneous inversion. The options are the two three-dimensional ray tracing routines (one shooting, one bending) and the two ART routines. Obviously the use of the latter two routines implies an additional level of approximation in the inversion, the effect of which is difficult to fully assess (see Chapter 3 for some analysis of this problem). Certainly their low cost and reasonable accuracy justifies their use in the preliminary exploratory stages of the modeling of an area.

2.7.3 THE INVERSE PROBLEM

Once the forward problem is complete for a single event, the modified Pavlis and Booker parameter separation procedure is carried out to yield the set of equations

$$\underline{\underline{M}}'_i \, \underline{\Delta m} = \underline{r}'_i$$

(see section 2.6). Rather than accumulate the entire matrix $\underline{\underline{M}}'$ of transformed velocity partial derivatives for eventual inversion, a matrix which continually grows in size as more and more earthquake data are added, we have chosen to accumulate the matrix $\underline{\underline{M}}' {}^{T}\underline{\underline{M}}'$. This process can be done

sequentially as each event is processed, and results in a fixed-size symmetric matrix which can be stored (and eventually inverted) easily. Naturally we also accumulate the vector $\underline{M}'^{T}\underline{r}'$. In other words, instead of solving for the velocity perturbations using SVD or perhaps QR decomposition on the transformed matrix $\underline{M}'$, we form the normal equations using the separated derivative matrix and data for the eventual inversion of $\underline{M}'^{T}\underline{M}'$. This particular procedure (for which it is assumed in practice that all of the singular values of the hypocenter submatrices are non-zero) is mathematically equivalent to the Spencer and Gubbins method (see Appendix B.3).

The next step in the algorithm is the inversion of the matrix equation

$$(\underline{M}'^{T}\ \underline{M}')\ \underline{\Delta m} = \underline{M}'^{T}\underline{r}' \qquad (2.32)$$

which is the normal equations form of equation 2.29. This system of equations is overdetermined (i.e. more equations than unknowns). In general there will be no unique solution (Lawson and Hanson, 1974), so we appeal to the least squares method to derive an answer. However the least squares solution

$$\underline{\Delta m} = (\underline{M}'^{T}\ \underline{M}')^{-1}\ \underline{M}'^{T}\ \underline{r}'$$

is known to be vulnerable to undesirable instability due to random data error (Aki and Lee, 1976). Thus we utilize the

Levenberg-Marquadt approach of damped least squares (DLS) to avoid the problem of large model perturbations for poorly constrained parameters. A full explanation of the DLS method can be found in Wolfe (1978). Briefly, the DLS sclution is given by

$$\underline{\Delta m} = (\underline{M}'^{T}\ \underline{M}' + \lambda^2\ \underline{I})\ \underline{M}'^{T}\ \underline{r}' \qquad (2.33)$$

where λ is called the damping parameter. Adding the quantity λ^2 to the diagonal elements of $\underline{M}'^{T}\underline{M}'$ has the effect of subduing the large changes which would occur for near-zero singular values in the standard least squares inversion (Crosson, 1976a). If λ is chosen to satisfy

$$\lambda^2 = C_d/C_m$$

where C_d is the data variance and C_m is the model variance, then the DLS solution is equivalent to that of the stochastic inverse of Franklin (1970).

2.7.4 ITERATION AND TERMINATION

Iteration of the algorithm is quite straightforward. If the decision is made to continue, the velocity parameter adjustments computed from equation 2.33 are applied to the velocity model. Generally an upper limit is imposed on the allowed velocity change per iteration in an effort to stay

within the linear range of the inversion (see Chapter 3). The entire set of earthquakes is then relocated using the perturbed velocity structure in exactly the same manner (and for the same reasons) as for the initial iteration step. The simultaneous inversion step is then carried out using parameter separation, and so on.

Finally, it is necessary to be able to systematically determine at what point to stop iterating. The data contain measurement errors, making it virtually impossible (and meaningless!) to reduce all the residuals to precisely zero. Aki (written communication, 1980) suggests that the F test provides a sensible measure for selecting a stopping point.

The F test is used to compare the variances of two normally distributed variables (De Groot, 1975). The variables to be tested are the arrival time residuals before and after one iteration step. Let the initial residual variance be σ_i^2 (sum of the squared residuals divided by the number of degrees of freedom n_i) and the final variance be σ_f^2 (with number of degrees of freedom n_f), and define the variance reduction ratio

$$R = \sigma_i^2/\sigma_f^2$$

If the residuals are normally distributed, R will obey the F distribution. For a given level of significance (let's use 0.05) the value of R is compared to the 95 per cent quantile

of the F distribution for the appropriate number of degrees of freedom $F(n_i, n_f, 0.95)$. If R exceeds F, then the final variance is smaller than the initial variance at the significance level of 0.05. This would indicate that a meaningful improvement in the model was achieved by the current iteration step, and a further iteration would be called for. If however R does not exceed F then the variance improvement for this step is not significant, and the iterations should be terminated.

TABLE 2.1

Velocity model parameters (Wesson, 1971)

C_0	4.2474
C_1	0.4514
A	0.9320
X_0	0.0
e	0.75
C_p	-1.1393
a	0.05
b	0.0005
Y_0	-38.00
d	0.10
Z_0	-1.0

TABLE 2.2

Regionally averaged one-dimensional velocity model

Depth to top of layer (km)	Layer velocity (km/s)
0.0	3.0
1.5	5.0
3.5	6.0

TABLE 2.3

Method of shot location	Relocation errors		
	Origin time (sec)	Hypocenter (km)	RMS residual (sec)
A. Ray Tracer	-0.01	0.38	0.08
B. ART	0.02	0.40	0.08
C. 1-D Velocity Model	-0.48	2.23	0.22

FIGURE CAPTIONS

Figure 2.1 a) One-dimensional velocity model is constructed from a lateral average of velocities at nearby grid points.

b) Travel times are determined by numerical integration along ray paths appropriate for the average structure.

Figure 2.2 a) One-dimensional velocity model used to illustrate the problem created by local minima in travel time. The medium has a multiply-branched travel time curve.

b) and c) Ray paths determined by the bending method (solid lines) using two different initial paths (dashed lines) in the velocity structure shown in a). Solution in b) uses a straight-line initial path and converges to a secondary arrival. Solution in c) uses the initial path from ART and converges to the minimum time ray path.

Figure 2.3 a) Cross-section of the three-dimensional velocity model of Wesson (1971) along section AA' in b).

b) Locations of the stations (triangles) and ficticious hypocenters (circles) used to test the accuracy of ART travel times. Integers denote hypocenter depths in kilometers. S indicates the location of the Bickmore Canyon shot point.

Figure 2.4 Travel time errors computed using ART (in a) and a layered earth model (in b). Errors are with respect to three-dimensional ray tracing travel times. Note tenfold change of time scale between a) and b).

Figure 2.5 ART by direct search
a) circular paths of different radii of curvature are constructed.

b) plane containing the paths is rotated about the source-receiver axis.

Figure 2.6 Travel time errors computed using ART2 compared to three-dimensional ray tracing. Compare with Figure 2.4.

Figure 2.7 Diagram for determining the change in travel time due to an infinitesimal source displacement in a homogeneous medium.

Figure 2.8 Diagrams for determining the change in travel time due to an infintesimal displacement in a heterogeneous medium.

a) source (P1), receiver (P2), ray vector ($\underline{r}$), and displacement vector ($\underline{d}$).

b) finding the point P1' such that the travel time from P1 to P2 equals that from P1' to P2.

c) the change in travel time due to the displacement $\underline{d}$ results from the change in total path length δs.

Figure 2.9 a) Computation of the travel time along a ray path using a discrete sum.

b) The velocity at a given point is interpolated from the velocity values at surrounding grid points

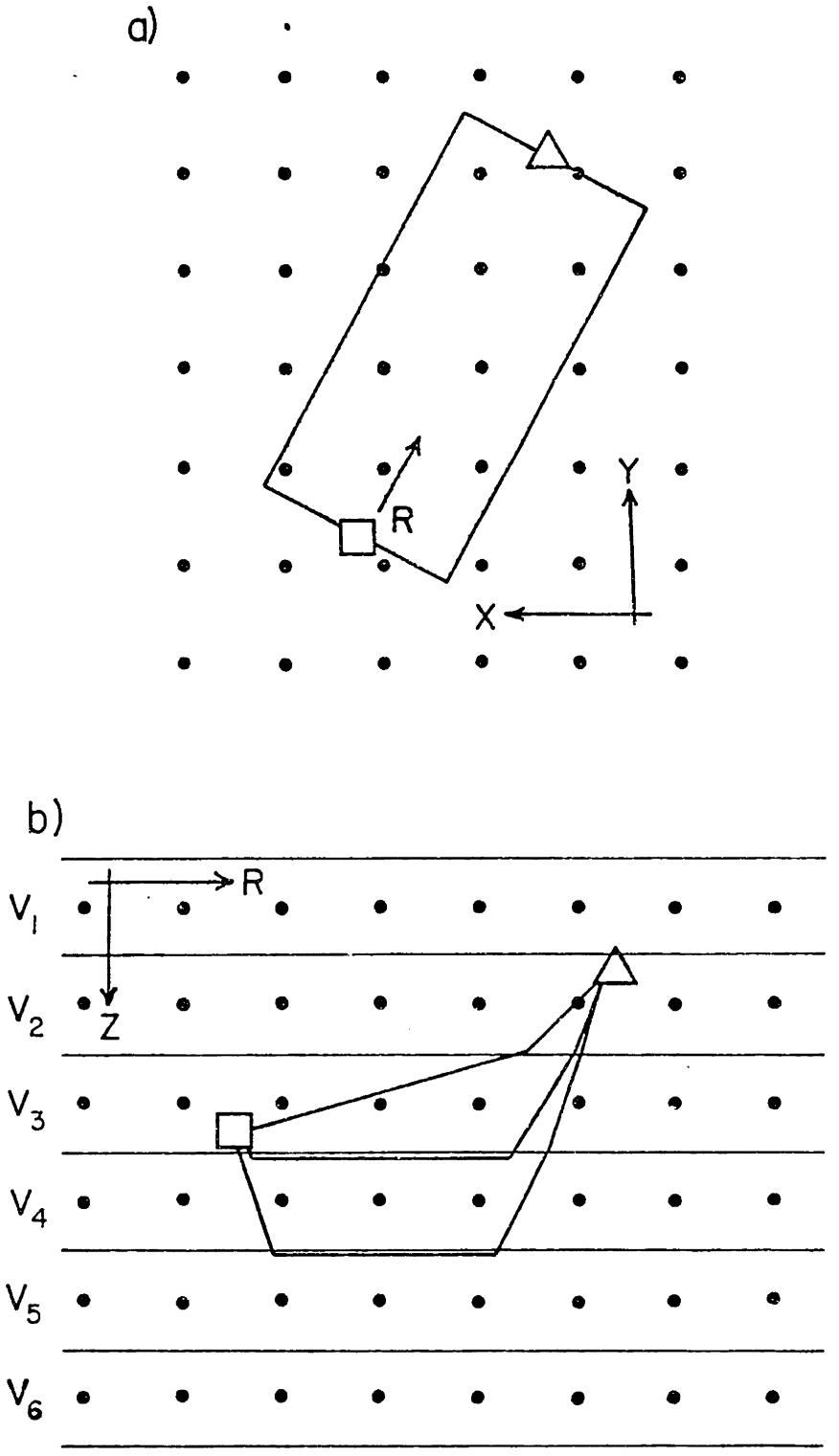

Figure 2.1

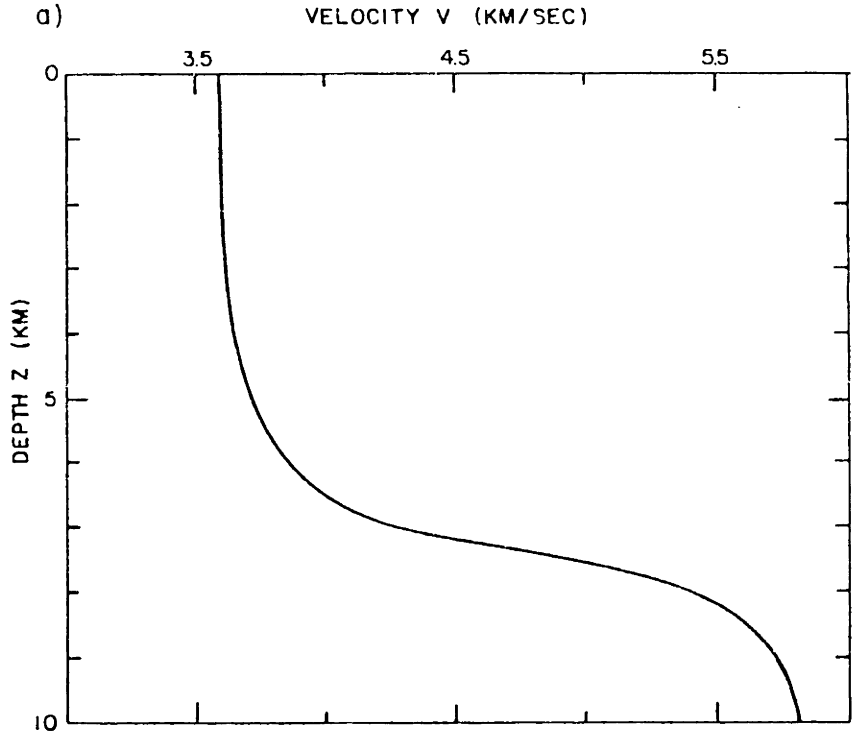

Figure 2.2

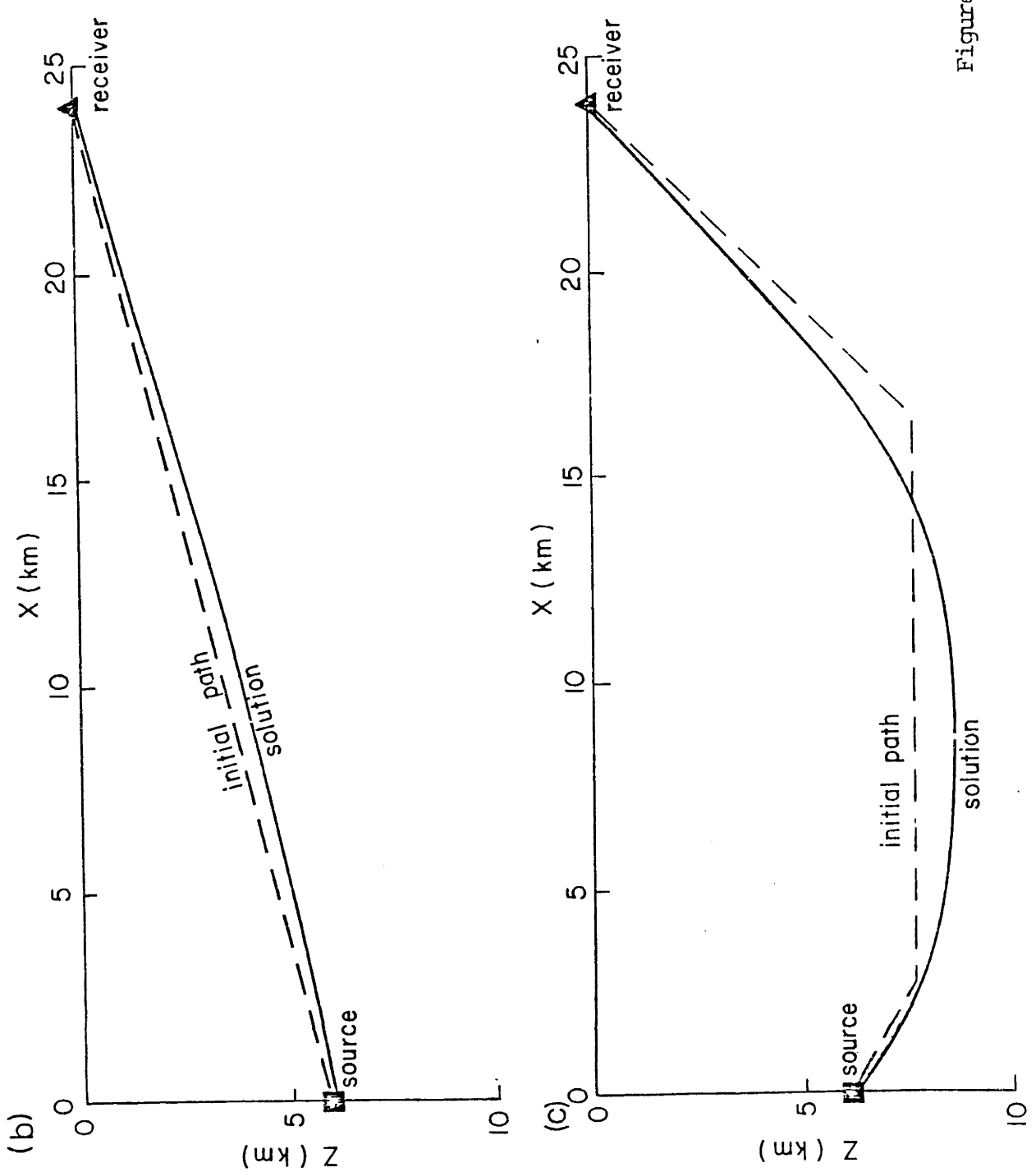

Figure 2.2 (cont)

a) CROSS SECTION OF VELOCITY MODEL

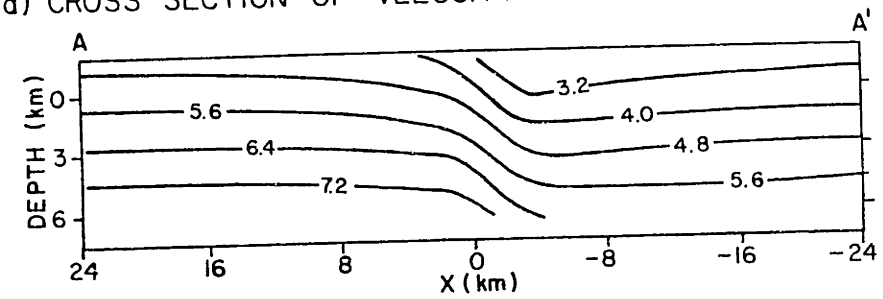

b) LOCATIONS OF SHOT, RECEIVERS AND HYPOTHETICAL SOURCES

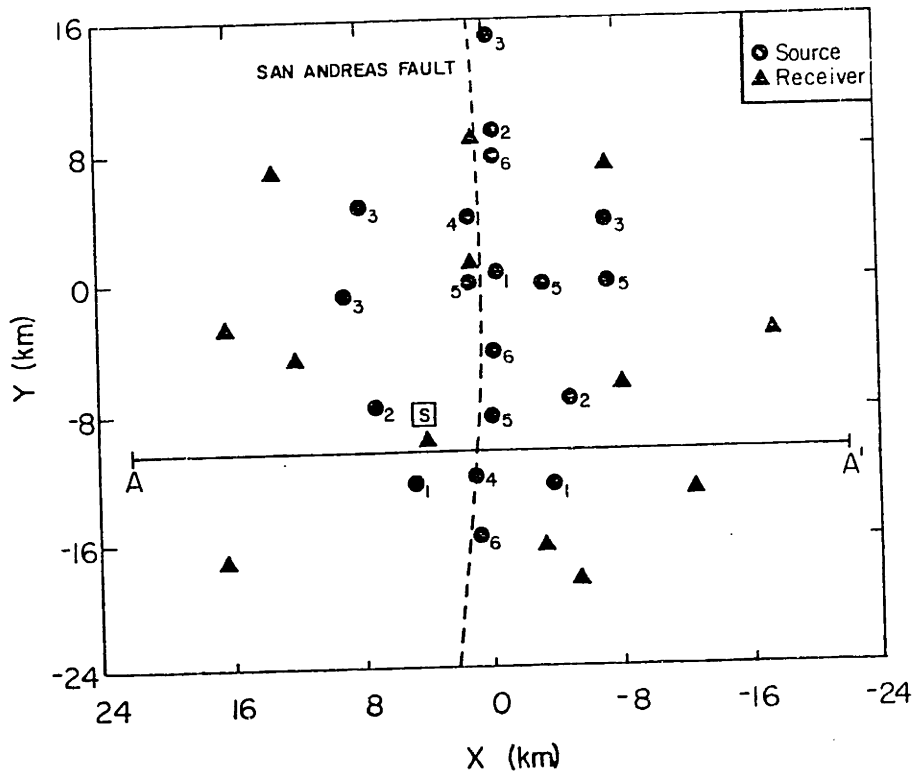

Figure 2.3

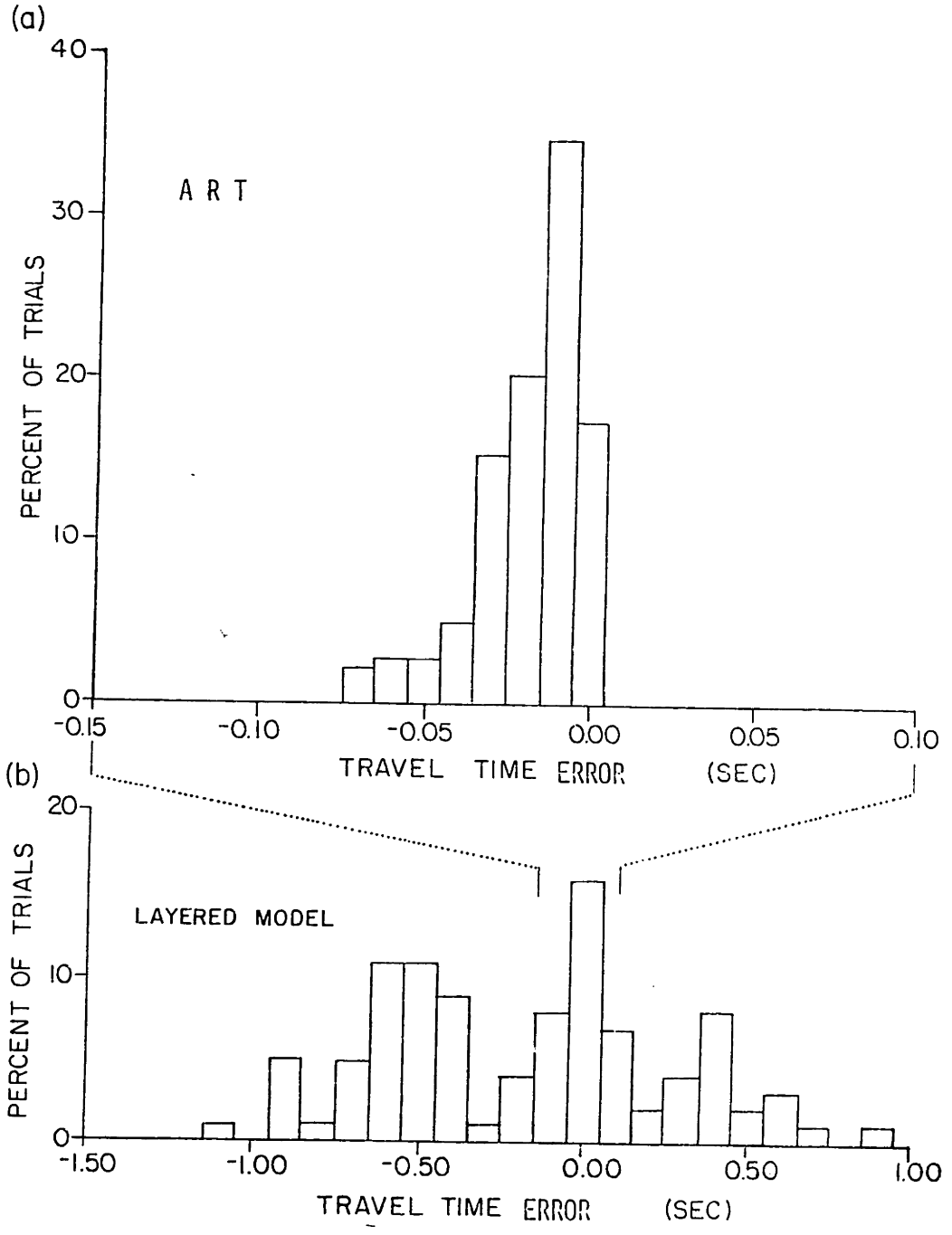
(a)
ART
PERCENT OF TRIALS
40
30
20
10
0
-0.15
-0.10
-0.05
0.00
0.05
0.10
TRAVEL TIME ERROR (SEC)
(b)
LAYERED MODEL
PERCENT OF TRIALS
20
10
0
-1.50
-1.00
-0.50
0.00
0.50
1.00
TRAVEL TIME ERROR (SEC)

Figure 2.4

a)

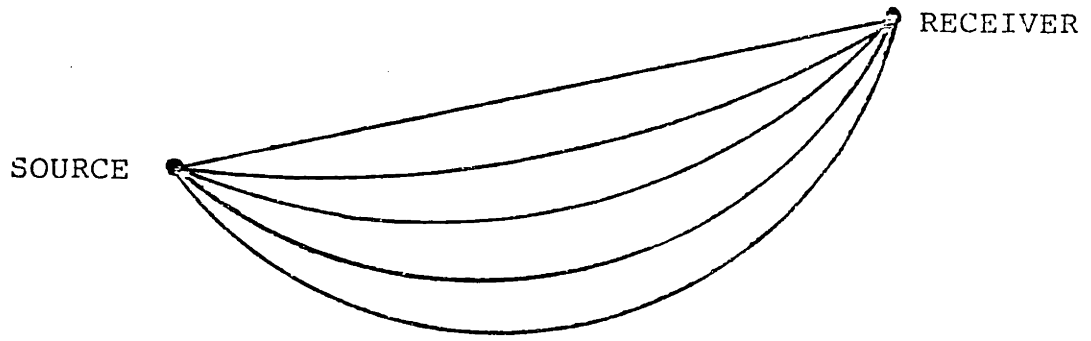

b)

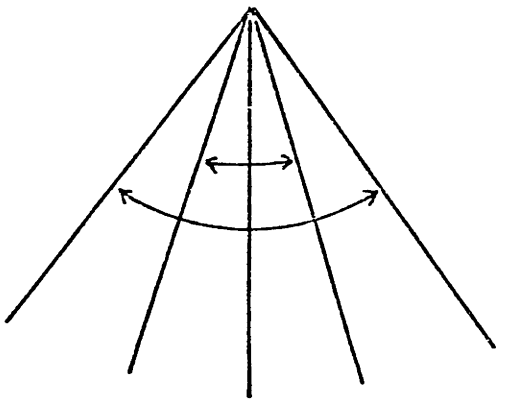

Figure 2.5

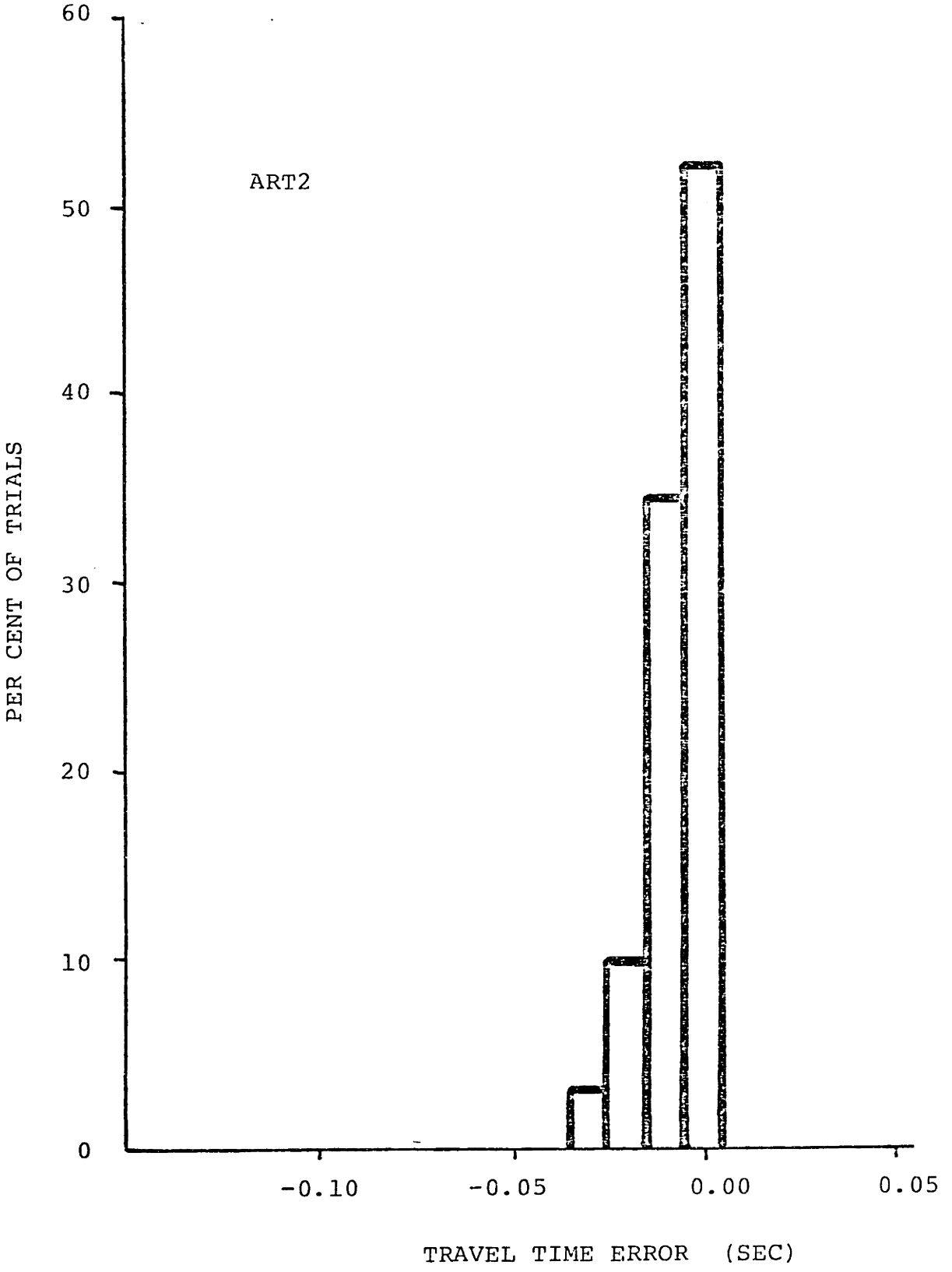
ART2
60
50
40
30
20
10
0
PER CENT OF TRIALS
-0.10
-0.05
0.00
0.05
TRAVEL TIME ERROR (SEC)

Figure 2.6

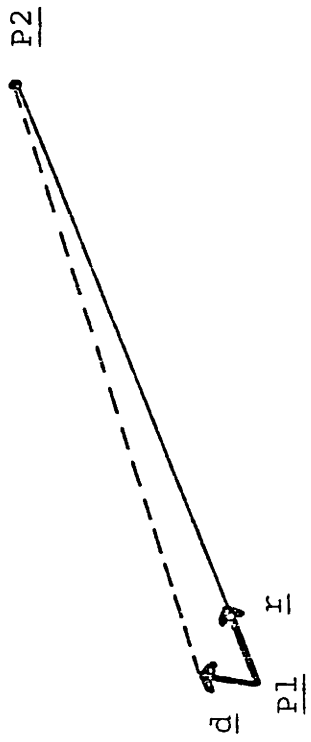

Figure 2.7

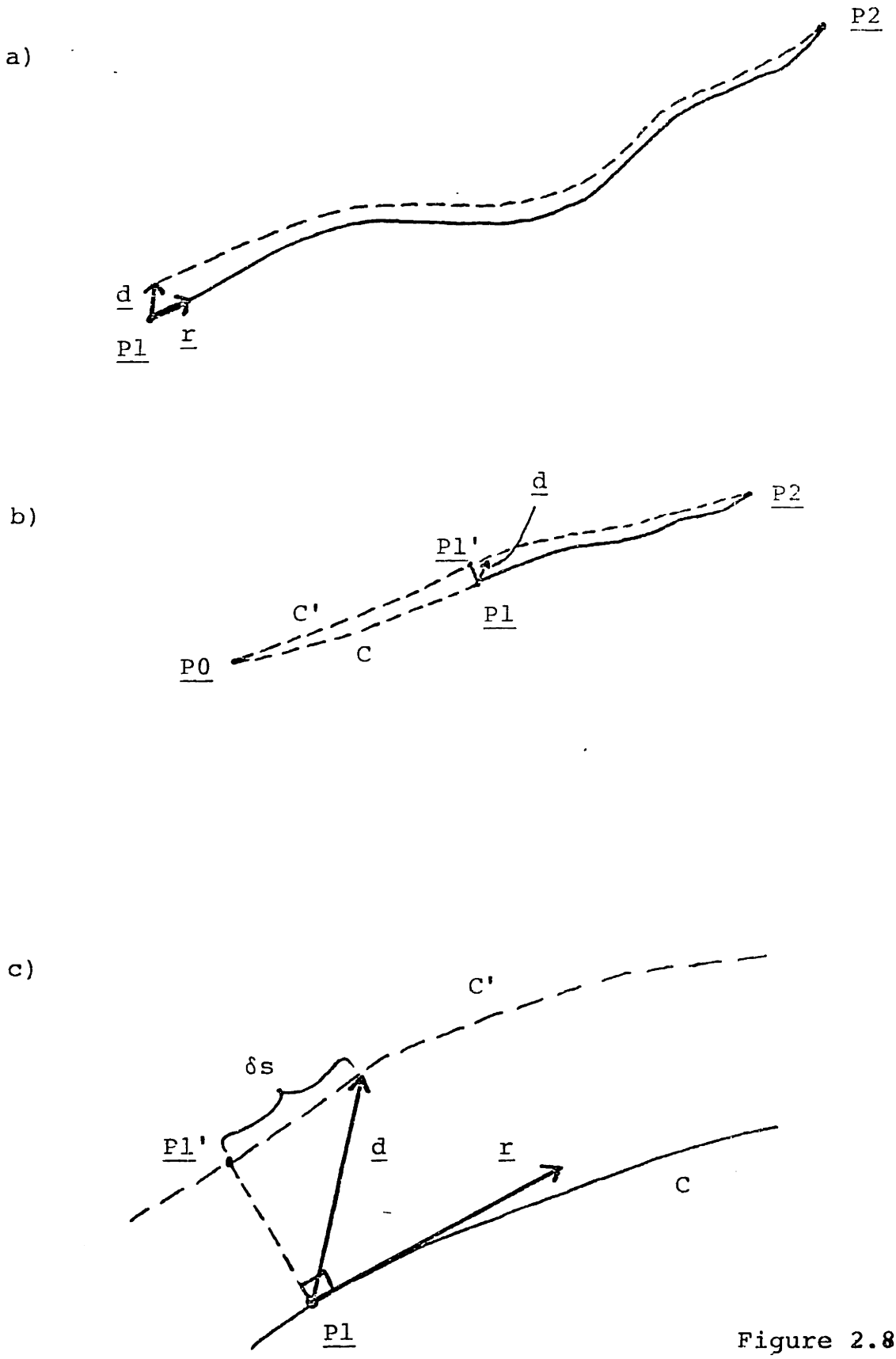

Figure 2.8

a)

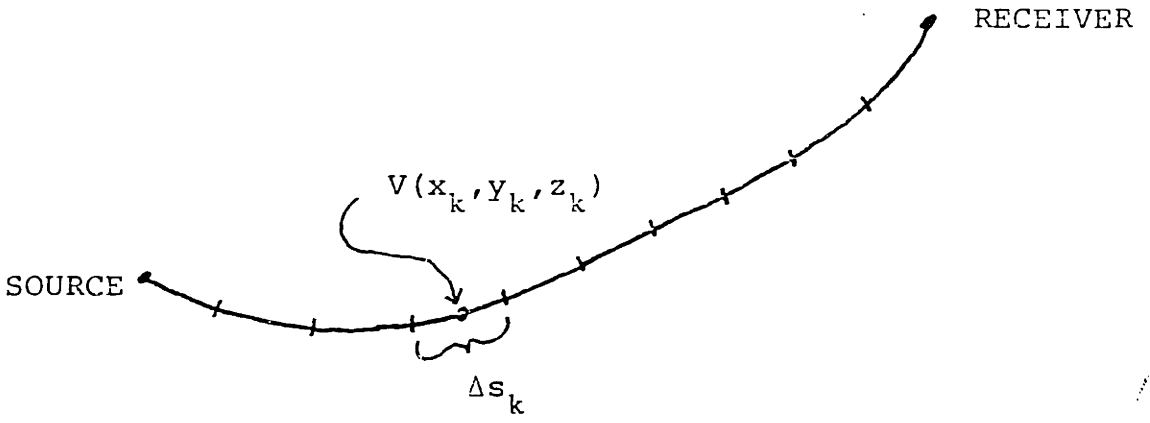
RECEIVER
$V(x_k, y_k, z_k)$
SOURCE
Δs_k

b)

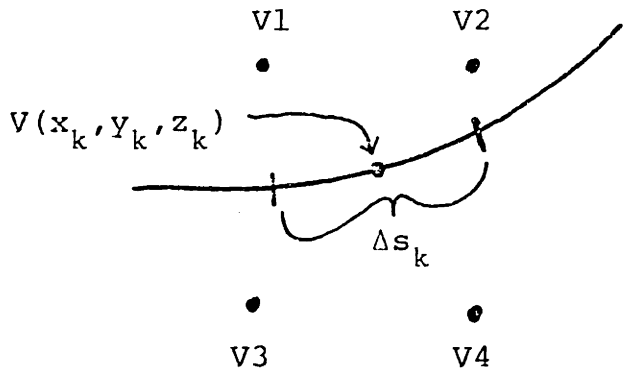
V1
V2
$V(x_k, y_k, z_k)$
Δs_k
V3
V4

Figure 2.9

CHAPTER 3

PROPERTIES OF THE INVERSION: NUMERICAL EXPERIMENTS

The theoretical basis for simultaneous inversion has been presented and a variety of necessary and/or useful techniques for implementing an inversion procedure have been discussed in Chapter 2. It is also important to know the limitations of simultaneous inversion, as well as to be able to measure the quality of a particular solution. These general subjects will be explored in this chapter primarily through the use of numerical experiments. Specific topics to be studied include the linearity and accuracy of hypocentral and velocity partial derivatives, the limits on the substitution of approximate ray tracing (ART) for three-dimensional ray tracing, the effectiveness of parameter separation, and the significance of measures of model resolution and error. The results of this chapter will be useful for providing guidelines for the actualization of the inversion procedure and the interpretation of its results.

3.1 HYPOCENTER PARTIAL DERIVATIVES: ACCURACY AND LINEARITY

The partial derivatives of the P-wave travel time with respect to the coordinates of the hypocenter are used in the event relocation process and in the simultaneous inversion

procedure. These partial derivatives, $\partial t/\partial x$, $\partial t/\partial y$, and $\partial t/\partial z$, represent estimates of how much the calculated travel time will change as a result of a unit displacement of the source in the x, y, or z directions. In practice the partial derivatives actually used will not precisely predict the corresponding change in travel time, for two reasons. First, the travel time is not linearly related to the coordinates of the source - higher order terms have simply been neglected in the derivation of section 2.5. Second, when approximate ray tracing is used for either relocation or simultaneous inversion, the resulting partial derivatives (as well as the travel times) are only approximations of the "true" values. Both of these topics are explored in this section.

3.1.1 LINEARITY OF THE HYPOCENTRAL PARTIAL DERIVATIVES

To solve a non-linear problem using an iterative linearized scheme, it is obviously important to make adjustments to parameter values at each iteration step which are within the range of validity of the linear approximation. Otherwise the procedure may be very slow to converge, or perhaps even become unstable and diverge.

The range over which the hypocenter partial derivatives accurately predict travel time changes can be assessed by investigating higher order terms in the Taylor expansion (a formidable task!), or by numerically comparing the change in

travel time δt due to a displacement, say δx, in a hypocenter coordinate to the change predicted by the linear approximation

$$\delta t^* = \frac{\partial t}{\partial x} \delta x \qquad (3.1)$$

By sampling a number of representative cases one can empirically define a range of δx (or δy or δz) for which δt^* is an adequate approximation to δt.

An analytic two-dimensional velocity model due to Wesson (1971) was used to perform this analysis (see Table 3.1 and Figure 3.1a). Figures 3.2 a to d illustrate the behavior of the actual travel time difference δt for a range of δx, δy, and δz when compared to that predicted using equation 3.1 (the ray paths are numbers 4, 7, 9 and 12 shown in Figure 3.3). If the linear approximation were exact, the quantity

$$\Delta T = \delta t - \delta t^*$$

would be exactly zero for all δx, δy and δz. Significant non-linearity is clearly seen in all cases. It is interesting to note that the Cartesian coordinate with the largest partial derivative (δx in 3.2 a and b, δz in c, and δy in d) deviates the least from being linear in these examples (and all others examined).

Examples such as these can be used to provide an empirical estimate of the range of linearity of the hypocentral partial derivatives. For a sample of 15

source-receiver pairs (see Figure 3.3) it was found that on average the difference ΔT exceeded 0.01 sec for displacements of 2 km or more, and ΔT exceeded 0.05 sec for displacements larger than 4 km. These numbers are of course derived for a specific velocity model, but the wide variety of source-receiver configurations used within the model suggests that these estimates may be appropriate in other cases as well.

A travel time error of 0.01 sec is certainly acceptable for use in earthquake relocations or simultaneous inversion, since this is well within normal errors for arrival time readings. However a difference of 0.05 sec is at or above the level of reading accuracy of the P-wave arrival times, so that hypocentral adjustments of size 4 km may often be introducing unacceptable non-linearity. Thus establishing an upper bound of roughly 3 km to the hypocenter adjustment permitted per iteration step is probably reasonable in terms of stability for the solution procedure.

3.1.2 ACCURACY OF THE HYPOCENTRAL PARTIAL DERIVATIVES FROM ART

It is important to know the limitations on the permissable use of approximate ray tracing (ART) as a replacement for three-dimensional ray tracing. In section 2.4 it was demonstrated that the travel times determined by ART are quite adequate for the purpose of hypocenter

location. However it is not immediately clear that the hypocentral partial derivatives derived from ART should be adequate as well. (Note: the ART2 routine was used for the analyses of this chapter).

The hypocenter partial derivatives are given by the components of the vector tangent to the ray path (the "ray vector") at the source multiplied by -1/V (also evaluated at the source; see section 2.5):

$$\begin{aligned} \partial t/\partial x &= -1/V \;\; dx/ds \\ \partial t/\partial y &= -1/V \;\; dy/ds \\ \partial t/\partial z &= -1/V \;\; dz/ds \end{aligned} \qquad (3.2)$$

This suggests an obvious way to estimate these partial derivatives when using ART. Simply use the first two points on the ray path determined by ART to construct an approximation of the ray vector at the source, and then evaluate the partial derivatives from equations 3.2. In other words use a finite difference approximation

$$\begin{aligned} \partial t/\partial x &= -1/V \;\; \Delta x/\Delta s \\ \partial t/\partial y &= -1/V \;\; \Delta y/\Delta s \\ \partial t/\partial z &= -1/V \;\; \Delta z/\Delta s \end{aligned} \qquad (3.3)$$

where Δx, Δy and Δz are given by $(x_2 - x_1)$, $(y_2 - y_1)$ and $(z_2 - z_1)$, and Δs is $\sqrt{\Delta x^2 + \Delta y^2 + \Delta z^2}$.

The partial derivatives computed from ART using equations 3.3 (finite difference) are compared to the "true" partial derivatives of equation 3.2 (from ray tracing) in Table 3.2 for the four ray paths used for Figure 3.2. The accuracy is not good, paricularly for the derivatives with respect to depth. Many values are reasonably close, but the average absolute error is over 35 per cent, and the partial derivative for depth has the wrong sign in one case (path a). It is questionable whether this approximation is fully adequate for hypocenter determination and simultaneous inversion purposes.

A reasonable alternative is available due to the very low cost of ART. The partial derivatives can be directly estimated by variation of the source end point. For example, displacing the source point a small distance Δx in the x direction will result in a change in travel time Δt. Then the hypocentral partial derivative can be estimated as

$$\partial t/\partial x = \Delta t/\Delta x$$

and similarly for y and z. This procedure, which requires the determination of three additional ray paths, is not economically feasible with three-dimensional ray tracing (and fortunately is not necessary as shown in section 3.1.1) but is quite practical using ART.

This "variational" estimate of the partial derivative is compared in Table 3.2 to the true derivative and the finite

difference estimate. The improvement is dramatic. All derivatives have the correct sign, and the average absolute error is only 4 per cent, with the largest single error being 13 per cent. Finally, Figure 3.4 shows the travel time as a function of displacement of the source (in the x and y directions) computed in three ways for path a: by ray tracing (R_x, R_y), approximate ray tracing (A_x, A_y), and by the prediction of the variational partial derivative (P_x, P_y), that is from

$$t(\text{predicted}) = t(\Delta x=0, \Delta y=0) + \frac{\partial t}{\partial x}\Delta x + \frac{\partial t}{\partial y}\Delta y$$

where $t(\Delta x=0, \Delta y=0)$ is the ART travel time. The agreement among the three is very good, both in terms of the closeness of the ART travel time to the ray tracing time, and the ability of the partial derivative to predict their values within acceptable error. This "variational" estimate of the ART partial derivatives is adopted for our inversions in which ART is employed.

3.2 VELOCITY PARTIAL DERIVATIVES: ACCURACY AND LINEARITY

The values of the partial derivatives of the P-wave travel time with respect to the parameters of the velocity model are required for the simultaneous inversion procedure. As in the case of the hypocenter partial derivatives, the velocity derivatives will not precisely predict the actual

travel time change. Two reasons are again the absence of a truly linear relation between change in velocity and change in travel time, and the additional approximations involved when three-dimensional ray tracing is replaced by ART. A third reason is the difficulty of realistically determining the partial derivatives themselves.

3.2.1 LINEARITY OF THE VELOCITY PARTIAL DERIVATIVES

Just as for the hypocenter adjustments (section 3.1.1), it is important to know the range for which changes in travel time are roughly linearly related to changes in velocity parameter values. This range can also be empirically determined through numerical experiments. For a given source and receiver, the travel time between the two points can be determined for a given velocity model. By systematically perturbing a single parameter of the velocity model, the relation between changes in velocity and changes in travel time can be studied.

The "true" partial derivative of travel time with respect to the velocity at a given grid point is determined by making a very small perturbation ε_{v_i} to the i'th velocity parameter and computing the corresponding change in travel time ε_t. The partial derivative is then well approximated by

$$\partial t/\partial v_i = \varepsilon_t/\varepsilon_{v_i} \qquad (3.4)$$

and the predicted travel time change resulting from a given change in velocity is

$$\delta t^{*} = \frac{\partial t}{\partial v_i} \delta v_i \qquad (3.5)$$

This predicted change can be compared to the actual computed change δt to study the linearity of velocity parameter perturbations.

A simple laterally homogeneous velocity model defined in two dimensions was chosen for performing this analysis (see Table 3.3). A set of pairs of sources and receivers were picked (see Table 3.4) and specific velocity parameters were selected to be systematically perturbed. The resulting relations between the size of the velocity change and the deviation from linearity (i.e. the difference between the computed δt and predicted δt^{*}) are shown in Figures 3.5 a to f. In all cases a velocity change of 0.5 km/sec or less is quite acceptably linear, while changes of 1.0 km/sec or greater are often seen to be dangerously non-linear. This suggests limiting the velocity change permitted per iteration step to no more than 0.5 km/sec.

3.2.2 SCHEMES FOR COMPUTING THE VELOCITY PARTIAL DERIVATIVES

In section 2.5 the velocity partial derivatives were

shown to be determined (in principle) by the choice of interpolatory function used to define the velocity between points of the grid. In practice this correct approach is not always feasible. In general an interpolation function defines the velocity at a certain point as a weighted sum of the velocities at surrounding points of the grid. In our case, when three-dimensional ray tracing is in use, the function is a three-dimensional spline under tension. As a result the velocity at a given point depends on the velocity at 32 points of the grid (at the very least!). This has some undesirable consequences, both practically and philosphically. First, the resolution of the velocity inversion will be affected. The "window" through which the velocity value at some point "sees" the velocity grid will be quite large. Smoothing of the velocity model will occur in an undefinable way. Second, the task of calculating the partial derivatives becomes intractable. There is no simple algorithm for extracting the interpolation weights needed for equation 2.23 from the spline under tension routine. And if there were, the computational effort of evaluating 32 or more weights for every segment of the ray path would be formidable. For these reasons a simpler scheme for estimating the partial derivatives is desirable.

Two practical schemes for approximately evaluating the velocity partial derivatives have been devised and tested. The first involves approximating the interpolation weights for equation 2.23 by using linear interpolation among only

the 8 nodes surrounding the given point (for a three-dimensional velocity model). The second method finds the node closest to the point in question on the ray path, and adds the quantity $-\Delta s/v$ to the partial derivative for that node, where s is the length of the path segment and v is the velocity at that point (see section 2.5.2). This is equivalent to using the first method above but then setting the largest of the 8 weights equal to unity and the rest to zero. The first method will be termed "linear", and the second "block".

Table 3.5 shows a comparison of the "true", linear, and block partial derivatives for the velocity model of Table 3.3, ray paths of Table 3.4, and velocity parameters of Figures 3.5 a to f. Except for case e (which is seen to be pathologically non-linear in Figure 3.5e), the agreement among the true derivative and the two estimates is reasonably good. The average absolute error is 22 per cent for the linear estimate, and only 13 percent for the block estimate (again leaving out case e, which would double both errors). The superior accuracy of the block estimate implies that the shape of the spline under tension interpolation function is closer to a three-dimensional box car (block) than a three-dimensional ramp (linear) function. Errors of this magnitude will not cause substantial errors in the inversion calculations, since velocity changes will be limited to 0.5 km/sec or less to maintain linearity. Thus both the block and linear estimates of the velocity

partial derivatives are acceptable for use in simultaneous inversion.

3.2.3 ACCURACY OF THE VELOCITY PARTIAL DERIVATIVES FROM ART

Most of the inversions for this thesis are to be carried out using solely approximate ray tracing, simply because of the one to two orders of magnitude savings in computation time. Therefore it is important to examine the accuracy of the velocity partial derivatives computed using ART. As in section 3.2.2, the partial derivatives determined by the "linear" and "block" procedures along the ART ray path can be compared to the "true" derivative from ray tracing, as well as the "true" derivative derived from equation 3.4 using ART (that is, the partial derivative predicted from making a very small change in the value of the given velocity parameter). This comparison is shown in Table 3.6.

On the whole the agreement among the various estimates of the derivatives from both Tables 3.5 and 3.6 is excellent, again aside from the apparently anomalous case e. The average correlation coefficient between any two sets of derivative estimates exceeds 0.95, indicating that the trends of the derivatives match well, while the average slope of the least-squares line relating any two sets slightly exceeds 0.9, showing that the magnitudes of the derivatives also match well (all excluding case e). Interestingly, the "linear" estimates are indistinguishable

from the "true" ART derivatives, while the "block" estimates closely match the "true" ray tracing derivatives in Table 3.6.

Finally it is of interest to compare the actual changes in computed travel time δt to the predicted change δt^* (see equation 3.5) using the "true" ART velocity partial derivatives, and in turn to compare them to the values of δt and δt^* from three-dimensional ray tracing. From Figures 3.6 a through f, which show $\delta t - \delta t^*$ as a function of ΔV, it is clear that $|\Delta V| <= 0.5$ again is a reasonable bound for maintaining linearity in the inversion. Also comparing these results with Figures 3.5 a to f from the ray tracing comparison reveals similar patterns for the linearity and non-linearity of the travel time changes due to the velocity perturbations, adding confidence to the claim that the use of ART should not drastically distort the results of an inversion.

3.3 SIMULTANEOUS INVERSION

Certain aspects of the overall simultaneous inversion problem can be investigated in a non-rigorous manner by performing numerical experiments with artificially generated data. Four specific topics will be explored in this section: first, the inadequacy of velocity inversion compared to simultaneous inversion; second, the effectiveness of the method of parameter separation; third,

the adequacy of inversion using ART alone; and fourth, the meaning and reliability of measures of resolution and error.

3.3.1 INADEQUACY OF VELOCITY INVERSION

In Chapter 2 it was suggested that simultaneous inversion is superior to simple velocity inversion; in other words, that solving for perturbations to velocity and hypocentral parameters simultaneously is significantly better than, say, solving sequentially for velocity perturbations, then hypocentral perturbations, etc. To examine this point, a set of error-free artificial arrival-time data was generated (using ART2 for economic reasons). The stations, sources, and velocity model used are shown in Figures 3.7 a and b and Table 3.7.

Starting with a slightly perturbed velocity model, a single step of simultaneous inversion was sufficient to recover the original structure with very small errors (see Tables 3.8 a and b in comparison to Table 3.7). To test the use of velocity inversion alone, the same initial velocity model was used (Table 3.8a), but the earthquake sources were randomly displaced first 2 km, then 4 km, and one step inversions were carried out varying the velocity parameters only. The resulting velocity models are shown in Tables 3.9 a and b. In both cases the final velocity model is substantially distorted from the true model, with the 4 km displacement case showing greater deviations. Another

measure of the model misfit is the rms residual for the explosion arrival times following the one-step inversion. For the simultaneous case, the average residual for the five shots is 0.037 sec, while for the two velocity inversion cases, the average residual was 0.061 sec and 0.089 sec respectively.

These findings imply that the simultaneous inversion approach does in fact produce superior results in comparison to straight velocity inversion. In reality the gap in accuracy between the two methods probably exceeds that indicated here. Our test involved randomly displacing the sources, but in practice the sources would more likely be systematically mislocated, producing an even greater distortion in the model determined by velocity inversion.

3.3.2 EFFECTIVENESS OF PARAMETER SEPARATION

In the preceding section it was demonstrated that a simple velocity inversion may be inadequate for accurately recovering the true velocity structure. It is also important to demonstrate that simultaneous inversion with parameter separation can yield the correct structure. This question can be investigated in an analogous manner to the test of the velocity inversion, and using the same data set (Figure 3.7 and Table 3.7).

As in section 3.3.1, the hypocenters were randomly displaced first 2 km and then 4 km. The single-step

inversion results for these two cases are shown in Tables 3.10 a and b. The final velocity models are quite close to the true model, although again the 4 km displacement case shows slightly more distortion. The average RMS residuals for the explosions are 0.042 sec and 0.046 sec, significantly better than the values of 0.061 and 0.089 sec from the velocity inversion tests.

Random arrival time errors (zero mean, 0.05 sec standard deviation) were then added to the synthetic data and the one-step inversion for the 2 km displacement case was repeated to provide a more demanding test of parameter separation. The velocity model after this single iteration is displayed in Table 3.10c. Except for two peripheral points in layer 3, the velocities are remarkably accurate. Altogether these results clearly indicate the advantage of using simultaneous inversion and the effectiveness of the parameter separation method.

3.3.3 SIMULTANEOUS INVERSION USING ART

Approximate ray tracing is a crucial key to the practical application of iterative simultaneous inversion with large amounts of data. Thus it is of interest to attempt to assess the reliability of solutions obtained using ART alone. Thurber and Ellsworth (1980) showed that ART can produce reasonable estimates of travel times, and in sections 3.1 and 3.2 it was shown that adequate estimates of

the hypocentral and velocity partial derivatives could be derived from ART as well. It remains to be demonstrated that accurate estimates of parameter adjustments can also be determined via ART.

A new set of error-free synthetic arrival time data was generated using the stations and sources of Figure 3.7 a and b and a two-dimensional analytic velocity model defined by

$$V = 3.0 + 0.3\ z - \frac{1}{1 + 0.15\ x^2} \qquad (3.6)$$

where x and z are in km and v is in km/sec (see Table 3.11). This model consists of a "wedge" of low velocity centered around x=0, superimposed upon a linear increase of velocity with depth. In this case the hypothetical P-wave travel times were calculated using the three-dimensional ray tracing program of Pereyra et al. (1980).

Initially this error-free data set was iteratively inverted for a solution in three dimensions - thus the velocity at gridpoints of different y value but same x and z value should be determined to be equal by the inversion (refer to equation 3.6). Travel times for the inversion were calculated using ART2 (see section 2.4.5). The velocity model results for a two-step inversion are listed in Table 3.12. The velocity values are recovered with quite satisfactory accuracy, the mean absolute error being roughly 0.11 km/sec for all the "observed" grid points. The overall root-mean-square (RMS) residual of less than 0.05 sec for

the five explosions reflects the combination of the adequate estimation of travel times and the satisfactory recovery of the velocity structure by the inversion.

The epicenters are also very well determined by the inversion, having a mean distance error of only 0.11 km. The total RMS residual for the earthquake arrival times is also less than 0.05 sec. The only significant shortcoming of the inversion results is a systematic error in the earthquake depth estimates, for which the average absolute error is 0.47 km while the average error itself is 0.46 km. We attribute this systematic error to the use of the finite difference estimate of the hypocenter depth partial derivative (see section 3.1.2). This problem will be examined later in this section.

A second more realistic test of this data set was carried out after adding errors to the travel times with zero mean and 0.05 sec standard deviation. The velocity model determined after two iteration steps is shown in Table 3.13. The overall accuracy of the solution is not significantly degraded from the error-free case. The average absolute error of the velocity values is below 0.15 km/sec, the RMS residual for the five explosions is less than 0.06 sec, and the average epicentral distance error is about 0.19 km. All of these error levels are comparable to the error-free test results. Again however we note a clear systematic error in the solutions for hypocentral depths, having a mean absolute error of 0.65 km and a mean error of 0.64 km.

The inversion of the data set with added error was repeated using the "variational" estimate of the partial derivative of the travel time with respect to hypocenter depth:

$$\frac{\partial t}{\partial z} \simeq \frac{\Delta t}{\Delta z}$$

(see section 3.1.2). This should provide a more accurate estimate of the true partial derivative, according to the results of section 3.1.2. The velocity solution is slightly improved, having a mean absolute error below 0.14 km/sec. The average explosion RMS residual is again less than 0.06 sec, and the mean epicentral distance error is 0.19 km. In contrast to the previous cases, though, the mean absolute error of the hypocenter depths is only 0.21 km and the mean error is 0.16 km, a dramatic improvement. These results confirm the findings of section 3.1.2, and emphasize the importance of using accurate partial derivative estimates, particularly for the hypocenter depth.

3.3.4 RESOLUTION AND ERROR

Two matrices which can be useful for investigating the quality of a given inversion solution are the resolution matrix (see Backus and Gilbert, 1968, or Wiggins, 1972) and the covariance matrix. Following Aki and Lee (1976), the damped least squares solution to the problem

$$\underline{r} = \underline{\underline{A}}\,\underline{x} + \underline{e} \qquad (3.7)$$

where $\underline{r}$ is the residual vector, $\underline{\underline{A}}$ is the matrix of partial derivatives, $\underline{x}$ is the parameter vector, and $\underline{e}$ is the (unknown) error vector, is given by

$$\underline{\hat{x}} = (\underline{\underline{A}}^T\,\underline{\underline{A}} + \lambda^2\,\underline{\underline{I}})^{-1}\,\underline{\underline{A}}^T\,\underline{r} \qquad (3.8)$$

where $\underline{\underline{I}}$ is the identity matrix, λ is the damping parameter and $\underline{\hat{x}}$ is the damped least squares solution. For the stochastic inverse, λ^2 should be chosen to equal the variance of the data (i.e. the error in the arrival time readings). The least squares solution of equation 3.7 satisfies

$$\underline{\underline{A}}^T\,\underline{\underline{A}}\,\underline{x} = \underline{\underline{A}}^T\,\underline{r} \qquad (3.9)$$

Combining equations 3.8 and 3.9 yields

$$\underline{\hat{x}} = (\underline{\underline{A}}^T\,\underline{\underline{A}} + \lambda^2\,\underline{\underline{I}})^{-1}\,\underline{\underline{A}}^T\,\underline{\underline{A}}\,\underline{x}$$

so that the resolution matrix for this problem is

$$\underline{\underline{R}} = (\underline{\underline{A}}^T\,\underline{\underline{A}} + \lambda^2\,\underline{\underline{I}})^{-1}\,\underline{\underline{A}}^T\,\underline{\underline{A}}$$

The size of the diagonal elements of $\underline{\underline{R}}$ reflect the

resolution of the corresponding model parameters (with unity being perfect resolution). See Wiggins (1972) for further discussion.

Again following Aki and Lee (1976), the covariance of the solution $\underline{C}$ is related to the covariance of the data by

$$\underline{C} = \underline{\Delta x}\ \underline{\Delta x}^T = (\underline{A}^T\ \underline{A} + \lambda^2\ \underline{I})^{-1}\ \underline{A}^T\ \underline{\Delta r}\ \underline{\Delta r}^T\ \underline{A}\ [(\underline{A}^T\ \underline{A} + \lambda^2\ \underline{I})^{-1}]^T \qquad (3.10)$$

If it is assumed that the data errors are uncorrelated

$$\underline{\Delta r}\ \ \underline{\Delta r}^T = \sigma^2\ \underline{I}$$

then equation 3.10 simplifies to

$$\underline{C} = \sigma^2\ (\underline{A}^T\ \underline{A} + \lambda^2\ \underline{I})^{-1}\ \underline{R}^T \qquad (3.11)$$

To examine some characteristics of resolution for our simultaneous inversion problem, we return to the error-free synthetic data set of sections 3.3.1 and 3.3.2 (see Figures 3.7 a and b and Table 3.7), for which the travel times were generated with approximate ray tracing. These data are to be inverted for velocities on a two-dimensional grid of points, using ART to compute the simultaneous inversion. Thus any errors in the calculated velocities should be due to only two causes: first, the inadequacy of the representation of the three-dimensional velocity model by a finely-spaced two-dimensional grid (see Table 3.15), and

second, the smoothing of the velocity model by the inversion as a result of a lack of complete information about the velocity structure. The severity of this latter source of error should hopefully be indicated by the resolution measure.

Four inversions were carried out using:

a) the entire data set of 50 earthquakes, 5 explosions, and all 30 stations;

b) all 55 sources but only 20 stations;

c) all 55 sources but only 10 stations;

d) only the 50 earthquakes with all 30 stations.

The actual velocity errors and computed resolution for these inversions are shown in Tables 3.16 a to d. All achieved an average RMS residual of about 0.025 sec after three iterations. However the resolution and accuracy of the velocities varies substantially. Table 3.17 lists the average resolution and the mean absolute velocity error for the four cases. The full data set (case a) resolves the structure quite well, with an average resolution exceeding 0.9, and the average magnitude of the velocity error is well under 0.1 km/sec. Not surprisingly the resolution and error degrade as the number of stations is reduced in cases b and c. It is important to note that for a given solution, the true error and computed resolution are almost uncorrelated (for example, a correlation coefficient ρ=0.07 for case a!). In contrast, the resolution for a given grid point is well

correlated ($\rho>0.69$ for case a) with a measure of the number of times that the grid point was assigned a non-zero velocity partial derivative for each incremental segment of all ray paths in the inversion (see section 3.2.2).

From these results it seems clear that the resolution measure by itself is not a useful discriminant. Grid points (or nodes) with low resolution can have accurate velocities, and nodes with high resolution are certainly not guaranteed to have accurate velocities. However the actual error does increase on average as the resolution decreases. For example, for case a, the average error is 0.07 km/sec for all nodes; for nodes with resolution $R<0.8$, the average error increases to 0.10 km/sec; and for $R<0.6$, the average error is 0.17 km/sec. Thus $R=0.7$ might provide a very conservative resolution cut-off value below which velocity values would be considered unreliable.

Another important observation is that the exclusion of the explosions (case d) results in a solution quality comparable in some ways to that due to leaving out 20 of the 30 total stations. The average resolution drops from 0.91 to 0.82, and the mean absolute error rises from 0.08 to 0.16 km/sec. Resolution is particularly low and error high for the near-surface grid points. This result confirms the value of including explosion data for aiding in the accurate determination of near-surface velocities.

To gain some insight into the meaning of the standard error measure (the square root of the diagonal element of $\underline{C}$

in equation 3.11), inversions a through c were repeated after adding random error with zero mean and 0.05 sec standard deviation to the arrival time data. Tables 3.18 a to c show the resolution, actual velocity error, and computed standard error for these cases. Three iterations achieved an overall RMS residual of 0.05 sec for each inversion. Once again the resolution and velocity accuracy vary considerably among the three cases, as does the computed standard error (see also Table 3.19 for their mean values). The actual velocity error is only weakly correlated with the standard error (ρ ranging from 0.19 to 0.34), and the mean absolute error is nearly twice the mean standard error. Overall the standard error does not seem to provide a useful estimate of the true velocity error at an individual grid point, and is an underestimate of the average error level.

Jackson (1979) takes a somewhat different approach to the stochastic inversion of equation 3.7. Let the desired inverse operator be given by $\underline{H}$; then

$$\underline{\hat{x}} = \underline{H}\,\underline{y}$$

or

$$\underline{\hat{x}} = \underline{H}\,\underline{A}\,\underline{x} + \underline{H}\,\underline{e}$$

where the resolution matrix $\underline{R} = \underline{H}\underline{A}$ in this case. Jackson

(1979) defines the "estimation error"

$$\hat{\underline{x}} - \underline{x} = (\underline{H}\ \underline{A} - \underline{I})\ \underline{x} + \underline{H}\ \underline{e} \qquad (3.12)$$

By making use of a priori information on the values of the parameters $\underline{x}$, one can assign to them a covariance matrix $\underline{C}_x$ analogous to the data covariance matrix $\underline{C}_e$. Then the covariance of the estimation error in equation 3.12 is

$$\underline{C} = (\underline{H}\ \underline{A} - \underline{I})\ \underline{C}_x\ (\underline{H}\ \underline{A} - \underline{I})^T + \underline{H}\ \underline{C}_e\ \underline{H}^T \qquad (3.13)$$

Jackson shows that the operator $\underline{H}$ which will minimize the total variance in equation 3.13 is

$$\underline{H} = (\underline{A}^T\ \underline{C}_e^{-1}\ \underline{A} + \underline{C}_x^{-1})\ \underline{A}^T\ \underline{C}_e^{-1}$$

which when substituted into equation 3.13 yields

$$\underline{C} = (\underline{A}^T\ \underline{C}_e^{-1}\ \underline{A} + \underline{C}_x^{-1})^{-1} \qquad (3.14)$$

According to Jackson the key feature of this expression for the covariance is that it includes both resolving errors and random errors of the data. If the data errors and parameter errors are uncorrelated, equation 3.14 can be rewritten as

$$\underline{C} = [\underline{A}^T\ \underline{A} + (C_e/C_x)\ \underline{I}]^{-1}\ C_e \qquad (3.15)$$

where C_e and C_x are the magnitudes of the data and parameter variances, respectively. Tables 3.18 a to c and 3.19 also include the velocity error estimates computed according to equation 3.15. These error estimates are not notably better correlated with the actual errors (ρ ranging from 0.21 to 0.36) than are the standard errors from equation 3.11. However the mean of the error estimates is much closer to the actual mean absolute error (see Table 3.19). Both of these error estimates will be calculated in the inversions.

Finally it is observed that the largest actual velocity errors occur in two principal places: at peripheral nodes of the model and at nodes where the velocity is rapidly varying laterally. The former are generally accompanied by lower resolution, whereas the latter are not. This must be kept in mind when evaluating the velocities determined using real data.

3.4 SUMMARY

The partial derivatives of the P-wave travel time with respect to hypocentral and velocity parameters are important components of the simultaneous inversion problem. We have found that a range of parameter perturbations can be empirically determined for which the partial derivatives can accurately predict the corresponding changes in travel time. The limiting range is conservatively estimated as 3 km for the hypocentral parameters and 0.5 km/sec for the velocity

parameters. The hypocentral derivatives can be directly derived from three-dimensional ray tracing, but explicit precise relations for the velocity partial derivatives are intractable. However both the "linear" and "block" schemes for estimating the velocity derivatives are quite adequate. It is also found that suitable estimates of the hypocentral and velocity partial derivatives can be determined via approximate ray tracing.

Various other aspects of the total simultaneous inversion problem have been investigated through numerical experiments. It has been shown that simultaneous inversion is superior to simple velocity inversion. Furthermore, parameter separation is effective in extracting correct velocity adjustments from an initial model with incorrect velocities and hypocenters, even for hypocentral errors as large as 4 km. This suggests that the range of "local independence" discussed by Pavlis and Booker (1980) is at least on the order of a few kilometers (see section 2.6.1). It is also found that inversion solutions determined using solely approximate ray tracing are satisfactorily accurate.

Finally, the resolution and error measures of the quality of an inversion solution have been examined. Resolution by itself is not an adequate indicator of the "correctness" of a given velocity value. For inversions using error-free data the actual velocity error is seen to increase steadily as resolution decreases, on average. Grid points with resolution $R<0.5$ tend to be unreliable, while those with

R>0.9 are generally more accurate. A value of R=0.7 might serve as a conservative cutoff point.

The standard error measure of Aki and Lee (1976) is found to underestimate significantly the level of velocity error. Jackson's error estimate (Jackson, 1979) is definitely more realistic. However both error measures on a grid point by grid point basis are poorly correlated with the true velocity errors. Overall these measures can only be used to estimate the average level of error in the solution as a whole. A useful observation is that peripheral grid points and grid points in areas where the velocity is changing rapidly are more frequently subject to large errors.

TABLE 3.1

Two-dimensional velocity model of Wesson (1971)

$$V = 3.7526 + 0.5506\ Z + \frac{1.02268\ X}{e^2 + |X|}$$

[e = 0.75]

TABLE 3.2

Comparison of hypocentral partial derivative estimates:

TR - true FD - finite difference VA - variational

	$\partial t/\partial x$			$\partial t/\partial y$			$\partial t/\partial z$		
PATH	TR	FD	VA	TR	FD	VA	TR	FD	VA
a	.106	.111	.107	-.064	-.055	-.068	-.014	.017	-.014
b	.104	.121	.092	.000	.000	.000	-.066	-.023	-.057
c	.033	.035	.032	-.034	-.035	-.032	.099	.098	.098
d	.049	.064	.050	-.164	-.192	-.167	-.128	-.068	-.129

TABLE 3.3

Velocity model for analyzing velocity partial derivatives

NX =		1	2	3	4	5	6	7
	X =	0.0	4.0	8.0	12.0	16.0	20.0	24.0
NZ	Z							
1	-1.0	3.0	3.0	3.0	3.0	3.0	3.0	3.0
2	2.0	3.9	3.9	3.9	3.9	3.9	3.9	3.9
3	5.0	4.8	4.8	4.8	4.8	4.8	4.8	4.8
4	8.0	5.5	5.5	5.5	5.5	5.5	5.5	5.5
5	11.0	5.8	5.8	5.8	5.8	5.8	5.8	5.8
6	14.0	6.1	6.1	6.1	6.1	6.1	6.1	6.1
7	17.0	6.3	6.3	6.3	6.3	6.3	6.3	6.3

TABLE 3.4

Paths for analyzing velocity partial derivatives

PATH	SOURCE (x,y,z)	RECEIVER (x,y,z)
a	(7.5,0.0,8.0)	(7.5,8.0,0.0)
b	(3.0,0.0,10.0)	(10.5,0.0,0.0)
c	(3.0,0.0,10.0)	(18.0,0.0,0.0)
d	(3.0,0.0,10.0)	(6.0,0.0,0.0)
e	(7.5,0.0,0.0)	(7.5,20.0,0.0)
f	(3.0,0.0,0.0)	(23.0,0.0,0.0)

TABLE 3.5

Comparison of "true", "linear", and "block" velocity partial derivatives

PATH	TRUE	LINEAR	BLOCK
a	-0.193	-0.173	-0.211
b #1	-0.175	-0.136	-0.166
b #2	-0.114	-0.091	-0.133
c	-0.252	-0.190	-0.281
d	-0.153	-0.118	-0.215
e	-0.080	-0.224	-0.186
f #1	-0.155	-0.110	-0.159
f #2	-0.289	-0.218	-0.278

TABLE 3.6

Comparison of "true", "linear", and "block" velocity partial derivatives for approximate ray tracing

	TRUE		ART	
PATH	RAY TRACING	ART	LINEAR	BLOCK
a	-0.193	-0.172	-0.172	-0.186
b #1	-0.175	-0.140	-0.141	-0.175
b #2	-0.114	-0.092	-0.092	-0.118
c	-0.252	-0.195	-0.196	-0.267
d	-0.153	-0.107	-0.107	-0.193
e	-0.080	-0.161	-0.161	-0.155
f #1	-0.155	-0.125	-0.125	-0.206
f #2	-0.289	-0.220	-0.220	-0.297

TABLE 3.7

Modified Wesson velocity model for synthetic tests

$$V = 4.2474 + 0.3\,Z + \frac{0.932\,X}{1.5^2+|X|} - \frac{1.1393}{1+0.05X^2+0.0005(Y+38)^2+0.1(Z+1)^2}$$

LAYER 1		Z = 0			
X=	-8	-3	0	3	8
Y=					
8	3.31	3.28	3.72	4.34	4.76
19	3.33	3.36	3.83	4.42	4.78
30	3.35	3.42	3.91	4.48	4.80

LAYER 2		Z = 4			
Y=					
8	4.57	4.69	5.20	5.75	6.03
19	4.58	4.71	5.23	5.78	6.04
30	4.59	4.73	5.25	5.80	6.05

LAYER 3		Z = 8			
Y=					
8	5.83	6.01	6.54	7.07	7.29
19	5.84	6.01	6.54	7.08	7.29
30	5.84	6.02	6.55	7.08	7.30

TABLE 3.8

a) INITIAL MODEL

LAYER 1 Z = 0

X=	-8	-3	0	3	8
Y=					
8	3.60	3.60	3.80	4.30	4.30
19	3.60	3.60	3.80	4.30	4.30
30	3.60	3.60	3.80	4.30	4.30

LAYER 2 Z = 4

Y=					
8	4.90	4.90	5.20	5.70	5.70
19	4.90	4.90	5.20	5.70	5.70
30	4.90	4.90	5.20	5.70	5.70

LAYER 3 Z = 8

Y=					
8	5.90	5.90	6.50	7.00	7.00
19	5.90	5.90	6.50	7.00	7.00
30	5.90	5.90	6.50	7.00	7.00

b) FINAL MODEL

LAYER 1 Z = 0

X=	-8	-3	0	3	8
Y=					
8	3.35	3.26	3.77	4.49	4.63
19	3.39	3.36	3.89	4.53	4.80
30	3.38	3.31	3.94	4.61	4.68

LAYER 2 Z = 4

Y=					
8	4.68	4.70	5.15	6.00	6.20
19	4.62	4.76	5.35	5.99	6.19
30	4.71	4.74	5.22	6.05	6.20

LAYER 3 Z = 8

Y=					
8	5.79	5.88	6.42	7.20	7.28
19	5.75	5.87	6.56	7.18	7.43
30	5.90	5.83	6.46	7.22	7.46

TABLE 3.9a

FINAL MODEL - VELOCITY INVERSION

LAYER 1		Z = 0			
X=	-8	-3	0	3	8
Y=					
8	3.33	3.46	3.68	4.59	4.60
19	3.42	3.39	3.88	4.54	4.80
30	3.31	3.35	3.68	4.54	4.71
LAYER 2		Z = 4			
Y=					
8	5.11	4.48	5.27	5.90	6.20
19	4.71	4.81	5.37	5.95	6.20
30	4.75	4.89	5.68	5.85	6.20
LAYER 3		Z = 8			
Y=					
8	6.40	5.97	6.99	7.48	7.70
19	6.40	5.42	7.00	6.86	7.70
30	5.90	6.40	7.00	7.50	7.70

TABLE 3.9b

FINAL MODEL - VELOCITY INVERSION

LAYER 1		Z = 0			
X=	-8	-3	0	3	8
Y=					
8	3.13	3.50	3.52	4.42	4.34
19	3.37	3.42	3.93	4.62	4.79
30	3.14	3.50	3.70	4.37	4.52
LAYER 2		Z = 4			
Y=					
8	5.40	4.74	5.42	6.15	6.20
19	4.95	5.04	5.22	6.20	6.20
30	4.66	4.95	5.70	6.06	6.20
LAYER 3		Z = 8			
Y=					
8	5.85	5.49	7.00	7.50	7.70
19	6.40	5.89	6.78	7.40	7.70
30	6.40	6.40	7.00	7.50	7.70

TABLE 3.10a

FINAL MODEL - PARAMETER SEPARATION

LAYER 1		Z = 0			
X=	-8	-3	0	3	8
Y=					
8	3.38	3.38	3.65	4.51	4.70
19	3.39	3.41	3.83	4.56	4.80
30	3.38	3.43	3.86	4.62	4.71
LAYER 2		Z = 4			
Y=					
8	4.67	4.64	5.18	5.87	6.13
19	4.62	4.76	5.24	5.90	6.08
30	4.69	4.74	5.16	5.92	6.13
LAYER 3		Z = 8			
Y=					
8	5.70	5.90	6.56	7.00	7.61
19	5.81	5.85	6.62	7.10	7.44
30	5.90	5.84	6.46	6.93	7.70

TABLE 3.10b

FINAL MODEL - PARAMETER SEPARATION

LAYER 1		Z = 0			
X=	-8	-3	0	3	8
Y=					
8	3.40	3.38	3.77	4.50	4.73
19	3.41	3.40	3.82	4.59	4.80
30	3.43	3.44	3.92	4.69	4.80
LAYER 2		Z = 4			
Y=					
8	4.70	4.61	5.18	5.77	6.12
19	4.59	4.78	5.19	5.82	5.99
30	4.66	4.72	5.18	5.79	6.06
LAYER 3		Z = 8			
Y=					
8	5.65	5.77	6.70	6.99	7.68
19	5.70	5.79	6.53	6.91	7.23
30	5.78	5.66	6.19	6.84	7.60

TABLE 3.10c

FINAL MODEL - PARAMETER SEPARATION WITH ERROR

LAYER 1		Z = 0			
X=	-8	-3	0	3	8
Y=					
8	3.36	3.38	3.64	4.53	4.69
19	3.39	3.40	3.79	4.54	4.80
30	3.35	3.47	3.86	4.72	4.80

LAYER 2		Z = 4			
Y=					
8	4.70	4.62	5.14	5.89	6.17
19	4.61	4.76	5.23	5.88	6.06
30	4.69	4.71	5.20	5.81	5.98

LAYER 3		Z = 8			
Y=					
8	5.76	5.87	6.56	6.64	7.38
19	5.80	5.85	6.58	7.05	7.63
30	5.90	5.96	6.44	6.90	7.58

TABLE 3.11

Velocity model for testing
simultaneous inversion using ART

Z= \ X=	-8	-3	0	3	8
0	2.91	2.57	2.00	2.57	2.91
3	3.81	3.47	2.90	3.47	3.81
6	4.71	4.37	3.80	4.37	4.71
10	5.91	5.57	5.00	5.57	5.91

$$V = 3.0 + 0.3\ Z - \frac{1}{1 + 0.15\ X^2}$$

TABLE 3.12

ART inversion, error-free data

layer 1: Z=0

X=	-8	-3	0	3	8
Y=					
6	2.94	2.75	1.96	2.71	2.94
18	3.08	2.65	1.94	2.62	3.03
30	2.88	2.73	2.06	2.59	2.98

layer 2: Z=3

Y=					
6	4.00	3.57	2.96	3.49	3.91
18	3.87	3.57	2.98	3.49	3.90
30	4.02	3.54	3.03	3.49	3.93

layer 3: Z=6

Y=					
6	5.03	4.53	3.68	4.50	5.04
18	4.81	4.52	3.86	4.42	4.83
30	4.95	4.54	3.77	4.43	5.00

layer 4: Z=10

Y=					
6					
18		5.71	5.35	5.66	
30					

TABLE 3.13

ART inversion, data with error

layer 1: Z=0

X=	-8	-3	0	3	8
Y=					
6	2.92	2.58	2.11	2.68	2.83
18	3.13	2.62	1.92	2.64	3.06
30	2.88	2.74	2.03	2.61	2.89

layer 2: Z=3

Y=					
6	4.08	3.61	3.19	3.70	4.10
18	3.85	3.67	3.00	3.63	3.93
30	4.11	3.51	3.20	3.63	4.19

layer 3: Z=6

Y=					
6	4.90	4.40	3.97	4.33	4.83
18	4.89	4.65	3.57	4.66	4.86
30	4.93	4.51	3.91	4.37	4.61

layer 4: Z=10

Y=					
6					
18		5.44	5.32	5.84	
30					

TABLE 3.14

ART inversion, data with error
Variational hypocenter depth derivative

layer 1: Z=0

X=	-8	-3	0	3	8
Y=					
6	2.92	2.57	2.13	2.66	2.83
18	3.14	2.63	1.92	2.64	3.06
30	2.88	2.74	2.04	2.60	2.89

layer 2: Z=3

Y=					
6	4.06	3.62	3.22	3.68	4.09
18	3.85	3.73	2.95	3.70	3.93
30	4.11	3.50	3.22	3.61	4.17

layer 3: Z=6

Y=					
6	4.88	4.31	3.95	4.32	4.84
18	4.78	4.58	3.64	4.48	4.82
30	4.94	4.36	3.85	4.34	4.67

layer 4: Z=10

Y=					
6					
18		5.23	5.18	5.83	
30					

TABLE 3.15

Two-dimensional velocity model for resolution and error analysis

X= / Z=	0		5		10		15		20		25		30
-0.5	3.20	3.20	3.18	3.16	3.15	3.19	3.63	4.17	4.43	4.60	4.70	4.78	4.82
	3.81	3.80	3.79	3.79	3.79	3.87	4.32	4.85	5.07	5.22	5.32	5.38	5.43
3.5	4.41	4.41	4.42	4.42	4.45	4.57	5.04	5.55	5.74	5.86	5.94	5.99	6.04
	5.02	5.03	5.04	5.06	5.11	5.24	5.73	6.22	6.40	6.49	6.56	6.61	6.64
7.5	5.63	5.64	5.66	5.69	5.75	5.89	6.38	6.87	7.04	7.12	7.18	7.22	7.25
	6.24	6.25	6.27	6.31	6.38	6.52	7.01	7.51	7.66	7.74	7.80	7.83	7.86
11.5	6.85	6.86	6.89	6.93	7.00	7.14	7.63	8.13	8.18	8.36	8.41	8.44	8.47

TABLE 3.16 a

Resolution and velocity error for case a, error-free data

X=	0	5	10	15	20	25	30
Z=							
-0.5	0.73 0.87 0.87 0.96 0.95 0.93 0.96 0.94 0.84 0.84 0.67 +.01 -.12 -.14 -.11 +.13 +.06 +.26 -.10 +.09 0.00 +.03						
	0.71 0.95 0.99 0.98 0.98 0.99 0.98 0.98 0.97 0.92 -.18 -.04 -.09 0.15 -.15 +.03 -.14 -.02 -.09 -.18						
3.5	0.96 0.98 0.98 0.99 0.99 0.98 0.98 0.97 0.92 +.01 +.03 +.05 +.02 +.14 +.12 -.04 +.02 +.04						
	0.94 0.98 0.98 0.93 0.99 0.98 0.97 0.96 0.77 -.07 -.05 +.02 -.02 +.16 +.06 -.09 -.01 0.00						
7.5	0.84 0.94 0.95 0.96 0.96 0.93 0.84 0.58 0.58 -.03 -.13 +.08 -.04 +.02 -.04 -.11 -.20 -.10						
				0.78 0.74 0.59 -.18 +.02 -.20			

TABLE 3.16 b

Resolution and velocity error for case b, error-free data

X=	0	5	10	15	20	25	30
Z=							
-0.5	0.68 0.83 0.85 0.98 0.94 0.91 0.95 0.90 0.79 0.70 0.43 -.02 -.17 -.21 +.18 -.20 +.10 +.26 -.16 +.11 +.08 -.12						
	0.66 0.93 0.98 0.96 0.98 0.98 0.98 0.96 0.95 0.85 -.10 -.04 -.12 -.14 -.15 +.01 -.03 -.01 -.14 -.19						
3.5	0.94 0.96 0.97 0.98 0.98 0.97 0.96 0.92 0.85 +.02 +.03 +.12 0.00 +.20 +.13 -.04 +.09 +.16						
	0.81 0.96 0.96 0.96 0.98 0.95 0.94 0.86 0.44 -.08 -.05 -.01 +.05 +.09 +.09 -.11 -.01 +.01						
7.5		0.84 0.89 0.89 0.95 0.88 0.60 0.45 -.13 -.12 +.06 +.09 -.05 -.19 -.07					
				0.55 0.63 0.41 +.18 +.22 -.25			

TABLE 3.16 c

Resolution and velocity error for case c, error-free data

X=	0	5	10	15	20	25	30
Z=							
-0.5	0.53 0.67 0.77 0.68 0.73 0.78 0.81 0.60 0.67 0.44 0.34 -.42 0.00 +.19 +.17 -.12 +.05 +.18 -.25 +.19 -.17 +.04						
		0.87 0.97 0.84 0.89 0.96 0.90 0.82 0.93 0.81 +.07 -.18 +.01 -.31 +.01 +.18 -.30 -.05 -.07					
3.5		0.86 0.92 0.92 0.92 0.94 0.94 0.91 0.86 0.75 -.13 -.06 +.15 +.01 +.08 +.19 -.17 -.02 +.10					
		0.68 0.90 0.91 0.93 0.95 0.89 0.87 0.76 0.33 +.01 -.05 -.11 -.10 +.13 -.05 -.06 -.03 -.05					
7.5			0.59 0.81 0.80 0.92 0.77 0.39 0.29 +.24 -.15 +.11 +.04 -.13 -.20 -.13				
				0.44 +.21			

TABLE 3.16 d

Resolution and velocity error for case d, error-free data

X=	0	5	10	15	20	25	30
Z=							
-0.5	0.56 0.68 0.55 0.73 0.80 0.65 0.72 0.68 0.51 0.57 0.48 +.44 +.14 +.55 +.08 -.22 +.26 +.65 +.19 -.15 -.32 -.19						
		0.67 0.93 0.95 0.94 0.95 0.96 0.95 0.94 0.93 0.90 -.05 +.18 +.04 +.06 +.12 +.22 +.08 +.13 +.25 +.15					
3.5		0.95 0.97 0.98 0.98 0.97 0.97 0.96 0.92 0.92 -.03 +.05 +.12 +.09 +.24 +.29 +.14 +.22 +.25					
		0.92 0.97 0.97 0.98 0.98 0.97 0.96 0.94 0.76 -.01 0.00 +.03 +.06 +.25 +.15 +.06 +.10 +.23					
7.5		0.81 0.93 0.95 0.95 0.95 0.91 0.77 0.55 0.24 +.03 -.03 +.01 +.04 +.12 +.05 +.01 -.15 -.16					
			0.57 0.64 0.43 -.14 -.02 -.25				

TABLE 3.17

Average resolution and mean absolute velocity error for inversions with error-free data

	CASE	RESOLUTION	ERROR (km/sec)
a)	30 stations all events	0.91	0.08
b)	20 stations all events	0.85	0.10
c)	10 stations all events	0.77	0.12
d)	30 stations earthquakes only	0.82	0.16

TABLE 3.18 a

Resolution, velocity error, standard error and Jackson error measure for case a, data with error

X=	0		5		10		15		20		25		30
Z=													
-0.5	0.74	0.87	0.88	0.96	0.95	0.93	0.96	0.94	0.85	0.83	0.64		
	+.08	-.24	0.00	+.13	-.12	-.05	+.31	+.02	-.17	+.36	+.18		
	0.08	0.06	0.06	0.04	0.04	0.06	0.05	0.06	0.10	0.11	0.13		
	0.11	0.07	0.07	0.04	0.04	0.06	0.05	0.07	0.12	0.13	0.20		
1.5	0.72	0.96	0.98	0.98	0.98	0.99	0.98	0.98	0.97	0.92			
	-.39	-.04	-.06	-.13	-.15	+.02	-.11	-.03	+.06	-.40			
	0.10	0.04	0.03	0.03	0.03	0.03	0.04	0.04	0.06	0.08			
	0.13	0.05	0.03	0.03	0.03	0.03	0.04	0.04	0.06	0.10			
3.5		0.96	0.98	0.99	0.99	0.99	0.98	0.98	0.97	0.92			
		+.03	+.07	+.02	+.05	+.18	+.12	-.03	-.05	-.35			
		0.05	0.04	0.03	0.03	0.04	0.04	0.05	0.06	0.09			
		0.06	0.04	0.03	0.03	0.04	0.04	0.05	0.07	0.10			
5.5		0.94	0.97	0.98	0.98	0.99	0.98	0.97	0.96	0.67			
		-.06	-.05	-.03	+.06	+.05	+.03	+.01	0.00	+.07			
		0.07	0.05	0.05	0.04	0.04	0.06	0.07	0.08	0.18			
		0.08	0.05	0.05	0.05	0.04	0.06	0.07	0.09	0.24			
7.5		0.84	0.94	0.96	0.96	0.97	0.93	0.84	0.65	0.51			
		-.13	-.15	+.06	-.14	+.19	-.36	-.25	0.00	-.22			
		0.13	0.08	0.07	0.07	0.07	0.11	0.15	0.20	0.21			
		0.15	0.09	0.07	0.07	0.07	0.12	0.18	0.30	0.35			
9.5					0.77	0.76	0.59						
					-.21	-.17	+.01						
					0.17	0.18	0.23						
					0.22	0.23	0.32						

TABLE 3.18 b

Resolution, velocity error, standard error and Jackson error measure for case b, data with error

X=	0		5		10		15		20		25		30
Z=													
-0.5	0.69	0.84	0.85	0.97	0.93	0.91	0.95	0.90	0.80	0.69	0.42		
	+.22	-.32	+.12	+.24	-.23	0.00	+.33	-.11	-.07	+.52	-.29		
	0.08	0.06	0.06	0.03	0.05	0.06	0.05	0.07	0.10	0.12	0.12		
	0.10	0.07	0.07	0.03	0.05	0.06	0.05	0.08	0.12	0.15	0.21		
1.5	0.69	0.94	0.98	0.97	0.97	0.98	0.97	0.95	0.96	0.85			
	-.41	-.13	-.08	-.12	-.17	-.02	-.06	0.00	-.08	-.32			
	0.10	0.05	0.03	0.04	0.03	0.03	0.04	0.06	0.06	0.09			
	0.12	0.05	0.03	0.04	0.04	0.03	0.04	0.06	0.06	0.12			
3.5		0.95	0.97	0.97	0.98	0.98	0.97	0.95	0.92	0.86			
		+.02	+.10	+.04	+.06	+.22	+.09	-.02	+.10	+.65			
		0.05	0.04	0.04	0.04	0.04	0.05	0.07	0.09	0.12			
		0.06	0.05	0.04	0.04	0.04	0.05	0.07	0.09	0.13			
5.5		0.80	0.96	0.96	0.96	0.98	0.96	0.94	0.88	0.37			
		+.06	-.05	+.06	-.04	+.03	+.13	-.07	+.02	+.12			
		0.11	0.06	0.06	0.05	0.05	0.07	0.08	0.12	0.18			
		0.13	0.06	0.06	0.06	0.05	0.08	0.09	0.14	0.30			
7.5			0.82	0.89	0.87	0.95	0.86	0.64	0.46				
			-.17	+.03	+.05	+.19	-.42	-.45	+.19				
			0.12	0.10	0.11	0.08	0.14	0.19	0.19				
			0.14	0.11	0.12	0.08	0.15	0.24	0.31				
9.5					0.54	0.61	0.36						
					+.34	+.04	+.09						
					0.18	0.20	0.20						
					0.25	0.25	0.34						

TABLE 3.18 c

Resolution, velocity error, standard error and Jackson error measure for case c, data with error

X= / Z=	0	5	10	15	20	25	30
-0.5	0.51 0.67 0.77 0.69 0.75 0.79 0.81 0.68 0.72 0.45 0.37 -.35 -.13 +.12 +.15 -.10 -.21 +.40 +.03 -.13 -.38 +.03 0.09 0.09 0.08 0.08 0.08 0.09 0.09 0.12 0.12 0.14 0.14 0.14 0.12 0.10 0.11 0.10 0.11 0.12 0.16 0.16 0.22 0.24						
1.5		0.87 0.96 0.84 0.89 0.97 0.91 0.78 0.93 0.82 +.31 -.14 0.00 -.36 +.04 +.10 -.37 +.22 -.14 0.07 0.04 0.08 0.07 0.05 0.08 0.13 0.08 0.11 0.09 0.05 0.10 0.08 0.05 0.09 0.15 0.09 0.15					
3.5		0.82 0.89 0.92 0.94 0.95 0.94 0.90 0.88 0.80 -.45 -.20 +.07 +.06 +.09 +.20 -.22 -.02 +.56 0.10 0.08 0.07 0.07 0.07 0.08 0.11 0.12 0.15 0.12 0.09 0.09 0.07 0.07 0.09 0.11 0.13 0.18					
5.5		0.73 0.91 0.90 0.92 0.90 0.86 0.86 0.82 0.33 +.10 -.10 -.03 +.07 -.09 -.31 -.15 -.21 +.28 0.14 0.09 0.10 0.09 0.10 0.13 0.14 0.16 0.19 0.17 0.10 0.10 0.10 0.11 0.15 0.16 0.19 0.34					
7.5			0.51 0.79 0.81 0.94 0.80 0.69 0.37 +.51 -.19 +.04 +.24 -.24 +.43 -.26 0.17 0.14 0.14 0.10 0.17 0.20 0.21 0.26 0.17 0.17 0.10 0.20 0.25 0.37				
9.5				0.33 -.25 0.21 0.40			

TABLE 3.19

Average resolution, mean velocity error, computed mean standard error and mean error estimate of Jackson (1979)

	CASE	RESOLUTION	ERROR	STANDARD ERROR	JACKSON ERROR
a)	30 stations all events	0.90	0.12	0.07	0.10
b)	20 stations all events	0.82	0.15	0.08	0.11
c)	10 stations all events	0.78	0.19	0.11	0.15

FIGURE CAPTIONS

Figure 3.1 Analytical velocity model (from Wesson, 1971) for testing the linearity and accuracy of the hypocentral partial derivatives.

Figure 3.2 Error in the predicted change in travel time due to displacement of the source in the X, Y, and Z directions.

Figure 3.3 Ray paths used in the hypocentral partial derivative study. Circles are the sources (with depth in km indicated); squares are the receivers (all at zero depth).

Figure 3.4 Travel time as a function of source displacement in the X, Y, and Z directions:

P_x, P_y - predicted travel time
R_x, R_y - ray tracing travel time
A_x, A_y - approximate ray tracing travel time

Figure 3.5 Error in the predicted change in (ray tracing) travel time due to a velocity perturbation at a specific grid point:

a: NX=3, NZ=3
b 1: NX=3, NZ=2
b 2: NX=2, NZ=4
c: NX=5, NZ=2
d: NX=2, NZ=2
e: NX=3, NZ=1
f 1: NX=4, NZ=3
f 2: NX=6, NZ=2

(See Tables 3.3 and 3.4).

Figure 3.6 Same as for Figure 3.5, but using approximate ray tracing.

Figure 3.7 a) Distribution of stations used in inversion tests.

b) Distribution of sources used in inversion tests, with depth in km indicated.

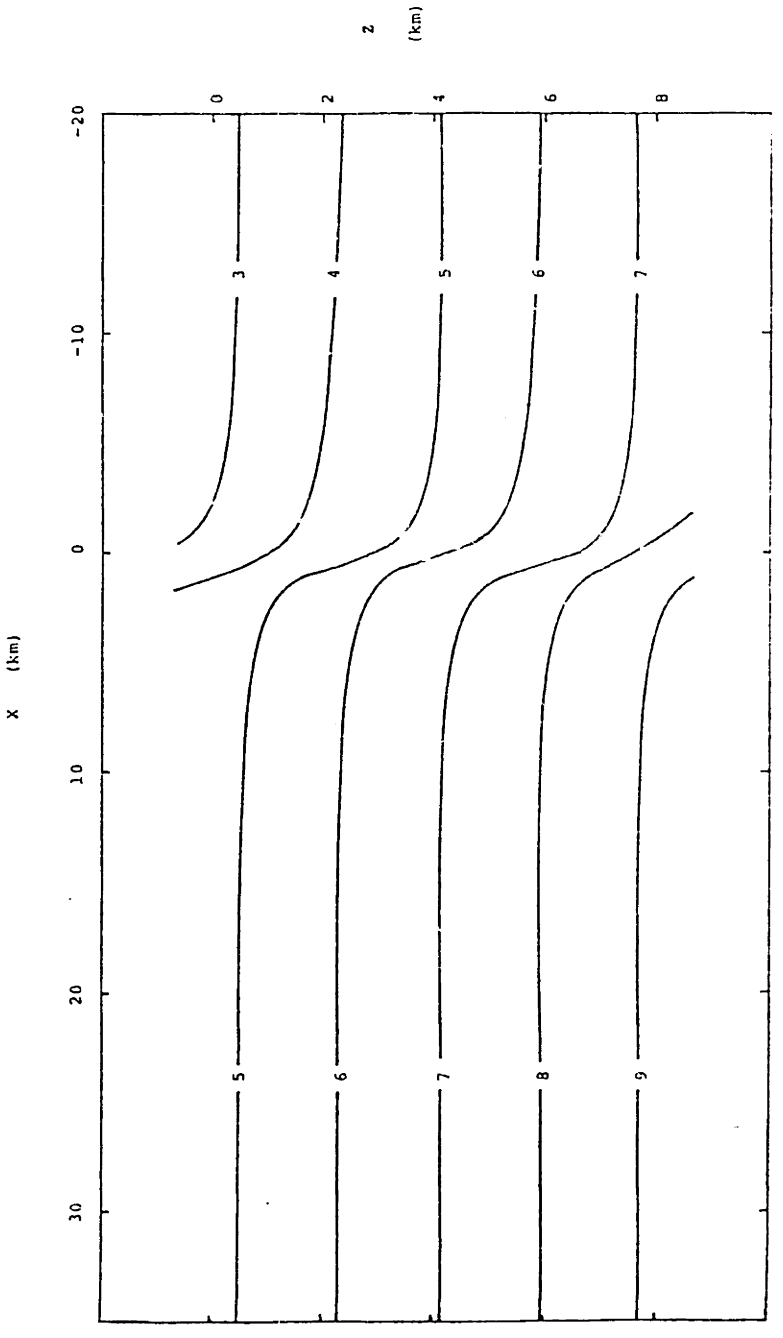

Figure 3.1

Figure 3.2

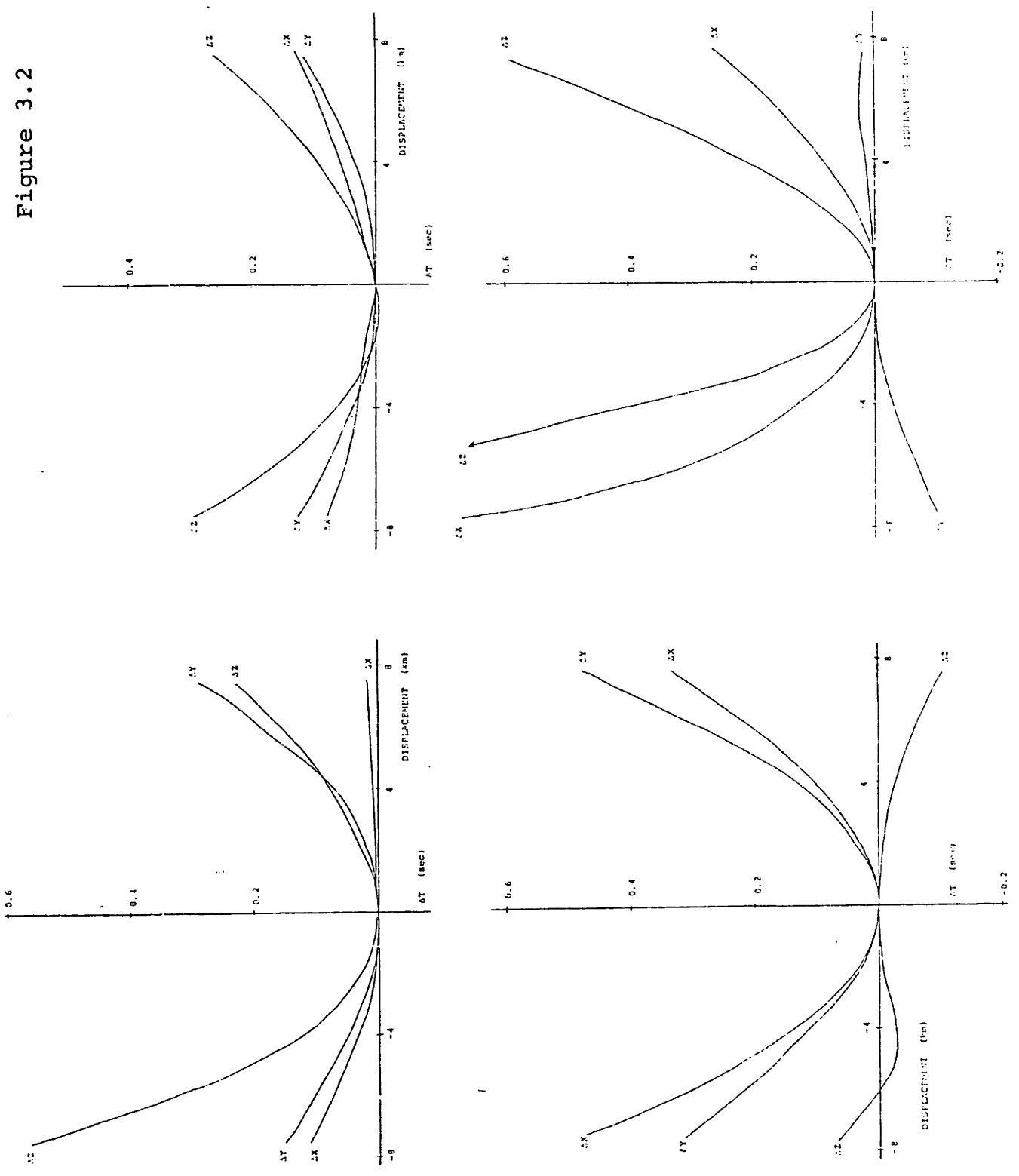

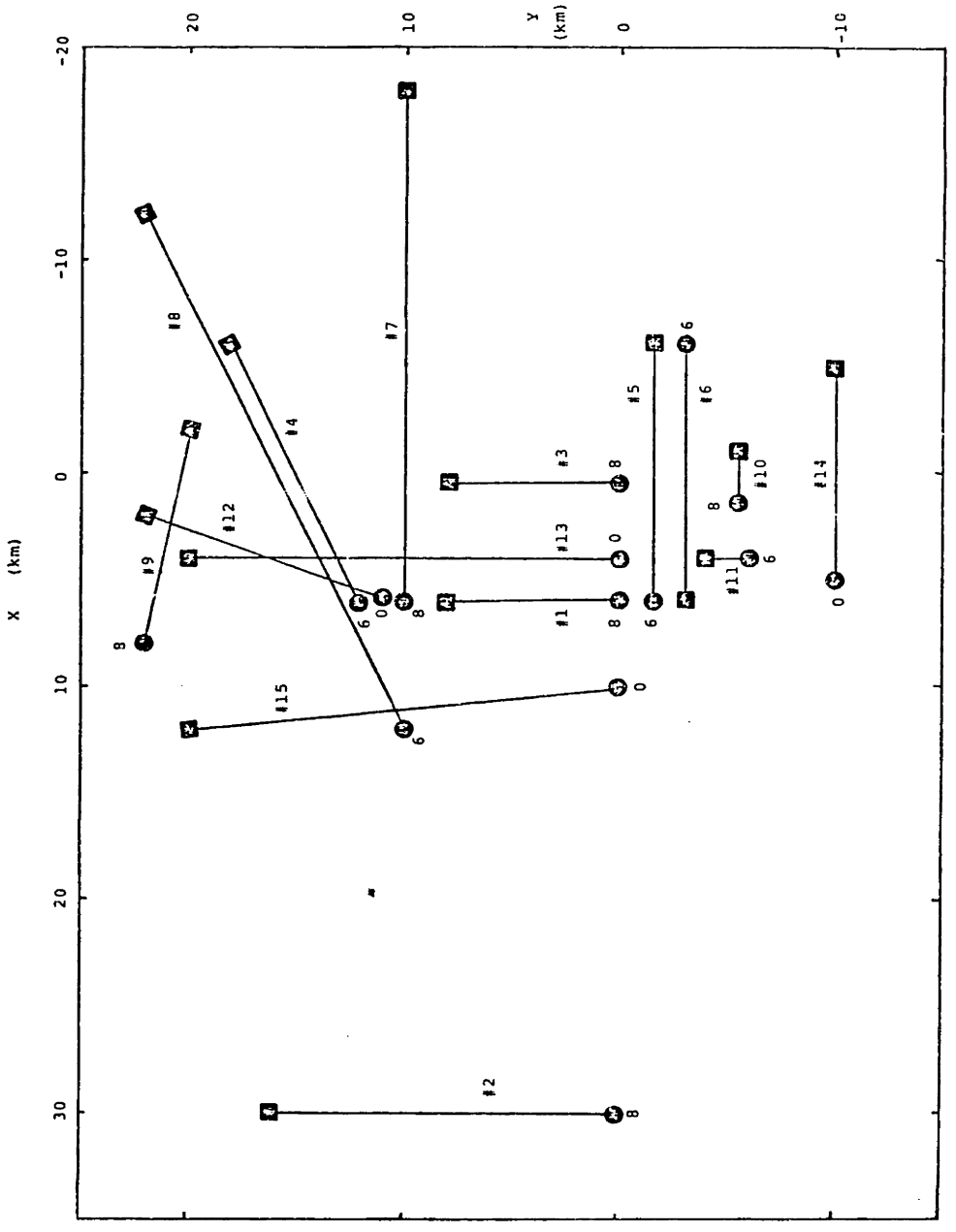

Figure 3.3

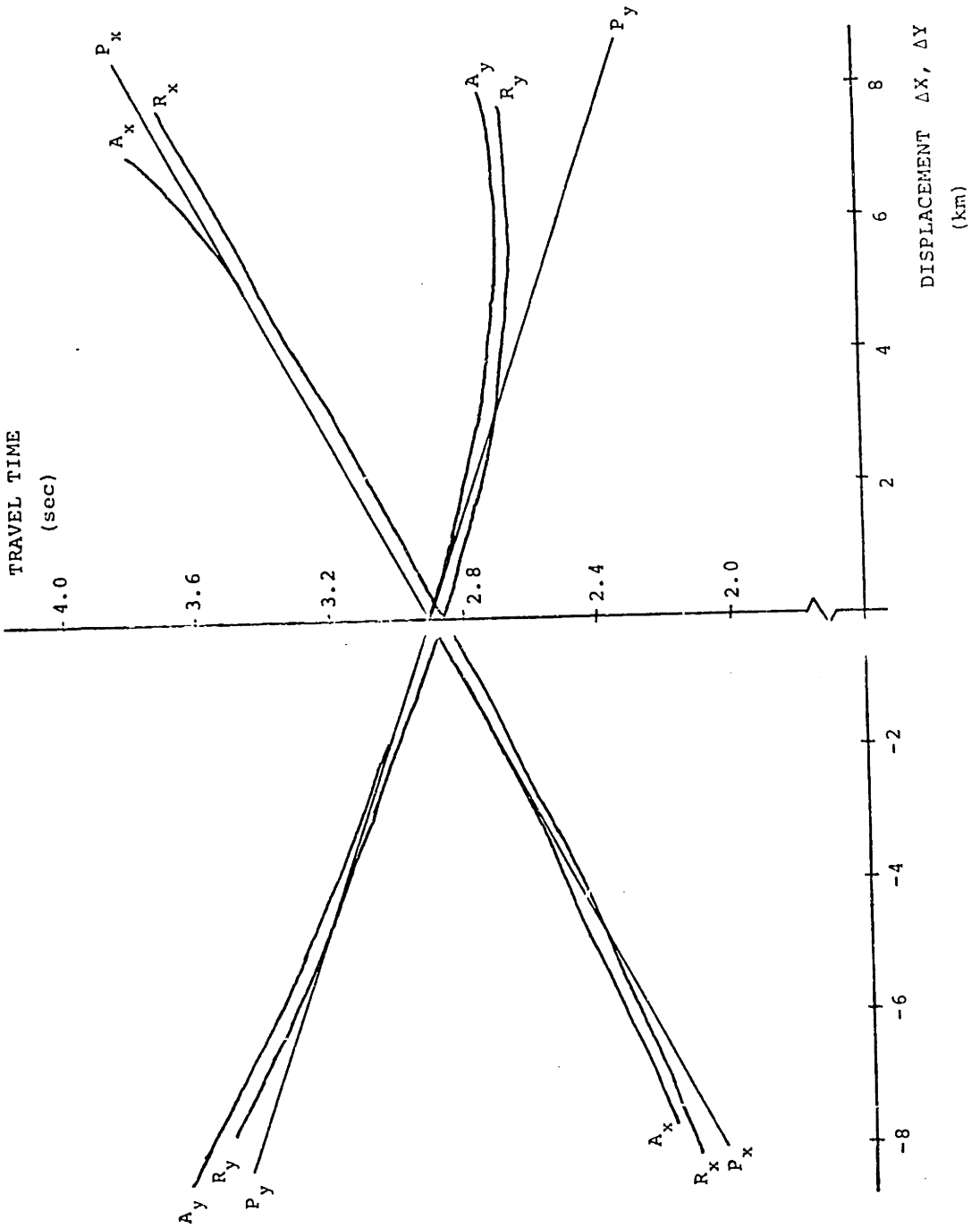
TRAVEL TIME
(sec)
4.0
3.6
3.2
2.8
2.4
2.0
P_x
A_x
R_x
A_y
R_y
P_y
A_y
R_y
P_y
A_x
R_x
P_x
2
4
6
8
-2
-4
-6
-8
DISPLACEMENT ΔX, ΔY
(km)

Figure 3.4

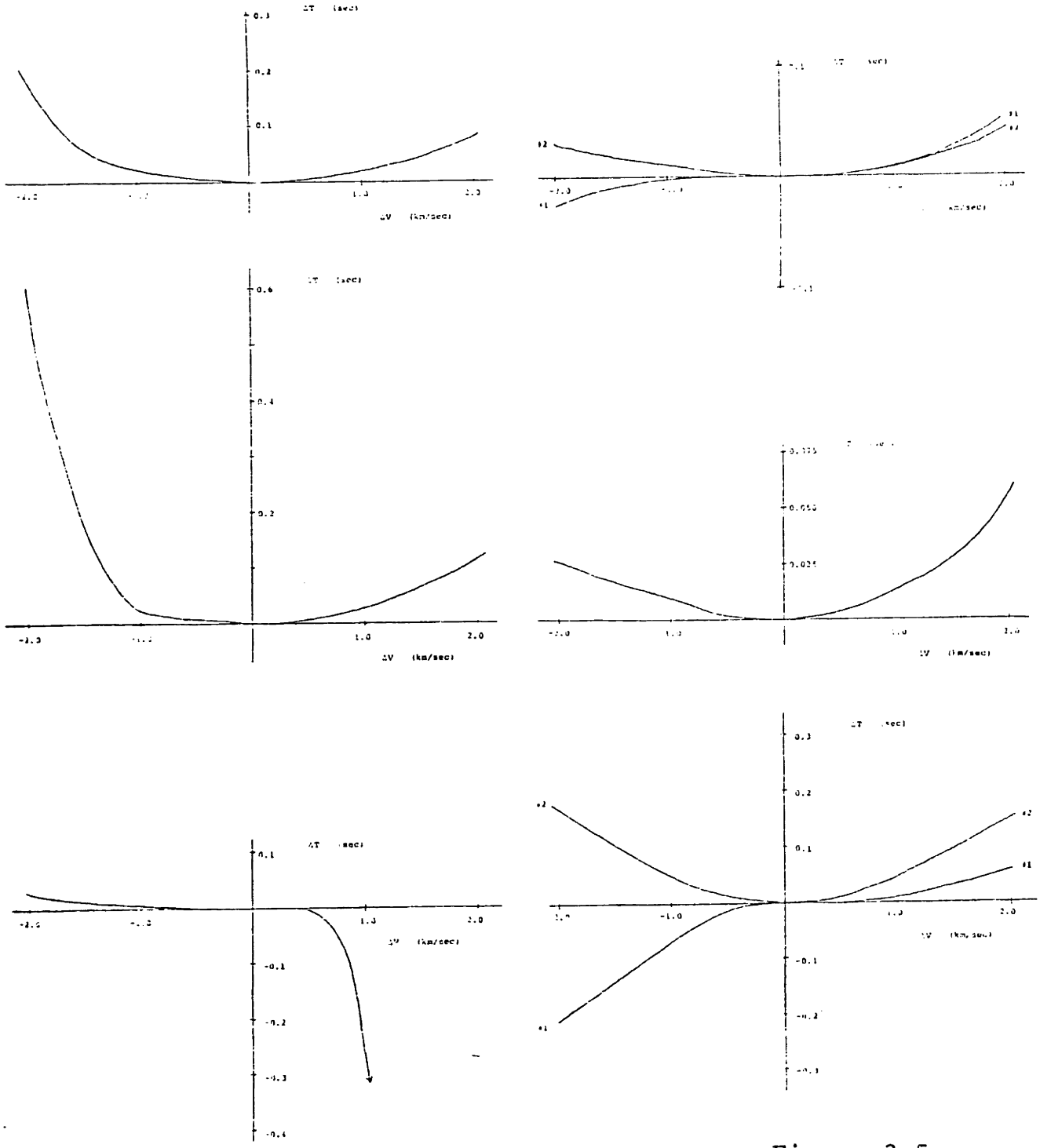

Figure 3.5

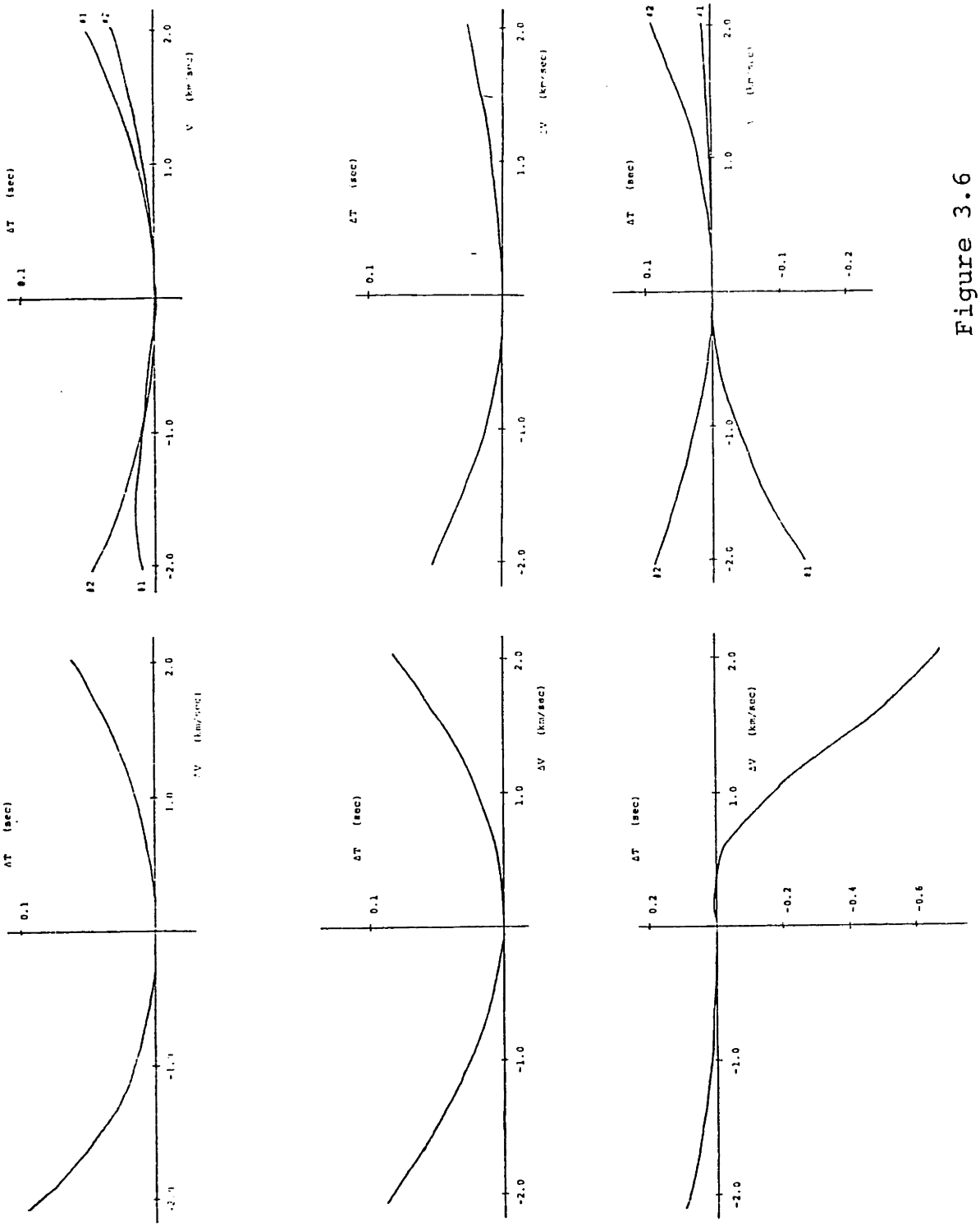

Figure 3.6

a)

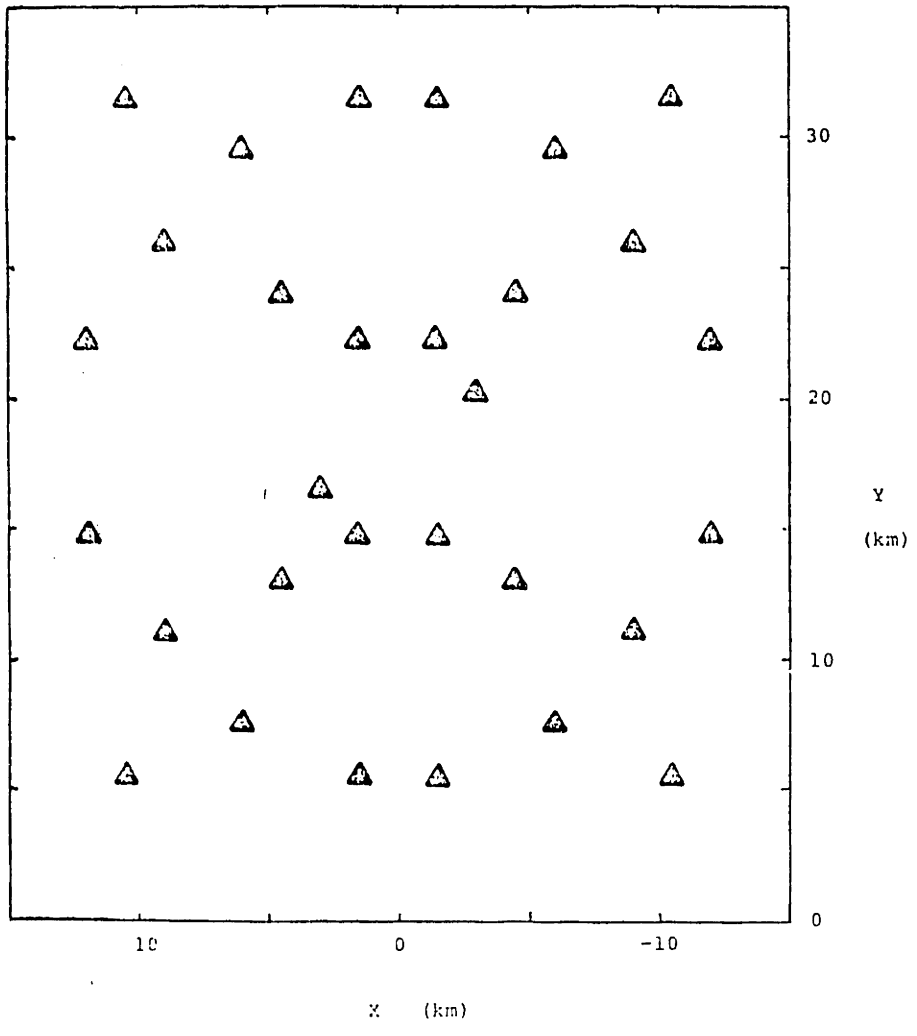
30
20
10
0
Y
(km)
10
0
-10
X (km)

b)

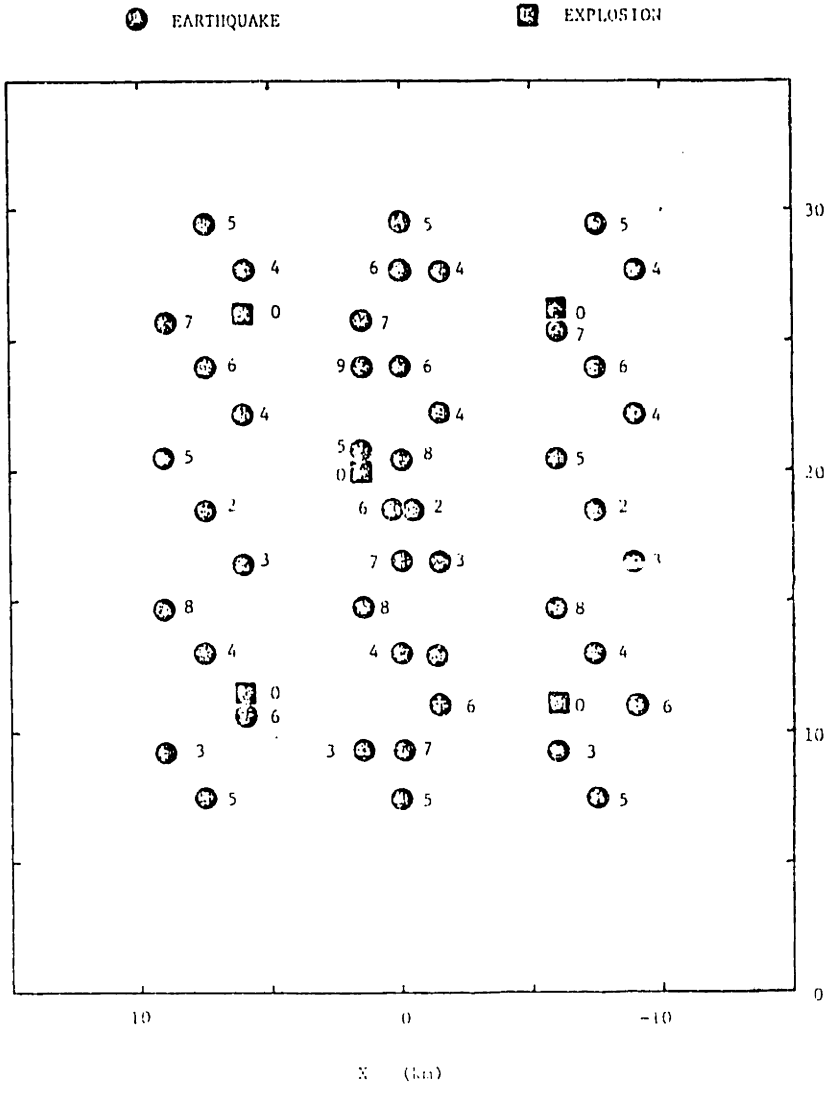
EARTHQUAKE
EXPLOSION
30
20
10
0
10
0
-10
X (km)

Figure 3.7

CHAPTER 4

CRUSTAL STRUCTURE IN THE COYOTE LAKE AREA

4.1 INTRODUCTION TO THE STUDY AREA

On August 6, 1979, an earthquake of magnitude 5.7 occurred near Coyote Lake, California. This event was one the largest in central California since the great 1906 earthquake (Uhrhammer, 1980). A large amount of interest has been generated for the study of various aspects of this earthquake and its aftershocks. One of the fundamental problems faced is the poor knowledge of the details of the structure of the crust in the Coyote Lake area.

The goals of this chapter are to determine the three-dimensional seismic velocity structure of the crust around Coyote Lake, and to investigate the locations of many recent earthquakes in this region. As an introduction to the area of study, the geology of the area is briefly described, and gravity and magnetic data for the area are presented and discussed. The recent tectonic history of the region is summarized in Appendix C.

4.1.1 GEOLOGY OF THE COYOTE LAKE AREA

The geology of the region around Coyote Lake (which will

occasionally be referred to as the Gilroy area - see Figure 4.1 and Table 4.1) is extremely complex. The principal units found in the area are the Franciscan formation, granitic rocks, Tertiary alluvial fill, Great Valley sequence rocks, and other marine and non-marine sedimentary rocks of primarily Tertiary age. Ultramafic rocks and Cenozoic volcanic rocks are also found in the area. The characteristics of most of these units are thoroughly discussed by Hanna et al. (1972).

The Franciscan formation, which dominates the study area, is composed of metamorphosed sedimentary and volcanic rocks (see Bailey et al., 1970). The types of sedimentary rocks found include graywacke, siltstone, bedded chert, and conglomerate, while the volcanic rocks are primarily pillow lavas, breccia, and tuff (Hanna et al., 1972). The granites, which predominate southwest of the San Andreas fault, are plutonic rocks similar to those of the Sierra Nevada (Evernden and Kistler, 1970).

Part of the reason for this enormous geologic complexity is the rather active recent tectonic activity of the area, which has resulted in the juxtaposition of radically different suites of rocks. A brief review of the recent history of California relevant to the area of study is presented in Appendix C in order to provide the background for identifying the basic rock types which are found and/or inferred to exist beneath the surface in the Coyote Lake area.

From the region depicted in Figure 4.1, an area of size 40 km by 60 km, oriented N 41° W, was chosen for detailed study (see Figure 4.2). The area was chosen primarily to encompass the aftershock zone of the Coyote Lake earthquake. Other influencing factors include the availability of coverage by seismic stations of the US Geological Survey Central California network (Figure 4.2) and the distribution of local seismicity (Figure 4.3). A simplified geologic map for the study area is shown in Figure 4.4.

4.1.2 GRAVITY AND MAGNETIC ANOMALY DATA

Gravity and magnetic data can be used to make some inferences about the local crustal structure. Figures 4.5 and 4.6 display Bouguer gravity and magnetic anomaly maps for the study region. The two most notable features on the two maps are a gravity low and magnetic high between the San Andreas fault and the southeastern part of the Calaveras fault, and a gravity high and magnetic low between the Sargent and Calaveras faults. The latter anomaly can probably be attributed to the presence of Franciscan basement at shallow depth in the area as found by Mooney and Luetgert (1980). The former anomaly corresponds to the shear zone between the San Andreas fault and the southwest extension of the Calaveras fault. The gravity suggests the presence of substantial thicknesses of sedimentary rocks and/or fault gouge in this zone, while the magnetic anomaly

has been interpreted as being due to buried serpentinized ultramafic rocks (Hanna et al., 1972).

Other features on the gravity map are a low in the southwest corner of the study area, and another low in the northwest corner west of the San Andreas. The latter low is likely due to increasing sediment thickness in the Santa Cruz basin area, while the former anomaly might be attributable to a locally substantial thickness of Great Valley sequence rocks.

4.2 BASIC CHARACTERISTICS OF THE EARTHQUAKE LOCATIONS, TRAVEL TIME ANOMALIES, AND VELOCITY STRUCTURE

The regional tectonic activity described in Appendix C continues today as evidenced by the large number of seismically active faults in the area. Figures 4.7 a and b show some of the surface mapped and/or seismically inferred faults, and Figure 4.3 shows a sample of the seismicity of the past decade. The latter figure also illustrates one of the more perplexing problems encountered constantly in the study of earthquakes in this area - the epicenters of earthquakes along the Calaveras and San Andreas faults are clustered a significant distance away from the mapped surface traces of the faults (see for example Bolt et al., 1968; Brown and Lee, 1971; Mayer-Rosa, 1973; Uhrhammer, 1980). Evidence from quarry blast and explosion data strongly suggests that along the Calaveras fault north of

the study area this offset is not real but is caused by complexities in the local velocity structure (Mayer-Rosa, 1973). There is similar evidence for the events along the San Andreas fault southwest of the Gilroy area in Bear Valley (Wesson, 1971; Engdahl and Lee, 1976).

In this section we examine the anomalies in travel time from earthquakes in three different sections of the study area. These three sections are shown in Figure 4.8. The Northeast section contains the Calaveras and related faults, the Central section contains the Sargent fault, and the Southwest section contains the San Andreas and related faults. Next, simple layered velocity models with variable station corrections are developed for each of these sections, and the resulting velocity models and station corrections are interpreted in terms of the basic character of the structure of the region.

4.2.1 THE CALAVERAS AND RELATED FAULTS

A very simple device for examining travel time anomalies is a plot of P-wave travel (or arrival) times (see Healy and Peake, 1975). If the earth were laterally homogeneous and all observing stations were at the same elevation, contoured travel time plots should appear as a set of concentric circles. Any deviations from this pattern could then be interpreted in terms of areas or zones of relatively high or low P-wave velocity.

Figure 4.9 shows the principal seismic stations in the study area used for these plots. The travel times (observed arrival time minus calculated source origin time) are all corrected for station elevation by the amount

$$\Delta t = -z_s/(3.0 \text{ km/sec})$$

where z_s is the station elevation in km, and 3.0 km/sec represents a crude average of the near-surface velocity.

Five events along the Calaveras fault and the small fault to the northeast (which we will call the Santa Ana fault since it lies in the Santa Ana Valley) were chosen based on their distribution and large number of observations. The elevation-corrected travel-time plots for these events are shown in Figure 4.10 a to e. All five plots show clear evidence for travel time delays along and northeastward of the Calaveras fault (refer to Figure 4.7b). Some of the most substantial delays are observed in the area between the Calaveras and San Andreas faults. In addition Figures 4.10 c to e suggest a delay for waves passing near the Busch fault. Finally, Figures 4.10 a and b show evidence for relatively high velocities in the much of the zone between the Calaveras and Sargent faults.

Travel times from 47 large (local magnitude > 2.5) well observed events in the northeast area were then quantitatively analyzed to determine a layered velocity model with optimal station corrections (and of course

hypocentral parameters). The events and stations used are shown in Figures 4.11 and 4.12. The basic method used for the solution of this inverse problem is similar to that of Crosson (1976a), but with the inclusion of parameter separation. The station corrections which result from such an inversion tend to reflect two types of lateral velocity heterogeneity - shallow variations local to the individual station, and deeper systematic variations which affect a number of stations (for example a low velocity zone along a fault).

The layered velocity model for the northeast section is shown in Figure 4.13. The near-surface velocity is less than 4 km/sec, and increases to over 5 km/sec by a depth of around 1 km. Below 5 km depth the velocity increases to about 6 km/sec. This model is quite similar to the model of Steppe and Crosson (1978) for the structure northeast of the San Andreas fault in roughly this same area, which is dominated by Franciscan bedrock. To a depth of about 7 or 8 km the velocities are comparable to laboratory-measured velocities of Franciscan rocks (Stewart and Peselnick, 1977, 1978; Lin and Wang, 1980). Below that depth the velocity of nearly 7 km/sec is too high for normal Franciscan racks, however, suggesting a compositional change below that depth.

The station corrections derived in the inversion are shown in Figure 4.14. The three stations lying between the Calaveras and Sargent faults show the largest negative correction, supporting the suggestion from the travel time

plots that this is a region of systematically higher velocity. The largest relative delays (positive and small negative corrections) are found near the Busch fault and along the southeast extension of the Calaveras, again consistent with the deductions from the travel time plots.

As an independent test of this model (both velocities and station corrections), 140 smaller events (local magnitude between 2.0 and 2.5) were relocated using HYPO71 (Lee and Lahr, 1975) with the given station corrections and velocity structure. The model was quite adequate for locating these earthquakes, achieving an RMS arrival time residual of 0.10 sec and below for 77 of the events, and with only 18 events having an RMS exceeding 0.15 sec. The final locations for 13 well-distributed, well-observed events along the Calaveras fault are shown in Figure 4.15. All the events are located less than 3 km from the fault trace, and the southernmost epicenters are less than 0.5 km/sec away.

4.2.2 THE SARGENT FAULT

Arrival time plots for five events along the Sargent fault and its southeast extension are shown in Figure 4.16 a to e. Again we observe evidence of strong lateral variations in velocity. All five plots indicate the presence of relatively high velocity in the zone between the Sargent and Calaveras faults. A second common feature among the plots is a strong delay for waves traveling through the

southernmost part of the zone between the Sargent and San Andreas faults and between the San Andreas and Calaveras faults. Higher velocities are found southwest of the San Andreas. The rapid travel time changes crossing the San Andreas in the southern part of Figures 4.16 a and b may be indicating the occurrence of laterally refracted waves.

A simultaneous inversion for hypocentral parameters, a layered velocity structure, and station corrections for this Central section was carried out using 36 events primarily along the Sargent fault (see Figure 4.17). The stations used in the inversion are shown in Figure 4.18. The resulting velocity model is plotted in Figure 4.13 along with the Steppe and Crosson (1978) and Gilroy Northeast models. All three models are basically comparable, which is expected since the Central section is presumed to be primarily Franciscan as well. The Gilroy Central model does show somewhat lower near surface velocity (3.5 versus 3.8 and 4.0 km/sec) and possibly slightly lower velocities below 7 km depth.

The station corrections derived from the Central inversion are plotted in Figure 4.19. Negative corrections are found southwest of the San Andreas and in between the Sargent and Calaveras faults, supporting the claim of relatively high velocities in those areas. Very large delays are seen between the San Andreas and Calaveras faults. In addition we find delays southwest of the San Andreas in the area of the Bouguer gravity low (see Figure

4.5).

4.2.3 THE SAN ANDREAS AND RELATED FAULTS

Arrival time plots for four events along the San Andreas and Vergeles faults are shown in Figure 4.20 a to d. High velocities are once again clearly indicated in the zone between the Sargent and Calaveras faults, and for the southern portion of the area southwest of the San Andreas. Systematic travel time delays are only observed in two areas: between the San Andreas and the southern extension of the Calaveras, and between the San Andreas and Vergeles faults. The latter area of low velocity overlaps the delay area mentioned in section 4.2.2. The Bouguer gravity map of Clark and Reitman (1973) shows this entire area to have a negative gravity anomaly (see Figure 4.21). They attribute it to downfaulting of the basement between the two faults and a resulting greater thickness of sedimentary fill.

The 18 events plotted in Figure 4.22 and the stations in Figure 4.18 were used to derive a layered velocity model with station corrections for the southwest section. The velocity model determined by the inversion is shown in Figure 4.23 along with the Gabilan Range velocity model of Healy and Peake (1975) for the Bear Valley area. The velocities of the southwest model below 3 km are substantially lower than those of the Healy and Peake model, but in fact they are quite close to the corresponding

laboratory-determined velocities of granites of Lin and Wang (1980).

The station corrections derived from the Southwest inversion are shown in Figure 4.24. Negative corrections are again found in the northern part of the zone between the Sargent and Calaveras faults. Otherwise all the corrections northeast of the San Andreas are large and positive. For the southern part of this area, the large delays are undoubtedly due to low velocities in the zone between the San Andreas and Calaveras faults. The smaller delays in the northern part are possibly due to somewhat lower velocities just to the northeast of the Calaveras, where Great Valley sequence rocks are exposed. There is no clear expression in the station corrections of the delays along the Vergeles fault seen in the travel time plots.

To again provide an independent test of this velocity model (and station corrections), 169 smaller earthquakes of local magnitude 2.0 to 2.5 were relocated using HYPO71. Of these events, 99 had a final RMS residual of 0.10 sec or less, and only 25 had an RMS above 0.15 sec. The final locations for 13 of these events distributed along the San Andreas are plotted in Figure 4.25. All epicenters are less than 1.5 km from the fault trace, and the six northernmost events are within 1 km of the fault.

4.2.4 SUMMARY

The general features of the velocity structure and distribution of seismicity have been revealed by the application of simple techniques of analysis. In general the velocity values are consistent with expectations from the geology and laboratory study of the local rock types. At moderate depth (about 3 to 8 km) the velocities match those of granites as the principal unit southwest of the San Andreas fault, and Franciscan to the northeast. Travel time delays and layered-model station corrections delineate zones of low velocity along and/or in between the major faults. The most prominent example is the area between the San Andreas and the southeast extension of the Calaveras fault. Finally, the evidence suggests that most epicenters do lie along the principal fault traces, and that their apparent systematic displacement away from the faults is truly due to the extreme lateral variations of velocity in the area. Perhaps the one exception is for events in the vicinity of Coyote Lake itself (Figure 4.15). Further modeling in sections 4.3 and 4.4 will explicitly permit such lateral variations, in order to analyze the velocity structure more quantitatively and hopefully to determine the earthquake hypocenters more accurately.

4.3 TWO-DIMENSIONAL MODELS OF THE VELOCITY STRUCTURE

Two-dimensional models for the crustal velocity structure under the Coyote Lake area have been determined as the next

step in constructing a complete three-dimensional picture of the structure of the study region. From the description of the region in section 4.1 and from inspection of Figures 4.4 through 4.7 (the geology, gravity, magnetic anomalies and faults of the study area) it is clear that a two-dimensional velocity model would not be adequate for describing the structure of the entire Coyote Lake region. Thus the area was subdivided into three strips approximately 40 km by 20 km within each of which a two-dimensional model has been constructed (see Figure 4.2). Velocity models for these three sections are presented and discussed in comparison with the knowledge of the local structure derived through other means (primarily from geology).

4.3.1 SECTION 1

The permanent stations and three explosions used in the inversion for section 1 (the southeasternmost section) are shown in Figure 4.26. The majority of the events in this area cluster along the San Andreas fault and the extension of the Calaveras fault (see Figure 4.3), but as noted earlier those along the San Andreas tend to be systematically displaced 2 to 5 km to the southwest of the surface trace of the fault. There are also a number of events along the Santa Ana fault to the northeast.

The inversion was started with a laterally homogeneous crustal model with grid points spaced 4 km apart in the x

direction and 3 km apart in the z direction. Three iterations achieved an 82 per cent reduction in the sum of squared residuals (henceforth SSQR) for the 516 observations: from 24.90 initially to 4.35. Further iterations could not significantly reduce the SSQR. See Table 4.2 for the convergence history for this model.

The relocated epicenters (Figure 4.27) differ substantially from the initial locations calculated with respect to the initial laterally homogeneous model, and they also differ from the USGS locations. The general trend is for events along the Calaveras and particularly the San Andreas fault to migrate towards the mapped fault traces by roughly 1 to 3 km, bringing them much closer to (but still not directly underneath) the fault traces. (Note: the location of the fault to the northeast, which we are calling the Santa Ana fault, is not well determined, so that no meaningful statement can be made relating the epicenters to that fault trace).

The final velocity model for section 1 (Figure 4.28) displays a striking correlation with the geology of the section. The most conspicuous feature of the velocity model is a pronounced low velocity wedge ($V \cong 4$ to 5 km/sec) located precisely between the San Andreas and Calaveras faults. A strong gravity low is observed directly over this zone. To the southwest of the wedge are much higher velocities ($V > 6$ km/sec) and a local gravity high, consistent with the presence of granitic basement rocks. To

the northeast first intermediate (V ≅ 5.5 km/sec) and then moderately high (V ≅ 6 km/sec) velocities are found, corresponding to Great Valley sequence and Franciscan rocks respectively (see Figure 4.4). A comparison of this model with the model proposed by Healy and Peake (1975; their Figure 21) for Bear Valley, located just to the southeast of this section, shows a remarkable similarity - the two are nearly identical in form. Thus the gross velocity structure of the crust appears to be resolved.

Additionally the near surface velocities derived relate well to the local geology. The lowest velocities are found in the northeastern part of the section (X small), corresponding to areas of primarily Quaternary alluvial fill and Cretaceous (Great Valley sequence) sedimentary rocks. Higher velocities are observed in the southwestern part where the granitic basement of the Gabilan Range is exposed.

4.3.2 SECTION 2

The permanent stations and two explosions used in the inversion for section 2 (the central section) are shown in Figure 4.29. The events in this section cluster along the three principal faults, the San Andreas, Sargent, and Calaveras (see Figure 4.3). The epicenters appear to be systematically displaced 1 to 4 km southwest of the San Andreas and northeast of the Calaveras fault traces.

The inversion was started with a laterally homogeneous

crustal model, again with grid point spacing of 4 km and 3 km in the x and z directions respectively. Three iterations achieved a 78 per cent reduction in the SSQR for the 482 observations: from 21.16 initially to 4.71. Further iterations did not significantly reduce the SSQR. See Table 4.3 for the convergence history for this model.

The relocated epicenters along the San Andreas show a significant displacement towards the mapped fault trace, moving to within 1 to 1.5 km of the fault (see Figure 4.30). Along the Sargent fault there is a slight trend of displacement towards the fault (though they were close to begin with), whereas along the Calaveras there is no clear trend at all. In the case of the Calaveras the presence of only a single station to the northeast of the fault probably accounts for the scatter in the epicenters.

The final velocity model for section 2 is shown in Figure 4.31. Once again a strong relationship is seen between the derived velocity model and the geology of the section. Two low velocity wedges are found, one along the Calaveras fault and one between the Sargent and San Andreas faults. The existence of mild gravity lows over these areas supports the presence of these two zones. High velocities ($V \cong 6$ km/sec) at depth between the Calaveras and Sargent faults indicate the probable presence of underlying Franciscan bedrock, which is exposed farther to the northeast. High velocities ($V > 6$ km/sec) southwest of the San Andreas fault are again consistent with the presence of the Gabilan granitic rocks.

The velocities at depth northeast of the Calaveras are unfortunately not sampled by this data.

The near surface velocities also correlate well with the mapped geology. In the southwest, fairly high velocities are found where two of the three stations lie on exposed granite (at HDL and HJG). Between the Sargent and Calaveras faults strong low velocities correspond to the Quaternary alluvial fill. To the northeast of the Calaveras moderate velocities are found on the Great Valley sequence rocks.

4.3.3 SECTION 3

The permanent stations and four explosions used in the inversion for section 3 are shown in Figure 4.32. The events in this section are found mainly along the Calaveras and Sargent faults, with very few along the San Andreas (note Figure 4.10). Epicenters along the Calaveras show the clearest displacement from the mapped fault trace, generally lying 3 to 4 km or so to the northeast.

The inversion was started with a laterally homogeneous crustal model, this time with a grid spacing of 6 km in the x direction (due to the unfavorable event and station distribution), and again 3 km in the z direction. Three iterations achieved a 58 per cent reduction in the SSQR for the 839 observations: from 32.22 initially to 13.42. Further iterations did not significantly reduce SSQR (note: the explosion data were primarily responsible for this high

overall residual sum). See Table 4.4 for the convergence history for this model.

The relocated epicenters (Figure 4.33) along the San Andreas and Sargent faults remain close to the fault traces, but along the Calaveras two trends are observed. The locations of one group change very little, remaining within about 2 km of the fault trace, but events of the other group are displaced to as far as 5 or 6 km from the fault. The events of the latter group are those farthest north along the fault. Three possible interpretations are that these events are occurring on a different part of the fault zone northeast of the main trace of the Calaveras, that the unfavorable station distribution cannot adequately constrain the locations of these events, or that the two-dimensional representation of the structure is inadequate, resulting in a severe mislocation of this set of events. We will return to this question in the next section.

The final velocity model for section 3 is shown in Figure 4.34. Again a strong correlation is observed between the velocity model and the geology. Mildly low velocity zones are found along the Calaveras and between the Sargent and San Andreas faults. Southwest of the San Andreas the velocities are moderately high at depth, corresponding to the granitic basement, and the low near-surface velocities reflect the sedimentary fill of the Santa Cruz basin. An observed gravity low is consistent with this interpretation. In between the Sargent and Calaveras faults an area of high

velocity extending close to the surface is indicative of rocks of the Franciscan formation starting at fairly shallow depth. A gravity high is seen over this area also. Intermediate to low velocities are found just northeast of the Calaveras, as expected for rocks of the Great Valley sequence.

4.4 THREE-DIMENSIONAL MODELS OF THE CRUSTAL STRUCTURE IN THE COYOTE LAKE AREA

The crustal modeling of section 4.3 is extended to three dimensions in this section. First a moderately coarse model encompassing the entire study area (sections 1, 2 and 3) is determined and compared to the geology and two-dimensional results. Then a more detailed three-dimensional model focusing on the combined sections 2 and 3 is developed. The implications of the structure models are discussed in relation to other geophysical and geological knowledge of the area. In Chapter 5 the detailed velocity structure model will be used to help investigate the spatial and temporal characteristics of the aftershock sequence of the Coyote Lake earthquake.

4.4.1 THREE-DIMENSIONAL STRUCTURE OF THE STUDY AREA

A set of 77 well-distributed earthquakes was selected covering essentially the entire study area. 42 permanent

stations and 9 explosions were used (see Figure 4.35) and an additional 108 temporary stations were included.

Two starting velocity models were employed, one laterally homogeneous and one laterally heterogeneous (synthesized to be a composite model from the three two-dimensional models). In the x and y directions the grid spacing was 6 and 8 km respectively, while in the z direction grid points were positioned at 0.0, 2.5, 6.0, and 10.0 km depth (based on experimentation and on the one and two-dimensional model results). Both inversions converged to quite similar velocity models after three iterations (see Table 4.5 a and b for the convergence histories and Figures 4.36 a and b and 4.37 a and b for the final velocity models). The final epicenter locations for the two cases are also quite comparable (Figure 4.38 a and b).

The epicenter relocations follow the same general trends as those observed for the two-dimensional models. Along the San Andreas, the relocated epicenters lie quite close to the fault trace, although they still remain about 1 to 2 km to the southwest. Considering the coarseness of the model, their close proximity along the entire length of the fault is rather encouraging. Similarly along the Sargent fault the epicenters are typically within 1 km of the fault trace.

The same is not true along the Calaveras fault, however. Along the southern part the epicenters are quite near the fault trace, but to the north many of the epicenters are still rather clearly displaced well away from the fault. By

analogy with the San Andreas fault (Engdahl and Lee, 1976) and other parts of the Calaveras fault (Mayer-Rosa, 1973), it is tempting to assume that the events are still simply mislocated due to inadequacies of the model of the velocity structure. However the trace of the Calaveras fault is quite complex in this area (Radbruch-Hall, 1974), showing multiple strands, so that the offset may be (in part) real. It is also possible that the orientation of the velocity model, aligned principally with the trend of the San Andreas fault and oblique to the Calaveras, may be hindering the proper determination of the structure along the Calaveras. Unfortunately it is not possible to determine more precisely the locations of these events. Most of them are aftershocks of the Coyote Lake earthquake, and the station CAD (which is absolutely critical for constraining the locations of these northerly events) was not in operation for nearly the entire first three weeks of the aftershock sequence. Also many of the velocity grid points close to these events are at the periphery of the velocity model. These are the grid points most vulnerable to large errors, as seen in Chapter 3. The earthquake locations in this area near and north of the Coyote Lake main shock will be examined with caution in the aftershock study of Chapter 5 because of this problem.

The velocity models (Figures 4.36 a,b and 4.37 a,b) bear strong resemblance to the corresponding two-dimensional models (Figures 4.28, 4.31 and 4.34). In the area of section 1 (Y $\cong$ 0 to 20 km), we find in the three-dimensional

models a strong low velocity wedge which appears to reach a depth of 10 km in one of the two models. To either side the velocities are significantly higher. This deep low-velocity wedge, directly northeast of the San Andreas fault, is the most conspicuous feature of the velocity model. This zone is also marked by a strong gravity low (Figure 4.5) and a strong magnetic high (Figure 4.6). Healy and Peake (1975) detected a similar zone of low velocity between the San Andreas and San Benito faults in Bear Valley, California, just to the southeast of section 1. Thus our model confirms the existence of this anomalous zone, and indicates that the zone extends to a depth of about 10 km and possibly more.

Wang et al. (1978) combined ultrasonic velocity measurements and gravity data to suggest that this wedge most likely consists of fractured rocks and fault gouge. Their wet gouge samples had measured P-wave velocities (as a function of pressure) ranging from 3.5 to 4.3 km/sec, with the highest velocity at a pressure corresponding to a depth of roughly 8 km. However our model shows the velocity increasing to 5.0 km/sec or greater by 6 km depth at most, implying a different rock type. According to Hanna et al. (1972) the magnetic high over this zone is best explained by a local concentration of serpentinite. A P-wave velocity of 5 km/sec is quite typical for serpentinite (Christensen, 1978). Thus our preferred interpretation of the constitution of this zone is primarily fault gouge to a depth of perhaps 4 km, grading into primarily serpentinite

which extends to a depth of as much as 10 km.

On either side of this wedge the velocities are notably higher. To the northeast the velocity is fairly uniform (except at very shallow depth) at about 5.9 km/sec. All available evidence is consistent with the interpretation of Franciscan basement below the Miocene volcanics and overthrust Great Valley sequence rocks seen at the surface. To the southwest the velocities are quite high ($V > 6$ km/sec) beginning at fairly shallow depth, as expected for the granitic rocks exposed in the area. Unfortunately the velocity at depths below roughly 7 km southwest of the San Andreas in this section are not sampled by the data set used.

Moving to the area of section 2 ($Y \cong 20$ to 40 km), it is again observed that the two and three-dimensional models are fundamentally similar. In each case two zones of low velocity are found, one extending up the Calaveras fault and the other sandwiched between the Sargent and San Andreas faults. Both of these zones appear to be extensions of the gouge and serpentinite wedge of section 1. Northeast of the Calaveras the Franciscan-like velocities ($V \cong 5.8$ km/sec) are evident but at slightly greater depth, suggesting a greater thickness of the sediments and/or Great Valley sequence rocks in this area. Both the two and three-dimensional models also show a hint of fairly high velocity between the Calaveras and Sargent faults in the section 2 area. Finally southwest of the San Andreas the

high velocities (V > 6 km/sec) typical of the granites are seen, but again at a greater depth. Significantly lower velocity (V ≅ 5.6 km/sec) is determined extending to perhaps 5 or 6 km depth. This is consistent with the work of Clark and Rietman (1973) discussed in section 4.2.3, showing evidence for basement downfaulting between the San Andreas and Vergeles faults. The 5.6 km/sec velocity could be the result of smoothing together of the true velocities of the deep sediments and the underlying granites.

For the area of section 3 the two and three-dimensional results are once again quite comparable. Northeast of the Calaveras the velocities are indicative of Franciscan underlying Great Valley sequence rocks. Between the Calaveras and Sargent faults the velocity is high (V ≅ 6.2 km/sec) starting at shallow depth. This result is consistent with the work of Mooney and Luetgert (1980), who find evidence for a similarly high velocity at shallow depth in this area from refraction work. Between the Sargent and San Andreas faults there is only a slight suggestion of a continuation of the low velocity wedge. Interestingly, southwest of the San Andreas fault we find very low velocities extending to perhaps 3 or 4 km depth overlying extremely high velocities (V ≅ 7 km/sec). This area is associated with a gravity low and a magnetic high. Hanna et al. (1972) attribute the gravity low to the thick, low density sediments of the Santa Cruz basin, and the magnetic high to underlying gabbroic rocks (most likely intrusives).

Their interpretation is entirely supported by the seismic velocities determined here.

4.4.2 DETAILED MODELING OF THE NORTHERN PART OF THE STUDY AREA

The aftershock zone of the Coyote Lake earthquake is encompassed by sections 2 and 3 of the study area. Therefore it is of particular interest to explore the structure of this area in somewhat greater detail. In this section the results of a suite of inversions covering the northern part of the study area are reported. The intent is to assess the effects of the choice of grid point spacing and grid point placement on the resulting models of the velocity structure, and to attempt to measure crudely the scale of the (detectable) velocity variations. Encouragingly, it is found that varying the placement of the grid points does not noticeably affect the model. However inversion using too coarse a grid does yield a poorer, somewhat distorted solution.

First a set of inversions ranging from coarse (10 by 10 km) to fine (4 by 4 km) lateral grid spacing were carried out. The results of these inversions (velocity models and epicenter relocations) are displayed in Figure 4.39 a to e. The final epicenters are basically similar in all cases, although there is a trend for the epicenters to lie closer to the mapped faults in the inversions with finer spacing.

This similarity is not surprising since earthquake locations have been shown to be only weakly dependent on assumed velocity structure (Peters, 1973).

The final velocity models are not completely comparable, however. The two coarsest inversions, with 10 by 10 km and 7 by 7 km horizontal spacings (Figure 4.39 a and b) obscure or distort some of the features seen in the other models. For example, the northern part of the low-velocity wedge northeast of the San Andreas, the low velocity zone along the Calaveras, and the low velocities of the Santa Cruz basin are far less prominent in the coarse models. These inversions also have significantly higher overall RMS arrival time residuals (see Table 4.6).

The resultant velocity models from the other three inversions (6 by 6 km, 5 by 5 km, and 4 by 4 km spacings) are basically similar, as are the final RMS residuals (see Figure 4.39 c to e and Table 4.6). All of the significant geological and geophysical features discussed in section 4.4.1 are apparent in these models. This suggests that the scale of "deterministic" lateral heterogeneity is on the order of 5 km in this area. Since the 5 by 5 km model produces the smallest overall residuals, further modeling will be done using 5 km horizontal grid spacing.

Three additional inversions using 5 by 5 km spacing are combined with the model of Figure 4.39 d to produce a final composite velocity model for the area. Two of the inversions using shifted grids are intended to be used to

average out any bias caused by the particular choice of grid point placement; the third uses a laterally heterogeneous starting velocity model constructed from the models of Figures 4.36 and 4.37.

The final velocity models and epicenter relocations from these three inversions are shown in Figure 4.40 a to c. The final model for the inversion using the laterally heterogeneous starting model (Figure 4.40 c) is virtually identical to the model in Figure 4.39 d. Thus we feel that the solution is not significantly biased by the choice of starting velocities. In addition, the models from the shifted-grid inversions have velocities which smoothly interpolate among the velocity values of the unshifted model. This is illustrated in Figure 4.41, in which the velocity values from the unshifted and two shifted inversions are plotted together. A composite model constructed using these velocities will be used in Chapter 5 for locating aftershocks of the Coyote Lake earthquake, although it is anticipated that some difficulties may be encountered as discussed in section 4.4.1.

4.5 SUMMARY

The crust in the Coyote Lake area of central California is the product of a long, complex tectonic history. The local geology, gravity and magnetics clearly reflect this complexity. A great deal of effort has gone into trying to

understand the past history and present structure of this area of California (as well as others). However the constitution of the subsurface is still very poorly known.

The continuing tectonic evolution is responsible for the substantial seismic activity of this region. A significant seismological puzzle is the tendency for earthquake epicenters in this area to fall systematically several kilometers away from the surface traces of the major faults, principally the San Andreas and Calaveras faults. Many workers have suggested that this phenomenon is a result of the complex seismic velocity structure in the vicinity of these faults (Bolt et al., 1968; Brown and Lee, 1971; Mayer-Rosa, 1973; Boore and Hill, 1973; Healy and Peake, 1975; Aki and Lee, 1976; Engdahl and Lee, 1976).

These two problems, the structure of the earth and the locations of earthquakes in the Coyote Lake area, have been studied together using the arrival times of P waves from local earthquakes and explosions. Arrival time plots are valuable for identifying areas of anomalous P-wave velocity, for example the very low velocities indicated between the San Andreas and the southern extension of the Calaveras fault. However systematic modeling is necessary in order to quantify velocity variations and thus determine the earthquake locations. The method of simultaneous inversion has been employed for this purpose.

Simultaneous inversion using flat-lying homogeneous layers and station corrections has become a common technique

in the past few years (see for example Crosson, 1976a,b; Steppe and Crosson, 1978; Hileman, 1979). This simple method has been applied to three separate areas of the Coyote Lake study region. The resulting velocity models resemble the layered structures for this general area derived by other workers (Healy and Peake, 1975; Steppe and Crosson, 1978) and the velocity values are typical of the principal rock types in the region, namely Franciscan and granitic. The only measure of lateral variations in velocity in such models are the station corrections. Some of the trends observed in the station corrections can be interpreted in terms of specific areas of anomalous velocity, which generally agree with the findings from the travel time plots, but again the variations are not quantifiable. An important result of these inversions is a tendency for the earthquakes to be relocated closer to the fault traces.

The simultaneous inversion method has been generalized to permit explicitly lateral heterogeneity in crustal structure (see Chapter 2). Models allowing velocity variations in two and three dimensions have been determined for the Coyote Lake study area. Overall the velocity models display striking correlations with the geology and the gravity and magnetic anomalies, and the earthquake epicenters generally are relocated closer to the mapped fault traces.

The most notable feature of the velocity model for the study area is a wedge of strongly low velocities located

between the San Andreas and the southern extension of the Calaveras fault. This zone apparently reaches to a depth of approximately 10 km, and is seen to divide and extend a short distance northwards along both faults. The combination of seismic velocities with gravity and magnetic data suggests that this zone probably consists of fault gouge and serpentinite.

Southwest of the San Andreas, the velocities found in the southern part of the area are typical of the Gabilan granites. In the central part, basement downfaulting between the Vergeles and San Andreas faults has apparently resulted in locally deeper sediment fill and hence lower seismic velocity. To the north the velocity is very low in the top 3 km or so, reflecting the substantial sediment thickness in the Santa Cruz basin area. Below roughly 5 km depth the velocities are more typical of gabbroic rock.

Between the Sargent and Calaveras faults we find a combination of a gravity high and magnetic low with relatively high P-wave velocity from the surface to the greatest resolvable depth. Franciscan rocks are exposed at the surface throughout this area, so the conclusion is that the Franciscan extends to a depth of 6 km or more in this part of the study area.

Finally northeast of the Calaveras fault the gravity and magnetic anomaly maps are rather featureless. The velocities are correspondingly fairly uniform and moderate in magnitude. However in the northern part of this area a

mild gravity low and somewhat low velocities (at roughly 2 to 4 km depth) hint at a more complex structure near and north of the epicenter of the Coyote Lake earthquake.

TABLE 4.1

KEY TO GEOLOGIC UNITS IN FIGURE 4.1

Unit Number	Description
1	Franciscan formation
2	Cretaceous marine (Great Valley)
3	Miocene volcanics
4	Granitic
5	Tertiary non-marine
6	Mesozoic ultrabasic
7	Tertiary marine
8	Pre-Cretaceous limestone or dolomite
9	Franciscan volcanics

Note: Unnumbered units are either Quaternary alluvium (e.g. the Santa Clara Valley) or simply unspecified (e.g. much of the southwestern corner of the map).

TABLE 4.2

CONVERGENCE HISTORY FOR SECTION 1 MODEL
(516 observations)

ITERATION	SSQR	RMS RESIDUAL
initial	24.898	0.220
1	11.544	0.150
2	6.093	0.109
3	4.354	0.092

TABLE 4.3

CONVERGENCE HISTORY FOR SECTION 2 MODEL
(482 observations)

ITERATION	SSQR	RMS RESIDUAL
initial	21.156	0.210
1	8.494	0.133
2	5.452	0.106
3	4.708	0.099

TABLE 4.4

CONVERGENCE HISTORY FOR SECTION 3 MODEL
(836 observations)

ITERATION	SSQR	RMS RESIDUAL
initial	32.224	0.196
1	16.834	0.142
2	14.832	0.130
3	13.422	0.126

TABLE 4.5

CONVERGENCE HISTORY FOR THE THREE-DIMENSIONAL INVERSIONS FOR THE ENTIRE STUDY AREA

a) Laterally homogeneous starting model.

ITERATION	SSQR	RMS RESIDUAL
initial	180.64	0.27
1	87.16	0.19
2	54.15	0.15
3	46.26	0.13

b) Laterally heterogeneous starting model

ITERATION	SSQR	RMS RESIDUAL
initial	145.70	0.24
1	70.39	0.17
2	53.21	0.15
3	47.82	0.14

TABLE 4.6

FINAL RESIDUALS FOR THREE-DIMENSIONAL INVERSIONS

	GRID SIZE	SSQR	RMS RESIDUAL
a)	10 x 10	41.79	0.17
b)	7 x 7	32.53	0.15
c)	6 x 6	26.27	0.13
d)	5 x 5	22.61	0.12
e)	4 x 4	24.39	0.13

TABLE 4.7

FINAL RESIDUALS FOR THREE-DIMENSIONAL INVERSIONS

	MODEL	SSQR	RMS RESIDUAL
a)	shifted in x	24.42	0.13
b)	shifted in y	22.49	0.12
c)	heterogeneous initial model	20.33	0.12
d)	unshifted	22.61	0.12

FIGURE CAPTIONS

Figure 4.1 Geology of the area around Coyote Lake. See Table 4.1 for key to geologic units.

Figure 4.2 Location of the study area, with US Geological Survey permanent seismometer stations indicated.

Figure 4.3 Seismicity in the Coyote Lake area. Events with magnitude above 2.5 from 1970 to 1979.

Figure 4.4 Simplified geologic map of the study area. Note that unmarked unit is Tertiary sediments.

Figure 4.5 Bouguer gravity map of the study area.

Figure 4.6 Magnetic anomaly map of the study area.

Figure 4.7 a) Faults in the area around Coyote Lake. b) Principal faults of the study area.

Figure 4.8 Subdivisions of the Coyote Lake region for individual layered-model inversions.

Figure 4.9 Permanent seismometer stations in the study area.

Figure 4.10 a-e) Travel time plots for events along the Calaveras and Santa Ana faults.

Figure 4.11 Events included in the Northeast section layered-model inversion.

Figure 4.12 Stations included in the Northeast inversion.

Figure 4.13 One-dimensional velocity models for the Northeast and Central sections of the Gilroy area, with the model of Steppe and Crosson (1978) for the same general area included for comparison.

Figure 4.14 Station corrections (in seconds) from the Northeast model.

Figure 4.15 Revised epicenters of representative events, using the Northeast model for relocation.

Figure 4.16 a-e) Travel time plots for events along the Sargent fault and the southern extension of

Figure 4.32 Permanent stations and explosions used in the section 3 inversion (see Figure 4.2 for location).

Figure 4.33 Section 3 event relocations.

Figure 4.34 Section 3 velocity model.
Average resolution: 0.88
Average error:
Standard = 3.8 percent
Jackson = 4.2 percent

Figure 4.35 Stations and explosions used in the three-dimensional inversion. Explosions indicated by *.

Figure 4.36 Three-dimensional velocity model starting from a laterally homogeneous initial velocity model.
a) Velocity in km/sec.
b) Pattern of velocity variations:
H = high
o = intermediate
L = low
Average resolution: 0.93
Average error:
Standard = 3.4 percent
Jackson = 3.7 percent

Figure 4.37 Three-dimensional velocity model starting from a laterally heterogeneous initial velocity model.
a,b) same as for Figure 4.36
Average resolution: 0.92
Average error:
Standard = 3.5 percent
Jackson = 3.9 percent

Figure 4.38 Event relocations for:
a) model in Figure 4.36;
b) model in Figure 4.37.

Figure 4.39 Pattern of velocity variations and event relocations for inversions using different grid point spacings:
a) 10 by 10 km;
b) 7 by 7 km;
c) 6 by 6 km;
d) 5 by 5 km;
e) 4 by 4 km;

Figure 4.40 Additional inversion results using 5 by 5 km grid:

a) grid shifted in x direction;
b) grid shifted in y direction;
c) laterally heterogeneous initial velocity model.

Figure 4.41 Velocity values from inversions shown in Figures 4.39d, 4.40a and 4.40b, illustrating the smoothness and consistency of the results.

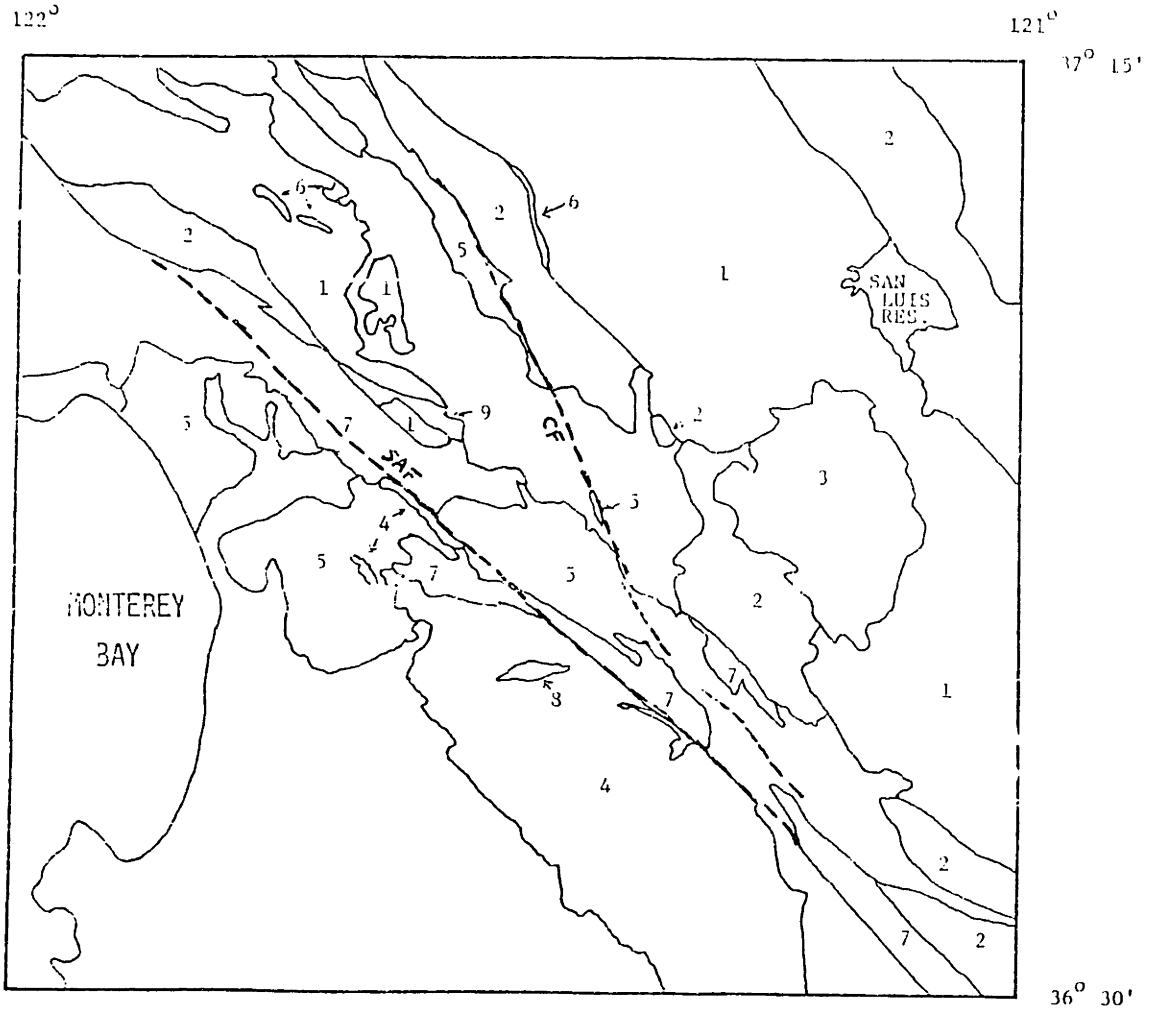

GILROY AREA - GEOLOGIC MAP

Figure 4.1

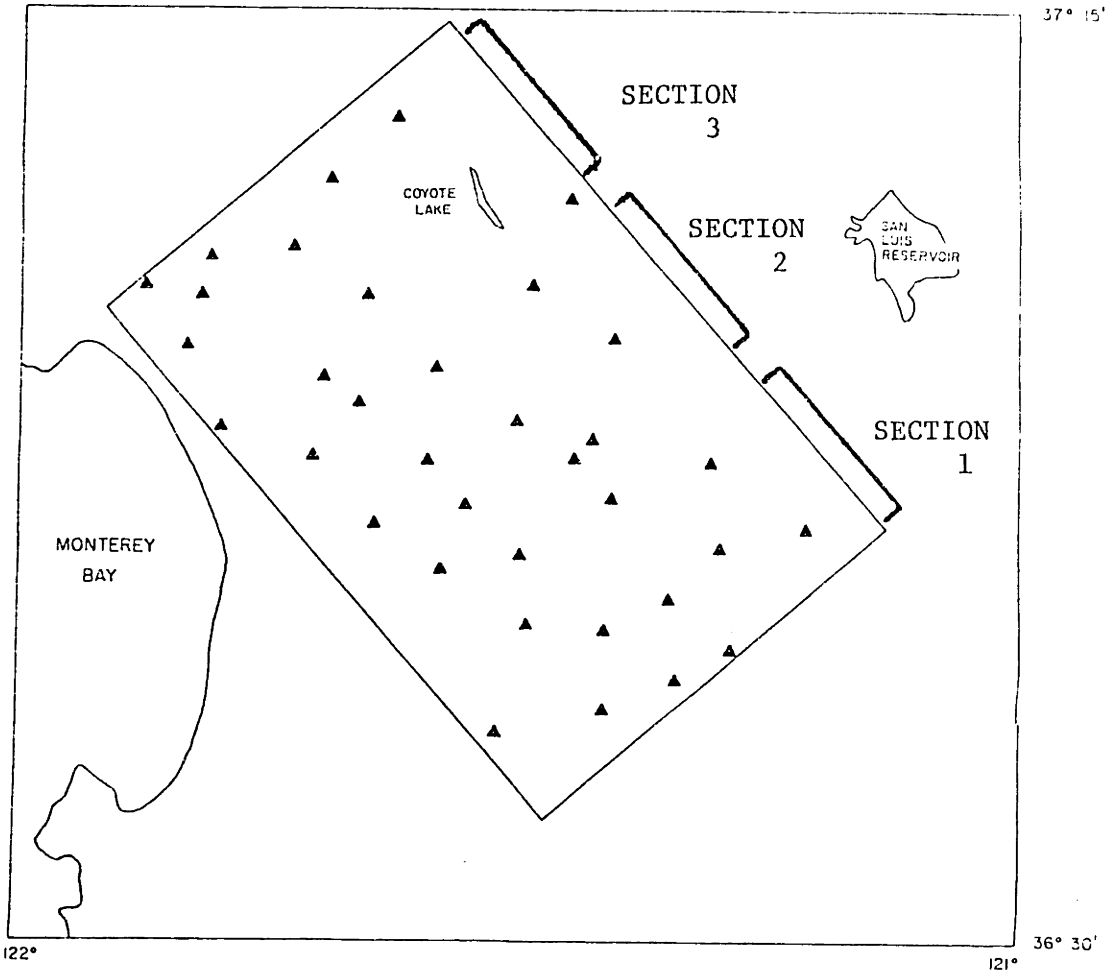
37° 15'
SECTION
3
COYOTE
LAKE
SECTION
2
SAN
LUIS
RESERVOIR
SECTION
1
MONTEREY
BAY
122°
121°
36° 30'

Figure 4.2

GILROY EVENTS >25

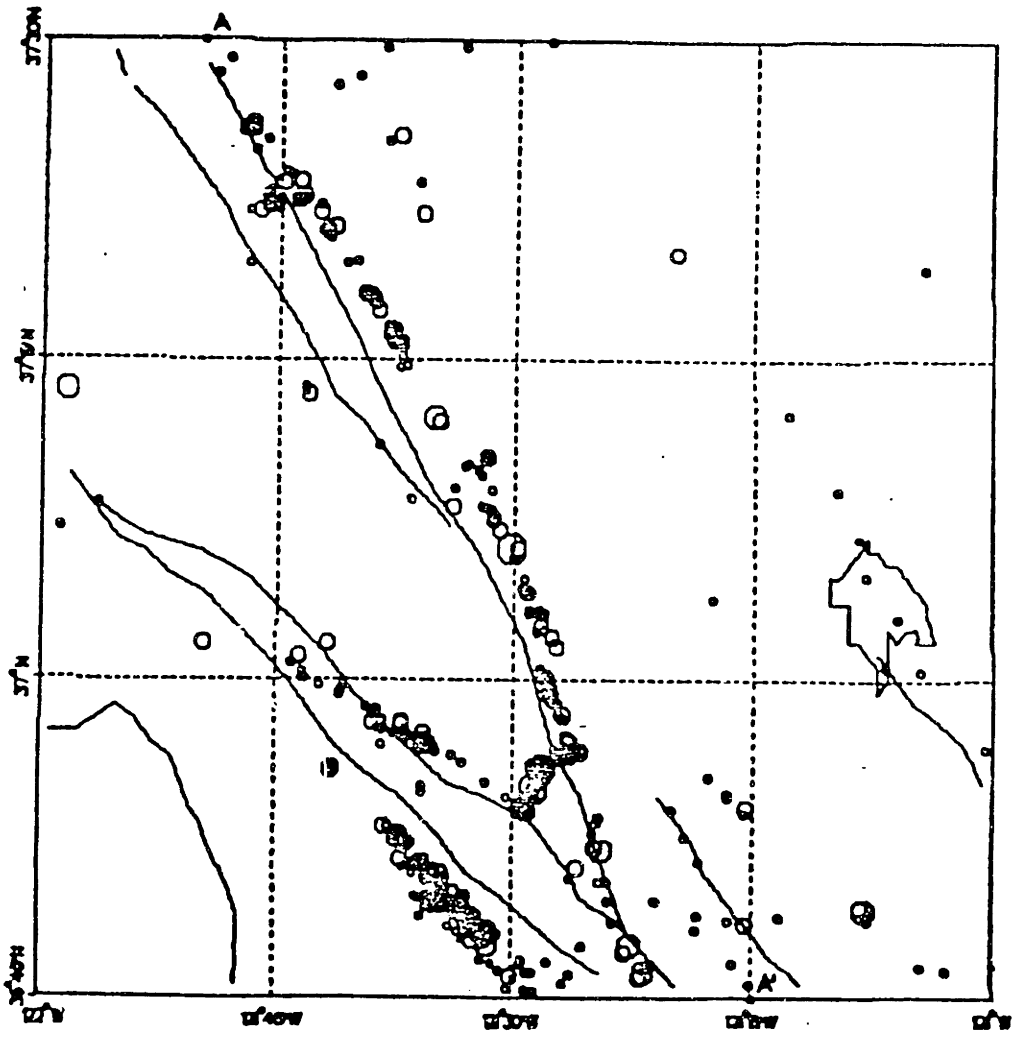

Figure 4.3

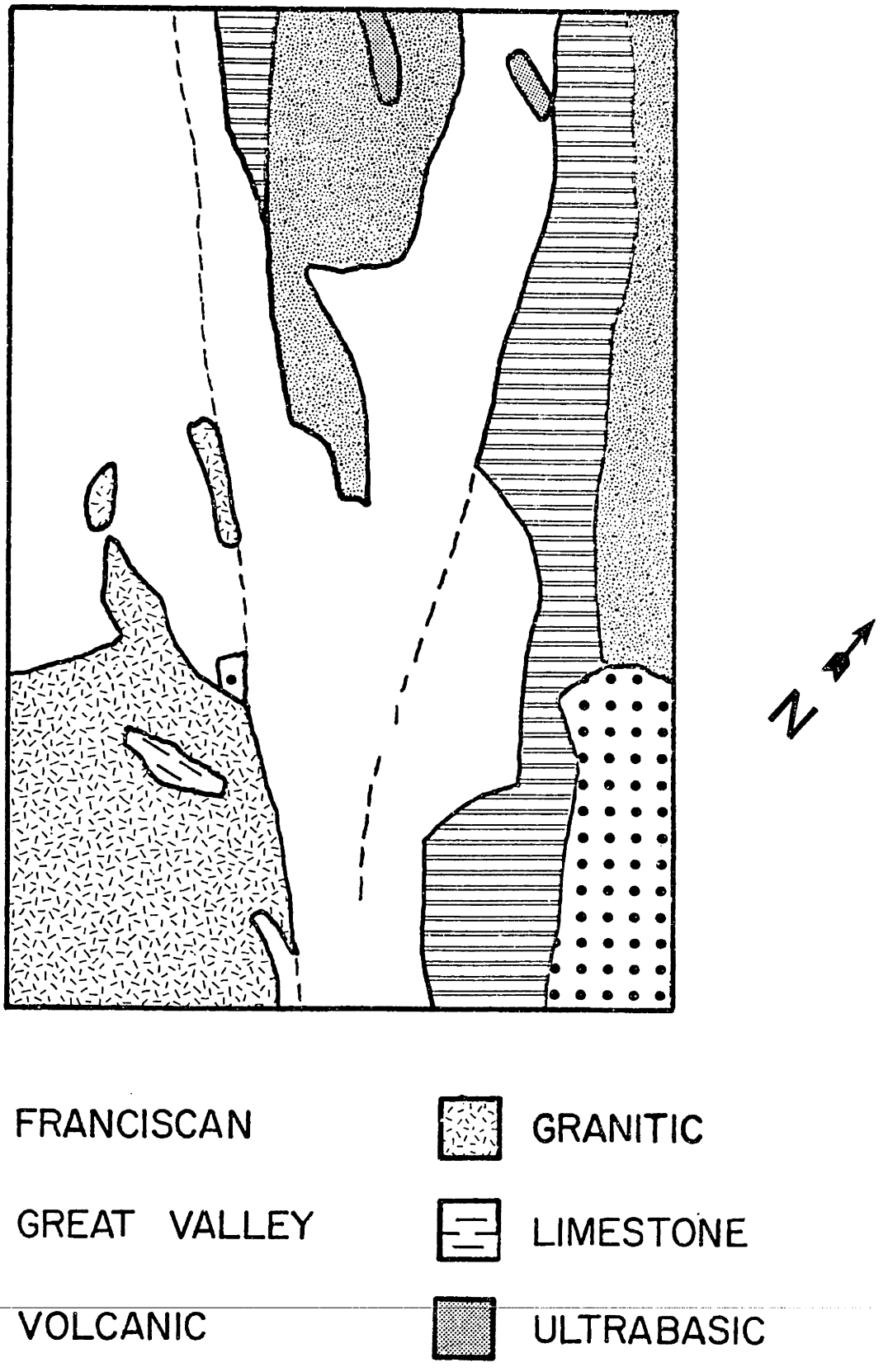
N
FRANCISCAN
GRANITIC
GREAT VALLEY
LIMESTONE
VOLCANIC
ULTRABASIC

Figure 4.4

BOUGUER GRAVITY

(mgals)

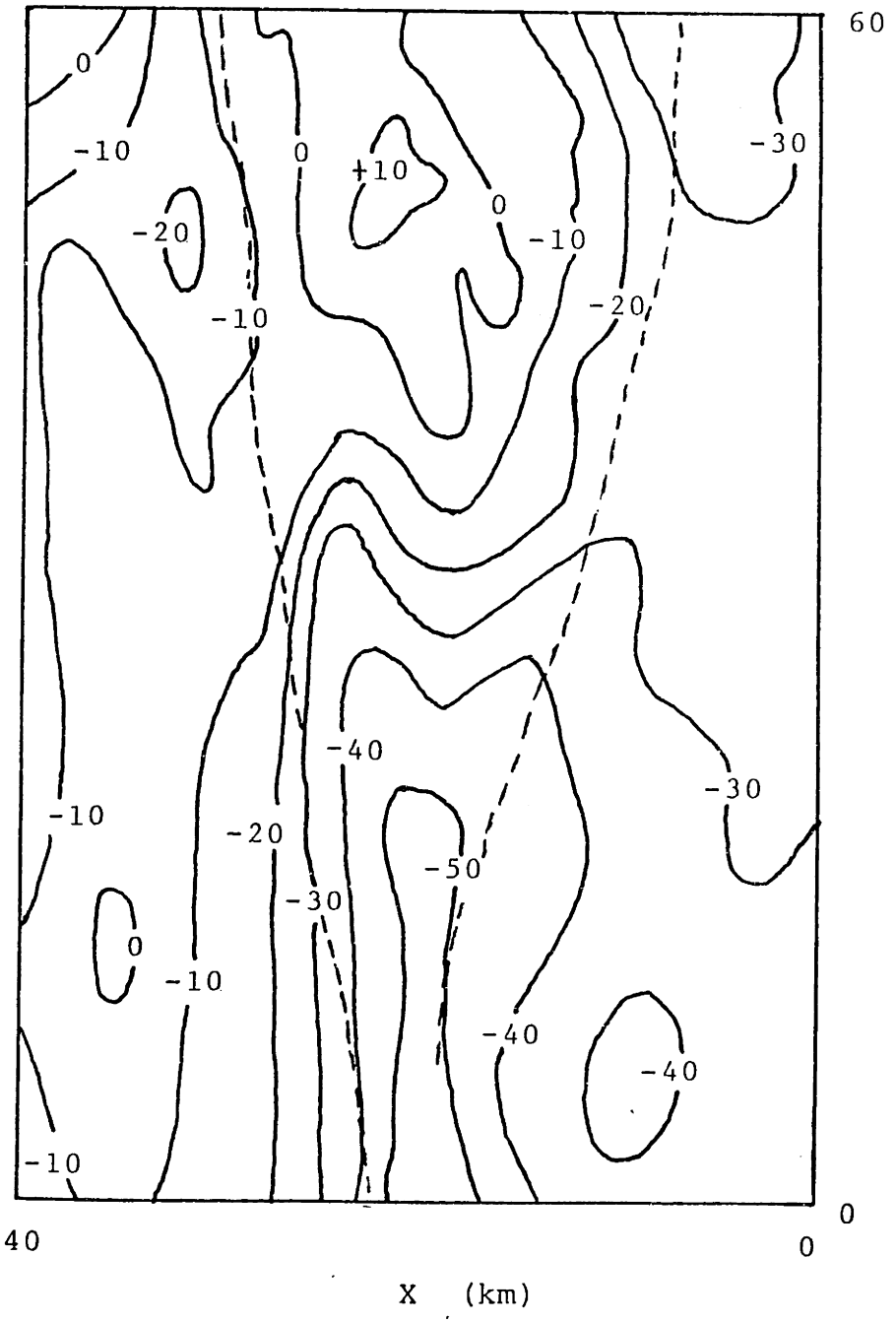

Figure 4.5

MAGNETIC ANOMALY

(gammas)

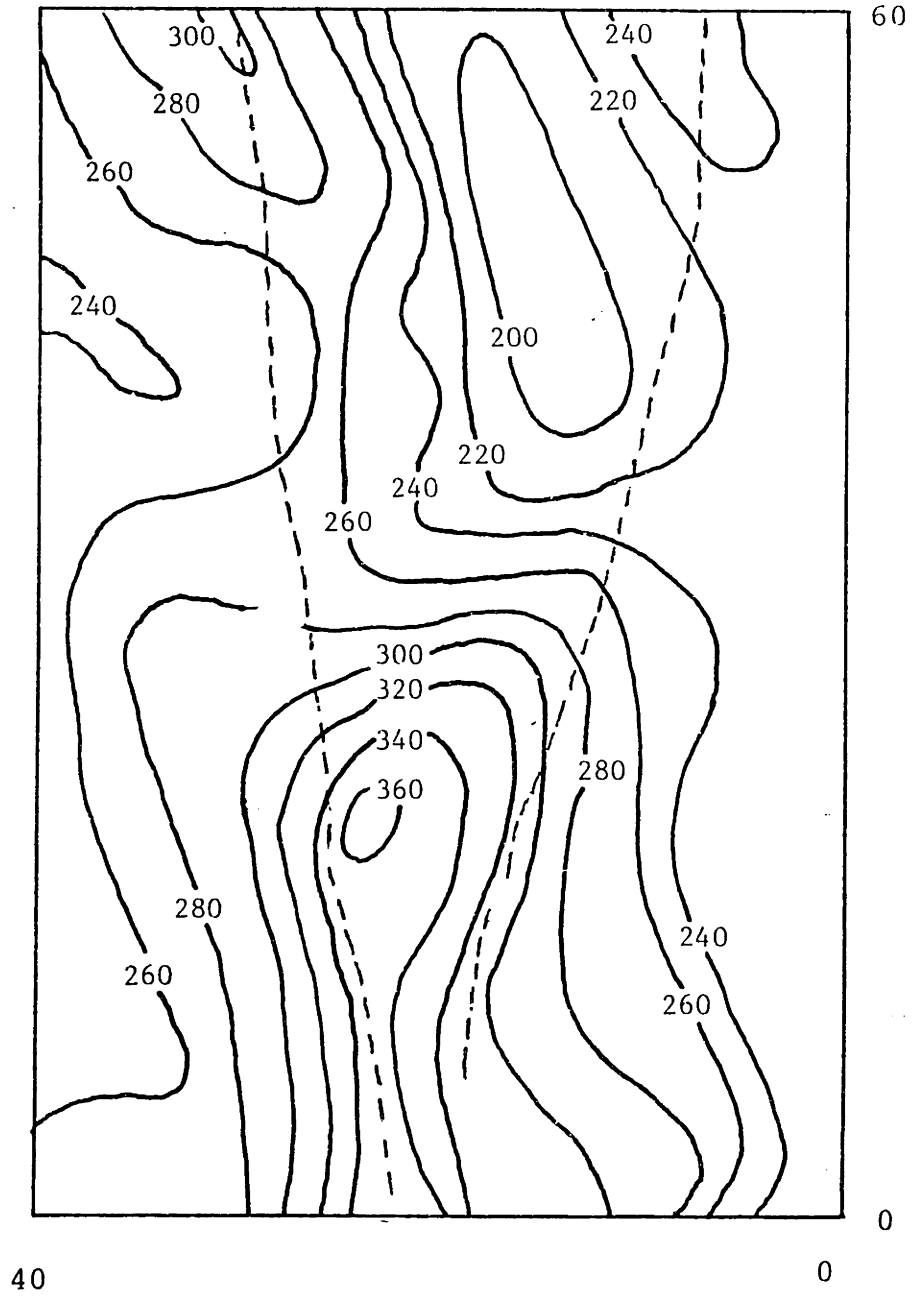

Figure 4.6

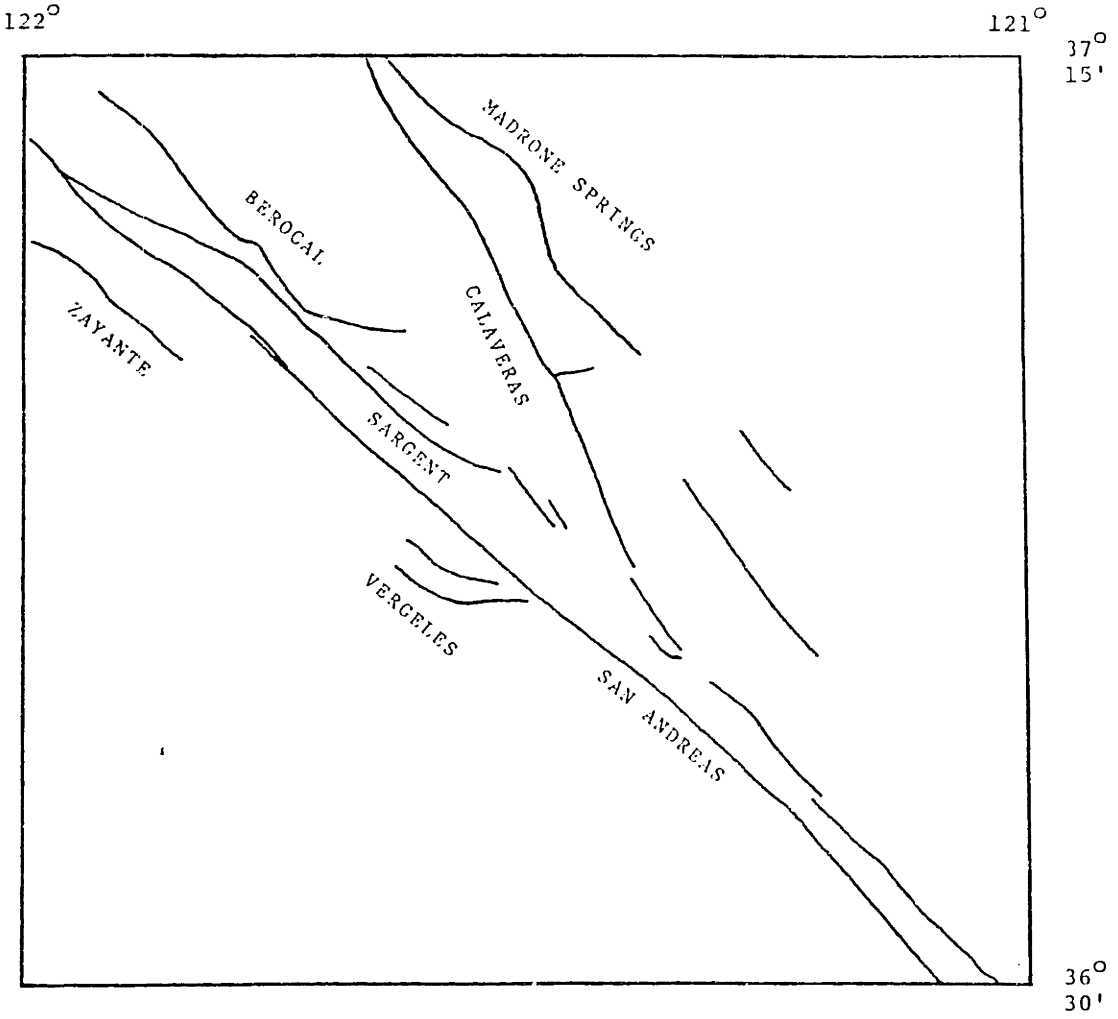

GILROY AREA - FAULT MAP

Figure 4.7 a

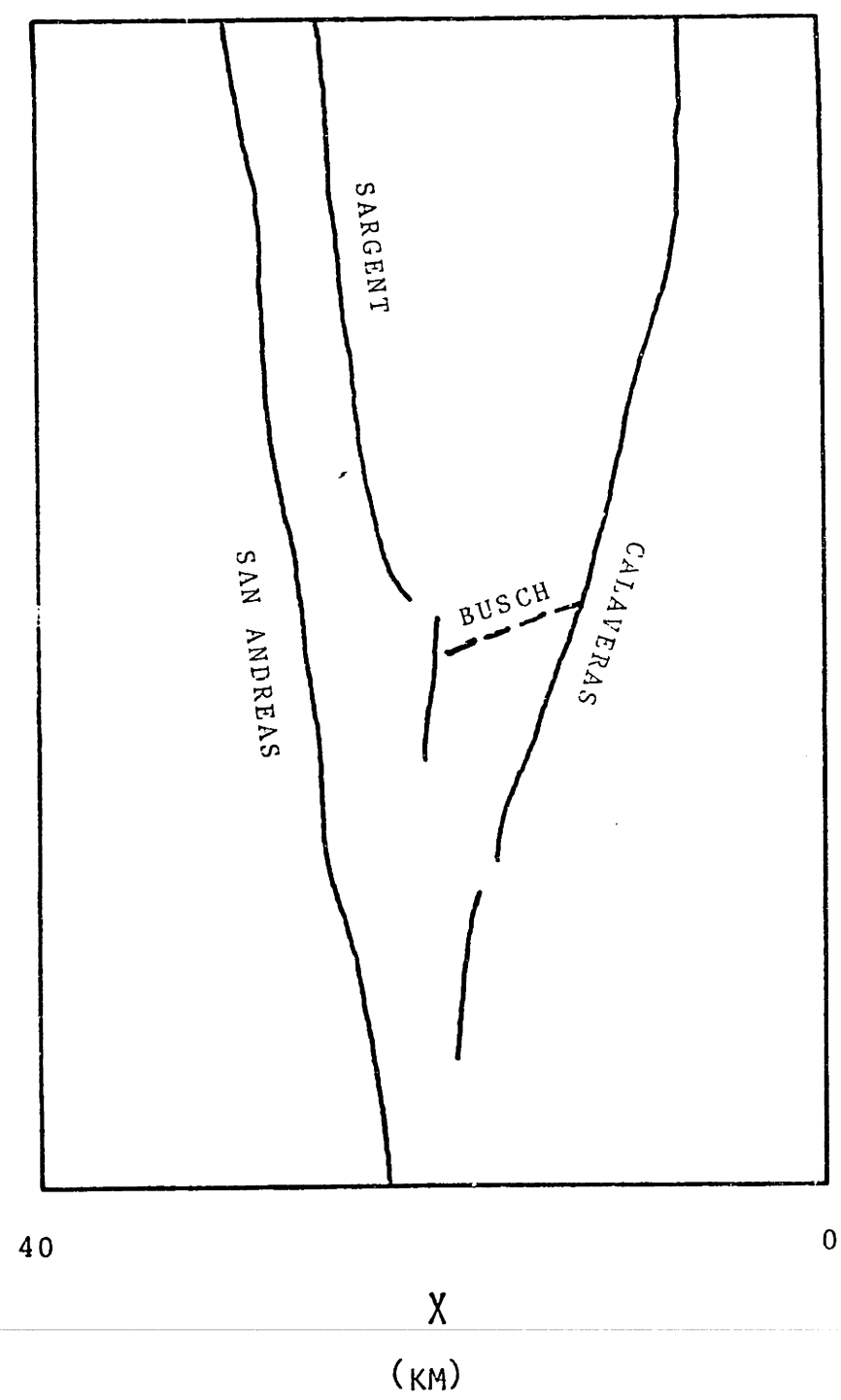

Figure 4.7 b

SUBDIVISIONS OF THE
GILROY STUDY AREA

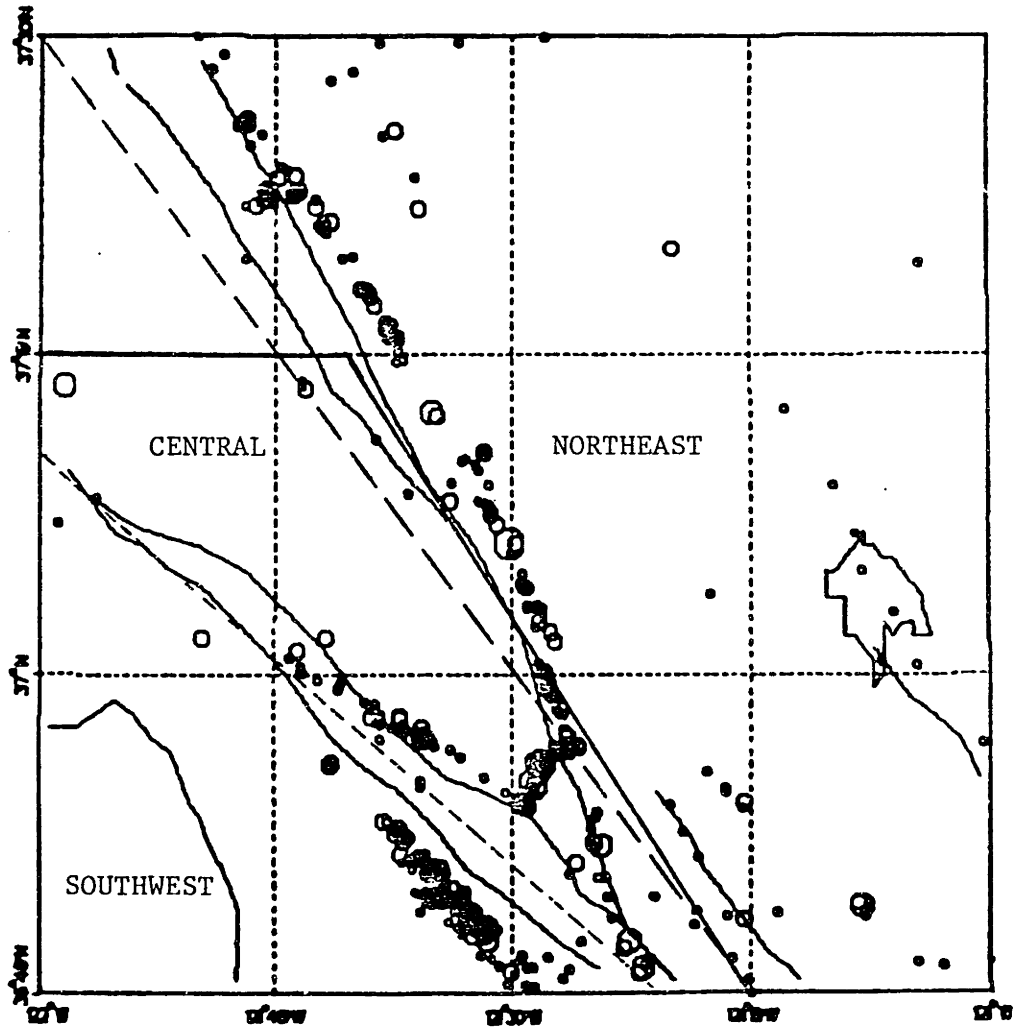

Figure 4.8

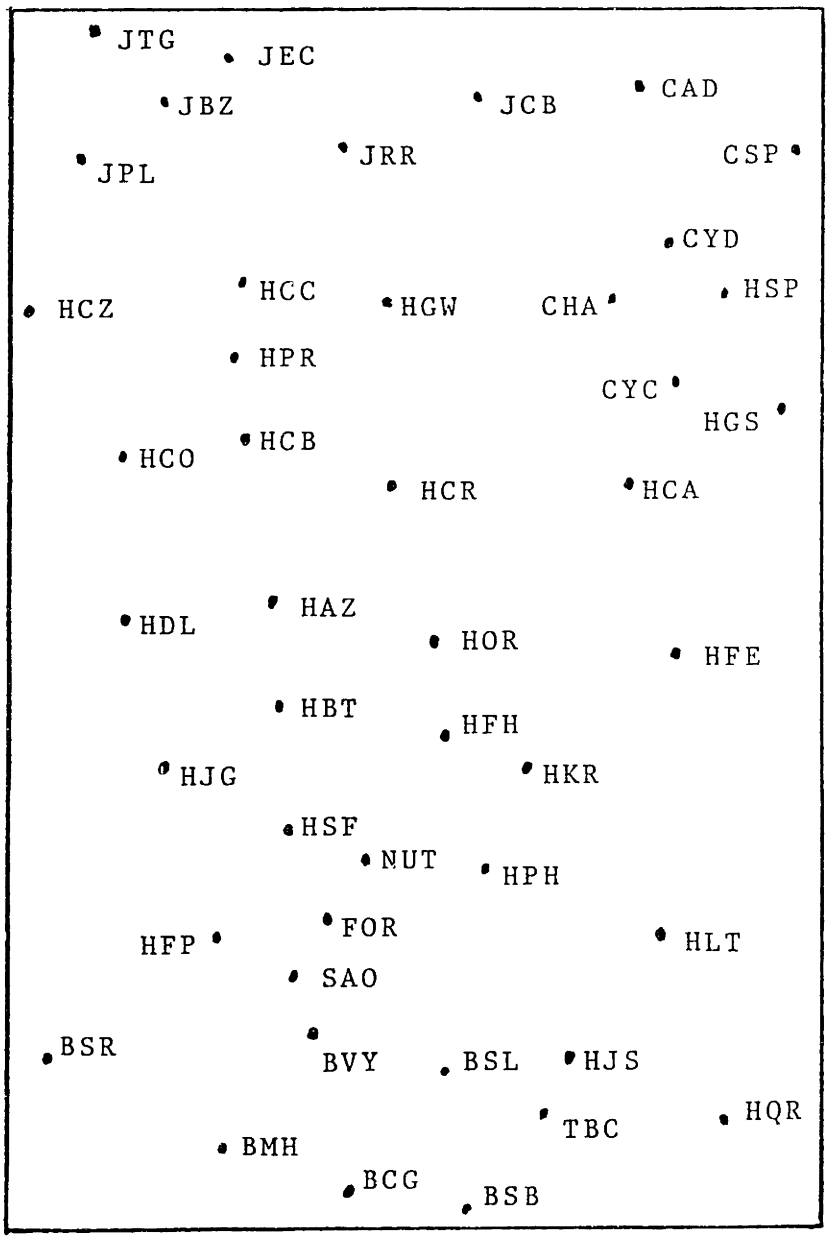
JTG
JEC
JBZ
JCB
CAD
JPL
JRR
CSP
CYD
HCZ
HCC
HGW
CHA
HSP
HPR
CYC
HGS
HCO
HCB
HCR
HCA
HDL
HAZ
HOR
HFE
HBT
HFH
HJG
HKR
HSF
NUT
HPH
HFP
FOR
HLT
SAO
BSR
BVY
BSL
HJS
HQR
TBC
BMH
BCG
BSB

Figure 4.9

EVENT 7909100616

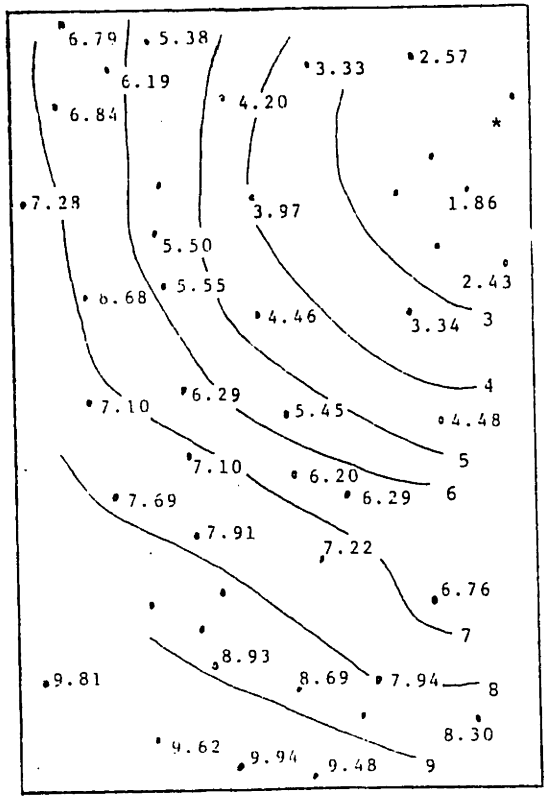

EVENT 7909082303

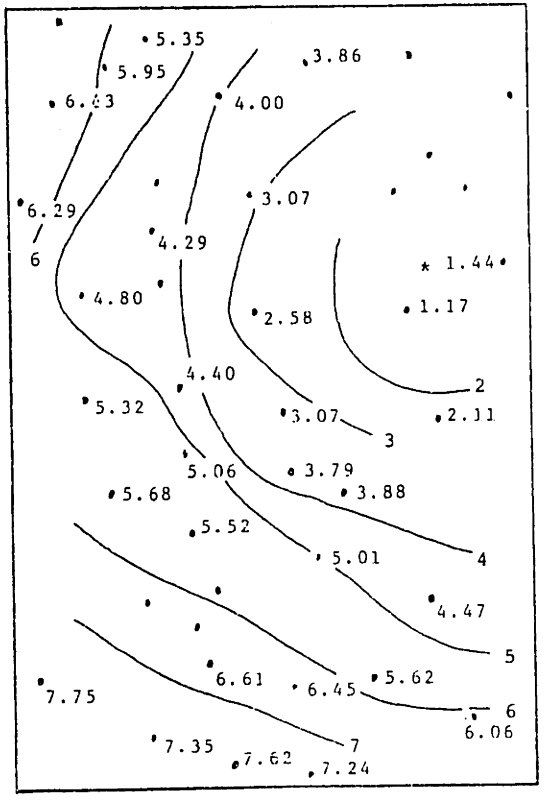

EVENT 7906170151

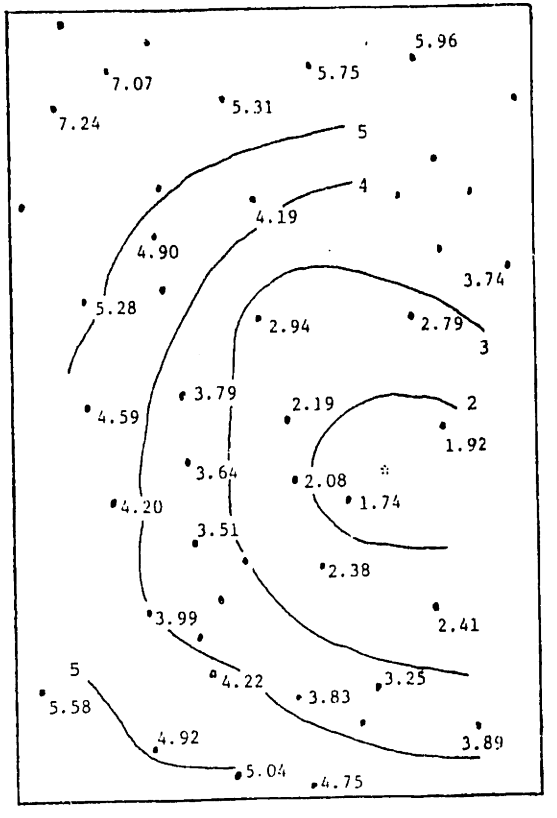

Figure 4.10

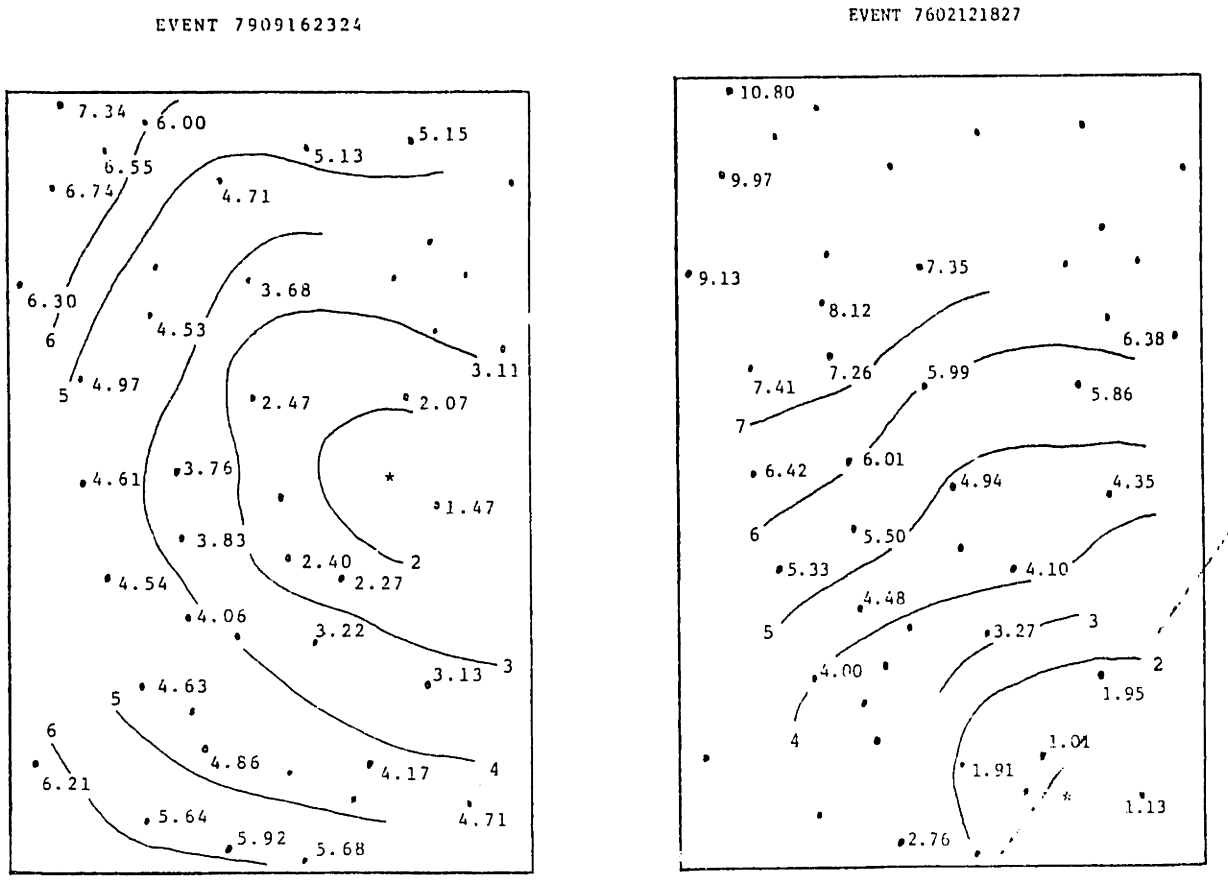

Figure 4.10 (cont)

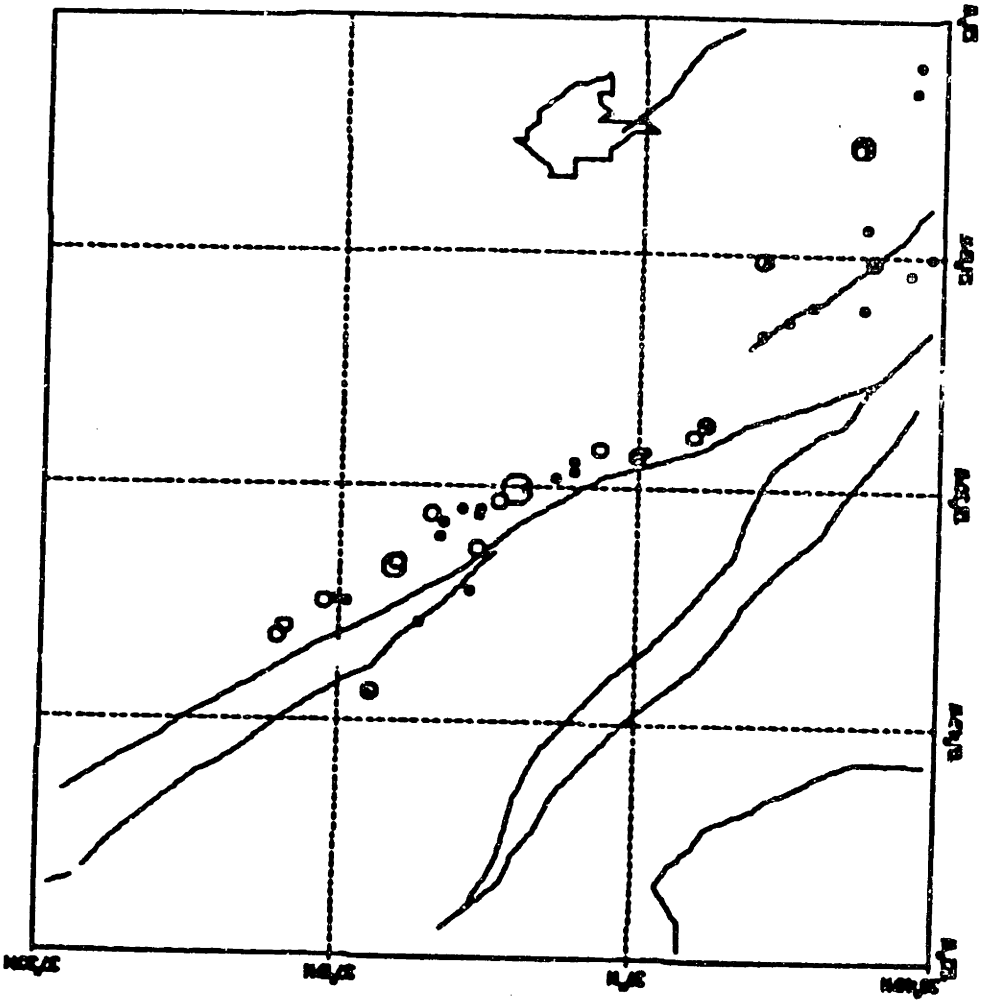

EVENTS FOR NORTHEAST SECTION

Figure 4.11

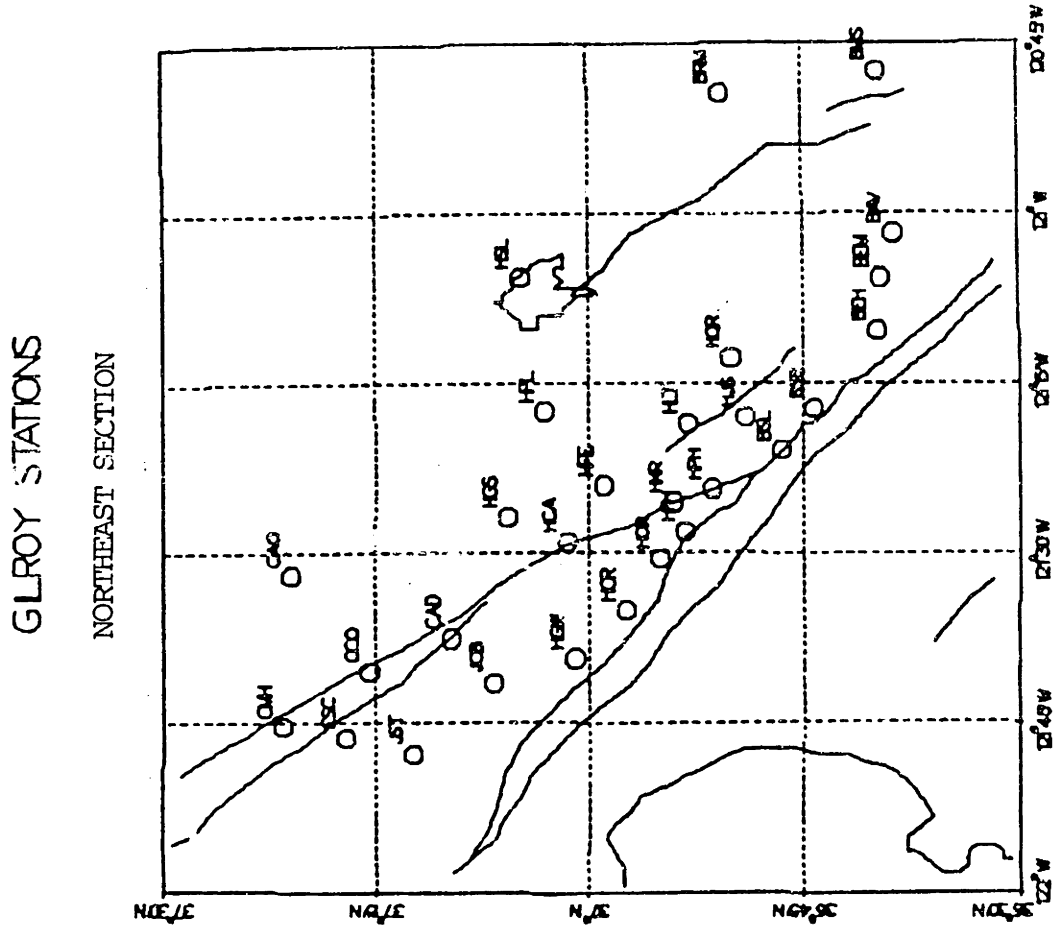

Figure 4.12

LAYERED MODELS - NORTHEAST OF SAN ANDREAS FAULT

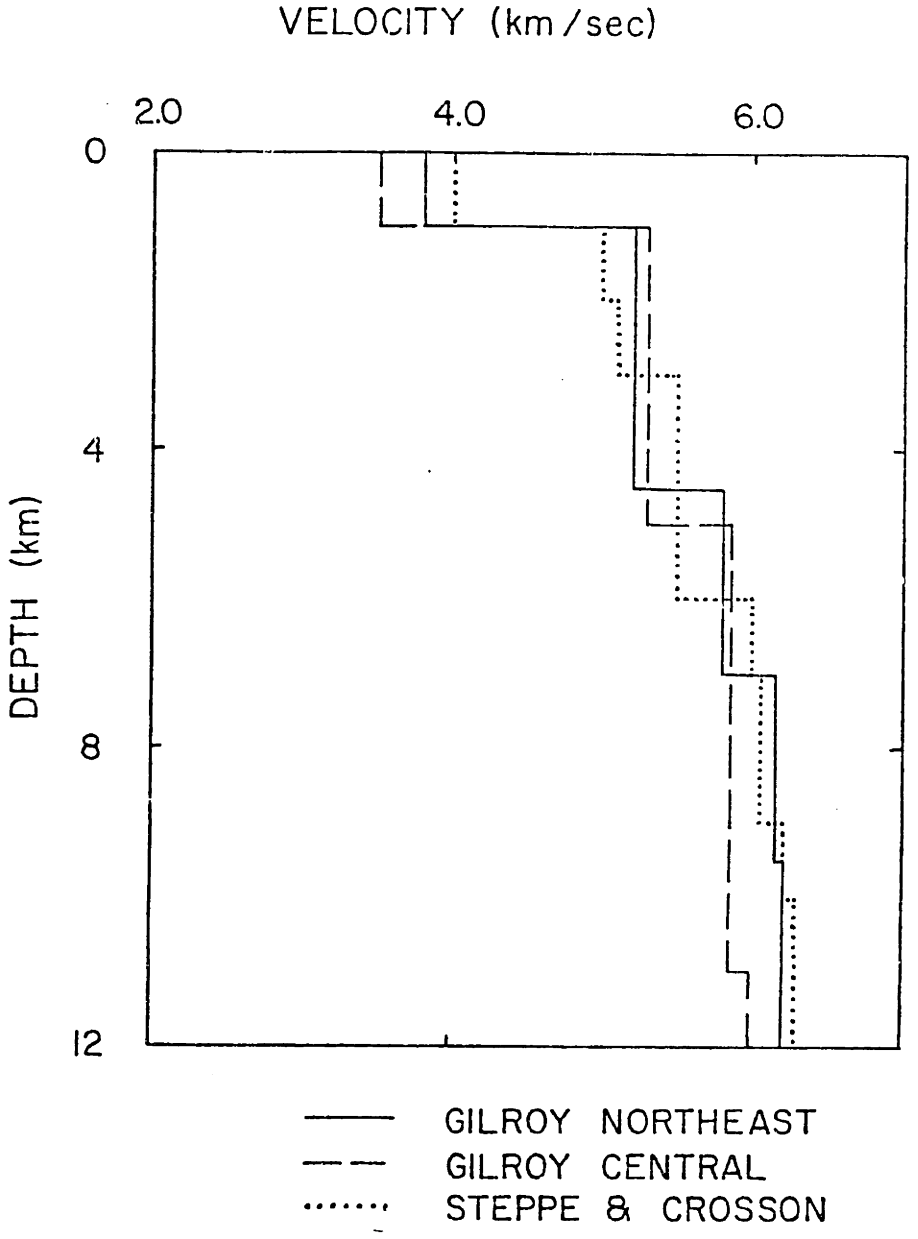

Figure 4.13

GILROY NORTHEAST

station delays (sec)

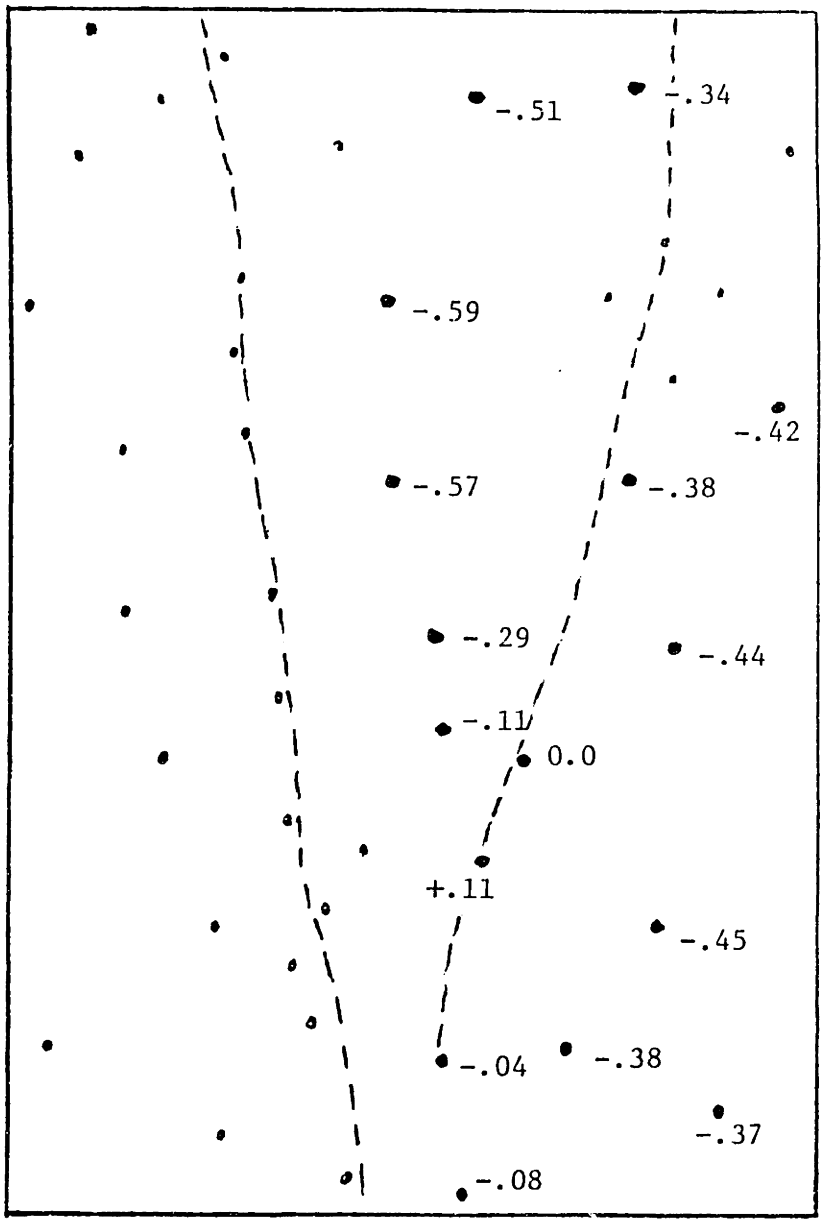

Figure 4.14

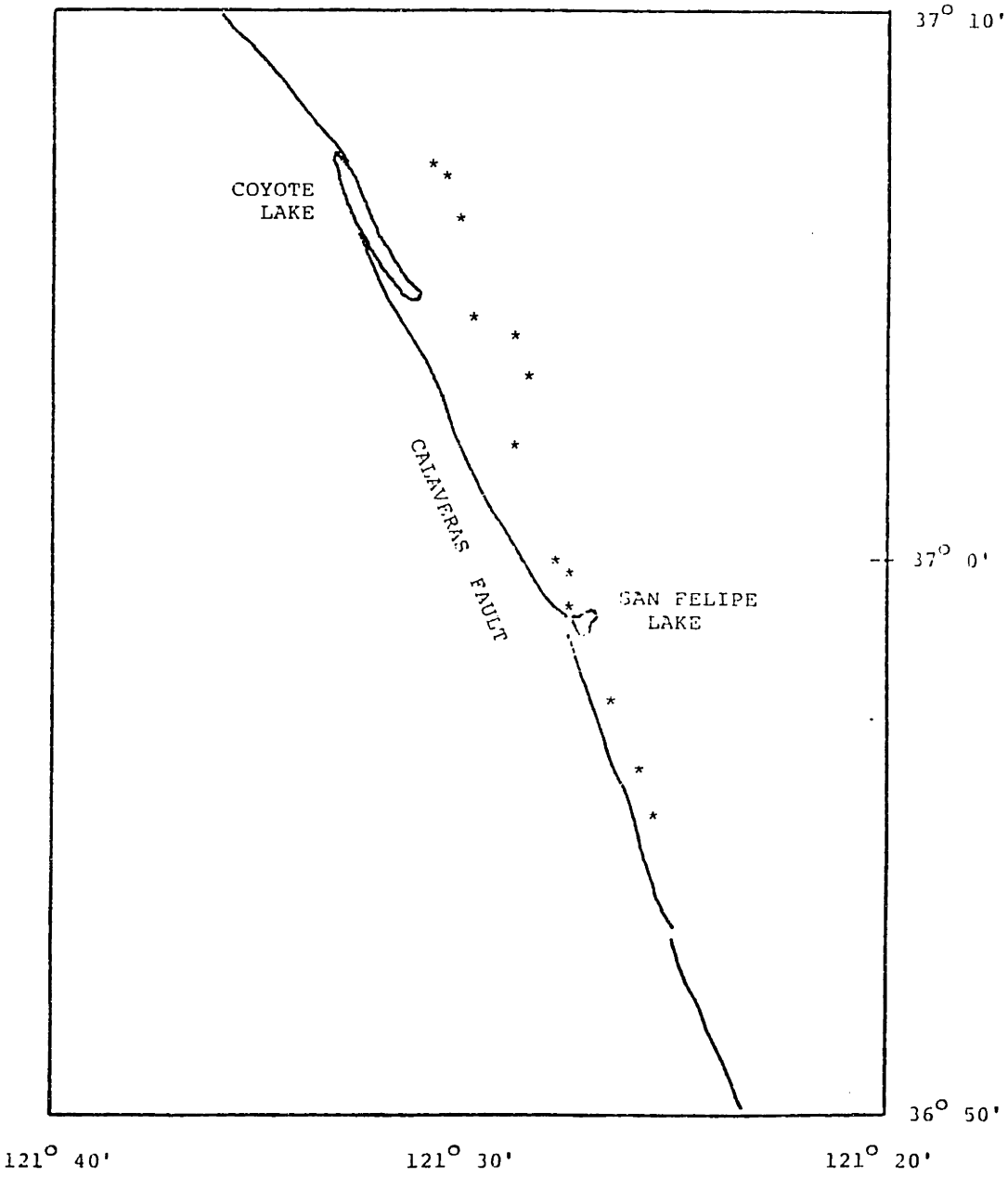
37° 10'
COYOTE
LAKE
CALAVERAS FAULT
SAN FELIPE
LAKE
37° 0'
36° 50'
121° 40'
121° 30'
121° 20'

Figure 4.15

EVENT 7612141049

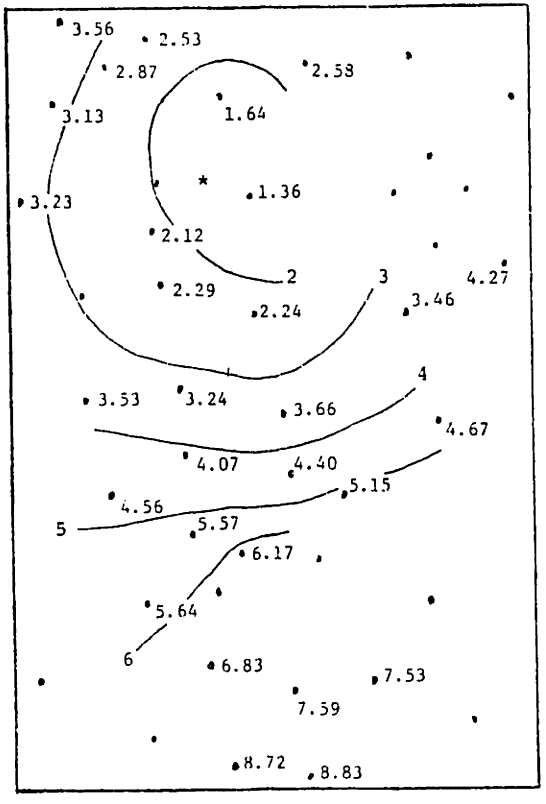

EVENT 7902180738

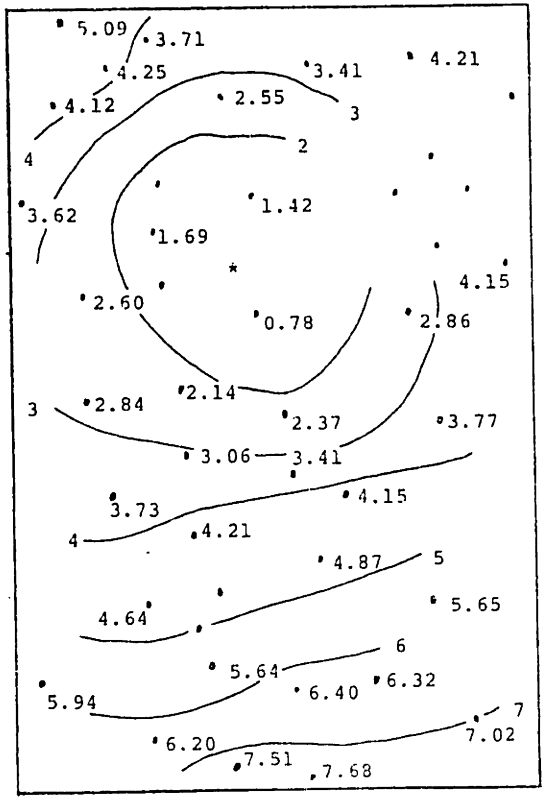

EVENT 7703120919

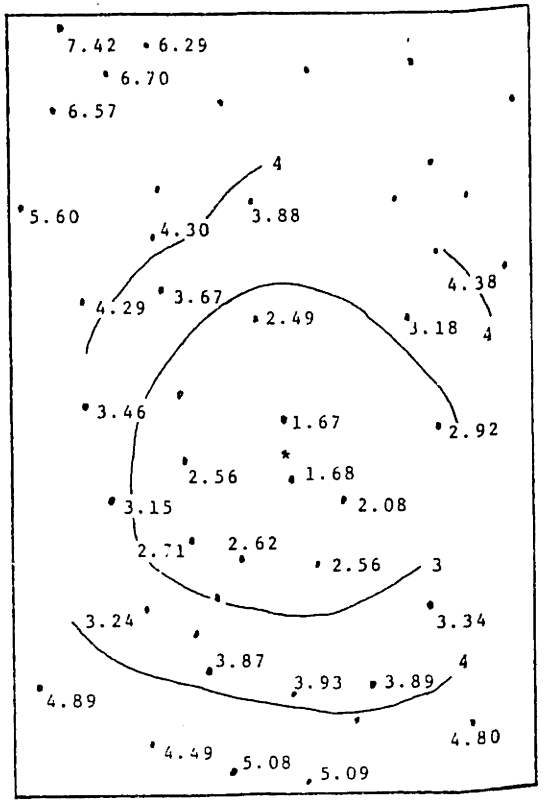

Figure 4.16

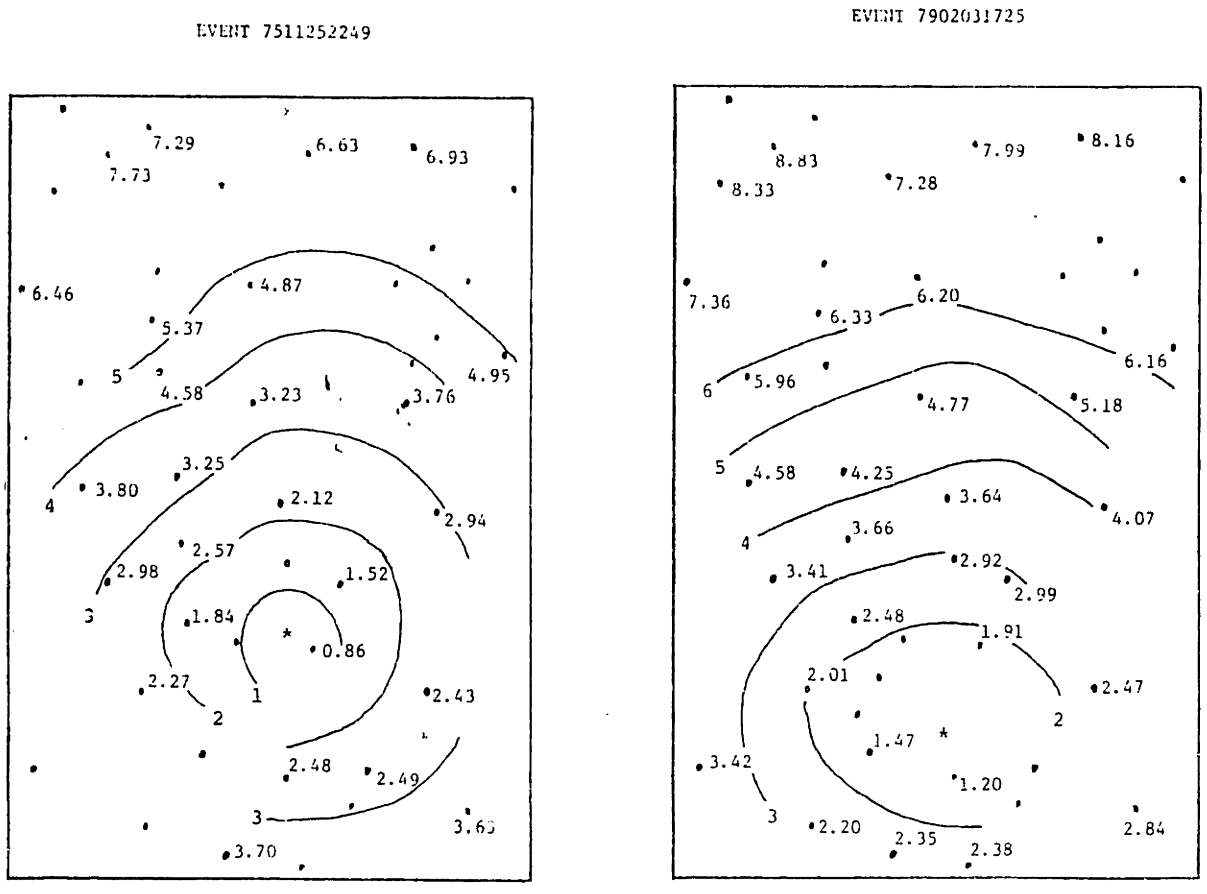

Figure 4.16 (cont)

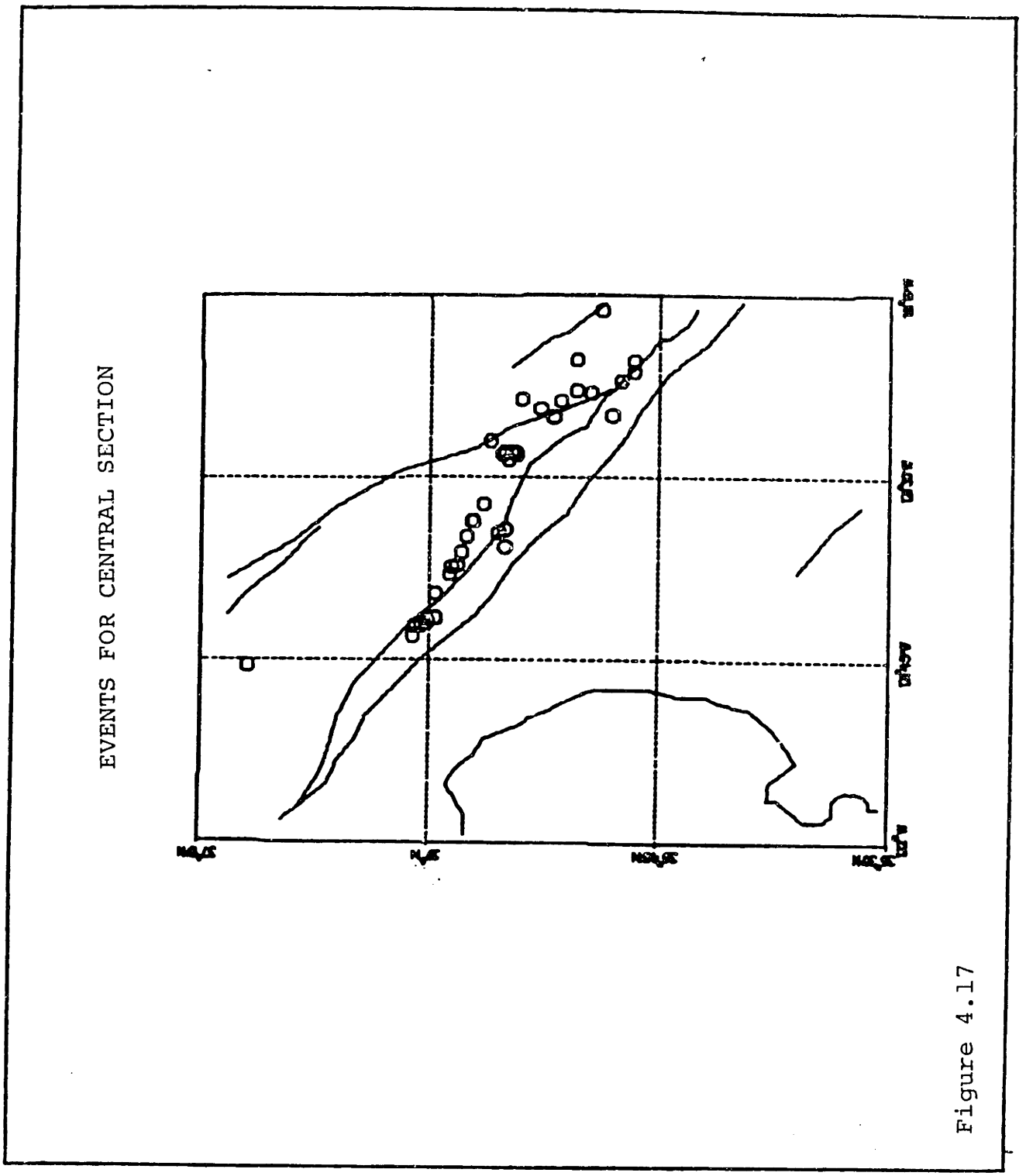

Figure 4.17

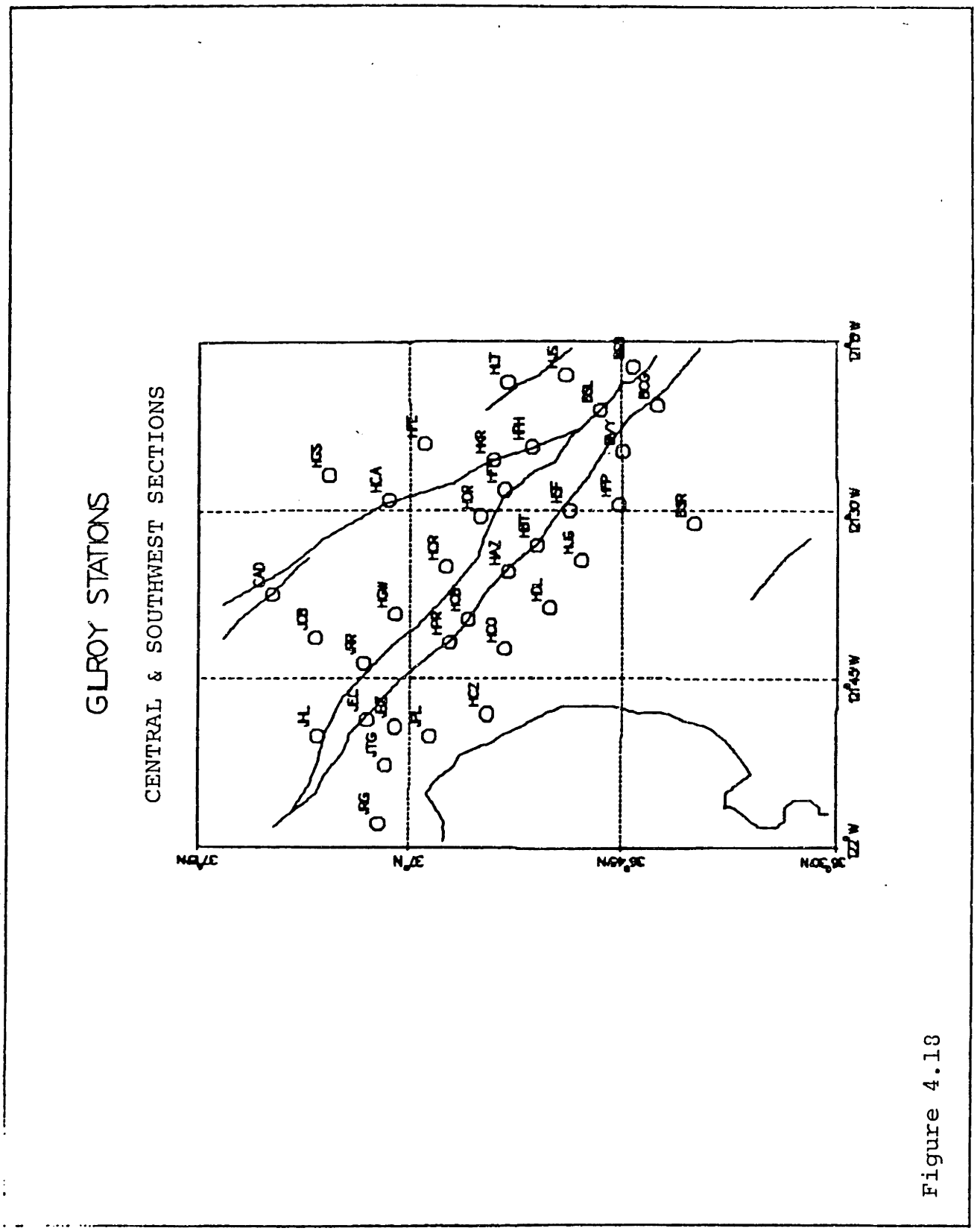

Figure 4.18

GILROY CENTRAL

station delays (sec)

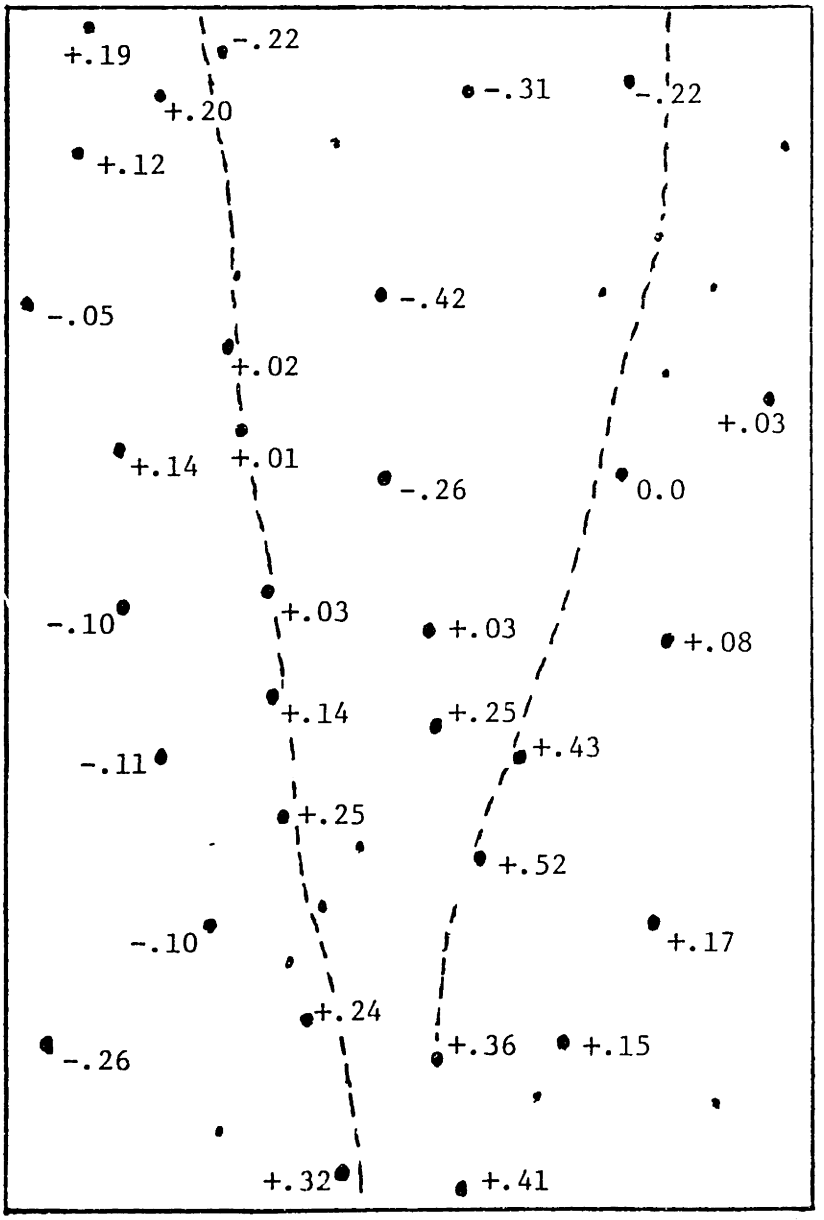

Figure 4.19

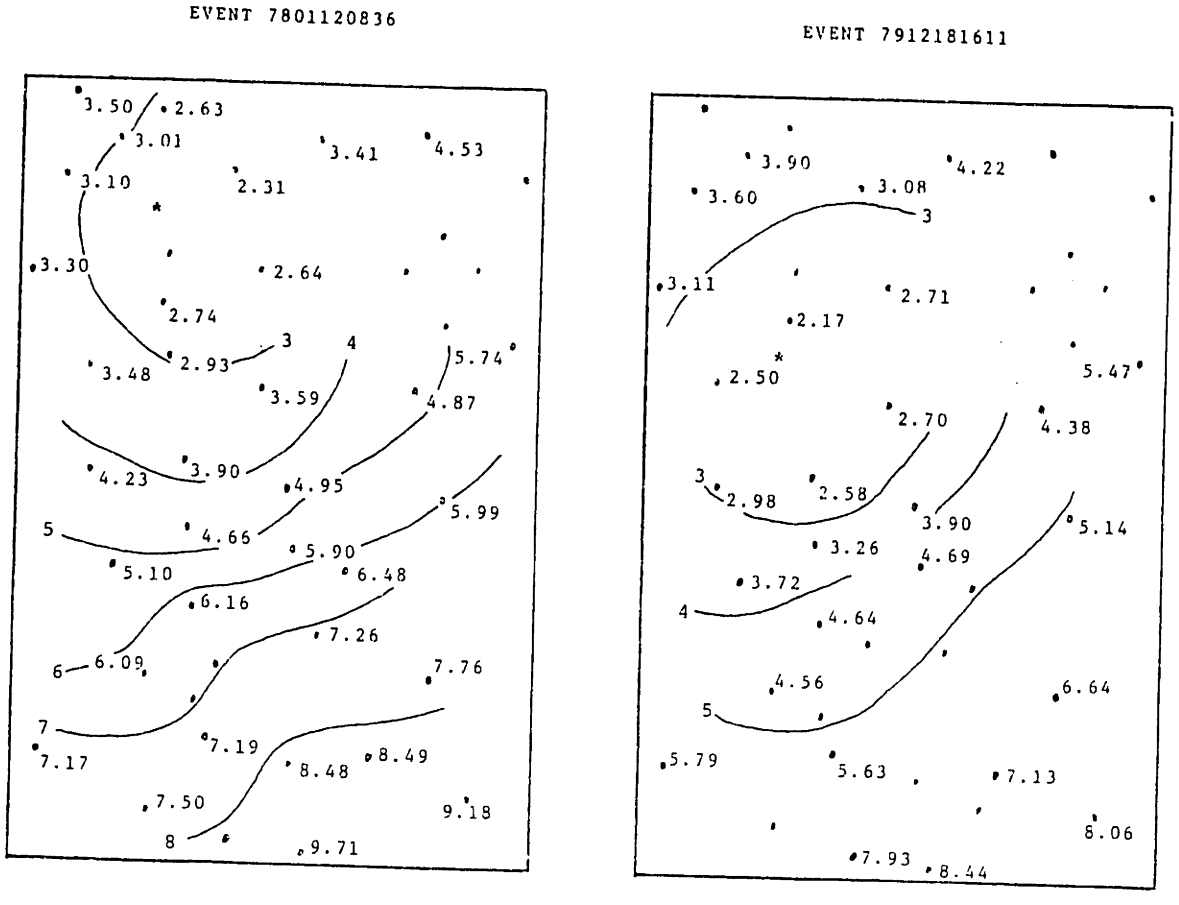
EVENT 7801120836
3.50
2.63
3.01
3.41
4.53
3.10
2.31
3.30
2.64
2.74
3
4
5.74
3.48
2.93
3.59
4.87
4.23
3.90
4.95
5
4.66
5.99
5.10
5.90
6.48
6.16
7.26
6
6.09
7.76
7
7.19
7.17
8.48
8.49
7.50
9.18
8
9.71
EVENT 7912181611
3.90
4.22
3.60
3.08
3
3.11
2.71
2.17
2.50
5.47
2.70
4.38
3
2.98
2.58
3.90
5.14
3.26
4.69
3.72
4
4.64
4.56
6.64
5
5.79
5.63
7.13
8.06
7.93
8.44

Figure 4.20

EVENT 7803280951

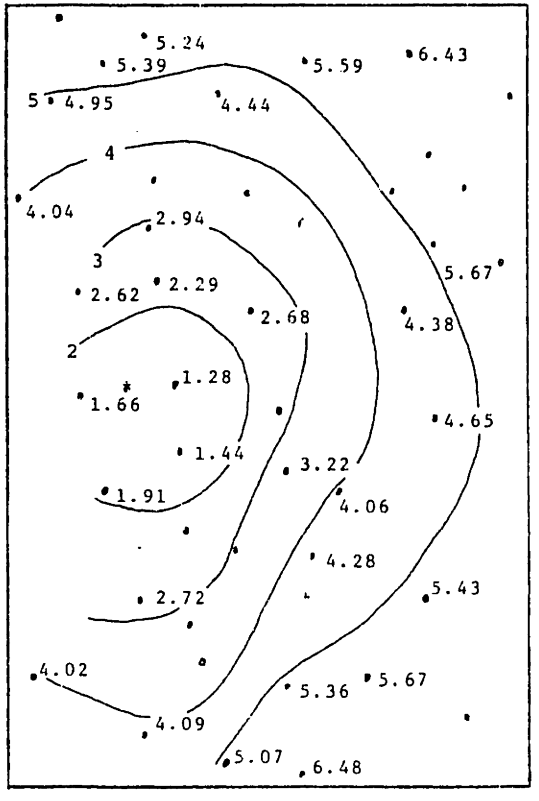

EVENT 7912101411

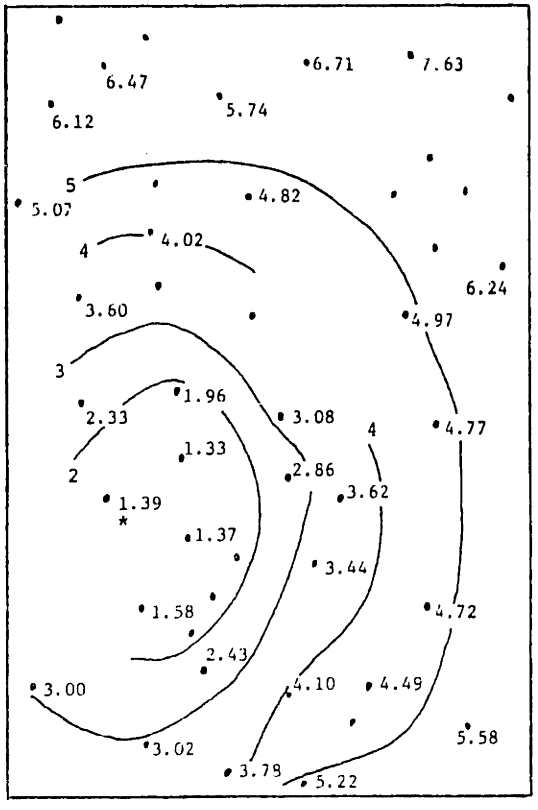

Figure 4.20 (cont)

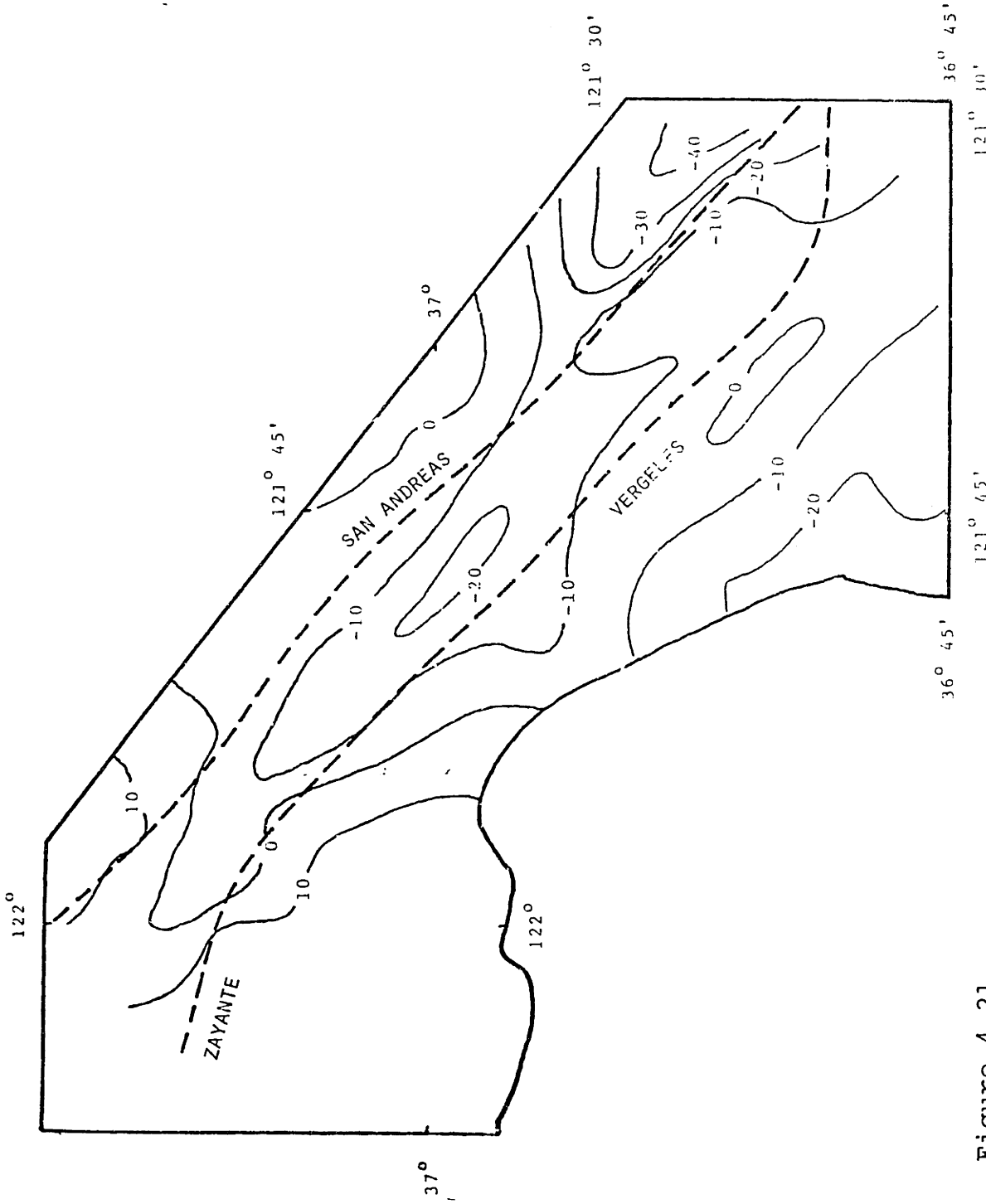
122°
37°
121° 45'
121° 30'
36° 45'
SAN ANDREAS
VERGELES
ZAYANTE
10
0
-10
-20
-30
-40

Figure 4.21

EVENTS FOR SOUTHWEST SECTION

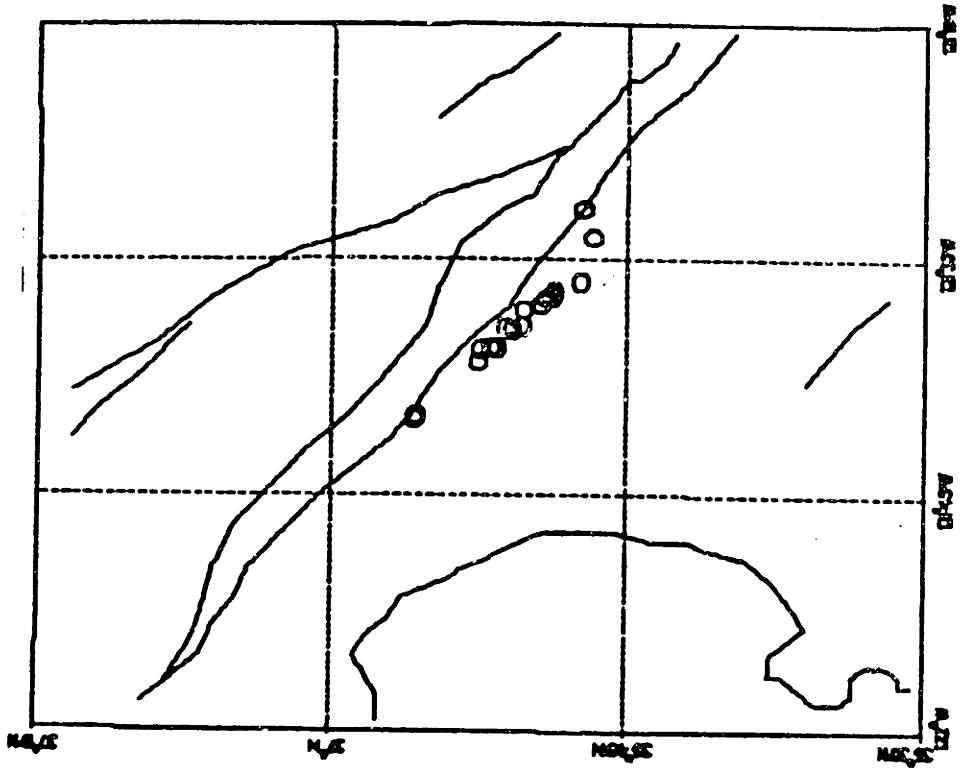

Figure 4.22

LAYERED MODELS - SOUTHWEST OF SAN ANDREAS FAULT

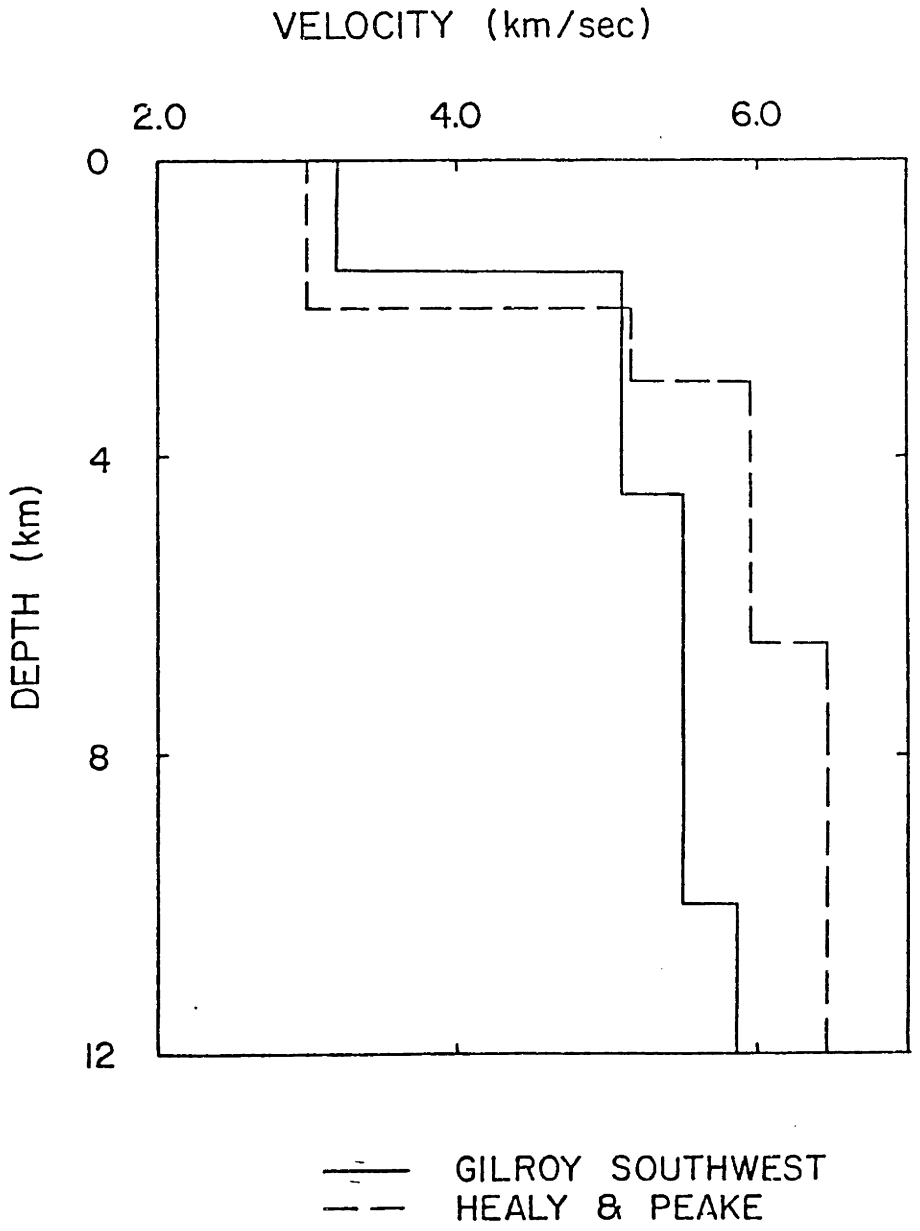

Figure 4.23

GILROY SOUTHWEST

station delays (sec)

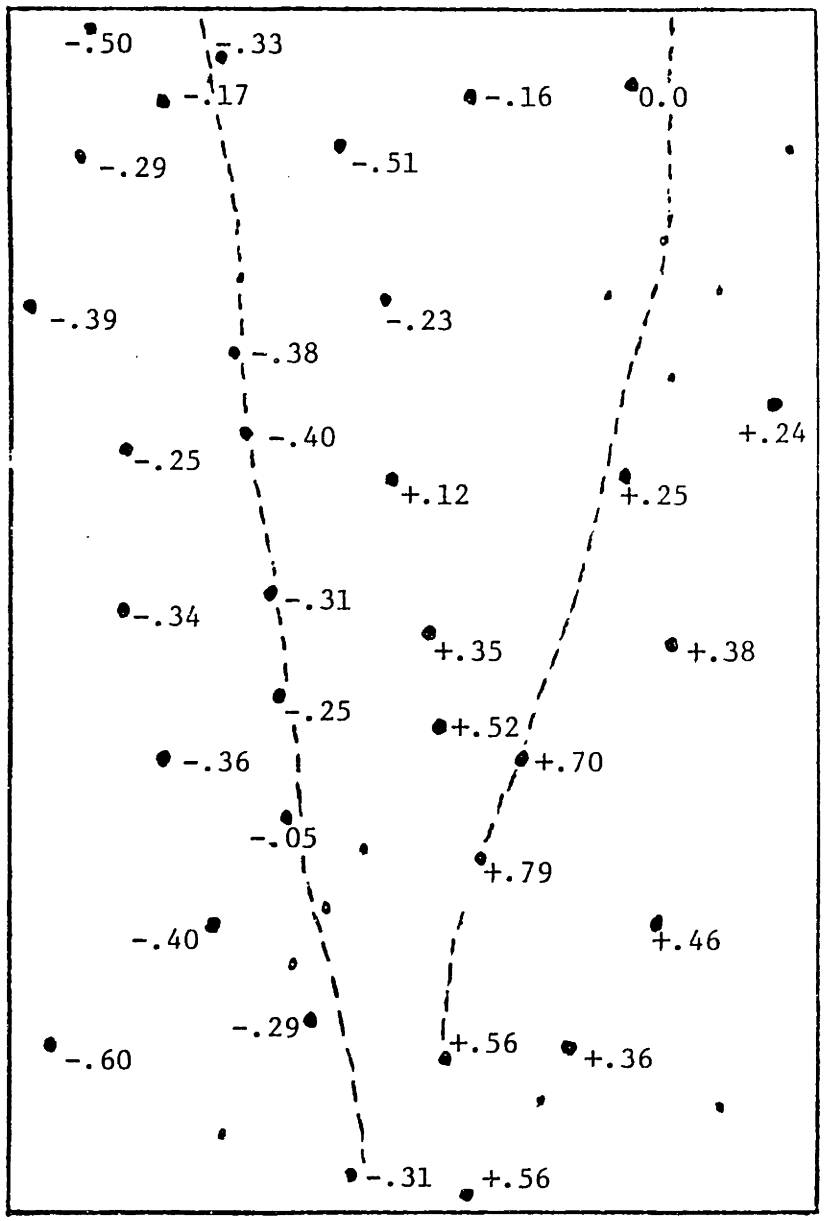

Figure 4.24

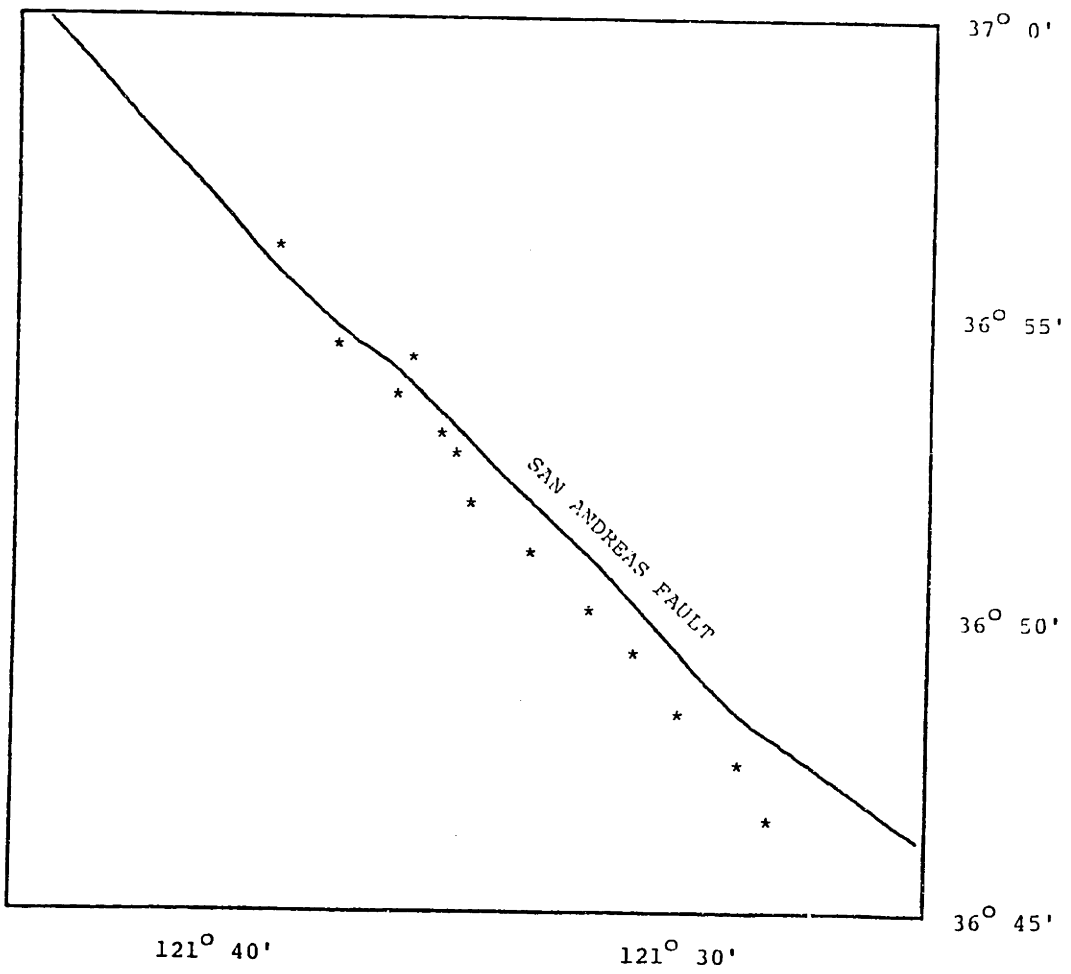

Figure 4.25

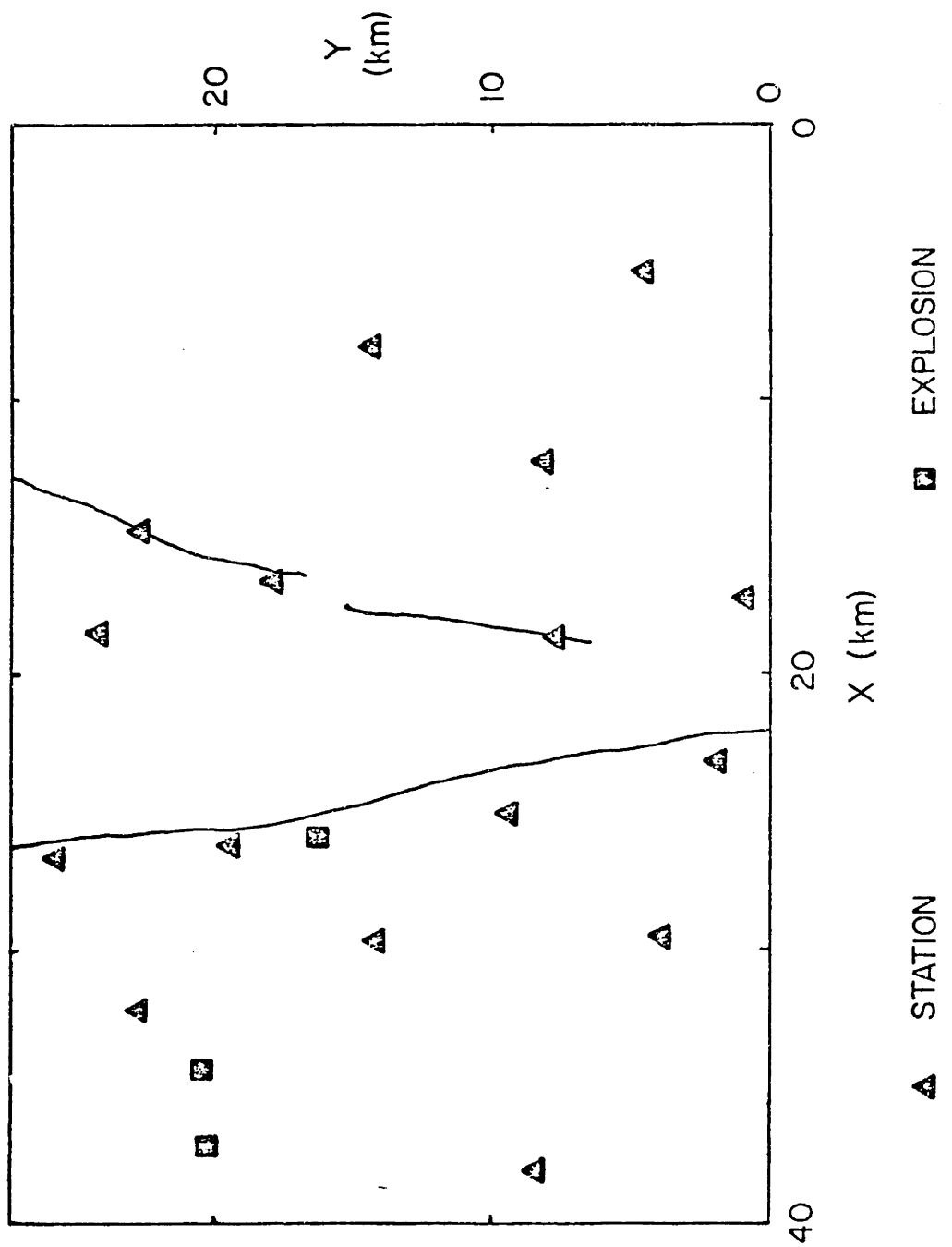

Figure 4.26

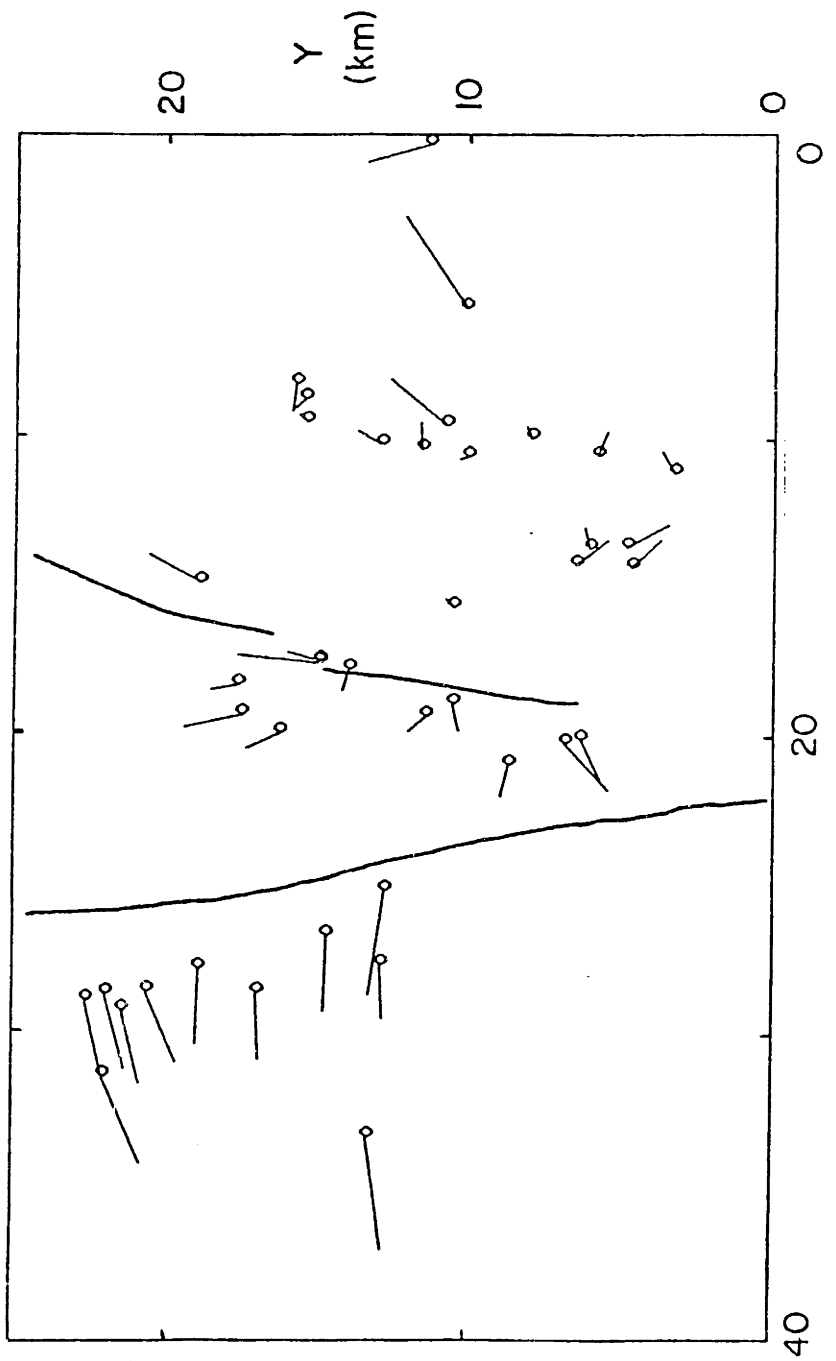

Figure 4.27

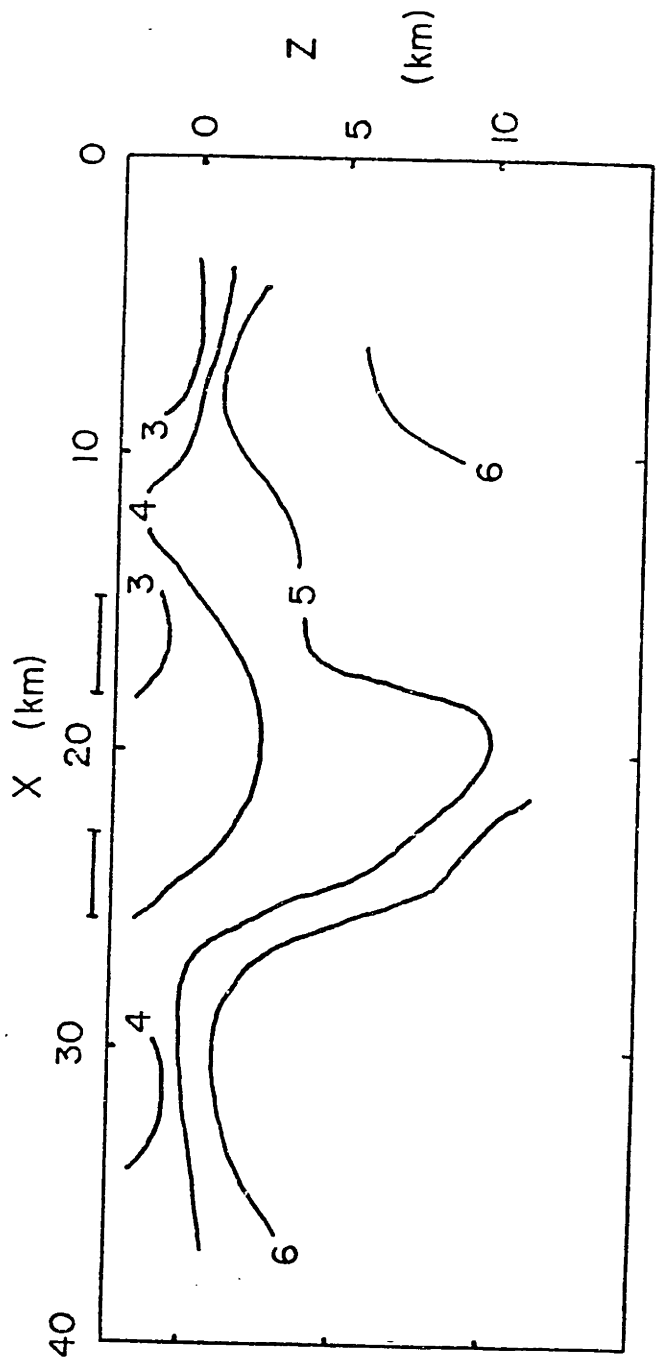
Z (km)
0
5
10
X (km)
0
10
20
30
40
3
4
5
6
SECTION I VELOCITY MODEL
(contour interval 1 km/sec)

Figure 4.28

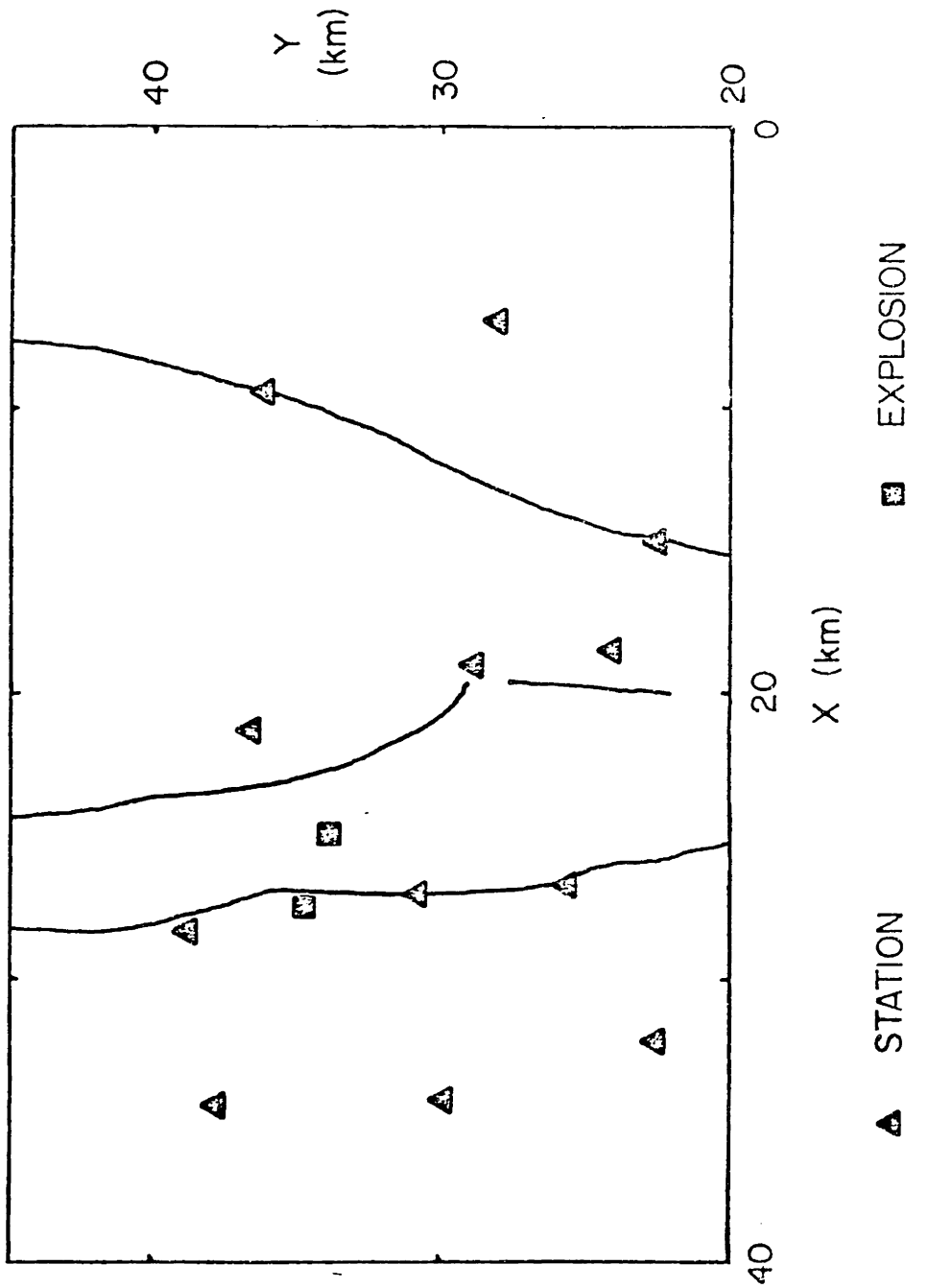

Figure 4.29

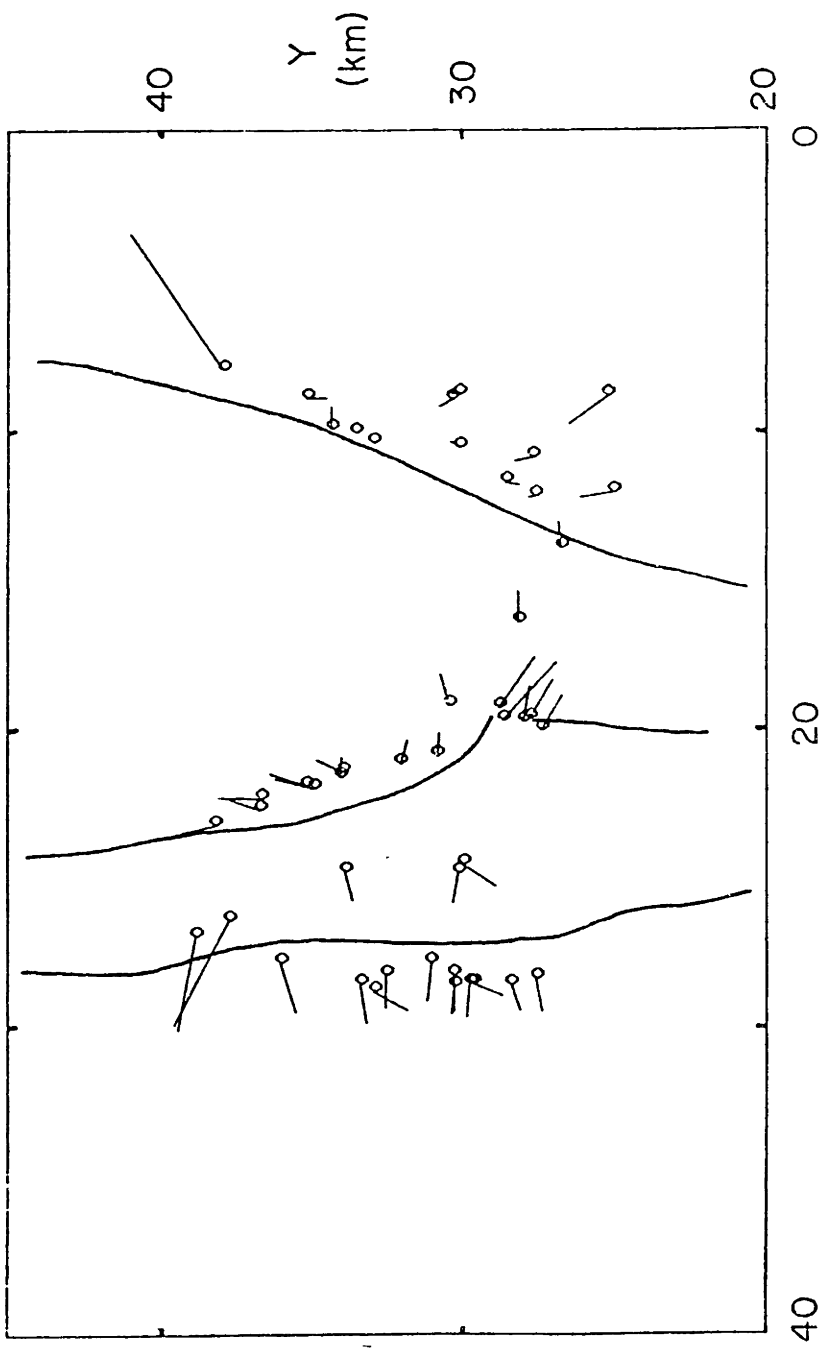

Figure 4.30

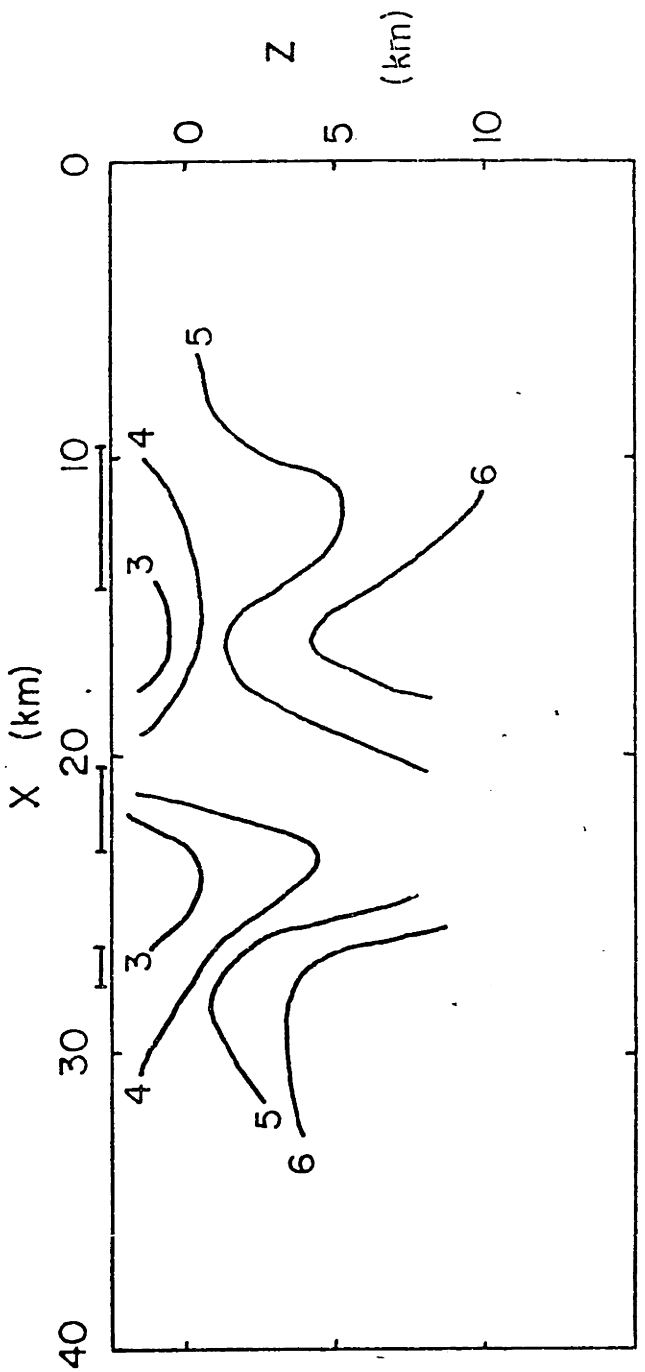

SECTION 2 VELOCITY MODEL

(contour interval 1 km/sec)

Figure 4.31

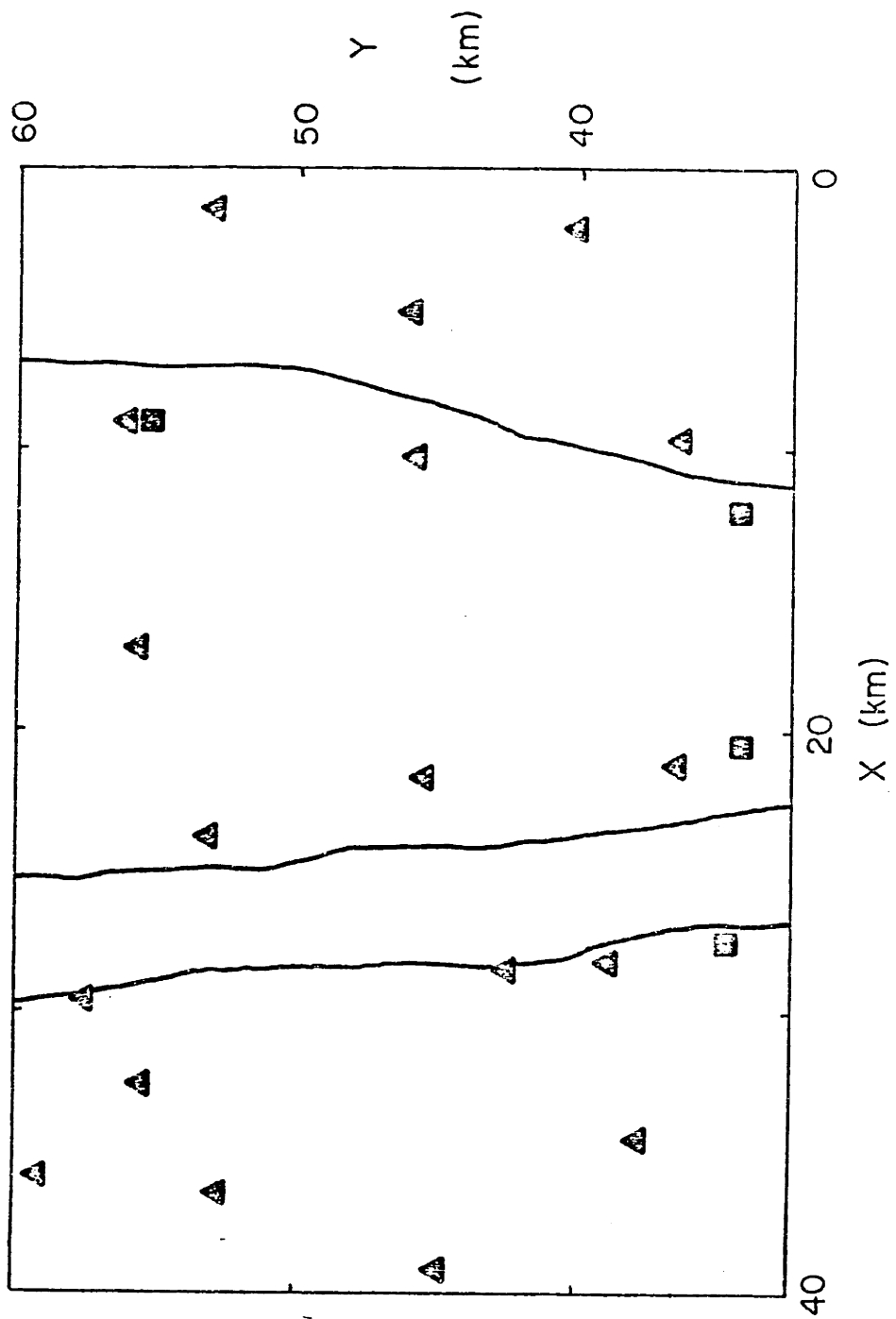

Figure 4.32

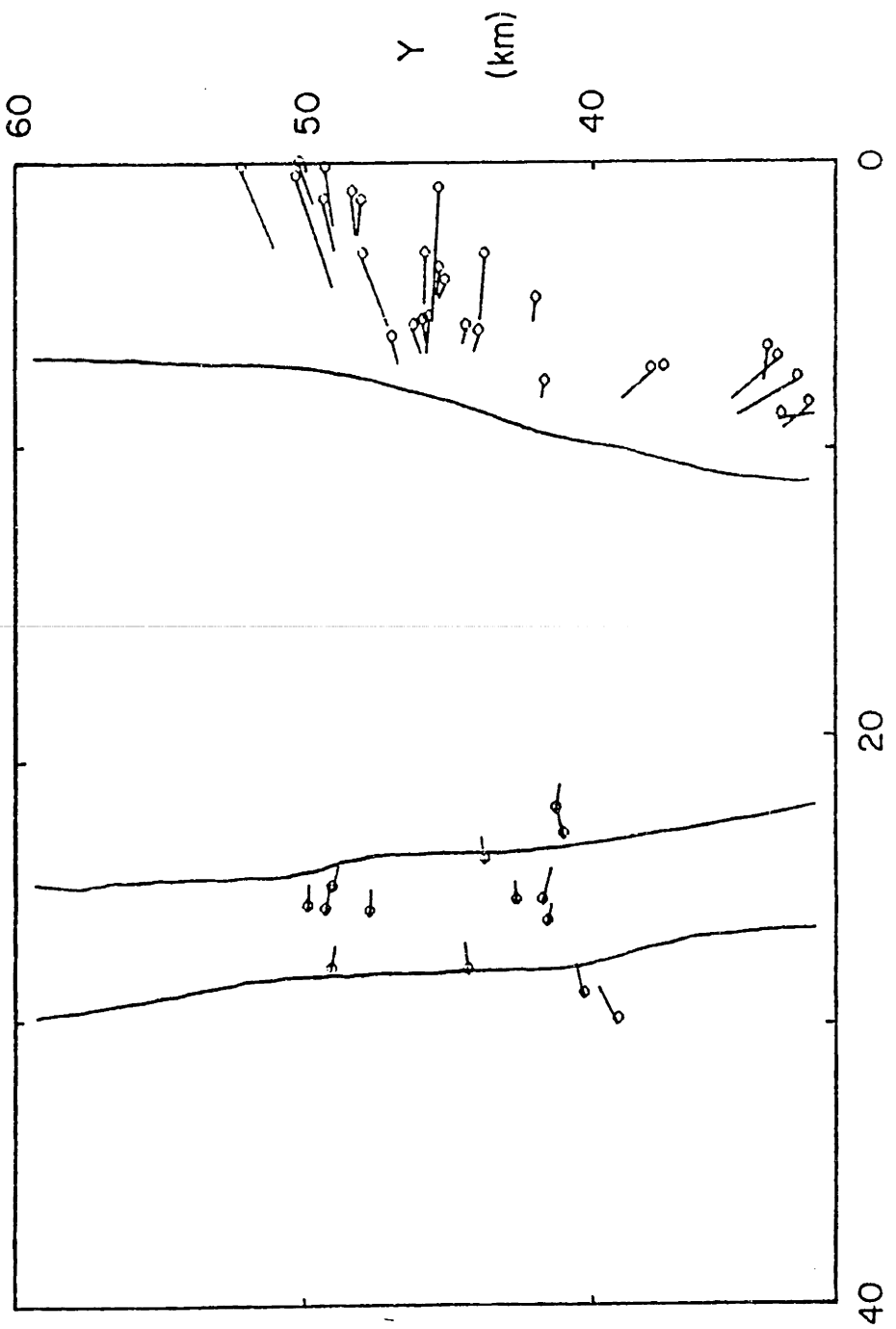

Figure 4.33 RELOCATIONS

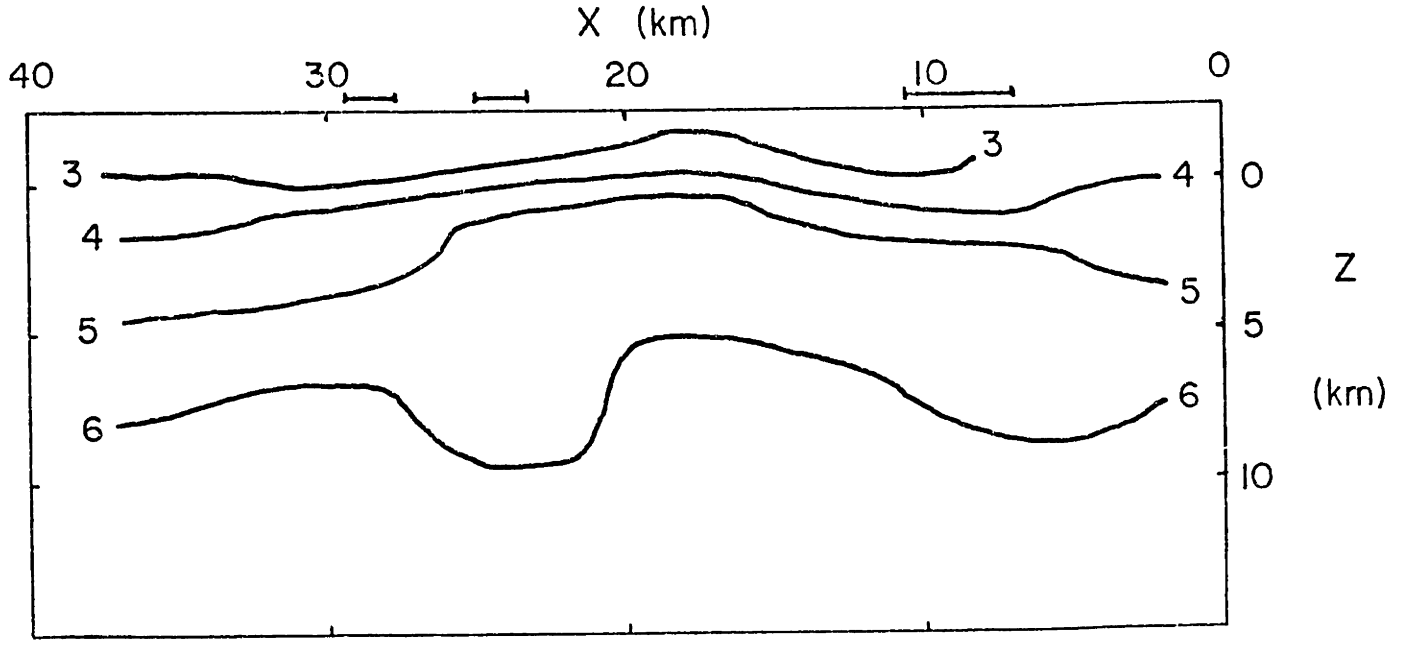

SECTION 3 VELOCITY MODEL

(contour interval 1 km/sec)

Figure 4.34

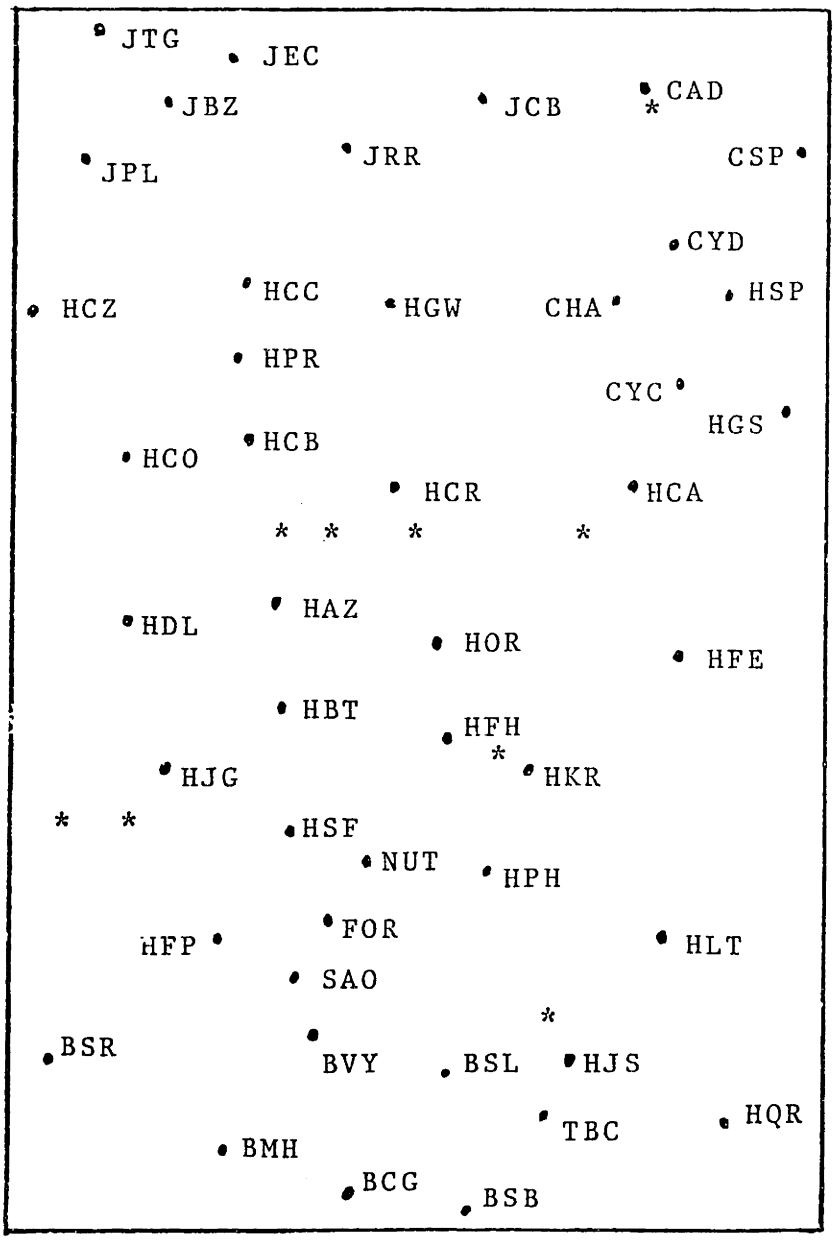
JTG
JEC
JBZ
JCB
CAD
JRR
JPL
CSP
CYD
HCZ
HCC
HGW
CHA
HSP
HPR
CYC
HGS
HCB
HCO
HCR
HCA
HAZ
HDL
HOR
HFE
HBT
HFH
HJG
HKR
HSF
NUT
HPH
FOR
HFP
HLT
SAO
BSR
BVY
BSL
HJS
HQR
TBC
BMH
BCG
BSB

Figure 4.35

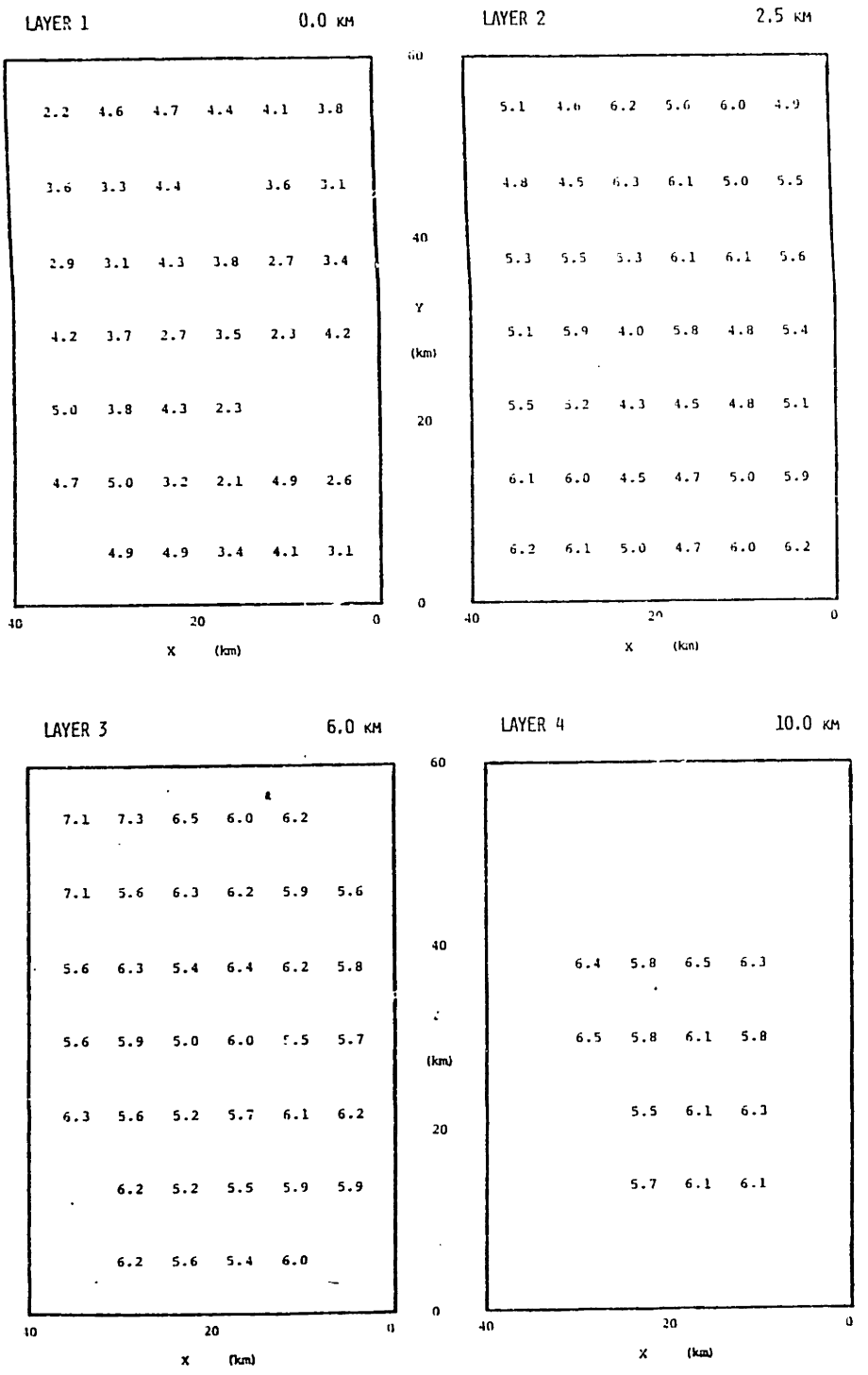
LAYER 1
0.0 KM
2.2 4.6 4.7 4.4 4.1 3.8
3.6 3.3 4.4 3.6 3.1
2.9 3.1 4.3 3.8 2.7 3.4
4.2 3.7 2.7 3.5 2.3 4.2
5.0 3.8 4.3 2.3
4.7 5.0 3.2 2.1 4.9 2.6
4.9 4.9 3.4 4.1 3.1
40
20
0
X (km)
LAYER 2
2.5 KM
5.1 4.6 6.2 5.6 6.0 4.9
4.8 4.5 6.3 6.1 5.0 5.5
5.3 5.5 5.3 6.1 6.1 5.6
5.1 5.9 4.0 5.8 4.8 5.4
5.5 5.2 4.3 4.5 4.8 5.1
6.1 6.0 4.5 4.7 5.0 5.9
6.2 6.1 5.0 4.7 6.0 6.2
60
40
20
0
Y (km)
40
20
0
X (km)
LAYER 3
6.0 KM
7.1 7.3 6.5 6.0 6.2
7.1 5.6 6.3 6.2 5.9 5.6
5.6 6.3 5.4 6.4 6.2 5.8
5.6 5.9 5.0 6.0 5.5 5.7
6.3 5.6 5.2 5.7 6.1 6.2
6.2 5.2 5.5 5.9 5.9
6.2 5.6 5.4 6.0
10
20
0
X (km)
LAYER 4
10.0 KM
6.4 5.8 6.5 6.3
6.5 5.8 6.1 5.8
5.5 6.1 6.3
5.7 6.1 6.1
60
40
20
0
(km)
40
20
0
X (km)

Figure 4.36 a

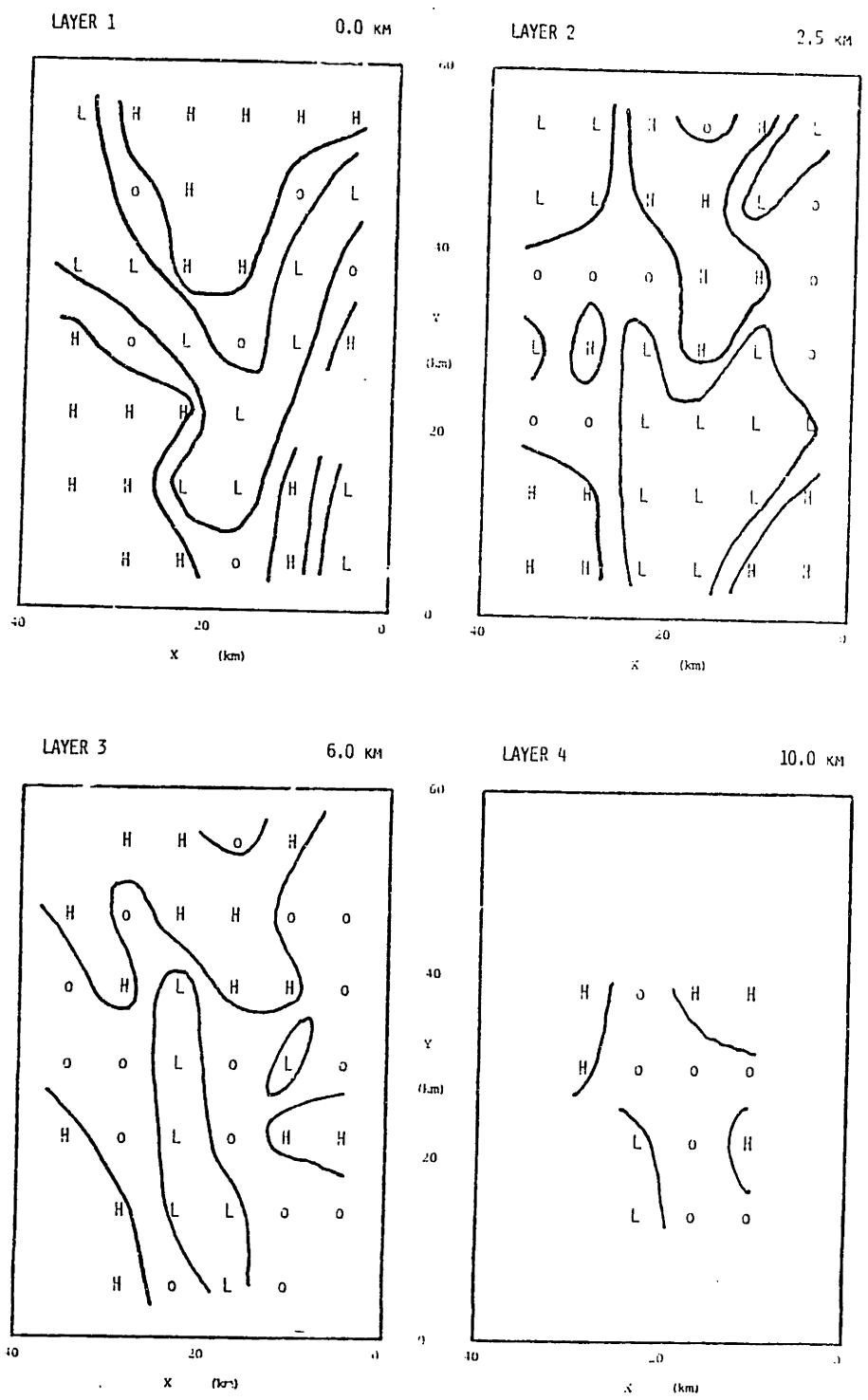

Figure 4.36 b

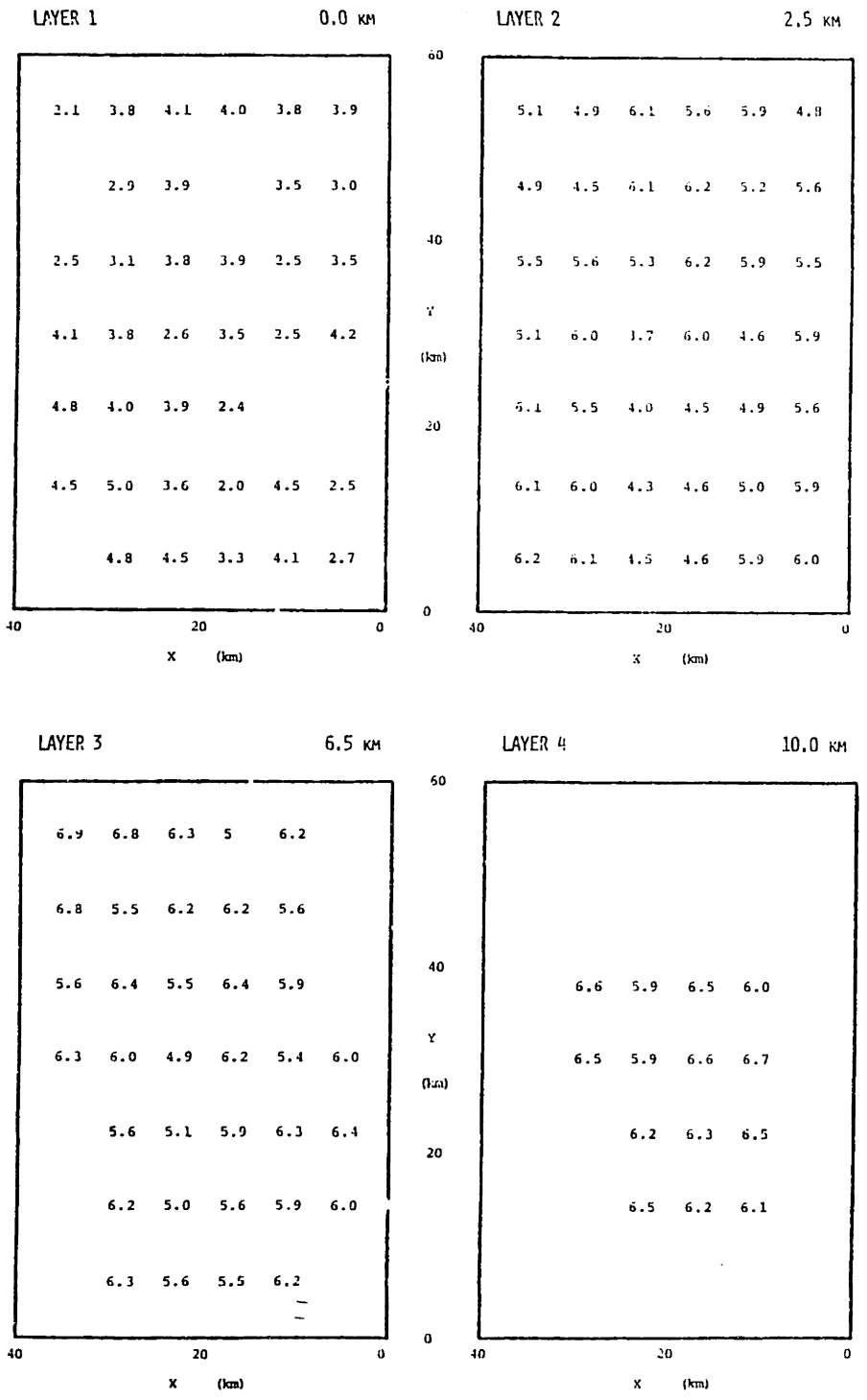
LAYER 1
0.0 KM
2.1 3.8 4.1 4.0 3.8 3.9
2.9 3.9 3.5 3.0
2.5 3.1 3.8 3.9 2.5 3.5
4.1 3.8 2.6 3.5 2.5 4.2
4.8 4.0 3.9 2.4
4.5 5.0 3.6 2.0 4.5 2.5
4.8 4.5 3.3 4.1 2.7
LAYER 2
2.5 KM
5.1 4.9 6.1 5.6 5.9 4.8
4.9 4.5 6.1 6.2 5.2 5.6
5.5 5.6 5.3 6.2 5.9 5.5
5.1 6.0 1.7 6.0 4.6 5.9
5.1 5.5 4.0 4.5 4.9 5.6
6.1 6.0 4.3 4.6 5.0 5.9
6.2 6.1 4.5 4.6 5.9 6.0
60
40
20
0
Y
(km)
40
20
0
X (km)
LAYER 3
6.5 KM
6.9 6.8 6.3 5 6.2
6.8 5.5 6.2 6.2 5.6
5.6 6.4 5.5 6.4 5.9
6.3 6.0 4.9 6.2 5.4 6.0
5.6 5.1 5.9 6.3 6.4
6.2 5.0 5.6 5.9 6.0
6.3 5.6 5.5 6.2
LAYER 4
10.0 KM
6.6 5.9 6.5 6.0
6.5 5.9 6.6 6.7
6.2 6.3 6.5
6.5 6.2 6.1
60
40
20
0
Y
(km)
40
20
0
X (km)

Figure 4.37 a

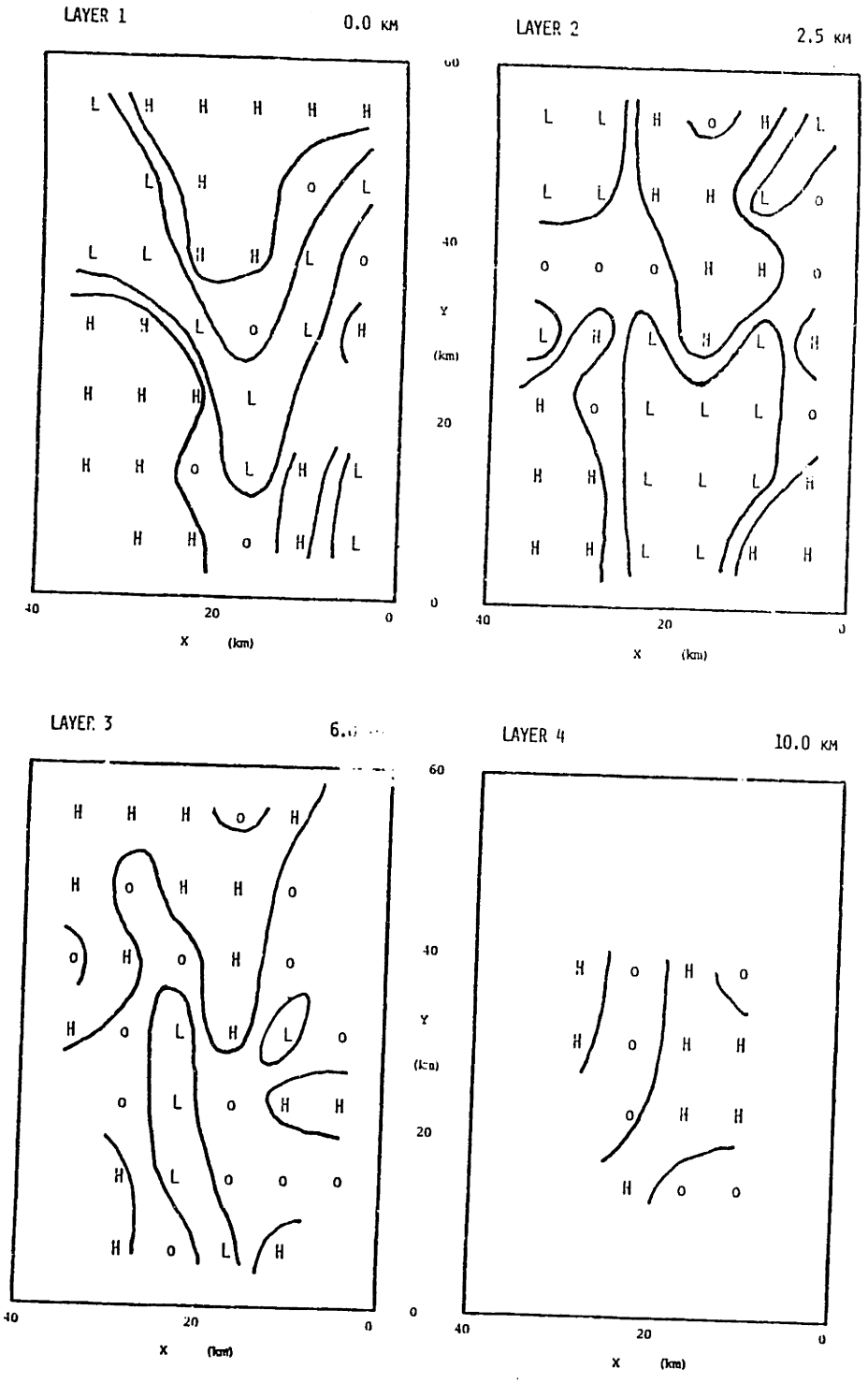
LAYER 1
0.0 KM
LAYER 2
2.5 KM
LAYER 3
LAYER 4
10.0 KM
Y
(km)
X
(km)
60
40
20
0
40
20
0

Figure 4.37 b

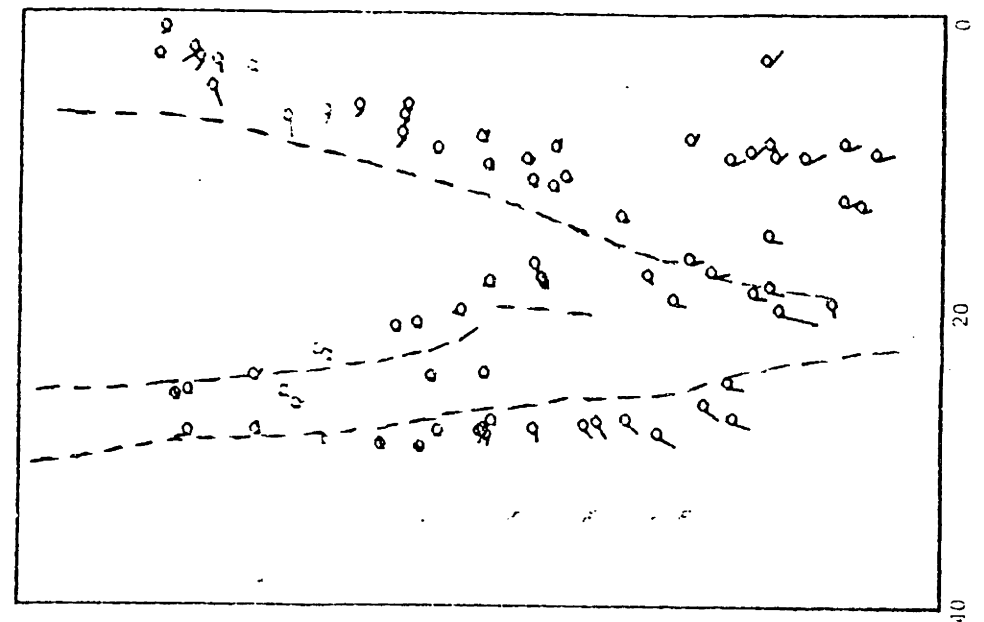

Figure 4.38 b

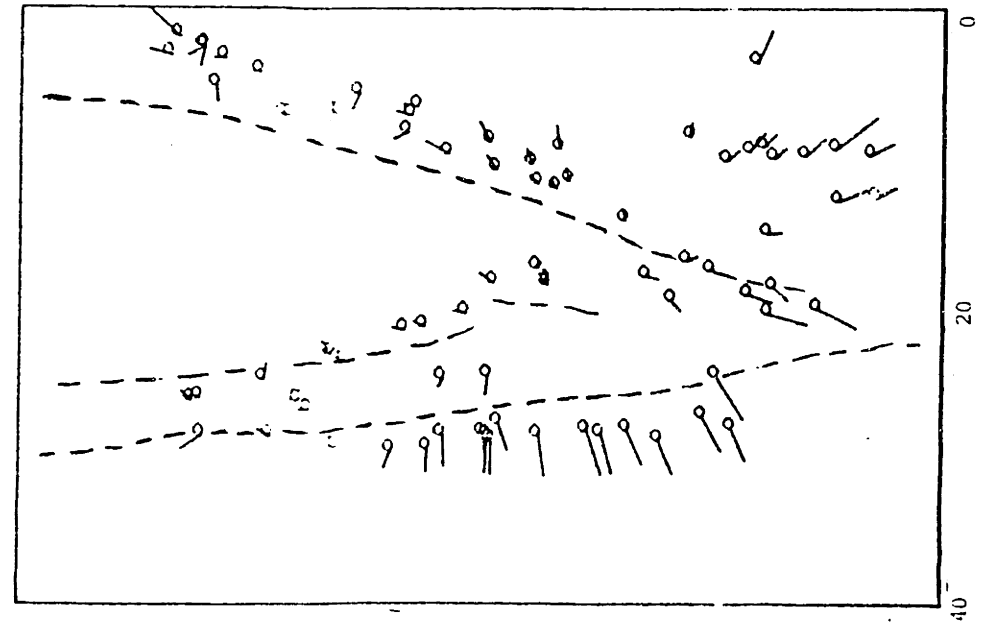

Figure 4.38 a

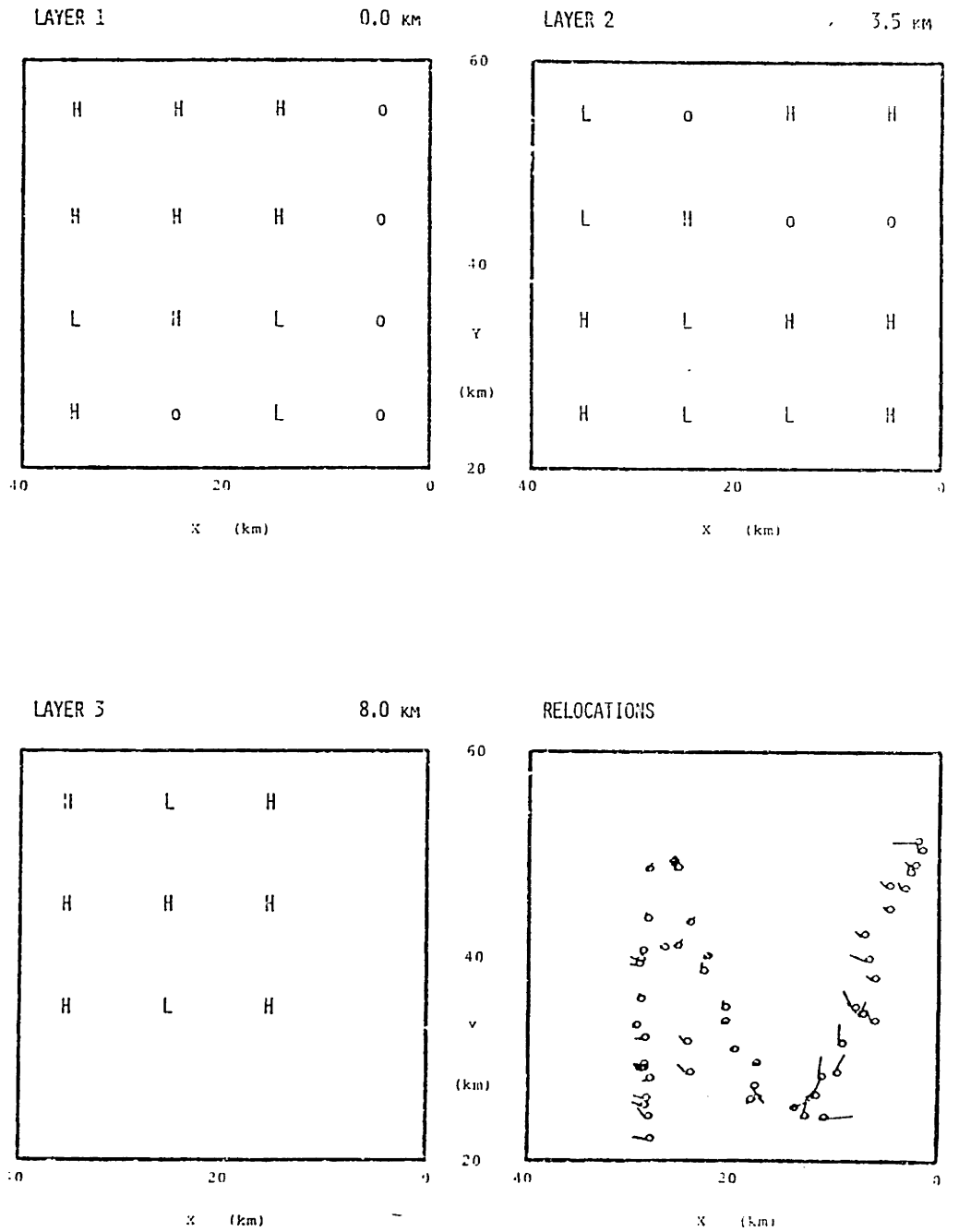
LAYER 1
0.0 KM
H H H o
H H H o
L H L o
H o L o
LAYER 2
3.5 KM
L o H H
L H o o
H L H H
H L L H
60
40
20
Y
(km)
40
20
0
X (km)
LAYER 3
8.0 KM
H L H
H H H
H L H
RELOCATIONS

Figure 4.39 a

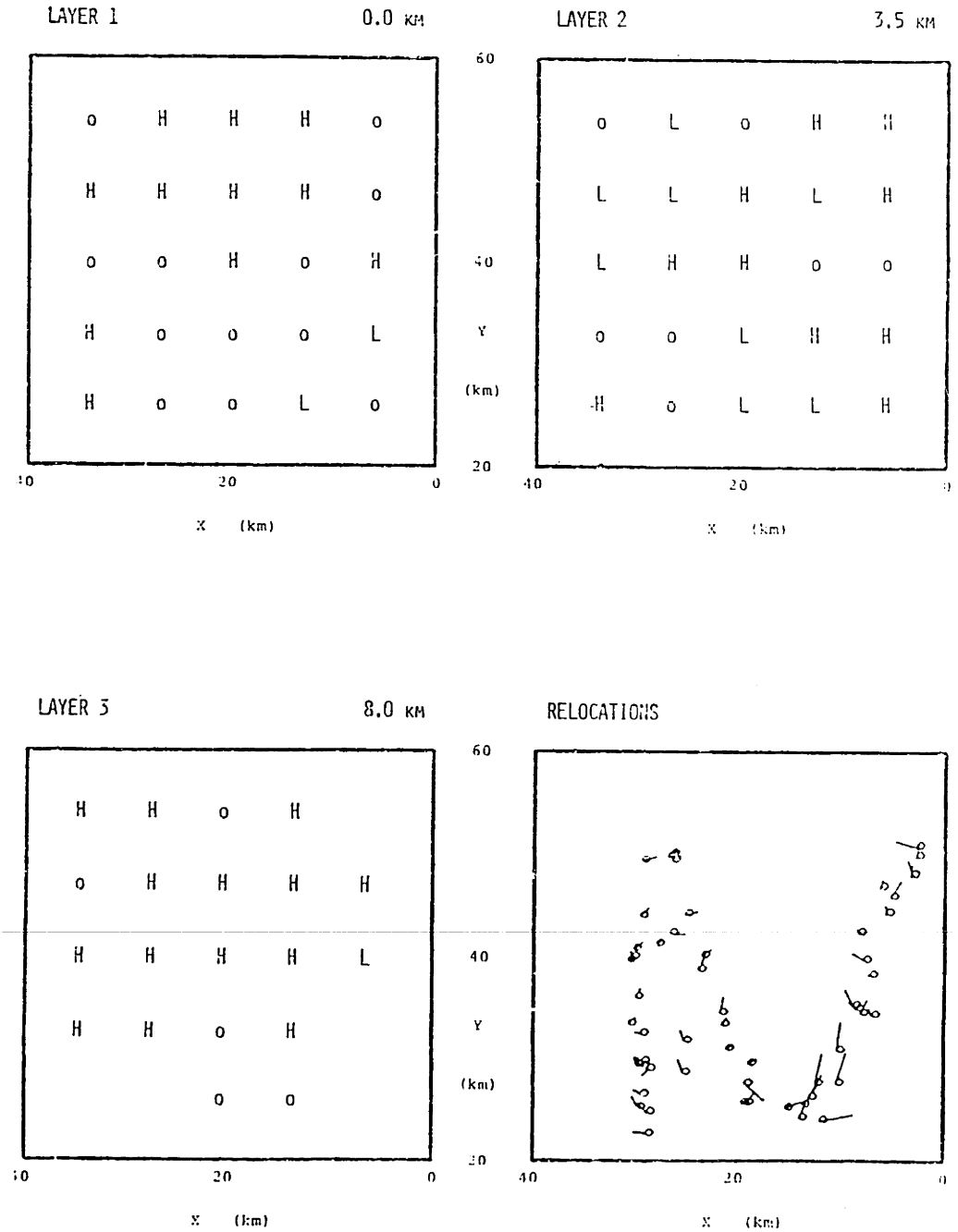
LAYER 1
0.0 KM
LAYER 2
3.5 KM
LAYER 3
8.0 KM
RELOCATIONS
60
40
20
Y
(km)
X (km)

Figure 4.39 b

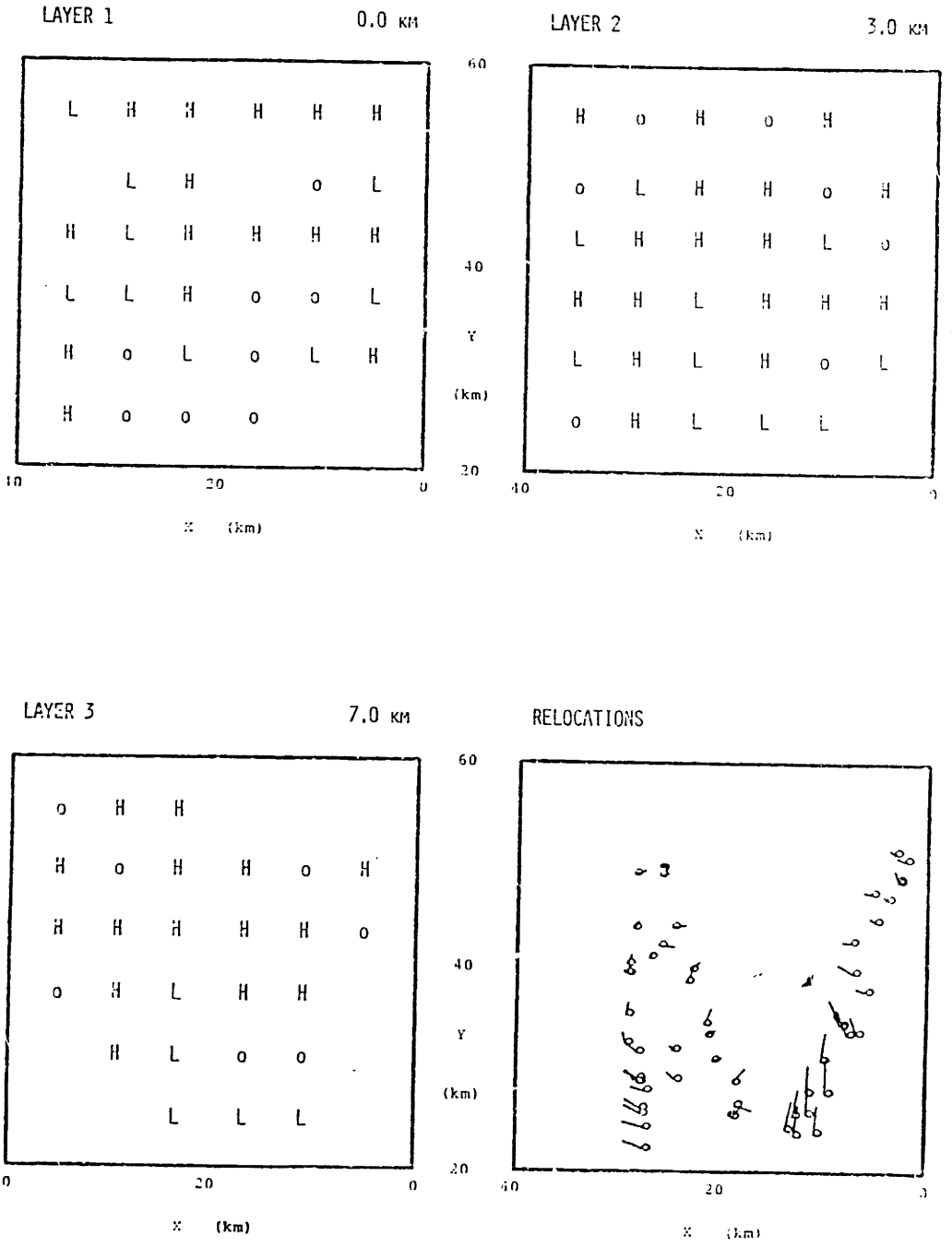
LAYER 1
0.0 KM
LAYER 2
3.0 KM
LAYER 3
7.0 KM
RELOCATIONS
60
40
20
Y
(km)
10
20
0
X (km)

Figure 4.39 c

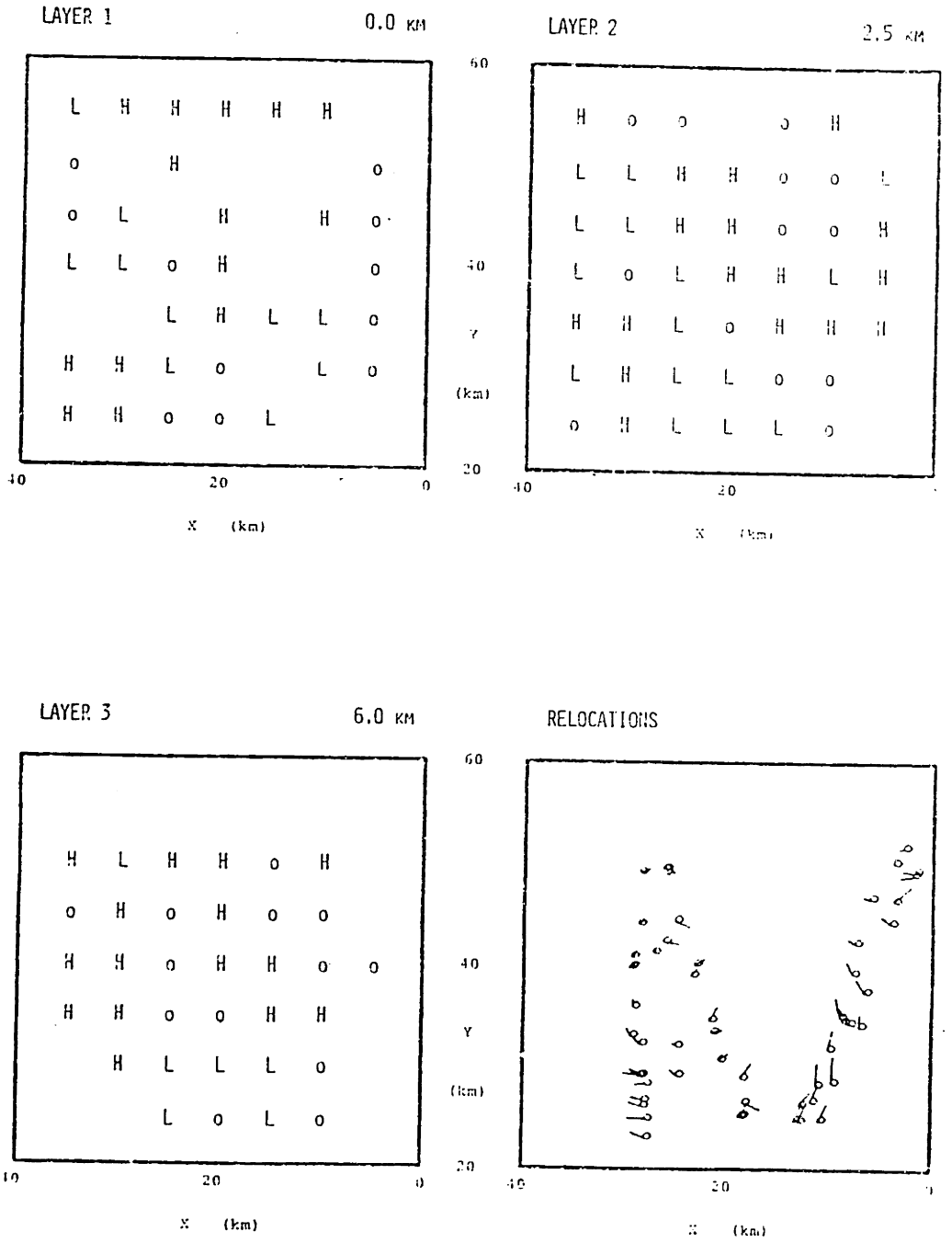
LAYER 1
0.0 KM
LAYER 2
2.5 KM
LAYER 3
6.0 KM
RELOCATIONS
60
40
20
Y
(km)
40
20
0
X (km)

Figure 4.39 d

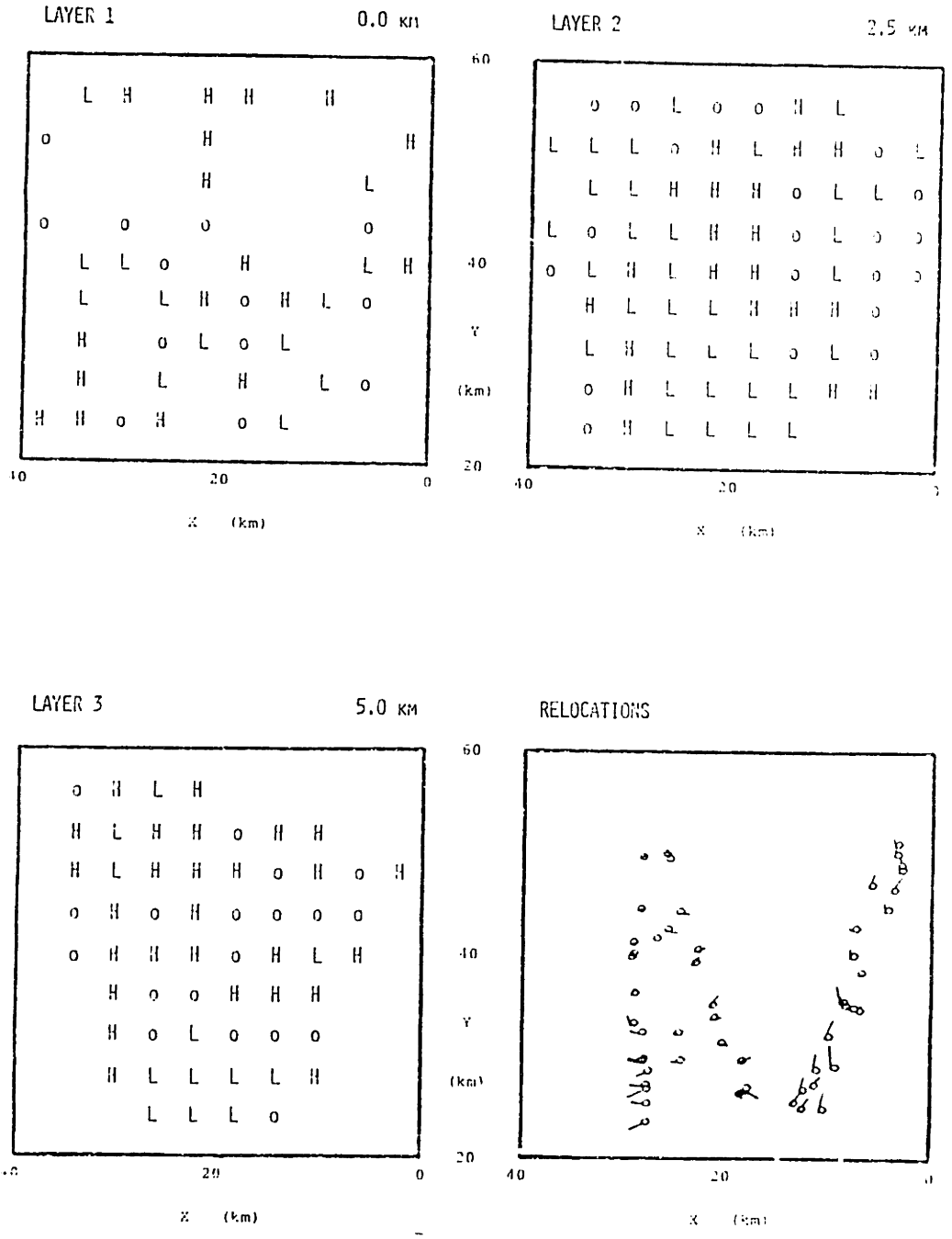
LAYER 1
0.0 KM
LAYER 2
2.5 KM
LAYER 3
5.0 KM
RELOCATIONS
60
40
20
Y
(km)
X (km)

Figure 4.39 e

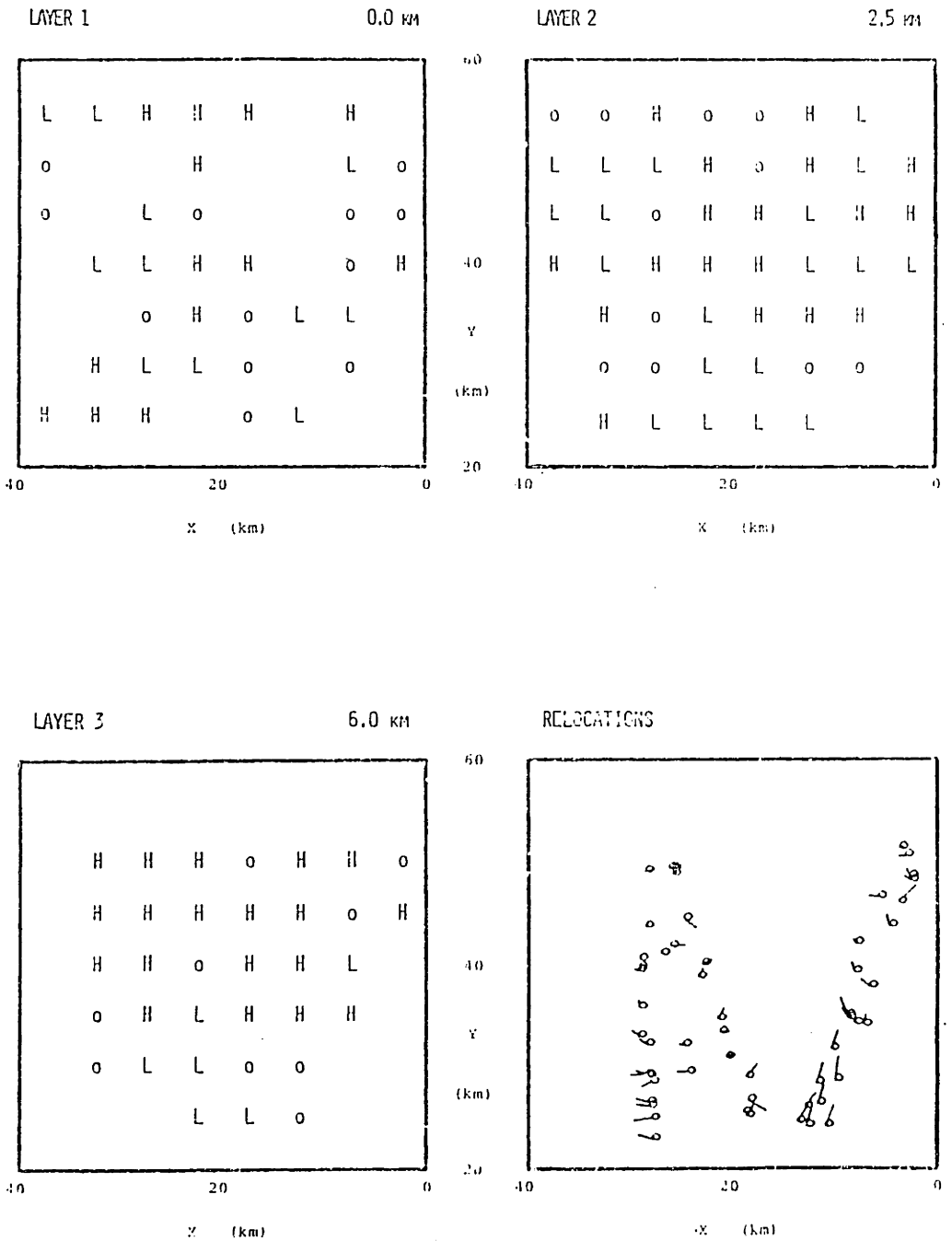
LAYER 1
0.0 KM
LAYER 2
2.5 KM
LAYER 3
6.0 KM
RELOCATIONS
60
40
20
Y
(km)
40
20
0
X (km)

Figure 4.40 a

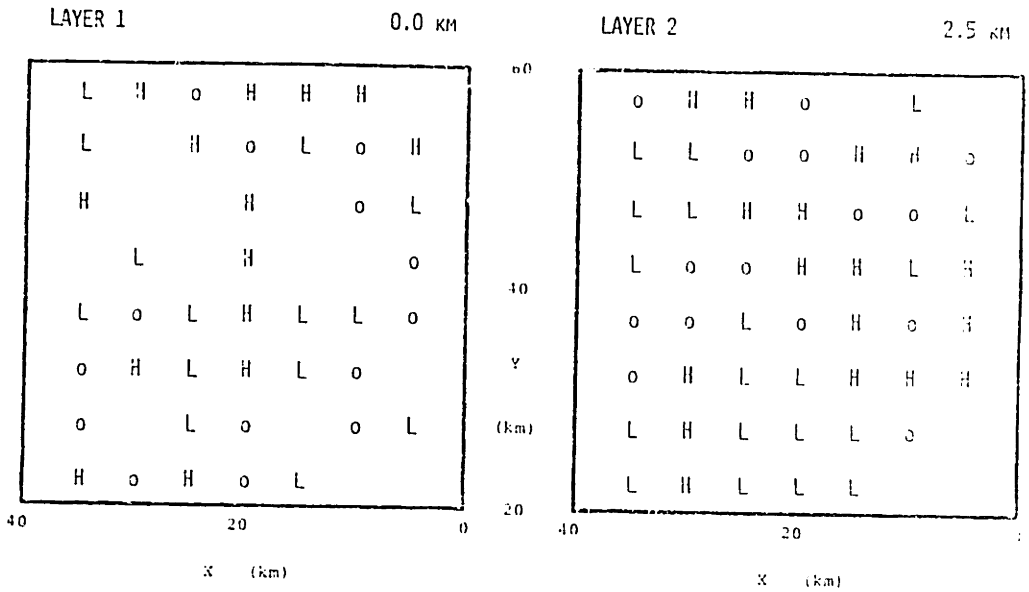
LAYER 1
0.0 KM
LAYER 2
2.5 KM
60
40
20
Y
(km)
40
20
0
X (km)
X (km)

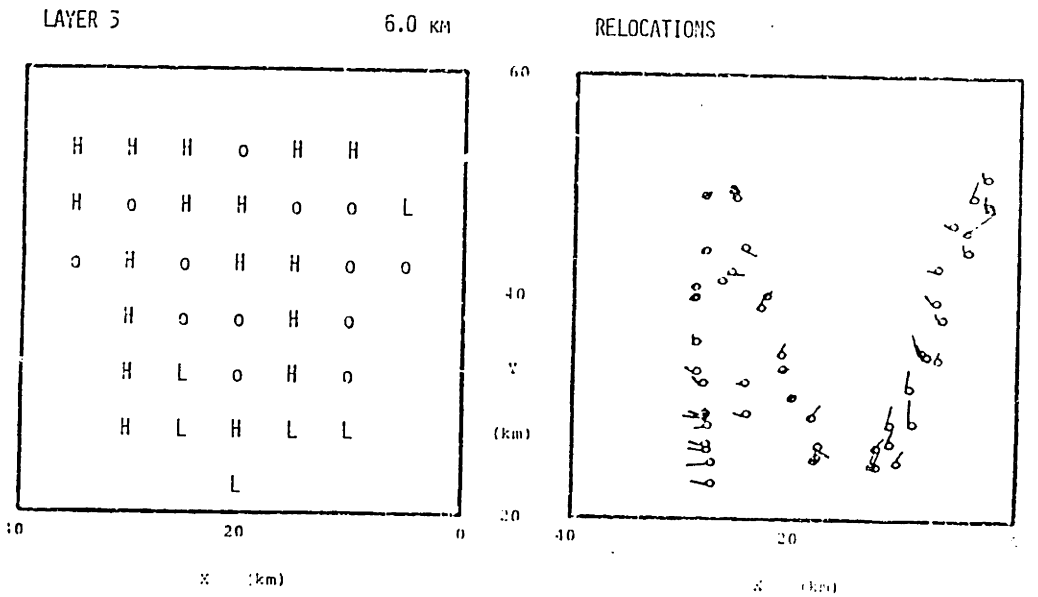
LAYER 3
6.0 KM
RELOCATIONS
60
40
20
Y
(km)
40
20
0
X (km)
X (km)

Figure 4.40 b

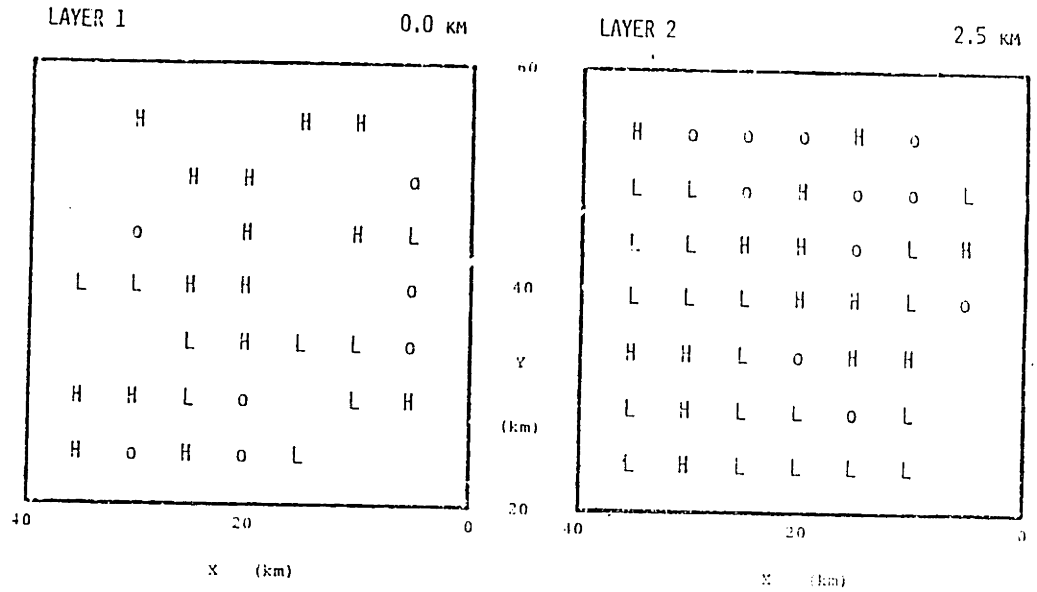
LAYER 1
0.0 KM
LAYER 2
2.5 KM
40
20
0
Y
(km)
X (km)

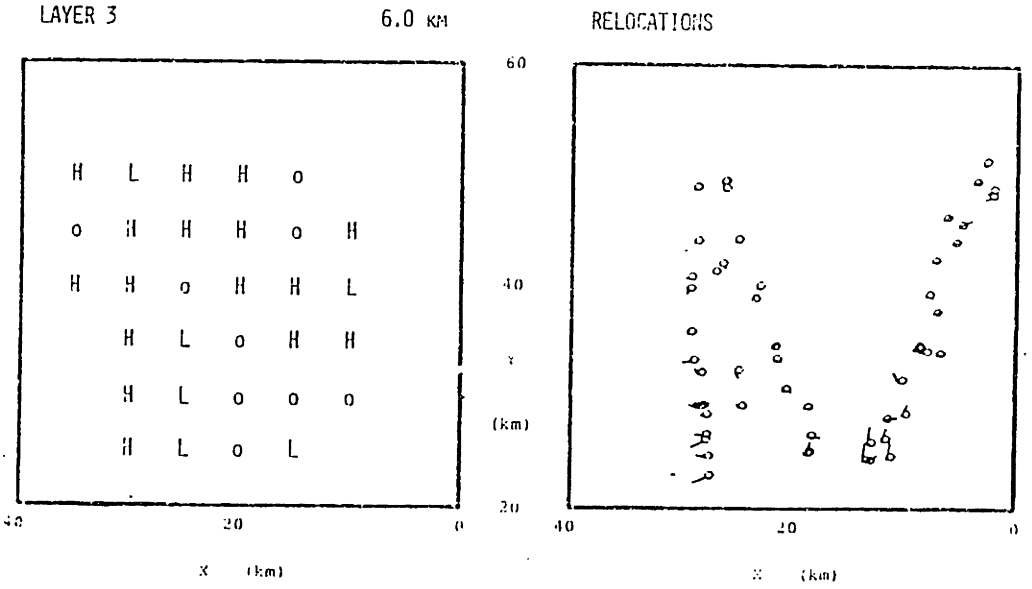
LAYER 3
6.0 KM
RELOCATIONS
60
40
20
0
Y
(km)
X (km)

Figure 4.40 c

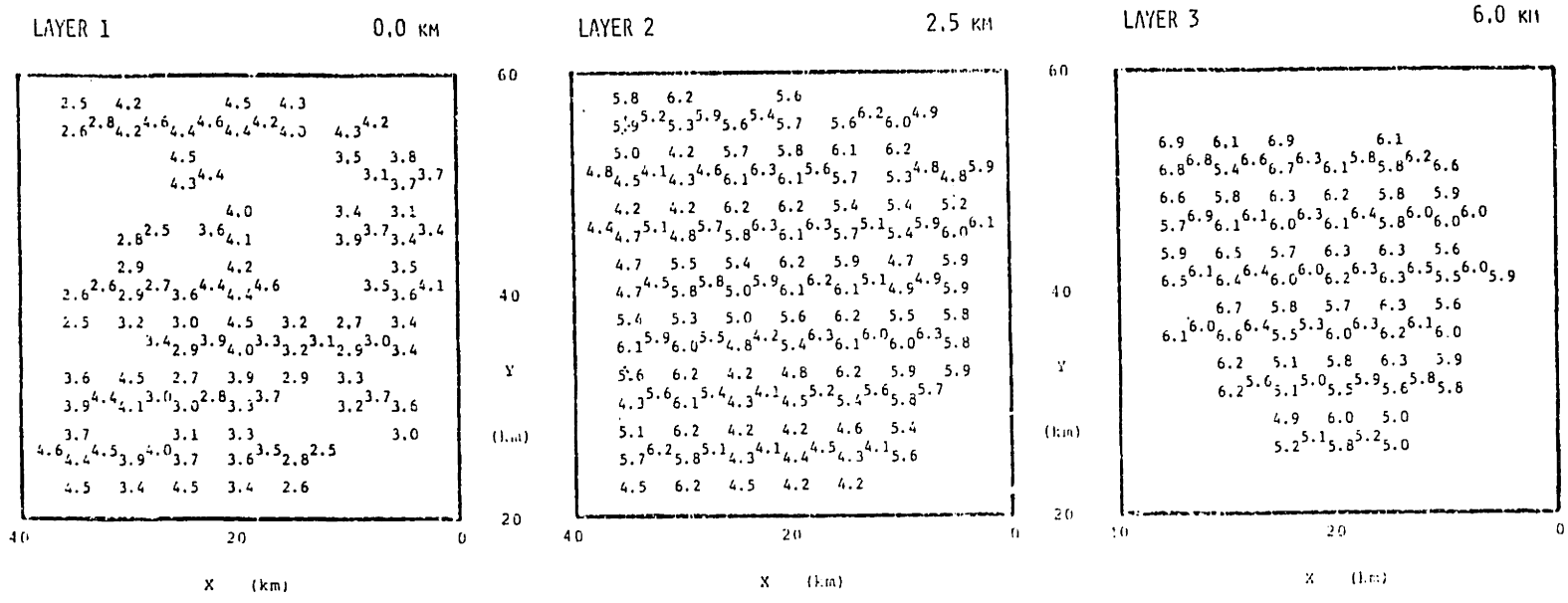

Figure 4.41

CHAPTER 5

AFTERSHOCK SEQUENCE OF THE COYOTE LAKE EARTHQUAKE

5.1 INTRODUCTION

The use of local earthquake arrival time data to infer the structure of the earth's crust was emphasized in Chapter 4. In this chapter, the focus is shifted to deriving information about seismicity and tectonics from the same type of data, plus the observed P-wave first motions. The aftershocks of the Coyote Lake earthquake provide an excellent data set for this purpose.

The first topic to be investigated is the problem of accurately locating the aftershock hypocenters. Estimates of the locations will be determined in a number of ways in order to assess the level of uncertainty both in the relative and absolute locations, and also hopefully to define a more reliable set of hypocenters. The distribution of aftershocks can then provide insight into the nature and extent of faulting during and after the Coyote Lake earthquake.

Next the P-wave first motion data are analyzed to derive constraints on the source mechanisms of a number of aftershocks. Careful attention is paid to the effects of heterogeneous crustal structure on the first motion data.

Three-dimensional ray tracing is used to partially overcome the problem of lateral refraction of rays. Focal mechanisms for events along the Calaveras fault trace are found to be consistent with the observed fault strike and sense of motion, as well as with the overall distribution of aftershocks.

Finally, the results are synthesized to provide an overview of the Coyote Lake earthquake sequence. The aftershock data combined with results from strong motion and teleseismic observations of the main shock produce a consistent overall picture of the nature of faulting in the Coyote Lake sequence.

5.2 DETERMINATION OF THE AFTERSHOCK HYPOCENTERS

The Coyote Lake event occurred on August 6, 1979, at 1705 UT. During the next two months over 300 aftershocks were recorded, with local magnitudes (determined by the US Geological Survey) ranging from 0.4 to 3.9. Parameters for the 22 largest aftershocks are listed in Table 5.1, along with the main shock.

The most difficult step in the process of accurately determining the locations of aftershocks of the Coyote Lake event is actually the task of defining an appropriate crustal model with respect to which the hypocenters will be calculated. The standard approach to this problem in the past has been to use refraction data to construct a

plane-layered velocity model, and perhaps a calibration source (explosion or earthquake) to determine station corrections (see, for example, Eaton et al., 1970; Hamilton, 1972). In other cases, station corrections have been established by trial and error so as to reduce the overall arrival time residuals (see, for example, Ellsworth, 1975).

Rather than selecting or defining one particular velocity structure for locating these aftershocks, we have chosen to investigate the results from a suite of models, both one-dimensional (with station corrections) and three-dimensional. All of the models were derived via simultaneous inversion, with the three-dimensional results determined using approximate ray tracing. From this suite the "best" solution for the aftershock locations will be chosen for closer study. First, a set of one-dimensional (layered) models will be examined. These results will be compared to the locations derived using the detailed three-dimensional model of Chapter 4, and also using a new three-dimensional model derived specifically for optimally locating the aftershocks.

5.2.1 LOCATIONS USING LAYERED MODELS

Four sets of location plots are displayed in Figures 5.1 to 5.4, resulting from four different layered velocity models with station corrections (See Figure 5.5 for geographic orientation). Each set contains an epicenter map

plus projections of the hypocenters onto vertical planes along and perpendicular to the average local strike of the Calaveras fault. Three hundred eleven events are plotted, ranging from local magnitude 5.7 (the main shock) down to magnitude 0.3. The first set shows the U.S. Geological Survey preliminary locations. For set two, the Gilroy Northeast model from Chapter 4 was used. The third and fourth sets were located with layered models and station corrections derived using simultaneous inversion and a subset of the aftershocks for which temporary-station arrival times were available (leaving out events north of the main shock for the reasons mentionned in Chapter 4). These last two sets differ in that for set three, no constraints were imposed on the inversion, while for set four, the inversion was carried out so as to minimize the arrival-time residuals subject to the constraint that the epicenters were located (approximately) along the fault trace. This last model merits further explanation.

If one assumes that the aftershocks truly fall along a vertical plane beneath the fault trace, then it is logical to attempt to derive a model (velocities and station corrections) which minimizes the overall arrival time residuals for a given set of events which are constrained during the inversion to remain along the fault plane. This constraint is imposed in practice by:

1) initially setting all x coordinates of the events to zero (where the x-axis is perpendicular

to the fault and the average x-coordinate of the fault trace is zero);

2) removing the terms corresponding to the x coordinates of the hypocenters from the system of equations in the inversion, so that the value of x will remain zero for all events.

The y and z coordinates (and origin time) are left free to vary.

During the constrained inversion procedure the events naturally remain on the fault (i.e. at X=0). However once a final model has been derived and the constraint is removed, the earthquakes will not necessarily lie along the fault when they are individually relocated. The reason is that the inversion, being overdetermined, produces a velocity model and station corrections which are a compromise among all the included events. If the constrained inversion were to be carried out with only one earthquake, then unconstrained relocation in the final model would always result in placing the event on the fault. With two or more earthquakes, this will not be the case (unless the actual velocity structure is laterally homogeneous).

Returning to the location plots, numerous features and trends are apparent. Most of the events fall within the depth range of 3 to 11 km along the entire length of the aftershock zone. Moving from Figure 5.1 through to Figure 5.4, the hypocenters as a whole are seen to cluster more noticeably along both the x and z directions. For set four this is most likely a direct consequence of the imposed

constraint (certainly for the x-direction). However, the extreme narrowness and limited depth extent of the seismic zone is quite evident in all but the USGS location set. In general, the sequence bears a stronger resemblance to the aftershocks of the 1966 Parkfield earthquake (see Eaton et al., 1970) than, for example, the 1968 Borrego Mountain sequence (see Hamilton, 1972).

Clustering of events is evident on a finer scale as well, similar to the sequences in Parkfield (Eaton et al., 1970) and Bear Valley (Ellsworth, 1975). Several distinct groups of events are consistently observed in the projections along strike of the fault in sets 2 through 4 (Figures 5.2b, 5.3b, and 5.4b). Five of the clusters are indicated in Figure 5.6. We also note the presence of two apparently distinct linear clusters visible in the epicenter maps at the southern end of the sequence.

The location plots projected perpendicular to the fault strike suggest an aftershock zone roughly 3 km wide dipping to the northeast by roughly 70 to 80 degrees (Figures 5.2c, 5.3c, and 5.4c). However, plotting the event locations from sets 3 and 4 in three separate groups complicates the picture somewhat (see Figures 5.7 and 5.8). To the north (Y>-5) the hypocenters occur in a very narrow (perhaps 1 km wide) zone dipping anywhere from 60 to 80 degrees to the northeast. In the central part (-5>Y>-13) the zone is broader, about 2 km wide, and dips more steeply (70 to 85 degrees). To the south there are apparently two separate

zones, both nearly vertical (possibly west-dipping) and 1 to 2 km wide. The extension of these near-vertical trends up to the surface generally intersects close to the mapped fault trace, except in the case of the eastwardly-branched seismic zone.

The characteristics just described are essentially independent of the model used for location. The most variable and therefore most uncertain aspect is the dip of the fault plane. However, it is difficult to avoid concluding that the dip does change along different parts of the aftershock zone. We now turn to the three-dimensional velocity modeling approach to see if this question can be resolved.

5.2.2 LOCATIONS USING THREE-DIMENSIONAL MODELS

With the results from the layered-model locations available for guidance, the next step is to make use of the detailed three-dimensional velocity model from Chapter 4 (Figure 4.48) for locating the events of the aftershock sequence. The location plots which result are shown in Figure 5.9. Except for the scatter near and north of the the main shock, the epicenters are comparable to those of set 3 in section 5.2.1 (the unconstrained inversion model; compare Figures 5.9a and 5.3a). South of San Felipe Lake the events are still located close to the fault trace, while to the north they fall about 3 km to the northeast. In

contrast, the projection plots parallel (Figure 5.9b) and perpendicular (Figure 5.9c) to the strike of the Calaveras reveal marked differences from the layered model results. First, the events are systematically shallower, with most falling in the 2 to 7 km depth range. Also, two of the clusters seen in the one-dimensional locations have vanished (compare to Figure 5.6). This disappearance is apparently due to a combination of factors: extremely poor azimuthal coverage (a gap in station coverage exceeding 180 degrees), and varying sets of observing stations for these northernmost, small magnitude events. The most extreme change is in the apparent dip of the fault plane, due to the systematic depth decrease. As a whole, the events appear to define a zone with an average dip of roughly 55 or 60 degrees. Plotted by section (Figure 5.10), the northern and central groups show dips of 55 and 60 degrees respectively, while the dip for the southern part is indeterminate. These results are in strong conflict with the self-consistent results from the layered models, motivating an effort to determine a more appropriate velocity model for the vicinity of the aftershock zone. This also points up the danger of the indiscriminate use of velocity values which are suspected of being vulnerable to large error due to being located at the periphery of a model.

To overcome this problem, a new set of stations and a new, fairly coarse velocity grid encompassing the aftershock area were established (see Figures 5.11 and 5.12). Two

velocity models were derived using 28 well-distributed and well-constrained events. For one, an inversion was carried out in two steps in which the earthquakes were first constrained to lie along the fault, as was done for model 4 of Section 5.2.1. Then the resulting model was used as a starting model for an unconstrained inversion. For the other, an inversion with a laterally homogeneous initial model with no constraints was carried out. The final locations for the two models generally differ by a kilometer or less, and the velocity values by no more than 0.5 km/sec, indicating the general consistency as well as probable level of uncertainty in the models. The final variance for the two-step model is 15 per cent lower than that for the initially laterally homogeneous model (0.00723 sec vs. 0.00834 sec , or an RMS of 0.067 sec vs. 0.072 sec), so the former model has been adopted as the "best" solution (see Figure 5.12).

The most significant difference between this model and the model from Chapter 4 is the presence of high near-surface velocities northeast of the Calaveras fault in the new model. In Chapter 4 the velocity was not resolved in this area, due to a lack of stations and therefore observations. The events should generally be relocated relatively farther to the southwest as a result.

5.2.3 IMPLICATIONS OF THE AFTERSHOCK DISTRIBUTION

The location plots for this solution are shown in Figure 5.13. The vast majority of the events fall within the depth range of 2 to 9 km. Again the epicenters occur principally in narrow linear zones, and the clusters discussed in section 5.2.1 are also present. Referring to Figure 5.14, it is apparent that these clusters are directly associated with offsets and/or complexities in the fault trace. All of the significant clusters occur at fault discontinuities (primarily right-stepping offsets, including the bend at San Felipe Lake), and each discontinuity within the aftershock zone has a corresponding cluster of events, consistent with the fault failure model of Bakun et al. (1980) developed for the San Andreas fault. Bakun (1980) also has noted peaks in the cumulative seismic moment during the Coyote Lake aftershock sequence corresponding to three of these clusters (those at Y=-7, Y=-12, and Y=-18 km). Thus these discontinuities at the surface seem to coincide with fault barriers or asperities at depth.

For a final look at the spatial distribution of aftershocks, the location plots for this model have been repeated leaving out the smaller events (local magnitude less than 1.5). The epicenter map and the projection along the fault strike are shown in Figure 5.15, while Figure 5.16 displays three cross-sectional plots perpendicular to the fault. The Coyote Lake earthquake is indicated by the asterisk, a large circle indicates an event with local magnitude above 3, a small circle an event between magnitude

2 and 3, and a dot an event between magnitude 1.5 and 2. There is an obvious deficit in aftershock activity in the vicinity of the main shock relative to the southern part of the aftershock zone in Figure 5.15, stretching from the main shock epicenter south to a cluster of events located at one of the fault discontinuities (at Y=-7 km; see Figure 5.14). The teleseismic body wave study of Nabelek and Toksoz (1981) indicates a complex multiple source for the main shock, with a rupture length of 8 to 10 km for the primary source. In addition, strong motion data indicate a total rupture length of roughly 14 km, propagating primarily unilaterally southward from the epicenter (Bouchon, written communication, 1981). Taken together, these results suggest that the fault discontinuity mentioned above and the discontinuity (or bend) at San Felipe Lake (roughly 12 km southeast of the main shock epicenter) formed barriers to the rupture propagation (see Das and Aki, 1977), the former causing a multiple source, and the latter terminating the rupture (as suggested also by Uhrhammer, 1980).

The plots in Figure 5.16 show the fault plane as defined by the aftershock distribution. South of San Felipe Lake the events fall along a vertical plane directly beneath the fault trace (except for a few small events off to the northeast). To the north, however, the events appear to define a plane dipping at 75 degrees to the northeast and paralleling the strike of the fault. This is in complete agreement with the work of Nabelek and Toksoz (1981), who

find that the teleseismic body-wave waveforms from the Coyote Lake earthquake require a rupture dipping roughly 75 degrees to the northeast.

5.3 AFTERSHOCK FOCAL MECHANISMS

First motion data are useful for providing information about the nature of faulting in an earthquake. The data required for each observing station are the sense of motion (compression or dilatation) and the take-off angle and azimuthal angle of the ray leaving the source which reaches the station. In areas with significant lateral heterogeneity, it is vital to properly account for the effects of structure on these angles (Engdahl and Lee, 1976).

Fault plane solutions for events on the Calaveras fault in the general area of Coyote Lake commonly show inconsistent polarities for stations nearly along the fault strike at distances of 20 km or so (Bakun, 1980; see also the fault-plane solution of Lee et al., 1979, for the Coyote Lake earthquake). These consistently reversed polarities can be attributed to laterally refracted first arrivals.

A number of aftershocks were examined to investigate the possibility of lateral refractions causing inconsistent first motions at three stations close to the Calaveras fault (see Figure 5.17). Three events for which some of these stations showed apparently reversed polarity were found.

First motion plots (lower hemisphere) were generated using ray tracing (the method of Pereyra et al., 1980) in the three-dimensional crustal model of section 5.2 to calculate azimuthal and take-off angles. These plots are shown in Figure 5.18a,b, and c. Also indicated are the true station azimuths, which would be used in a normal first motion plot. In each case the effect of ray tracing is to eliminate (in a and b) or at least reduce (in c) the polarity discrepancy. It would appear that use of a more detailed velocity model could result in a significant improvement in the polarity reversal problem.

Focal mechanisms for an additional eleven reasonably well constrained aftershocks were determined employing the three-dimensional model and ray tracing (or occasionally approximate ray tracing). The mechanisms fall into two distinct groups. The majority of the events show a northeast-dipping (70 to 80 degrees) strike-slip mechanism striking 25 to 30 degrees west of north. With one exception, these events are distributed along the Calaveras fault north of San Felipe Lake (see Figure 5.20). This orientation is consistent with the known right-lateral displacement along the Calaveras (Lee et al., 1979), which strikes N 27° W along this segment, and supports the fault dip determined in section 5.2 from the aftershock locations.

The single exception mentionned (event 0809 1610) is intriguing because it is located south of the bend at San Felipe Lake, but is situated well northeast of the fault

trace. This is one of a group of small aftershocks (magnitudes 2 or below) which appear to delineate an eastwardly-splayed branch in the fault (see Figure 5.9).

The remaining three events are located directly along the Calaveras fault trace south of San Felipe Lake (events 0814 0315, 0810 1236, and 0810 0751). Here the fault strike is rotated some 10 degrees to roughly N 15° W. The focal mechanisms (also strike-slip) are consistent with this orientation. In addition the dip is nearly vertical, and possibly southwest dipping.

5.4 SUMMARY: SPACE-TIME HISTORY OF THE COYOTE LAKE SEQUENCE

The Coyote Lake earthquake was not preceded by detectable foreshocks (Uhrhammer, 1980). There was, however, a distinct gap in seismic activity (at least for magnitudes greater than or equal to 2.5) throughout the Coyote Lake aftershock zone for at least 15 months prior to the main event (see Figure 5.21a and b). Inspection of Figure 5 of Uhrhammer (1980) suggests that this absence of moderate-sized earthquake activity extends back to 1966. Perhaps the only seismological clue to the then-impending earthquake was the sequence of moderate-sized events north of the main shock beginning in mid-1978 (see Figure 5.21b).

Figure 5.22 shows a similar plot of the history of the aftershocks of the Coyote Lake earthquake (local magnitude greater than 2.5). Two striking features of the sequence

history are the nearly total absence of sizable aftershocks north of the main shock, and the steady southward progression of aftershocks for the first 10 hours following the occurence of the main shock (see also Lee et al., 1979, and Uhrhammer, 1980). These events are shown in ordered sequence in map view and projected onto a vertical plane along the fault strike in Figure 5.23a and b (see also Table 5.1).

Combining the available information, we arrive at the following scenario for the Coyote Lake earthquake sequence. The main shock initiated just to the south of a right-stepping offset in the fault and propagated primarily unilaterally to the southeast (Bouchon, written communication, 1981) along a plane dipping 75 degrees to the northeast (Nabelek and Toksoz, 1981, and this work). Rupture was somewhat impeded by a barrier (offset) in the fault roughly 8 km southeast of the epicenter, causing complexity in the source as seen at teleseismic distances. The initial rupture probably extended as far as the San Felipe Lake fault bend. Most of the larger aftershocks occurred along the segment between the above barrier and the San Felipe bend (see Figure 5.14), indicating locally incomplete stress release during the main shock (unbroken barriers of Das and Aki, 1977). Moderate activity was also observed south of the bend, as expected for a right-stepping offset when slip occurs on one side of the discontinuity (Bakun et al., 1980). This activity was concentrated in two

zones, one following the main surface trace of the Calaveras; and the other displaced roughly 2 km to the northeast. The one focal mechanism derived for an event of the latter group shows it to be quite similar to those north of the San Felipe bend, and quite distinct from those on the main fault trace south of the bend. Continuing seismicity was concentrated in a number of clusters along the aftershock zone, each of which appears to be associated with an offset or discontinuity in the fault as seen at the surface.

TABLE 5.1

THE COYOTE LAKE EARTHQUAKE AND ITS PRINCIPAL AFTERSHOCKS

ORIGIN TIME DATE	HOUR	SEC	LATITUDE	LONGITUDE	DEPTH	X	Y	Z	MAG
79 8 6	17 5	22.36	37 5.57	121 31.07	6.05	-1.56	-2.45	6.05	5.7
79 8 6	1710	42.93	37 4.43	121 30.11	7.48	-1.88	-4.97	7.48	3.3
79 8 6	1722	47.01	37 2.27	121 28.64	8.34	-2.03	-9.52	8.34	2.9
79 8 6	2221	1.20	37 1.76	121 28.31	6.78	-2.04	-10.57	6.78	3.2
79 8 6	2233	34.68	37 0.13	121 28.66	4.41	-0.21	-13.04	4.41	3.8
79 8 6	2235	56.65	37 0.02	121 28.64	4.56	-0.16	-13.23	4.56	3.5
79 8 6	2335	59.91	37 1.63	121 28.95	6.97	-1.08	-10.36	6.97	2.6
79 8 7	232	30.84	36 58.04	121 27.79	6.64	0.37	-17.06	6.64	2.8
79 8 7	556	51.14	37 3.20	121 29.44	6.34	-1.74	-7.44	6.34	2.8
79 8 7	1911	25.15	36 58.61	121 27.98	5.01	0.15	-16.00	5.01	2.8
79 8 8	2256	7.51	37 1.65	121 28.25	6.32	-2.03	-10.80	6.32	3.0
79 8 9	528	47.99	36 58.02	121 27.78	6.28	0.37	-17.10	6.28	2.6
79 8 9	7 3	19.70	37 0.62	121 27.52	7.51	-2.14	-12.98	7.51	3.1
79 8 9	1249	11.22	36 58.05	121 27.85	3.87	0.44	-17.02	3.87	2.8
79 8 9	1251	40.86	36 57.76	121 27.57	6.19	0.31	-17.67	6.19	2.6
79 810	025	20.36	37 1.05	121 27.91	6.60	-1.98	-12.01	6.60	3.0
79 810	450	39.22	36 57.71	121 27.69	6.45	0.51	-17.69	6.45	2.8
79 811	940	18.83	36 58.82	121 27.86	6.65	-0.19	-15.74	6.65	2.6
79 811	2029	34.89	37 7.59	121 31.81	8.97	-2.26	1.39	8.97	3.1
79 814	315	56.49	36 59.08	121 28.04	6.38	-0.16	-15.19	6.38	3.2
79 9 3	640	15.78	37 3.60	121 29.72	4.46	-1.70	-6.59	4.46	2.8
79 910	616	3.76	37 8.23	121 32.50	5.83	-1.88	2.91	5.83	2.6
79 917	1919	12.42	37 2.45	121 28.79	6.41	-1.98	-9.11	6.41	2.6

FIGURE CAPTIONS

Figure 5.1 US Geological Survey locations of 311 aftershocks of the Coyote Lake earthquake:
a) map view of epicenters;
b) projection along a vertical plane parallel to the Calaveras fault;
c) projection along a vertical plane perpendicular to the Calaveras fault.

Figure 5.2 Aftershock relocations in the Gilroy Northeast one-dimensional model (see Figure 5.1).

Figure 5.3 Aftershock relocations in a layered model derived via simultaneous inversion for 28 well-distributed and well-constrained aftershocks (see Figure 5.1). "Unconstrained" model.

Figure 5.4 Aftershock relocations in a layered model derived via simultaneous inversion with 28 events subject to the constraint that the events lie directly along the fault (see text and Figure 5.1). "Constrained" model.

Figure 5.5 Map of area shown in Figures 5.1a to 5.4a, with the Calaveras fault, Coyote Lake, San Felipe Lake, and several nearby seismometer stations illustrated.

Figure 5.6 Clusters of events observed in Figures 5.2b to 5.4b (shown projected onto a vertical plane parallel to the Calaveras fault).

Figure 5.7 Projection of locations onto vertical planes perpendicular to the Calaveras fault for the "unconstrained" model:
a) $Y > -5$
b) $-5 > Y > -13$
c) $Y < -13$

Figure 5.8 Same as Figure 5.7, but for the "constrained" model.

Figure 5.9 Aftershock relocations using the detailed three-dimensional model from Chapter 4. Compare to Figures 5.1 through 5.4.

Figure 5.10 Same as Figure 5.7, but for the Chapter 4 three-dimensional model.

Figure 5.11 Map of permanent stations used for aftershock three-dimensional inversion.

Figure 5.12 Velocity model derived from two-step aftershock inversion.

Figure 5.13 Aftershock relocations in the velocity model of Figure 5.12. Compare to Figures 5.1 through 5.4.

Figure 5.14 Aftershock cluster locations related to fault complexities and/or discontinuities (locations from Figure 5.13b).

Figure 5.15 Locations of the larger aftershocks:
. = local magnitude > 1.5 and < 2.0;
o = local magnitude > 2.0 and < 3.0;
O = local magnitude > 3.0 and < 4.0;
* = Coyote Lake earthquake.
(Velocity model of Figure 5.12).

Figure 5.16 Same as Figure 5.7, but for model of Figure 5.12. Note apparent change in fault dip going from north (in a) to south (in c). See Figure 5.15 for magnitude symbols.

Figure 5.17 Sources (a, b and c) and stations for investigating polarity reversals.

Figure 5.18 Focal mechanisms showing improvement in polarity reversal problem when true station azimuths are replaced (arrows) by "take-off azimuths" from three-dimensional ray tracing (see text).

Figure 5.19 Sample focal mechanisms determined using three-dimensional ray tracing, along with computer solutions for permissible configurations of P, T and B axes. The first 7 events pictured (0811 2029 to 0809 0703) are all located north of San Felipe Lake (see Figure 5.20) and show very similar mechanisms; average strike N 15 W, average dip 75 NE. Of the remaining four, three lie directly along the fault trace and show comparable mechanisms: average strike N 15 W, average dip 85 SW (0814 0315, 0810 1236, 0810 0751). The epicenter of event 0809 1610 lies over 2 km northeast of the fault trace, and it has a mechanism more similar to those north of San Felipe Lake.

Figure 5.20 Map showing locations of events in Figure 5.19.

Figure 5.21 a) Map of locations of events plotted in b.

b) Seismicity along the Calaveras fault (section AA' in a) preceding the Coyote Lake sequence, starting in May, 1978. Note the total quiesence along the aftershock zone itself.

Figure 5.22 Space-time chronology of the Coyote Lake sequence. Events with local magnitude above 2.5 are plotted, with the ordinate being time following the occurence of the main shock and the abscissa the Y coordinate of the event (refer to Figure 5.23).

Figure 5.23 Map and projection views of the sequence of events starting with the main shock (number 1). See Table 5.1 for a complete listing of these events.

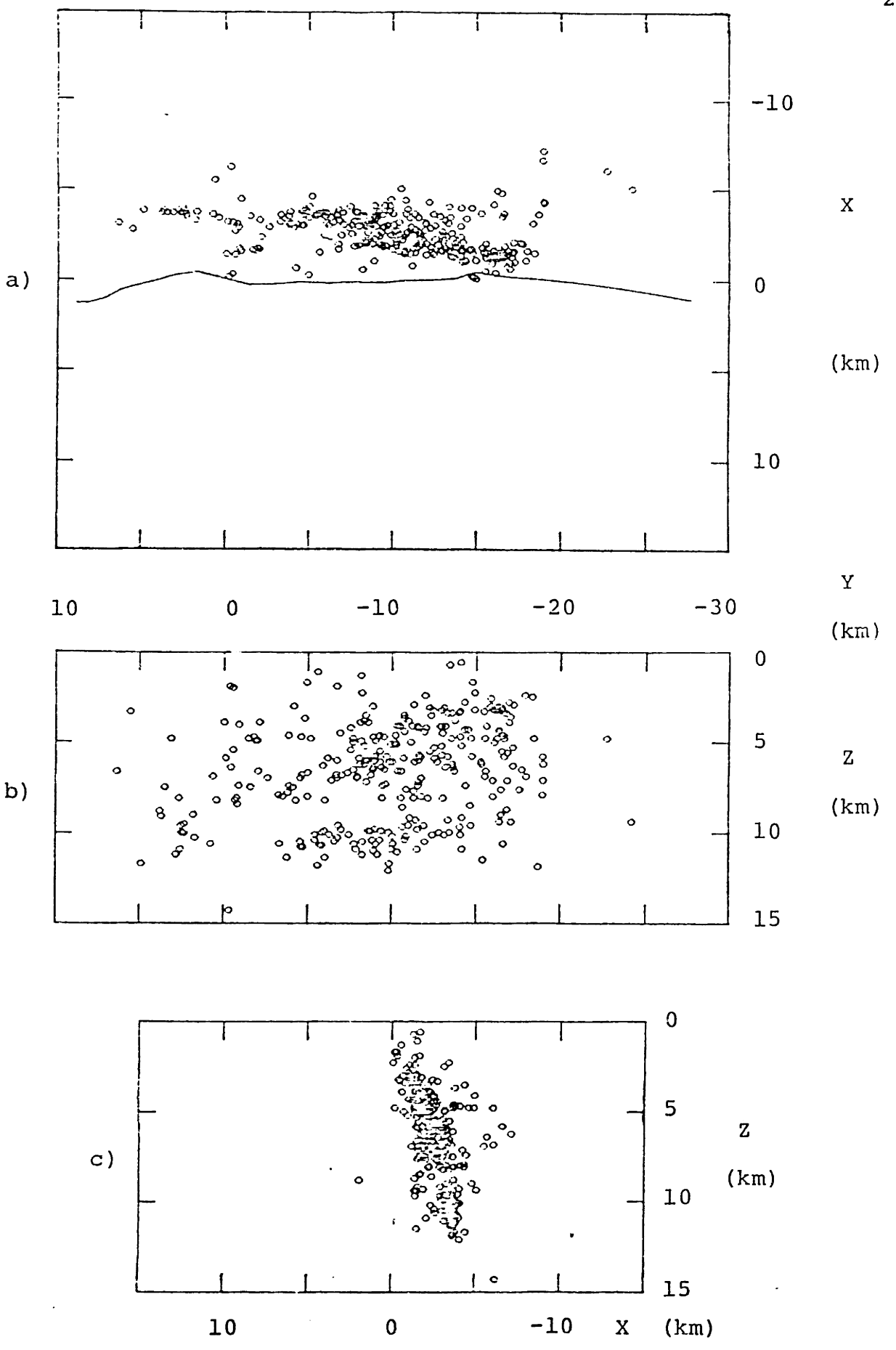

Figure 5.1

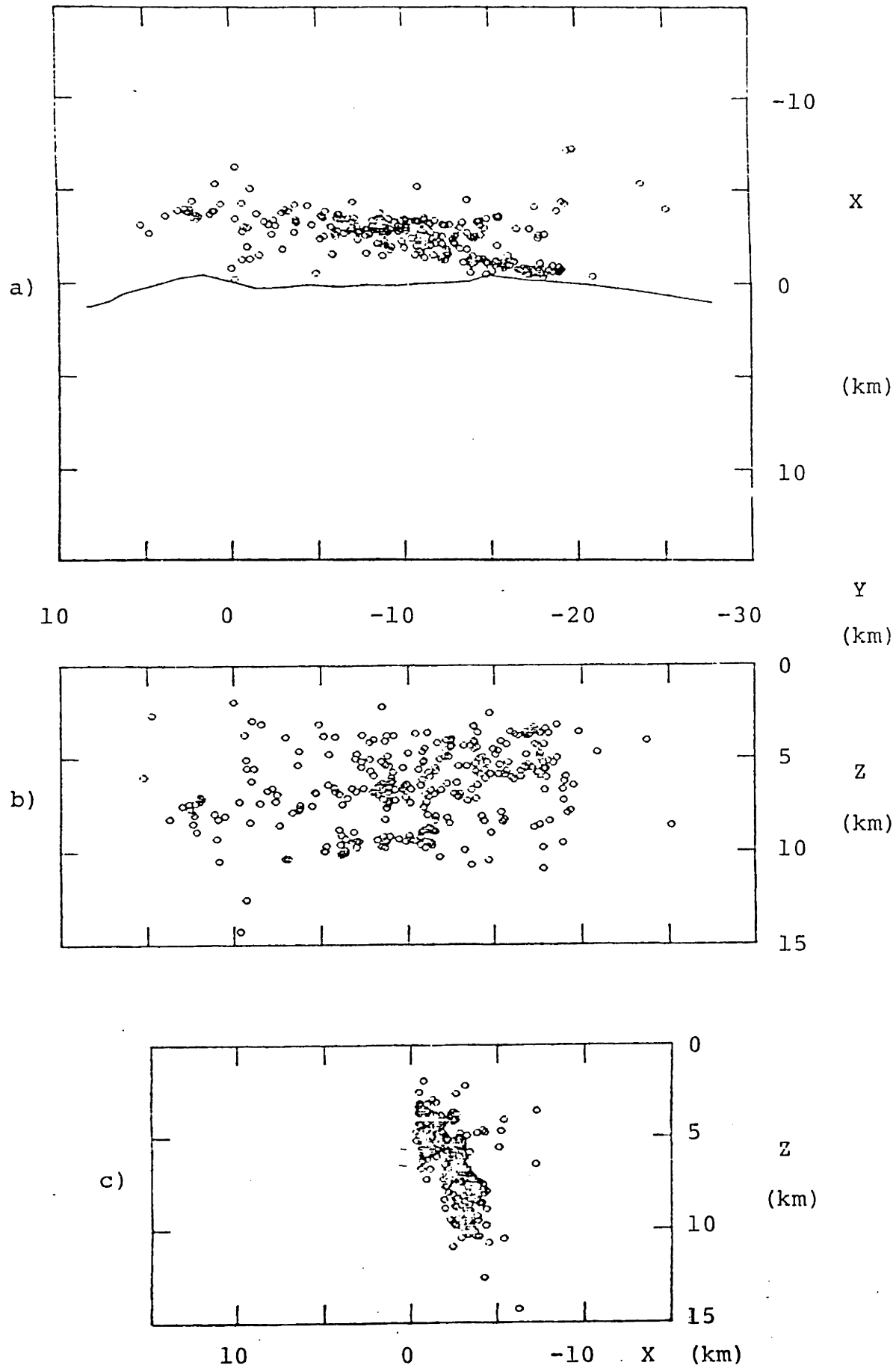

Figure 5.2

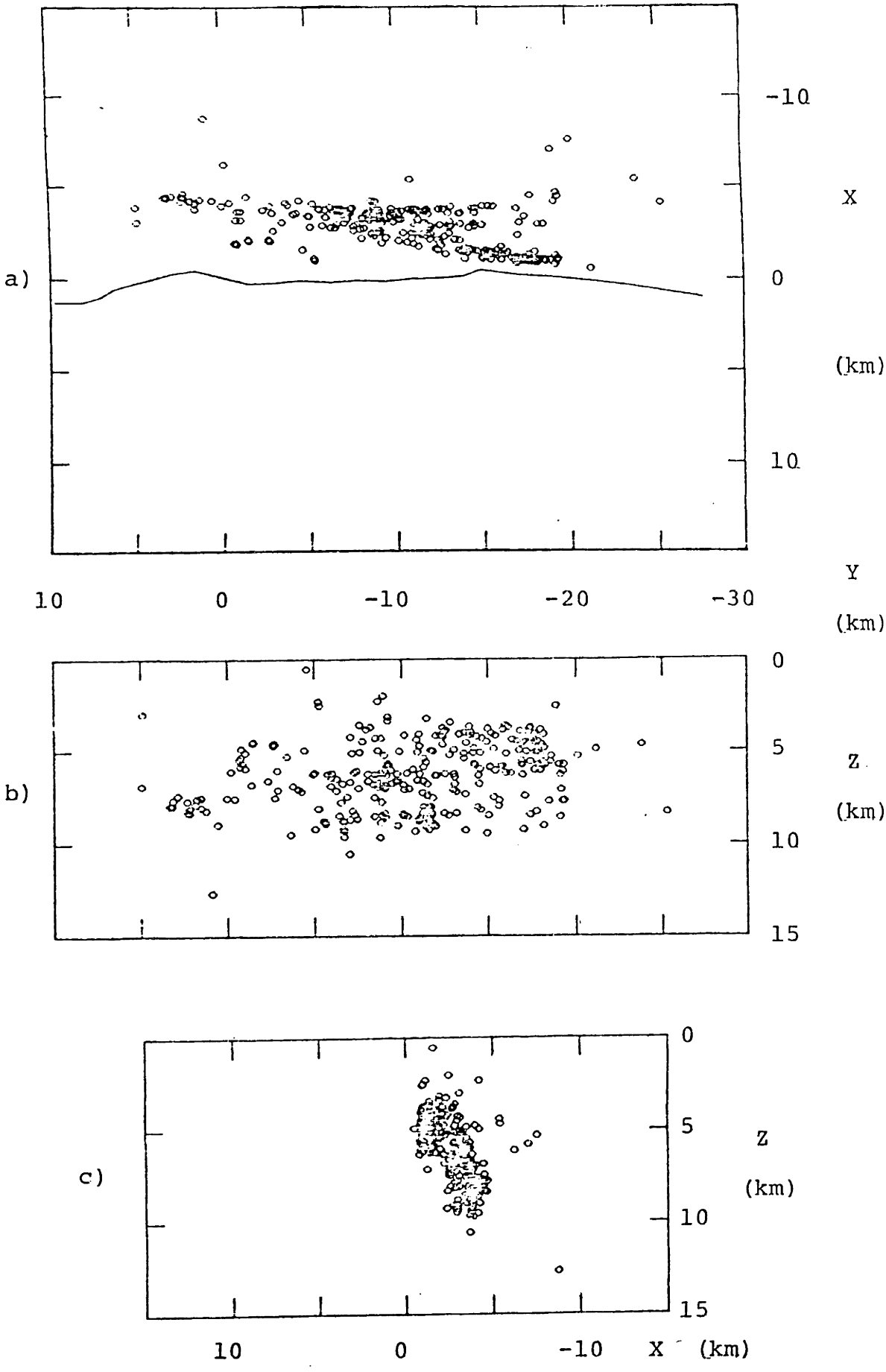

Figure 5.3

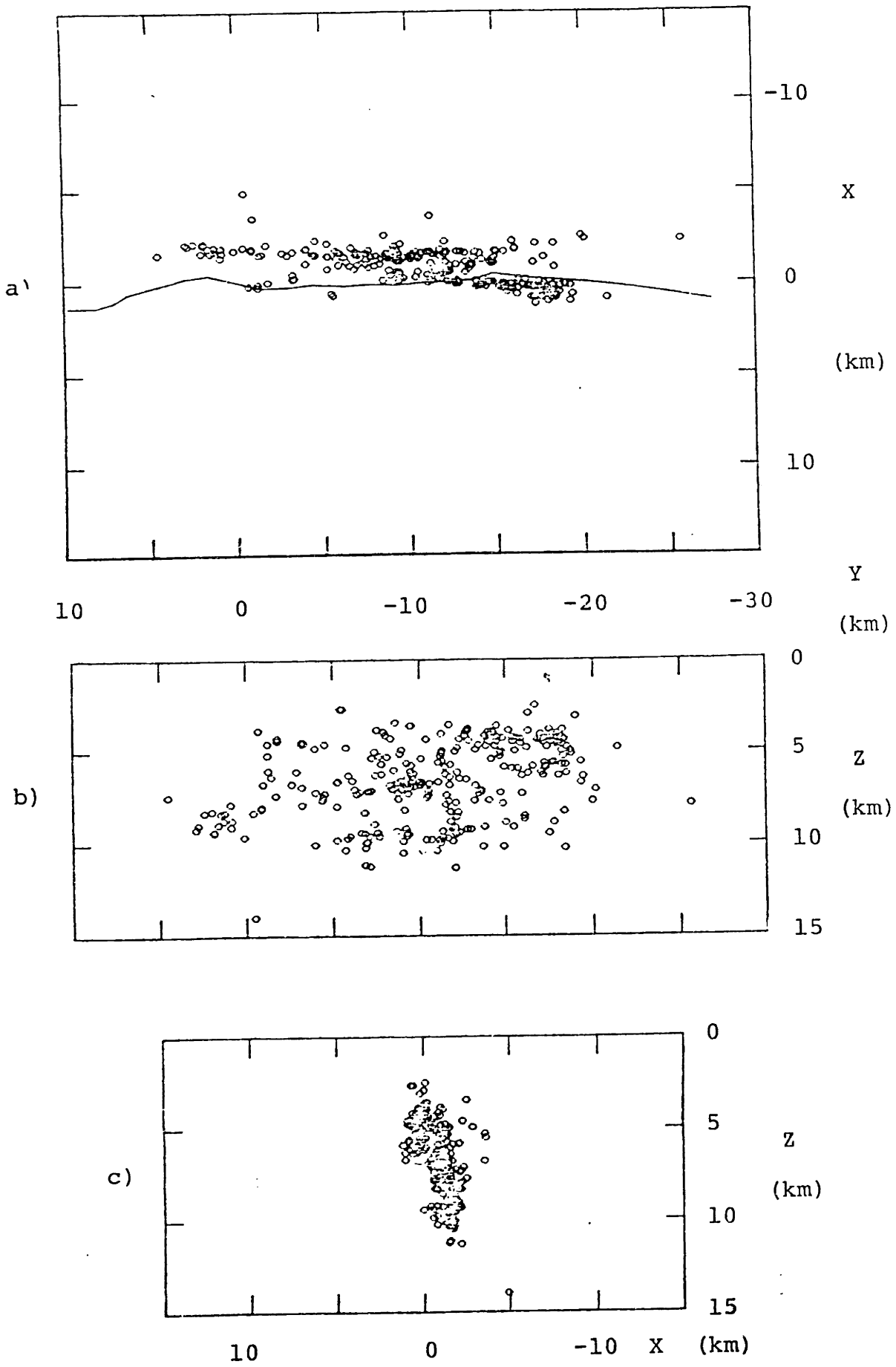

Figure 5.4

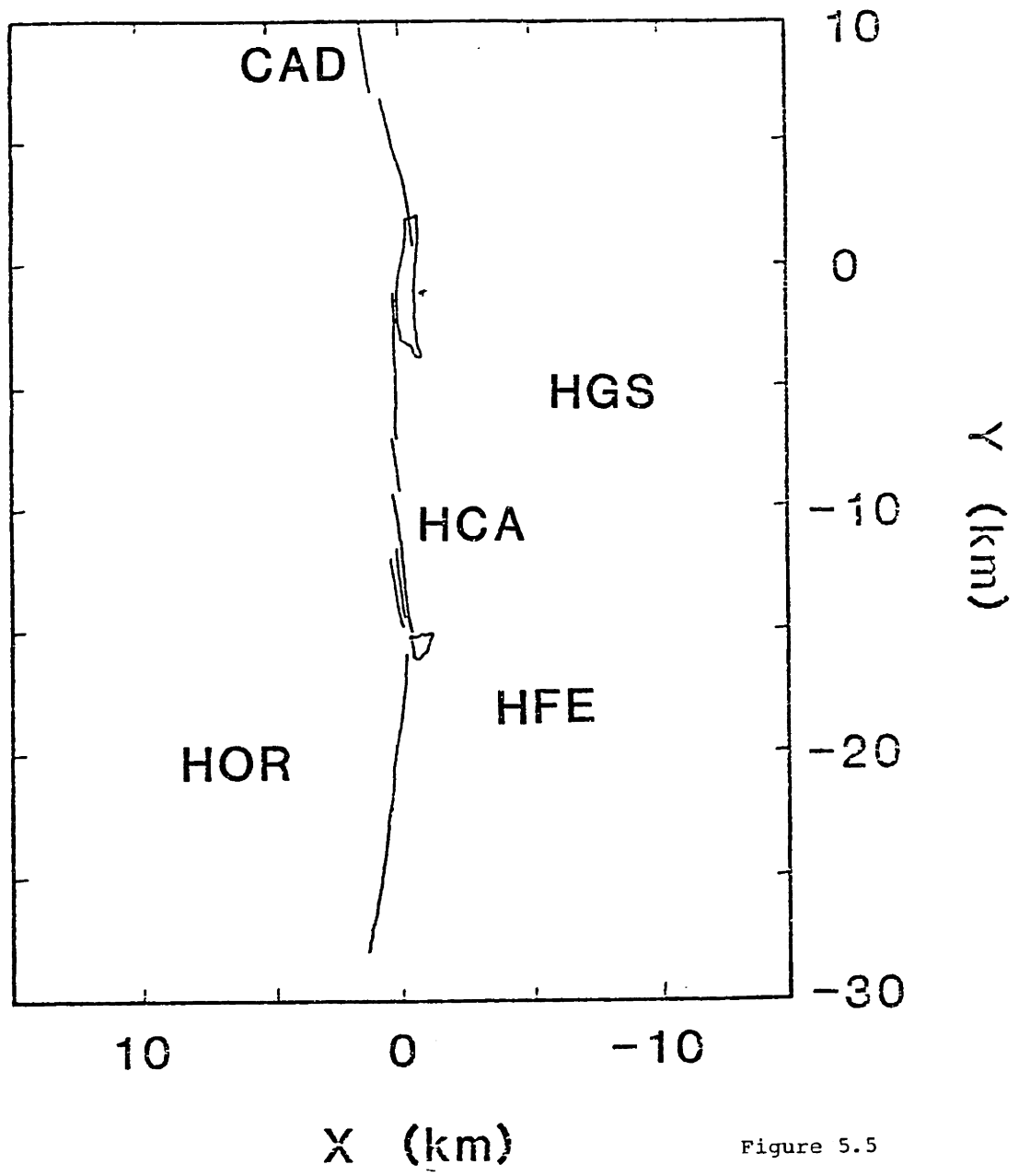

Figure 5.5

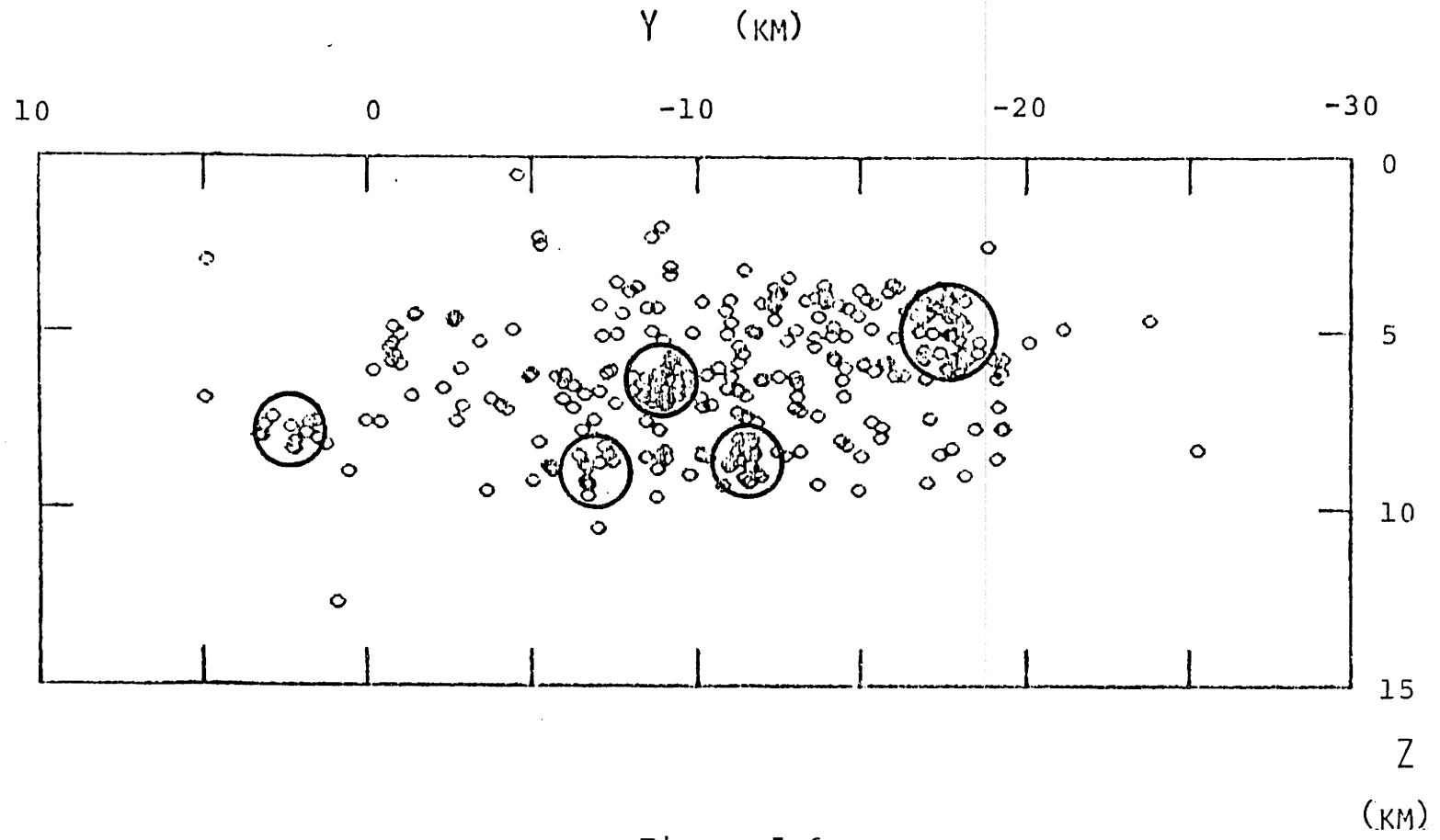

Figure 5.6

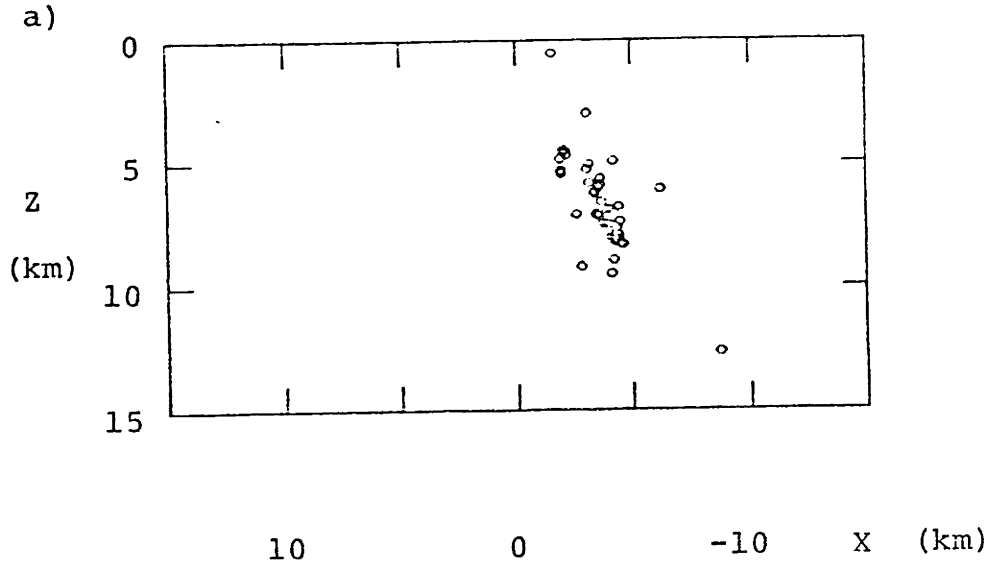

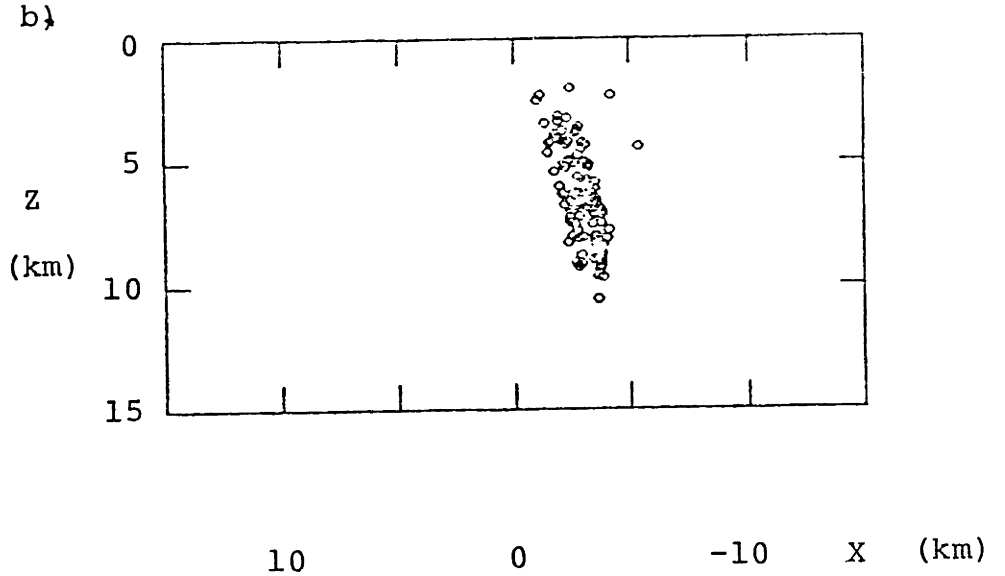

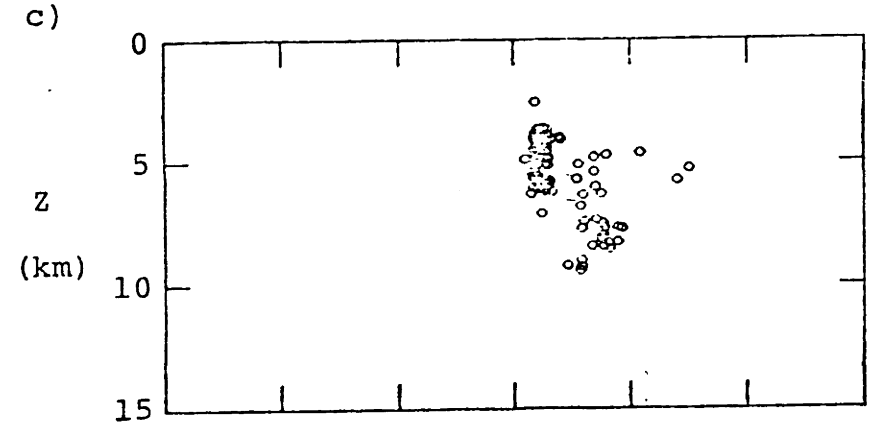

Figure 5.7

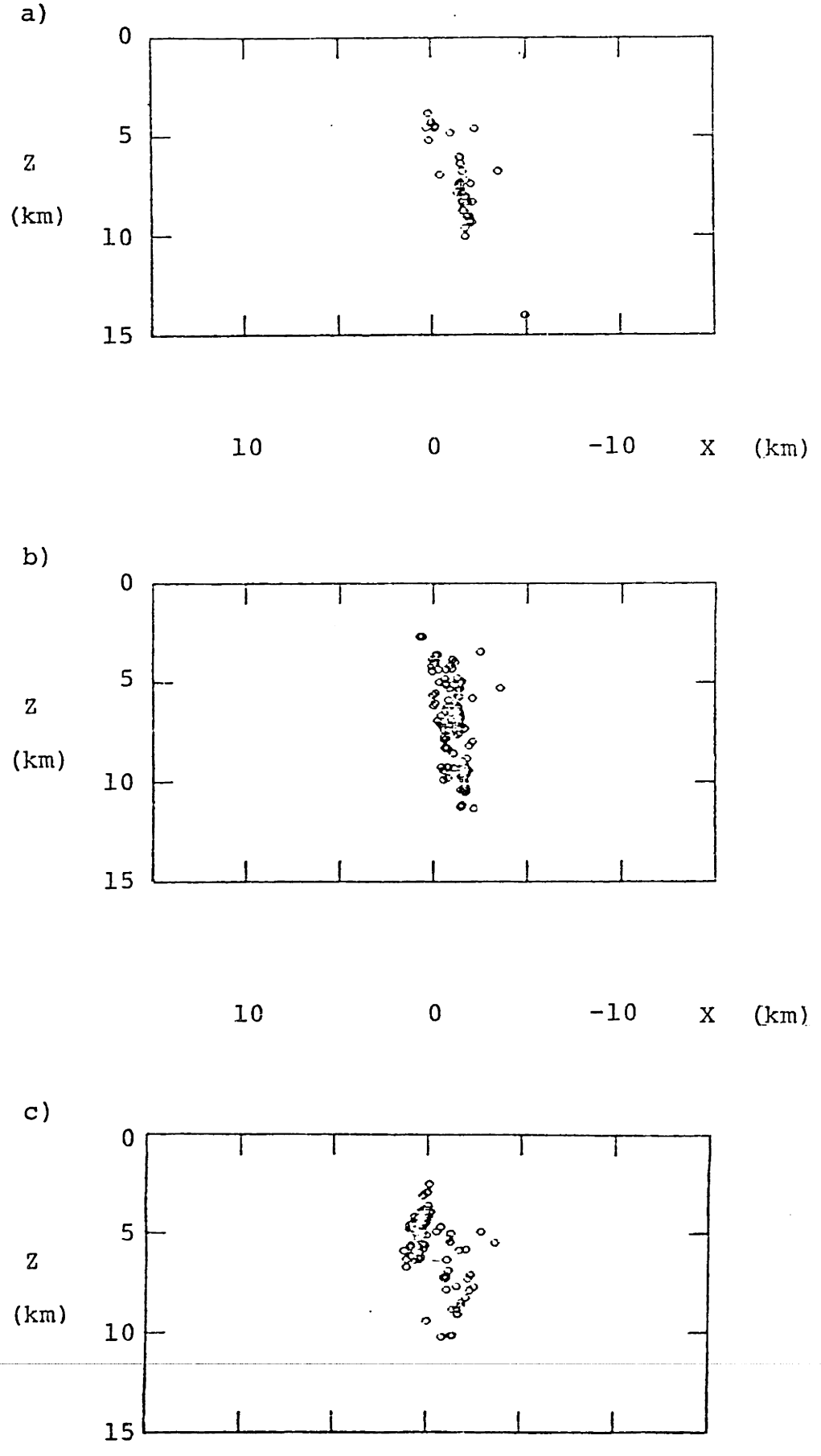

Figure 5.8

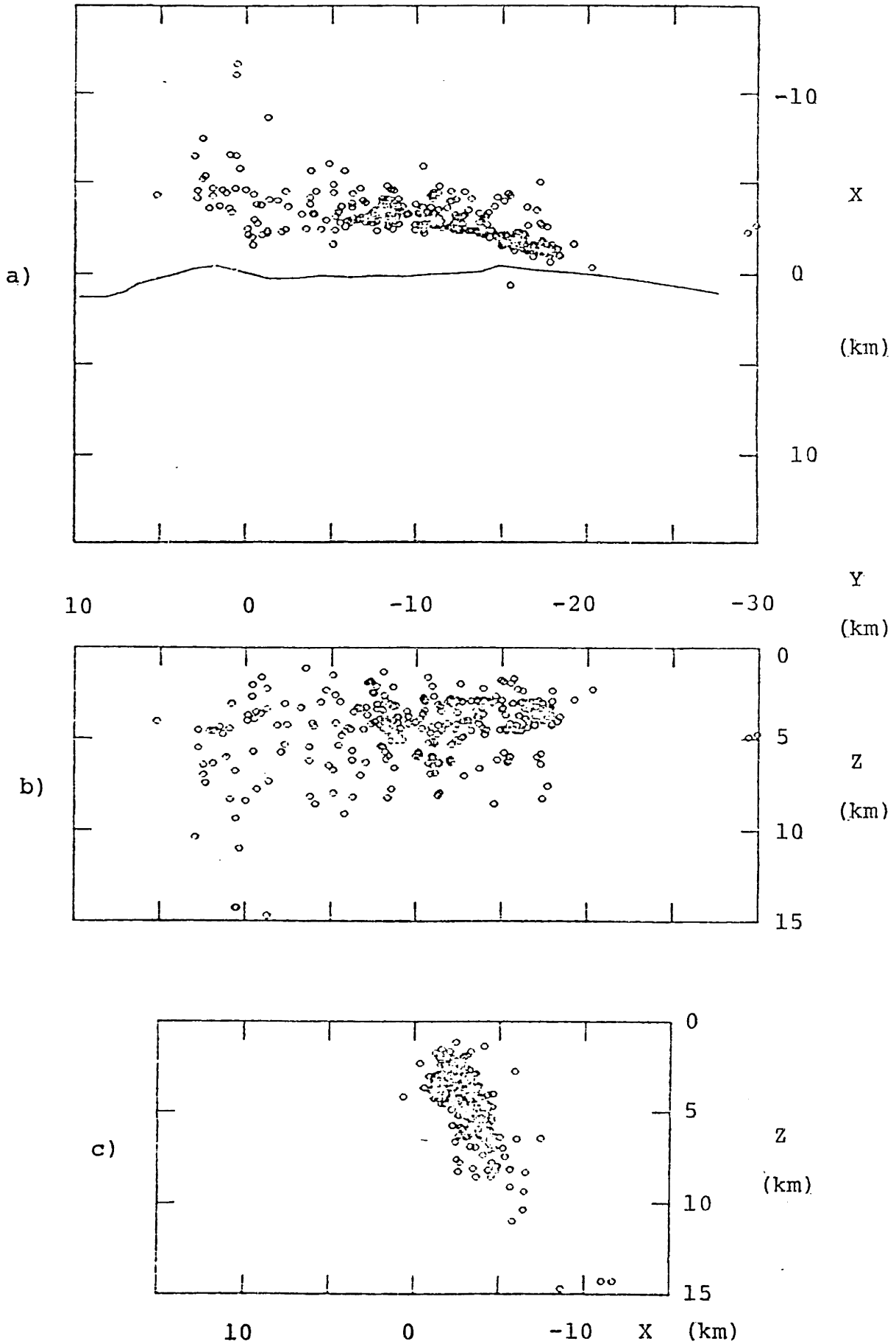

Figure 5.9

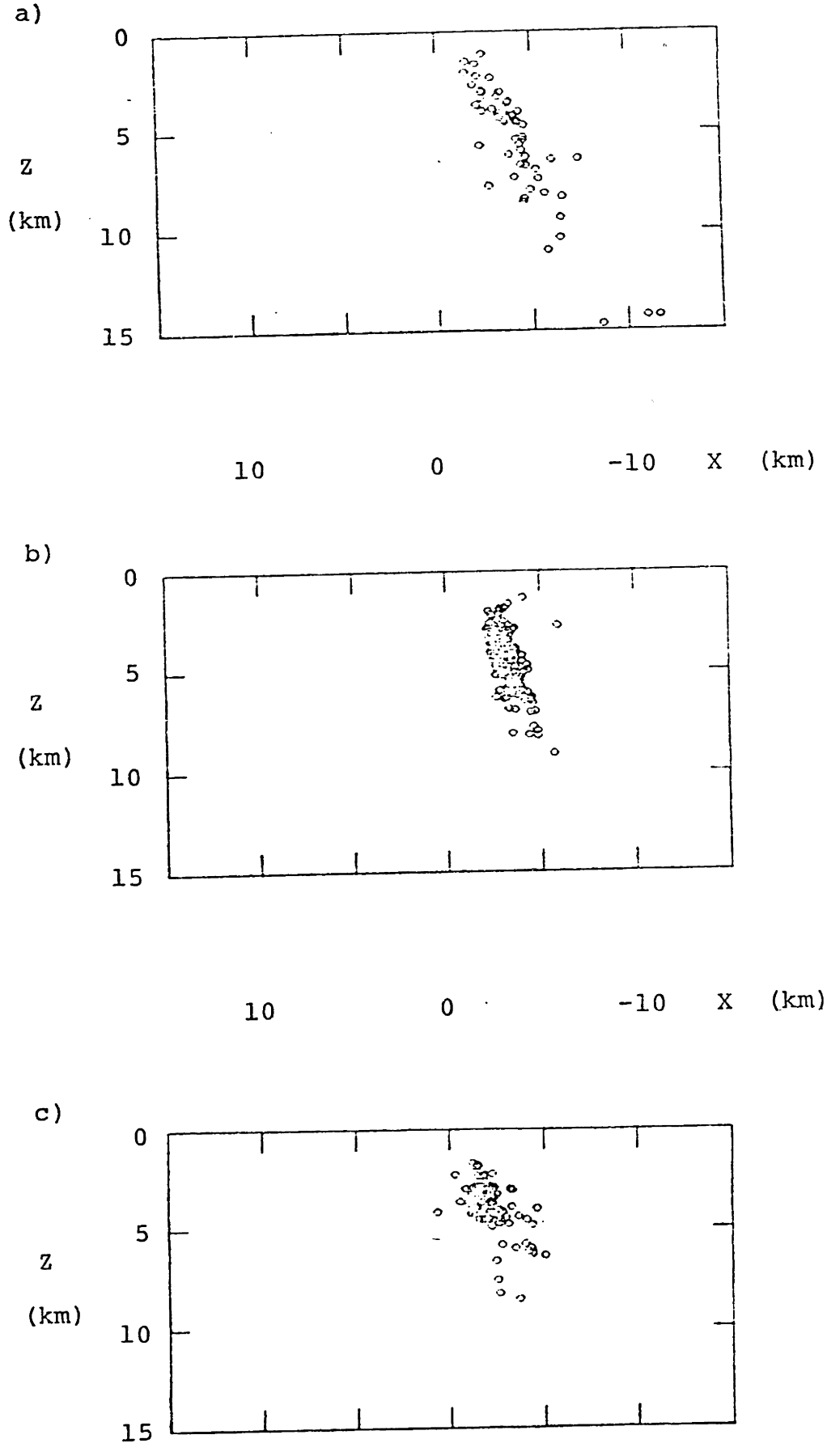

Figure 5.10

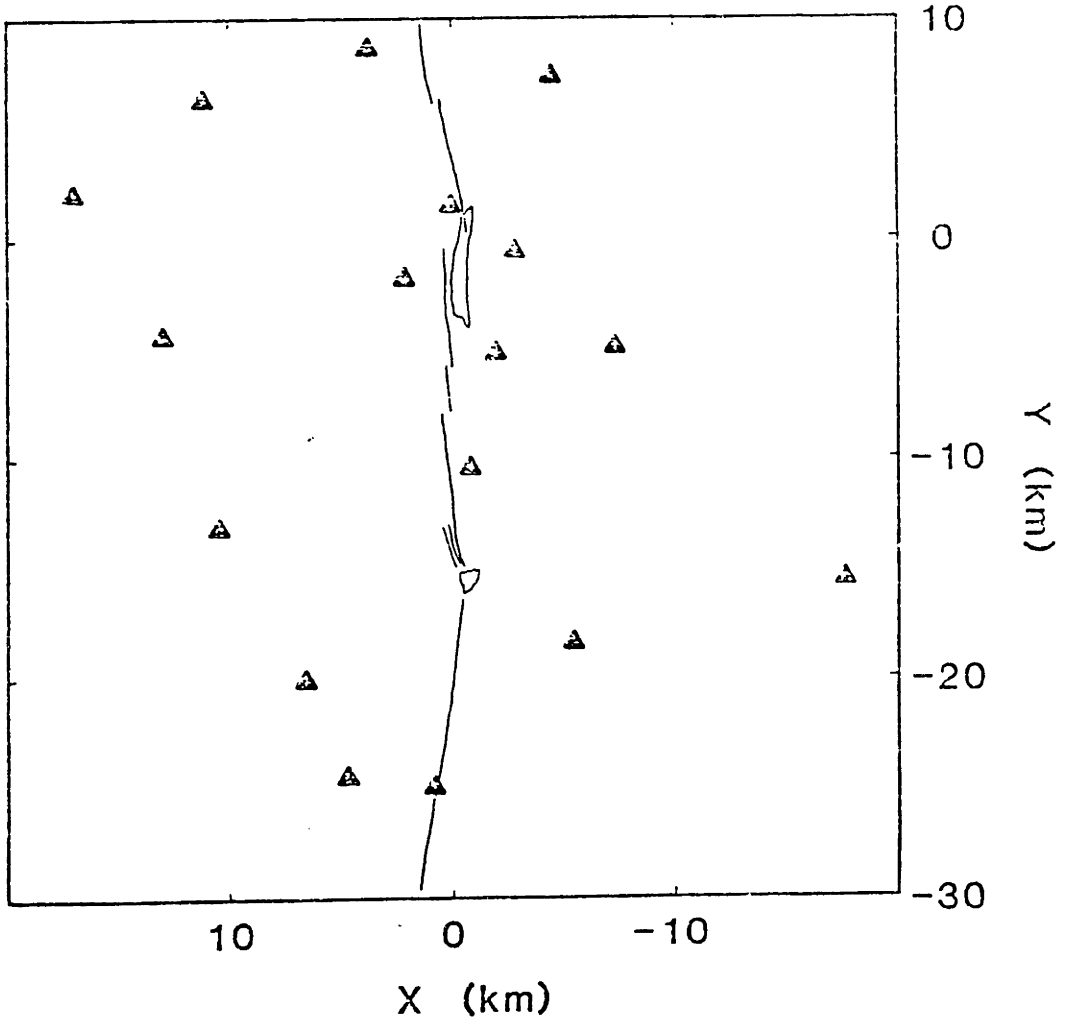

Figure 5.11

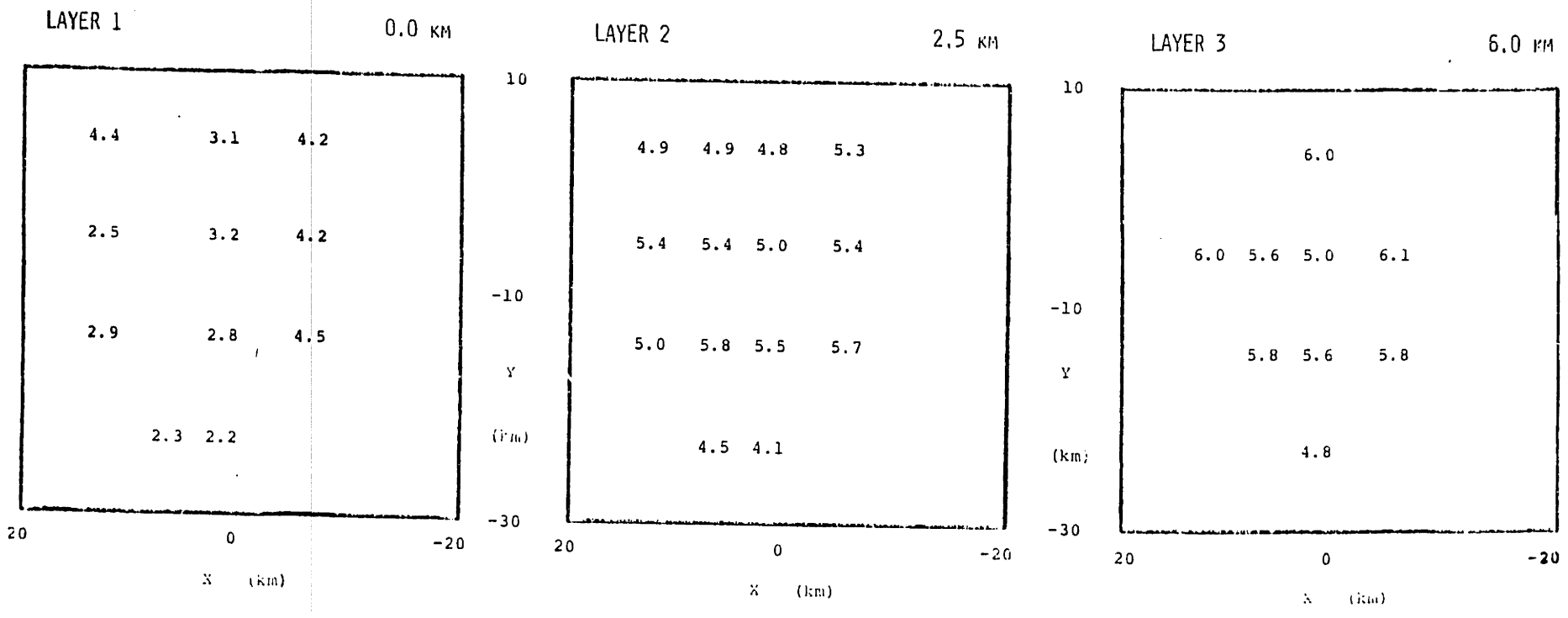
LAYER 1
0.0 KM
4.4 3.1 4.2
2.5 3.2 4.2
2.9 2.8 4.5
2.3 2.2
10
-10
-30
Y
(km)
20
0
-20
X (km)
LAYER 2
2.5 KM
4.9 4.9 4.8 5.3
5.4 5.4 5.0 5.4
5.0 5.8 5.5 5.7
4.5 4.1
10
-10
-30
Y
20
0
-20
X (km)
LAYER 3
6.0 KM
6.0
6.0 5.6 5.0 6.1
5.8 5.6 5.8
4.8
10
-10
-30
Y
(km)
20
0
-20
X (km)

Figure 5.12

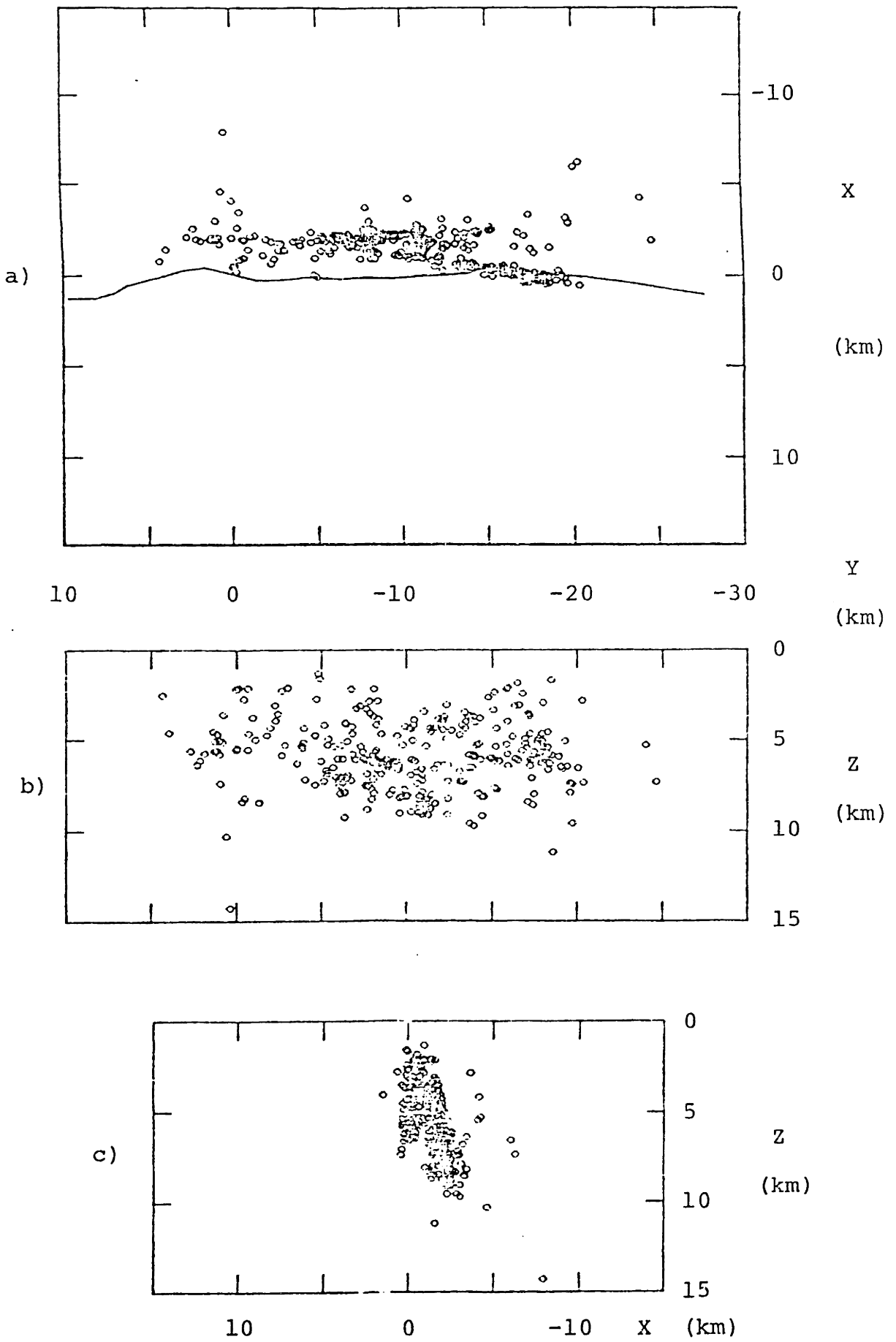

Figure 5.13

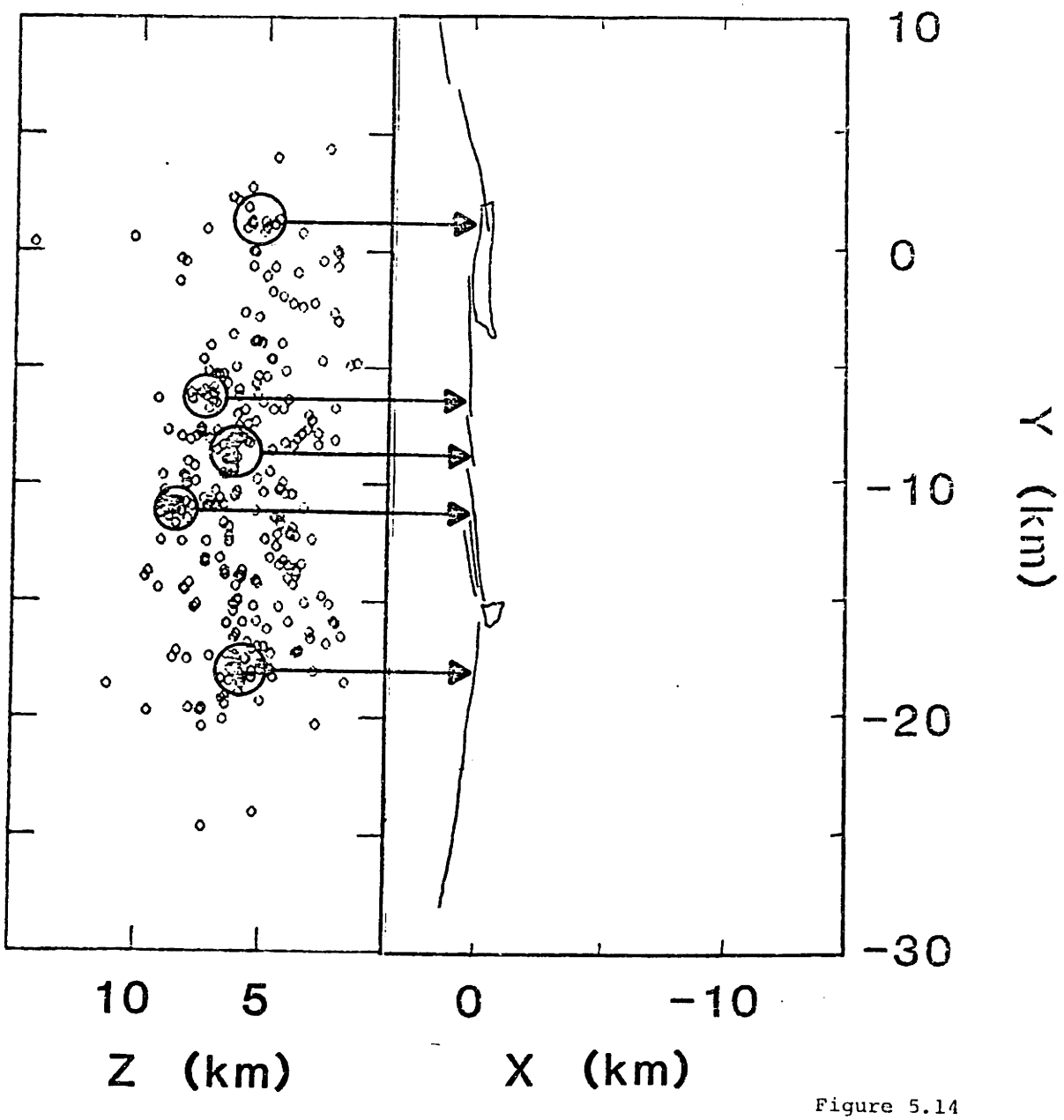

Figure 5.14

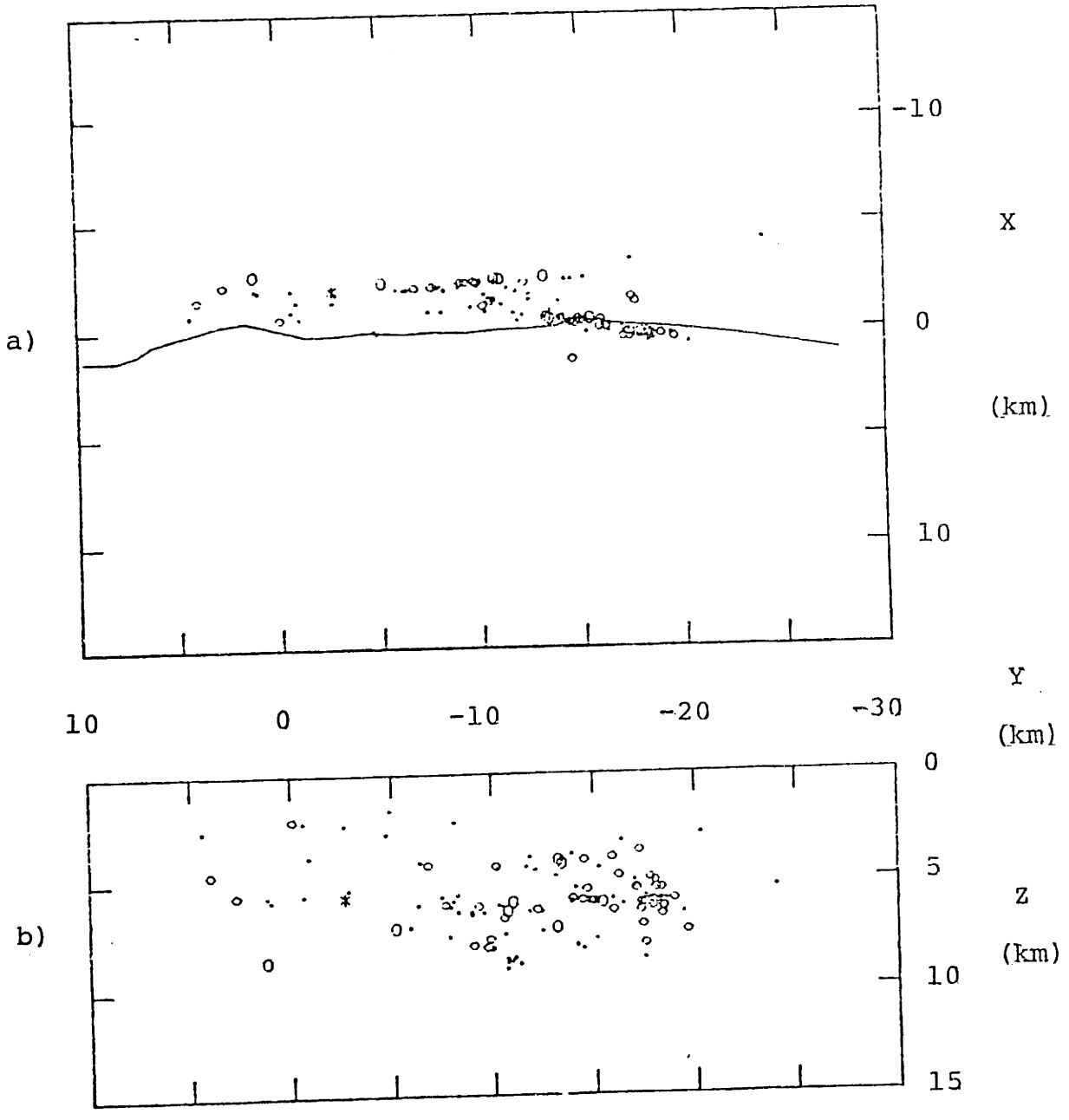

Figure 5.15

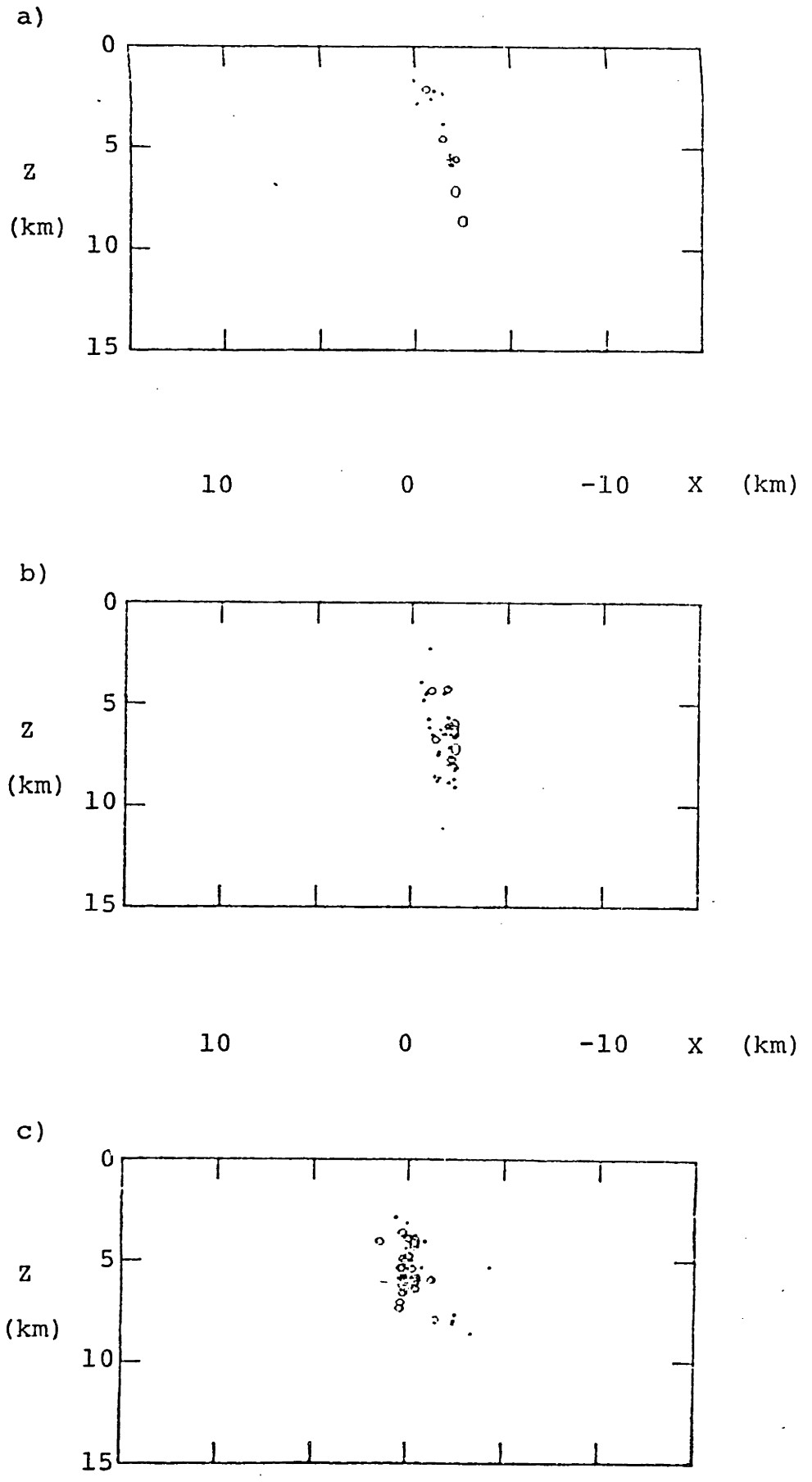

Figure 5.16

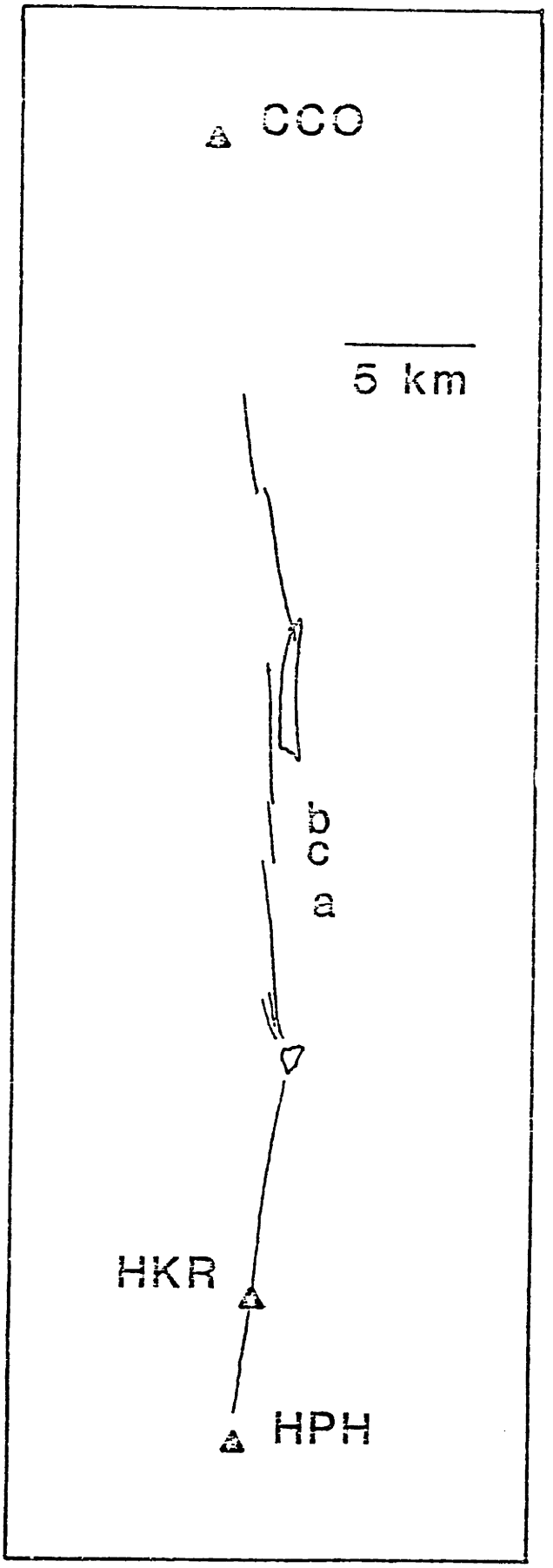

Figure 5.17

a) 0806 1722

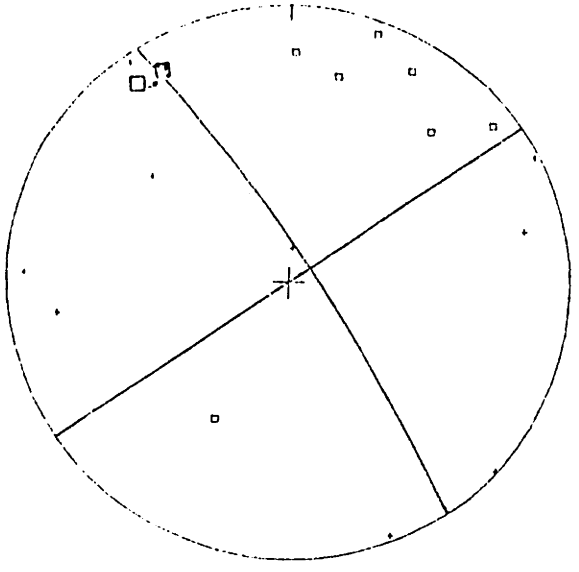

b) 0903 0640

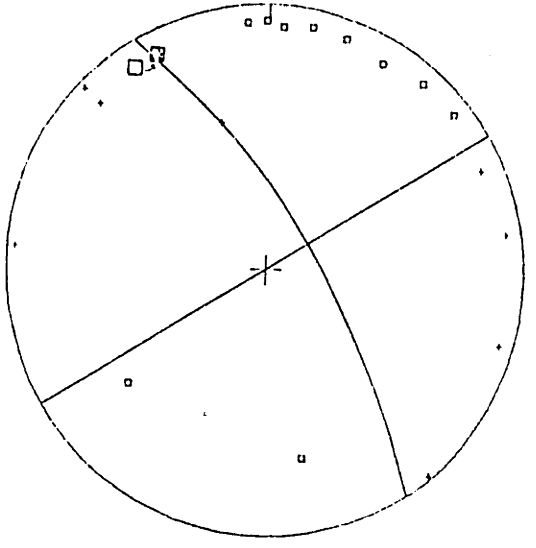

c) 0807 0556

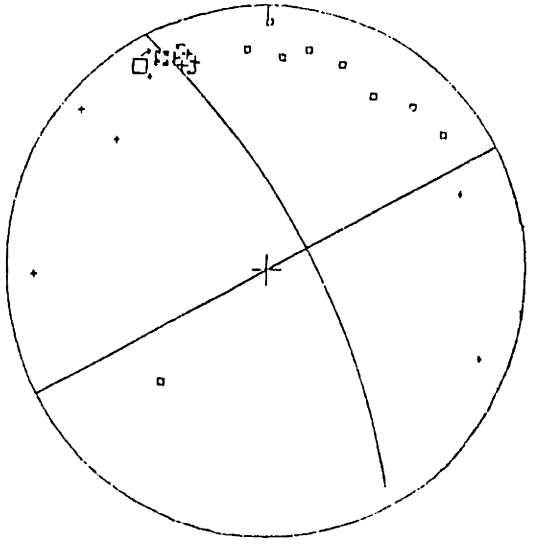

+ =compression
□ =dilatation

Figure 5.18

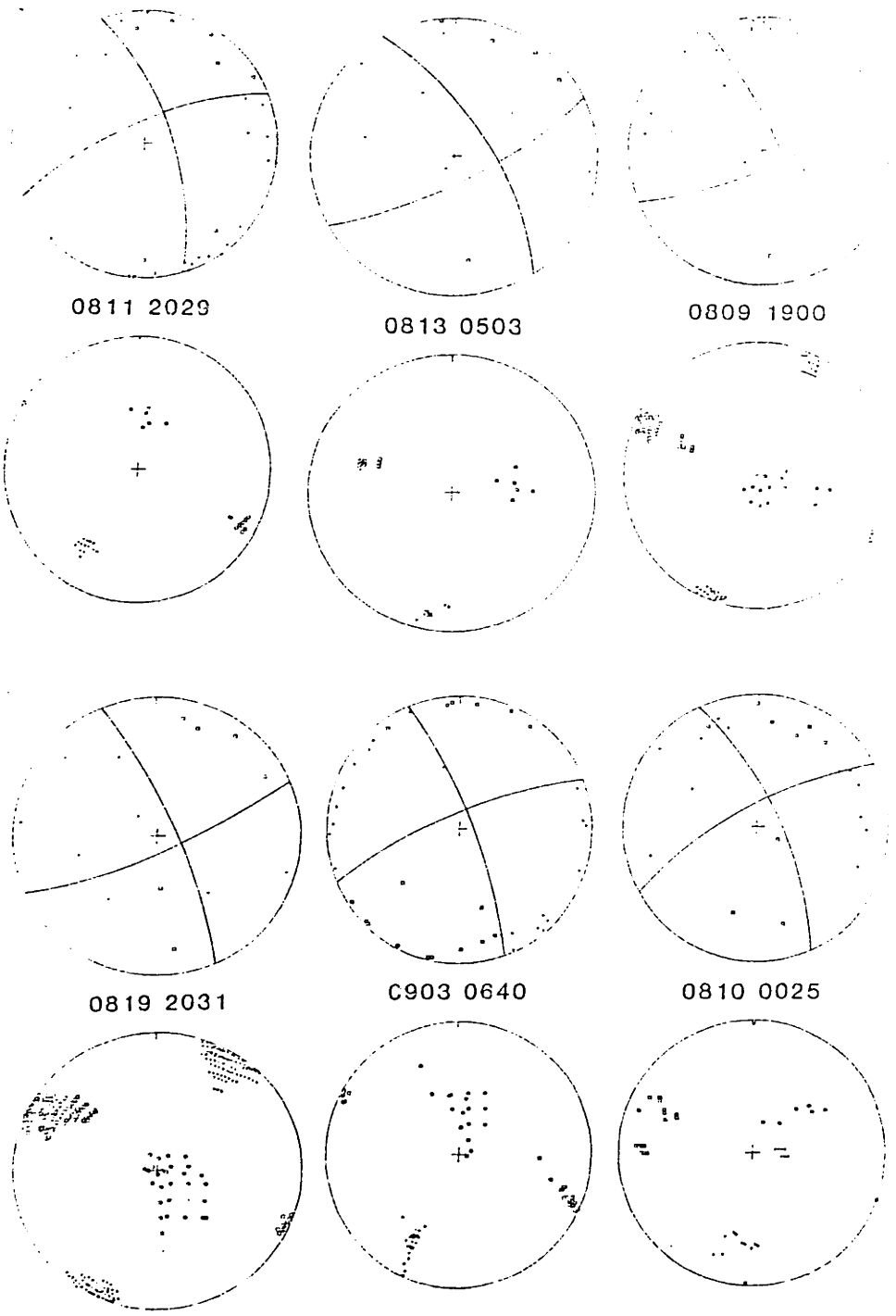

Figure 5.19

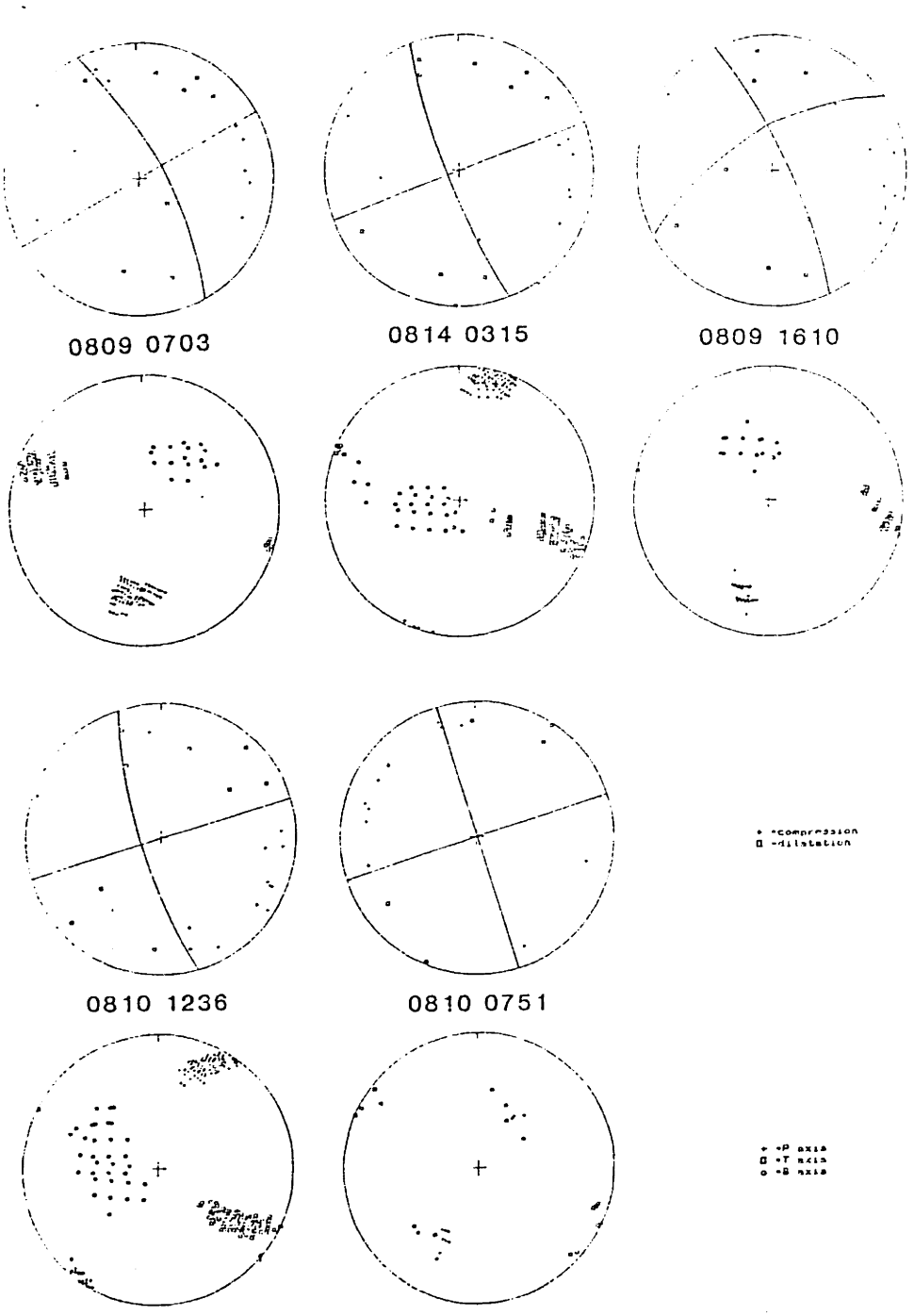

Figure 5.19 (cont.)

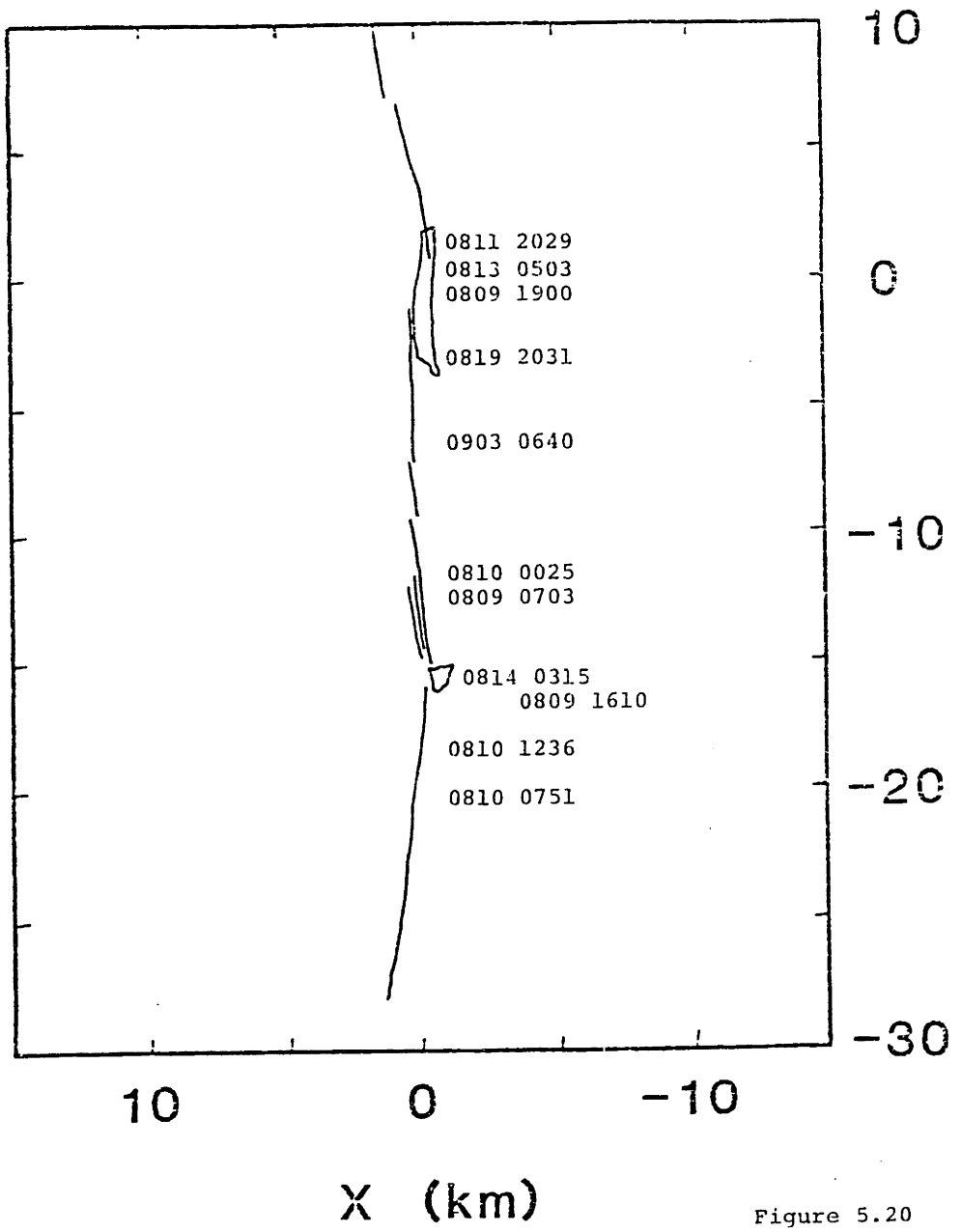
0811 2029
0813 0503
0809 1900
0819 2031
0903 0640
0810 0025
0809 0703
0814 0315
0809 1610
0810 1236
0810 0751
10
0
-10
-20
-30
10
0
-10
X (km)
Y (km)

Figure 5.20

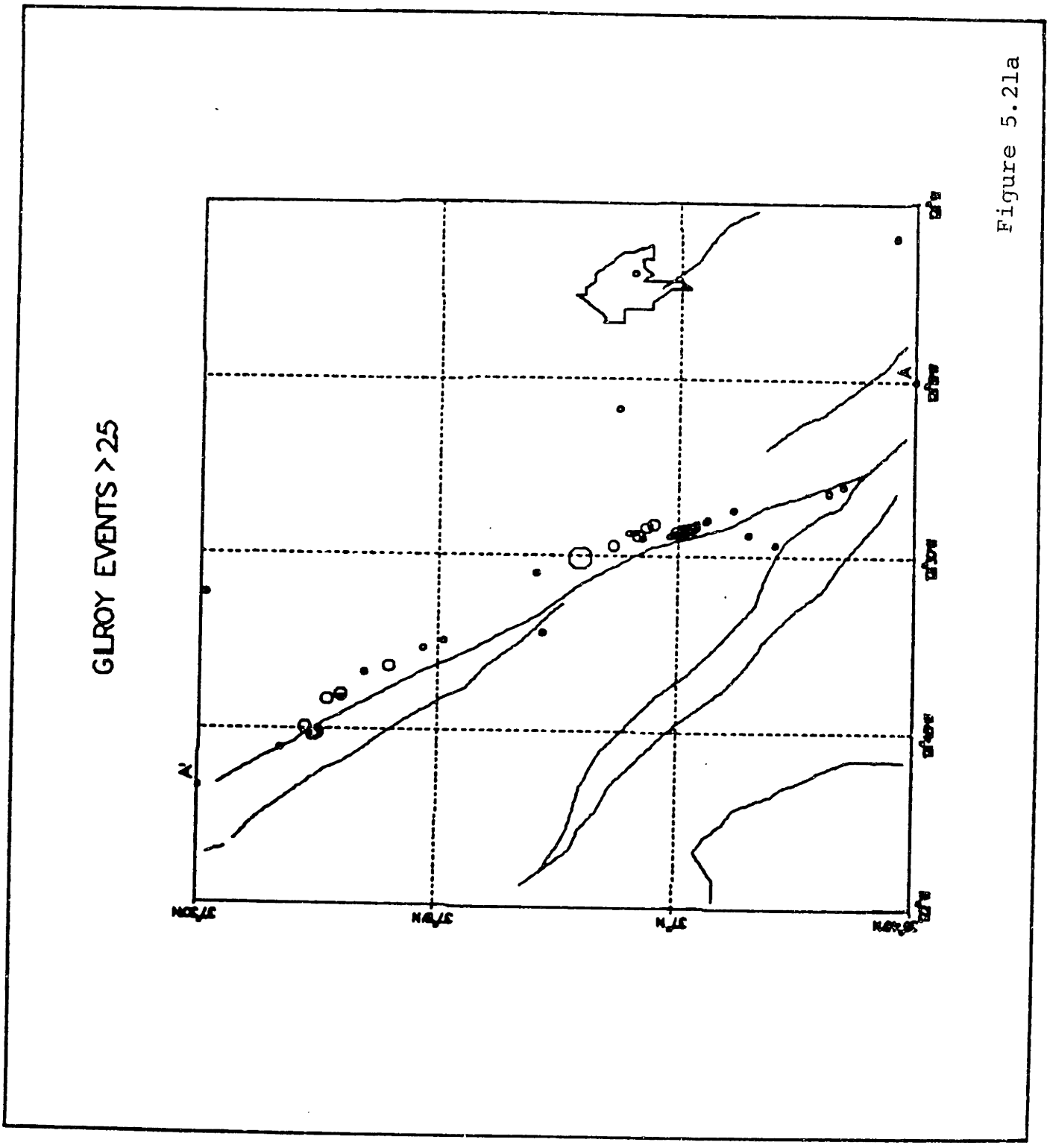

Figure 5.21a

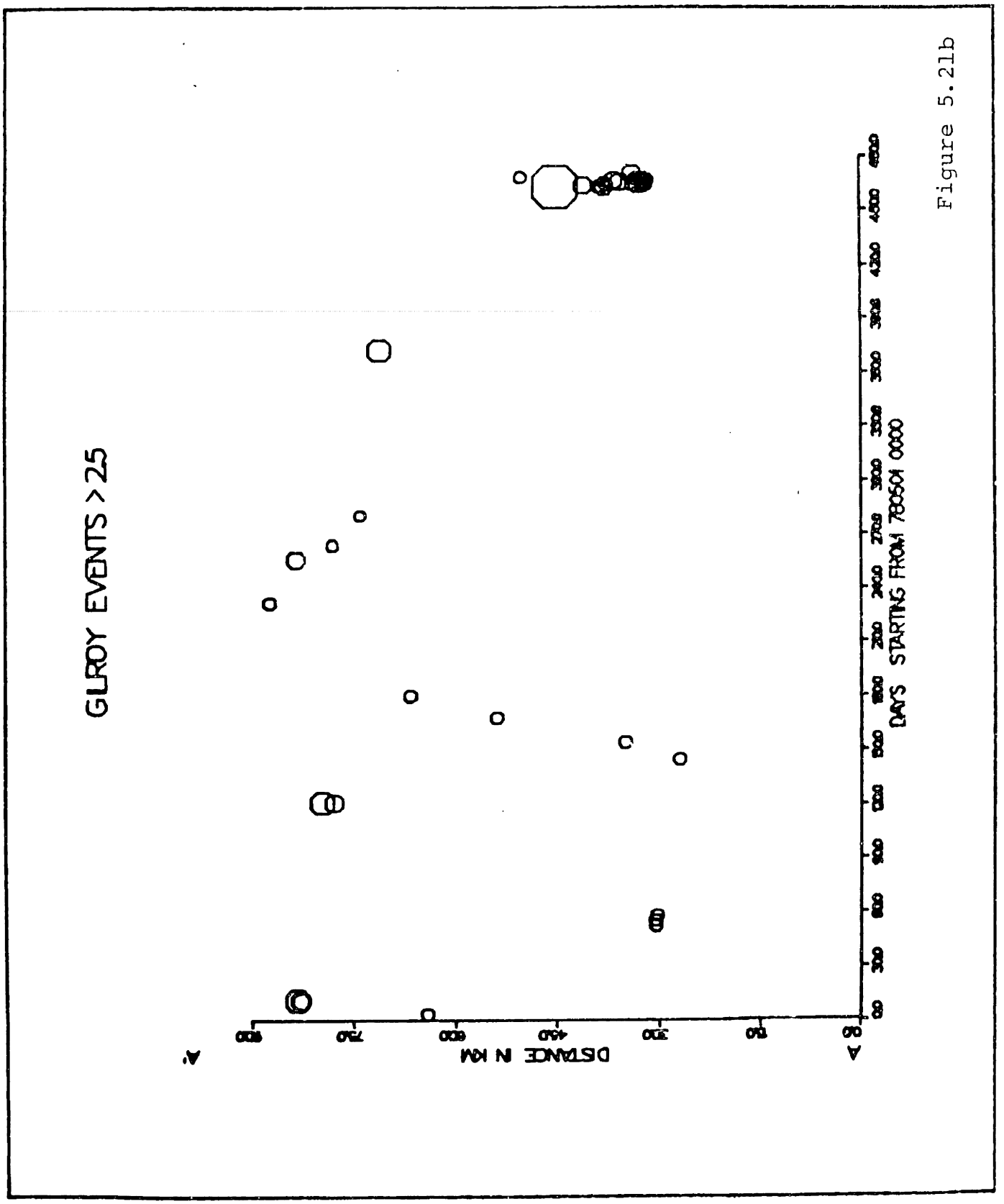
GLROY EVENTS > 25
DISTANCE IN KM
DAYS STARTING FROM 780501 0000
A
A'

Figure 5.21b

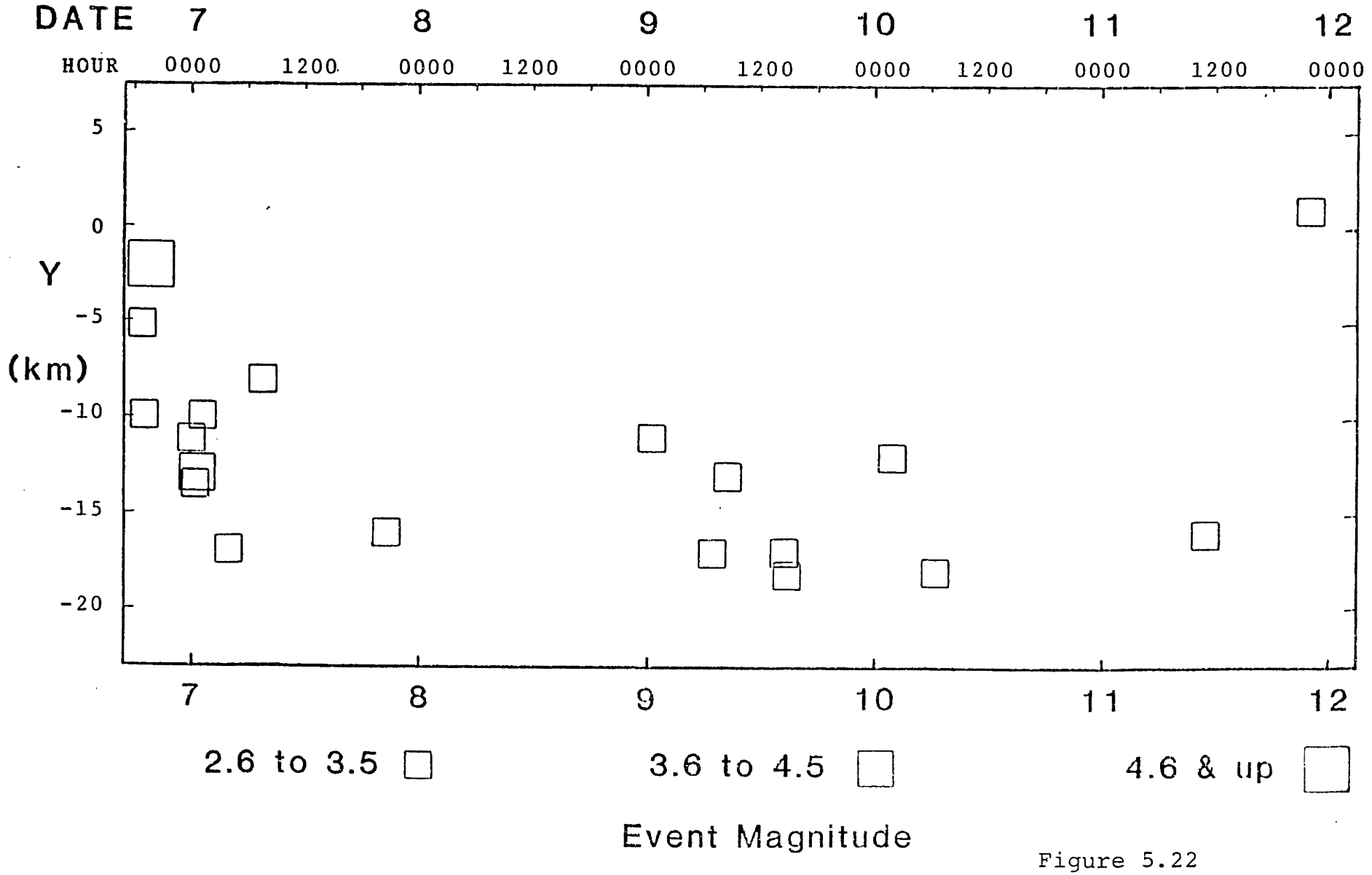
DATE 7 8 9 10 11 12
HOUR 0000 1200 0000 1200 0000 1200 0000 1200 0000 1200 0000
5
0
Y
-5
(km)
-10
-15
-20
7 8 9 10 11 12
2.6 to 3.5
3.6 to 4.5
4.6 & up
Event Magnitude

Figure 5.22

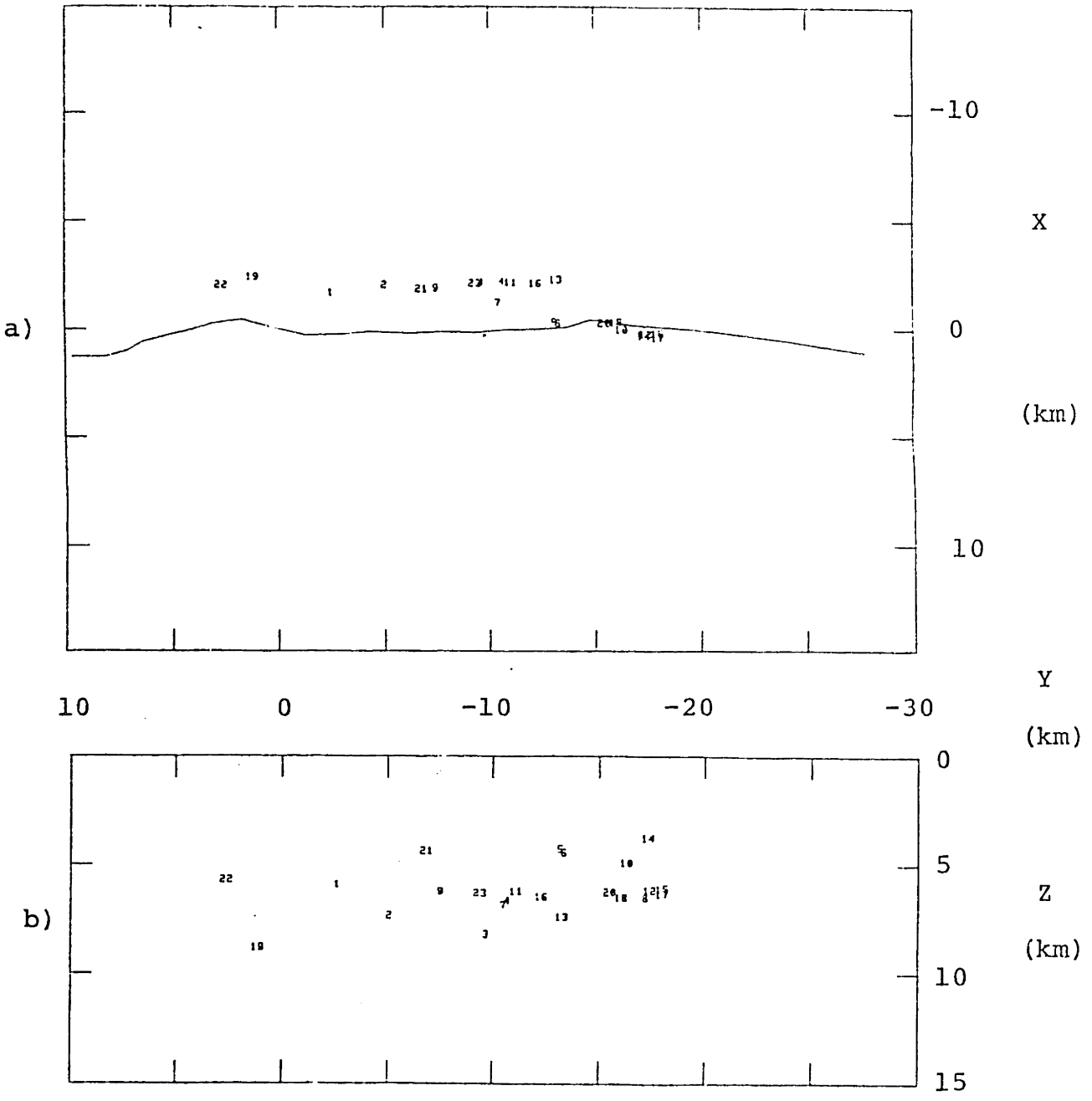

Figure 5.23

CHAPTER 6

DISCUSSION AND CONCLUSIONS

Crustal heterogeneity has been demonstrated to be the rule rather than the exception in the Coyote Lake area of central California. A number of seismological and geological questions have been answered by means of properly accounting for laterally varying crustal structure.

The method adopted for investigating the P-wave crustal velocity structure (iterative, linearized simultaneous inversion for laterally varying velocities and earthquake locations using local earthquake arrival time data) has been formally developed in Chapter 2. The approach taken is conceptually similar to that of Aki and Lee (1976) and Crosson (1976a). The former solved for laterally varying structure, but were restricted to a single-step solution. The latter incorporated an iterative solution, but was restricted to laterally homogeneous structure (i.e. a layered earth model). To combine these two desirable features, iterative solution and laterally varying structure, two recent practical developments have been utilized. One is parameter separation (Pavlis and Booker, 1980; Spencer and Gubbins, 1980), which facilitates the inclusion of the large amounts of data needed for resolving the velocity structure in three dimensions. The other is approximate ray tracing (Thurber and Ellsworth, 1980; this

work; also Horie, 1980), which permits the rapid calculation of travel time estimates in a laterally heterogeneous velocity structure.

In Chapter 3, numerical experiments simulating the analysis of real data have yielded some insight into the limitations of the inversion method. First, empirical estimates of the linear range of the inversion with respect to perturbation of the model parameters (both hypocentral and velocity model parameters) have been determined. These estimates of 3 km for hypocenter parameters and 0.5 km/sec for velocity parameters provide an important guideline for limiting the size of parameter adjustments which should be permitted at each iteration step in order to remain within the bounds of the linear approximation. Second, it has been demonstrated that approximate ray tracing (ART) can be successfully used to carry out all the required computations in the inversion problem. One can derive suitable estimates of travel times and partial derivatives (with respect to hypocentral and velocity model parameters) using ART. Tests using artificially generated data have also shown that the substitution of ART for true ray tracing does not significantly affect the results of an inversion. Finally, the resolution and error measures have been studied, again employing artificial data. It is found that these measures can not be used to assess the accuracy of individual parameter values, but rather they can provide an estimate of the average quality of a solution as a whole.

A thorough study of the structure of the crust and the locations of earthquakes in the Coyote Lake area has been presented in Chapter 4. Traditional methods for the analysis of travel time data reveal the basic character of the velocity structure (through layered earth models) and deliniate specific areas of anomalous velocity (through travel time plots and station corrections). With these qualitative results as a guide, quantitative models have been derived for the laterally varying crustal structure along with improved estimates of earthquake locations using the method of simultaneous inversion.

One of the most salient results of the inversions is the tendency for relocated epicenters to move much closer to the mapped fault traces. This trend is most evident along the San Andreas fault, where the relatively dense station distribution probably results in better-constrained hypocenter locations. Events near and north of the Coyote Lake earthquake generally do not follow this trend, however. This general improvement in the agreement between the locations of epicenters and the corresponding fault traces is directly attributable to the explicit modeling of laterally varying crustal structure (see also Engdahl and Lee, 1976).

The velocity models derived from the inversions provide a consistent picture of the upper crustal structure in the Coyote Lake area. The results have been shown to be insensitive to the particular starting model, and also to

the placement of the velocity grid points in the model. Information from geology, gravity and magnetic studies aid the interpretation of the seismic velocities.

The most extreme lateral variations in velocity are associated with a wedge of low velocity located between the San Andreas fault and the southern extension of the Calaveras fault. The position of the wedge coincides with a strong gravity low and a strong magnetic high. This zone has been interpreted to be composed primarily of a few kilometers of fault gouge overlying serpentinite, which extends to a depth of as much as 10 km. The wedge divides and extends northwestward along both the San Andreas and Calaveras faults. Along the San Andreas, the wedge appears to terminate at roughly the same point that the fault becomes seismically quiet (and where fault creep stops). Allen (1968) and Irwin and Barnes (1975) discuss the possible relation between fault creep and the presence of serpentinite (which may act as a lubricant for fault slip). The evidence for a direct relationship is suggestive but not conclusive.

The wedge along the Calaveras fault appears to terminate near the intersection of the Busch and Calaveras faults. There is no evidence for a substantial low velocity serpentinite wedge along the aftershock zone of the Coyote Lake earthquake, although certainly a very narrow zone would not be resolved by these models. The gravity and magnetic data also show no evidence for serpentinite in this area.

The pattern of seismicity in the eight years preceding the Coyote Lake event suggests a relationship between fault behavior and rock type for this part of the Calaveras fault. Figure 6.1 a to e show the distribution of seismicity in the Gilroy area for two-year intervals beginning in 1971 (see Figure 6.1f for identification of faults, etc.). The rate of activity along the creeping part of the San Andreas (indicated in Figure 6.1 f) is relatively constant compared to the dramatic increase in seismicity observed along the Calaveras in 1979, due of course to the Coyote Lake sequence. In addition there is marginal evidence from geodetic data that creep halted on at least the southern part of the rupture zone for a year preceding the Coyote Lake event (King et al., 1981). Thus this section of the Calaveras may be a small scale analogue of the locked portions of the San Andreas fault, with a cycle of quiescence, then increased seismic activity north and south of a locked section of the fault, and finally a large earthquake. We would expect this section of the fault to return to a state of relative quiescence in the near future, if indeed such a cycle exists. Other sections of the Calaveras fault should be studied to test the hypothesis that episodic seismicity is related to the absence of serpentinite.

Other structural features can be identified in the crustal velocity models for the Coyote Lake area. The near surface velocities correlate well with the surface geology.

In particular, high velocities are associated with exposed Franciscan terrain and Gabilan granites, and low velocities with sediments and alluvium in the Santa Clara Valley and the Santa Cruz basin. At depth the correlations are equally strong. High velocities persist beneath the areas of exposed granites and Franciscan. Apparent basement downfaulting between the San Andreas and Vergeles faults is reflected by locally lower seismic velocity. Finally northeast of the Calaveras fault, where Franciscan is the predominant rock type, the velocity structure, gravity and magnetic anomalies are all relatively featureless.

Chapter 5 contains a study of the aftershock sequence of the Coyote Lake earthquake. Ray tracing and simultaneous inversion methods have been utilized to study focal mechanisms and hypocenter locations of the aftershocks. It is found that the problem of reversed first-motion polarities observed at several stations along the Calaveras is lessened by accounting for the effects of heterogeneous crustal structure on the focal angles (azimuth and take-off angles at the source). The source mechanisms for aftershocks along the main rupture zone agree with the orientation of the fault as determined by both the locations of aftershocks and teleseismic body-wave analysis of the main shock (Nabelek and Toksoz, 1981). Beyond the southern end of the main rupture (i.e. south of San Felipe Lake), bifurcation of the fault is implied by the existence of two distinct zones of aftershocks characterized by different

source mechanisms. Finally, we find a strong relationship between the locations of aftershock clusters and fault discontinuities (barriers), in agreement with the work of Bakun (1980). One such barrier may be partly responsible for the complex rupture history of the Coyote Lake event as reported by Nabelek and Toksoz (1981). Another may be responsible for the termination of the main shock rupture. More detailed study of available strong motion data from the main shock may reveal further connections between the initial rupture and the clustering of aftershock activity.

In conclusion, fundamental improvements have been achieved in the method of simultaneous inversion of local earthquake P arrival time data. Application of the method to the Coyote Lake area, central California, has improved the knowledge of the structure of the crust and the locations of earthquakes in the region, and also has contributed to the understanding of the rupture process of the Coyote Lake earthquake and its aftershocks. Simultaneous inversion promises to be an increasingly valuable tool for exploring earth structure in seismically active areas.

FIGURE CAPTION

Figure 6.1 a to e) Seismicity in the Gilroy area displayed in two-year intervals starting in 1971 (Note that the 1979-1980 data are incomplete: most of the 1980 events are not included). Earthquakes with local magnitude above 1.5 are plotted. The Calaveras fault shows little seismic activity prior to the Coyote Lake sequence in 1979.

f) Faults in the area pictured in Figures 6.1 a to e

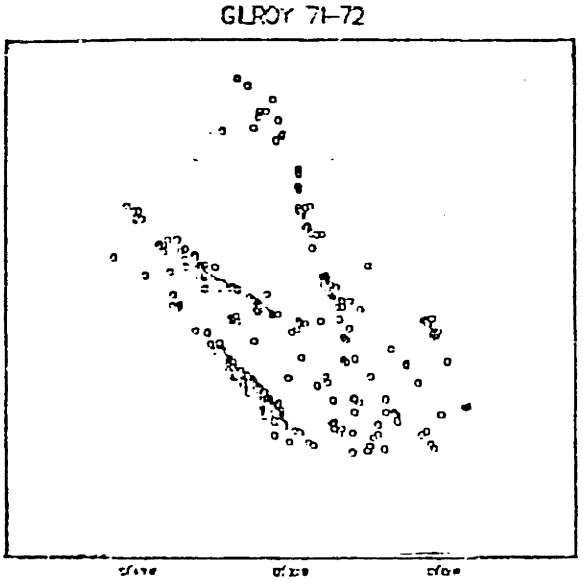
GILROY 71-72

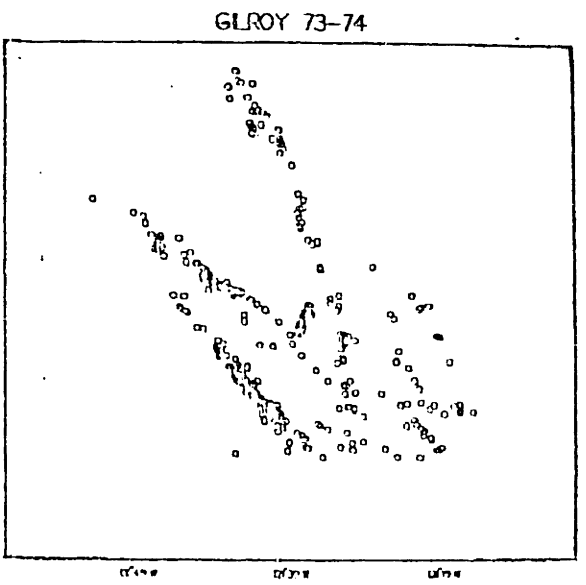
GILROY 73-74

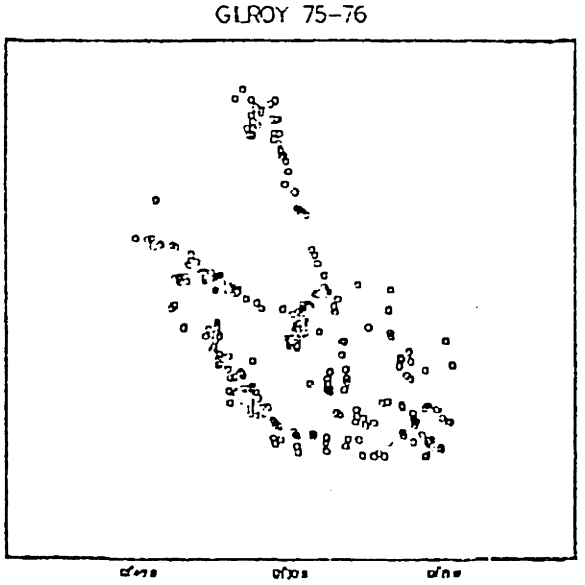
GILROY 75-76

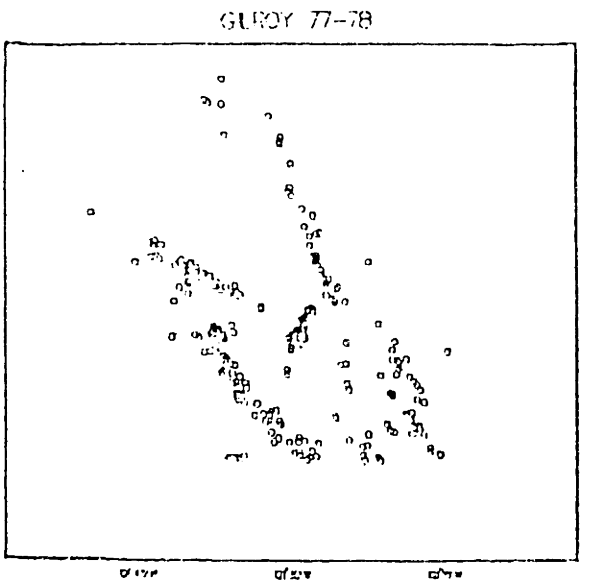
GILROY 77-78

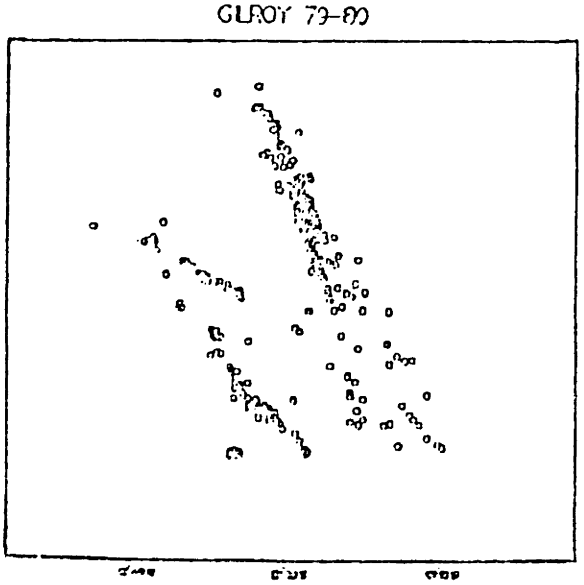
GILROY 79-80

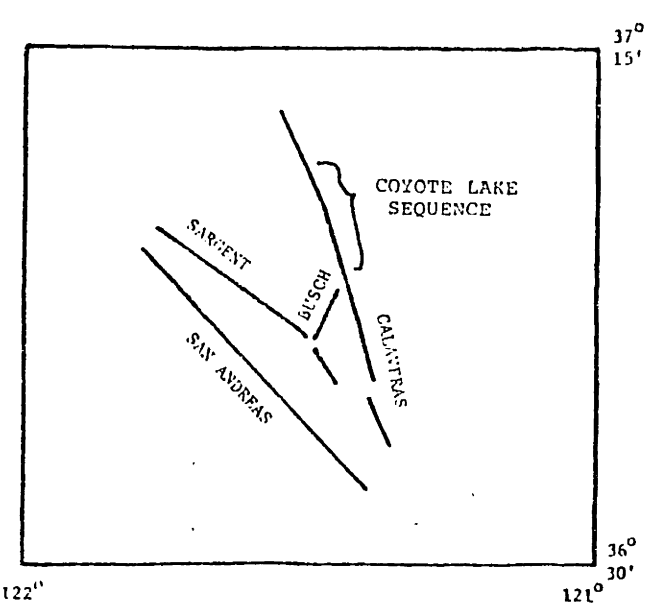
37°
15'
COYOTE LAKE
SEQUENCE
SARGENT
BUSCH
CALAVERAS
SAN ANDREAS
36°
30'
122°
121°

Figure 6.1

REFERENCES

Acton, F. S., Numerical Methods That Work, Harper and Row, New York, 541 pp., 1970.

Ahlberg, J. H., E. N. Nilson and J. L. Walsh, The theory of splines and their applications. Academic Press, New York, 284 pp., 1967.

Aki, K., A. Christoffersson and E. S. Husebye, Determination of the three-dimensional seismic structure of the lithosphere. J. Geophys. Res., 82, 277-296, 1977.

Aki, K. and W.H.K. Lee, Determination of three-dimensional velocity anomalies under a seismic array using first P arrival times from local earthquakes. 1. A Homogeneous initial model. J. Geophys. Res., 81, 4381-4399, 1976.

Allen, C. R., The tectonic environments of seismically active and inactive areas along the San Andreas fault system, in Proceedings of conference on geological problems of the San Andreas fault system, Standord Univ. Pubs., Geol. Sci., 11, 70--82, 1968.

Armstrong, R.L. and J. Suppe, Potassium-Argon geochemistry of Mesozoic igneous rocks in Nevada, Utah, and southern California. Geol. Soc. Amer. Bull., 84, 1375-1392, 1973.

Atwater, T., Implications of plate tectonics for Cenozoic evolution of western North America. Geol. Soc. Amer. Bull., 81, 3513-3536, 1970.

Atwater, T. and P. Molnar, Relative motion of the Pacific and North American plates deduced from sea-floor spreading in the Atlantic, Indian, and South Pacific Oceans. In Conference on tectonic problems of the San Andreas fault system, Proc., Stanford Univ. Pubs., Geol. Sci. 13, 136-148, 1973.

Backus, G.E. and F. Gilbert, The resolving power of gross Earth data. GJRAS, 16, 169-205, 1968.

Bailey, E.H. and M.C. Blake, Jr., Late Mesozoic tectonic development of western California. Geotectonics, 3, 148-154, 1969a.

Bailey, E.H. and M.C. Blake, Jr., Tectonic development of western California in the Late Mesozoic. Geotectonics, 4, 225-230, 1969b.

Bailey, E.H., M.C. Blake, Jr. and D.L. Jones, On-land Mesozoic oceanic crust in California Coast Ranges. U.S. Geol. Survey Prof. Paper 770-C, C70-C81, 1970.

Bakun, W. H., Seismic activity on the sourthern Calaveras fault in central California. Bull. Seim. Soc. Am., 70, 1181, 1197, 1980.

Bakun, W. H., R. M. Stewart, C. Gl Bufe and S. M. Marks, Implication of seismicity for failure of a section of the San Andreas fault, Bull. Seism. Soc. Am. 70, 185-201, 1980.

Bolt, B.A., C. Lomnitz and T.V. McEvilly, Seismological evidence on the tectonics of central and northern California and the Mendocino escarpment. BSSA, 58, 1725-1767, 1968.

Boore, D.M. and D.P. Hill, Wave propagation characteristics in the vicinity of the San Andreas fault. Stanford Univ. Publ., Univ. Ser., Geol. Sci., 13, 215-224, 1973.

Brown, R.D., Jr. and W.H.K. Lee, Active faults and preliminary earthquake epicenters (1969-1970) in the southern part of the San Francisco Bay region. U.S. Geological Survey Map MF-307, 1971.

Burchfiel, B.C. and G.A. Davis, Structural framework and evolution of the southern part of the Cordilleran orogen, western United States. Amer. J. Sci. 272, 97-118, 1972.

Burchfiel, B.C. and G.A. Davis, Nature and controls of Cordilleran orogenesis, western United States: Extensions of an earlier synthesis. Amer. J. Sci., 275-A, 363-396, 1975.

Cerveny, V., I.A. Molotkov and I. Psencik, Ray Method in Seismology, Univerzita Karlova, Prague, 214 pp., 1977.

Chou, C.W. and J.R. Booker, A Backus-Gilbert approach to inversion of travel-time data for three-dimensional velocity structure. GJRAS, 59, 325-344, 1979.

Christensen, N.I., Ophiolites, seismic velocities and oceanic crustal structure. Tectonophysics, 47, 131-157, 1978.

Clark, J.C. and J.D. Rietman, Oligocene stratigraphy, tectonics, and paleogeography southwest of the San

Andreas fault, Santa Cruz Mountains, and Gabilan Range, California Coast Ranges. U.S. Geological Survey Professional Paper 783, 18 pp., 1973.

Cline, A.K., Scalar- and planar-valued curve fitting using splines under tension. Numer. Math., 17, 218-220, 1974.

Coney, P.J., Cordilleran tectonics and North American plate motion. Amer. J. Sci., 272, 603-628, 1972.

Cowan, D.S., Deformation and metamorphism of the Franciscan subduction zone complex northwest of Pacheco Pass, California. Geol. Soc. Amer. Bull., 85, 1623-1634, 1974.

Crosson, R.S., Crustal structure modeling of earthquake data. 1. Simultaneous least squares estimation of hypocenter and velocity parameters. J. Geophys. Res., 81, 3036-3046, 1976a.

Crosson, R.S., Crustal structure modeling of earthqauke data. 2. Velocity structure of the Puget Sound region, Washington. J. Geophys. Res., 81, 3047-3054, 1976b.

Das, S. and K. Aki, Fault plane with barriers: A versatile earthquake model. J. Geophys. Res., 82, 5658-5670, 1977.

De Groot, M.H., Probability and Statistics, Addison-Wesley, Reading, MA, 607 pp., 1975.

Drewes, H., The Cordilleran orogenic belt between Nevada and Chihuahua. Geol. Soc. Amer. Bull., 89, 641-657, 1978.

Eaton, J. P., M. E. O'Neill and J. N. Murdock, Aftershocks of the 1966 Parkfield-Chalome, California, earthquake: A detailed study. Bull. Seism. Soc. Am., 60, 1151-1197, 1970.

Ellsworth, W. L., Bear Valley, California, earthquake sequence of February-March, 1972, Bull. Seism. Soc. Am., 65, 483-506, 1975.

Ellsworth, W.L., Three-dimensional structure of the crust and mantle beneath the island of Hawaii, Ph.D. thesis, Department of Earth and Planetary Sciences, M.I.T., Cambridge, MA, 327 pp., 1977.

Engdahl, E.R. and W.H.K. Lee, Relocation of local earthquakes by seismic ray tracing. J. Geophys. Res., 81, 4400-4406, 1976.

Evernden, J.F. and R.W. Kistler, Chronology of emplacement of Mesozoic batholith complexes in California and western Nevada. U.S. Geol. Survey Prof. Paper 623, 43 pp., 1970.

Franklin, J. N., Well-posed stochastic extensions of ill-posed linear problems, J. Math. Anal Appl., 31, 682-716, 1970.

Hamilton, W., Mesozoic California and the underflow of Pacific mantle. Geol. Soc. Amer. Bull., 80, 2409-2430, 1969.

Hamilton, R. M., Aftershocks of the Borrego Mountain earthquake from April 12 to June 12, 1968. U. S. Geological Survey Professional Paper 787, 31-54, 1972.

Hanna, W.F., R.D. Brown, Jr., D.C. Ross and A. Griscom, Aeromagnetic reconnaissance and generalized geologic map of the San Andreas fault between San Francisco and San Bernadino, California. U.S. Geological Survey Map GP-815, 1972.

Healy, J.H. and L.G. Peake, Seismic velocity structure along a section of the San Andreas fault near Bear Valley, California. Bull. Seis. Soc. Amer., 64, 1177-1197, 1975.

Hileman, J.A., Inversion of phase time for hypocenters and shallow crustal velocities, Mojave Desert, California. Bull. Seis. Soc. Am., 69, 387-396, 1979.

Horie, A. Three-dimensional seismic velocity structure beneath the Kanto district by inversion of P-wave arrival times, Ph.D. Thesis, Department of Earth Sciences, Yamagata Univ., Yamagata, Japan, 215 pp.

Irwin, W. P., and I. Barnes, Effect of geologic structure and matamorphic fluids on seismic behavior of the San Andreas fault system in central and northern California, Geology, 3, 713-716, 1975.

Jackson, D.D, The use of a priori data to resolve non-uniqueness in linear inversion, Geophys. J. R. astr. Soc. Am., 57, 137-157, 1979.

Jacob, K.H., Three-dimensional seismic ray tracing in a laterally heterogeneous spherical earth. J. Geophys. Res., 75, 6675-6689, 1970.

Julian, B.R., Ray tracing in arbitrarily heterogeneous media. Tech. Note 1970-45, Lincoln Lab, Lexington, MA, 17 pp., 1970.

Julian, B.R. and D. Gubbins, Three-dimensional seismic ray tracing. J. Geophys., 43, 95-114, 1977.

King, N. E., J. C. Savage, M. Lisowski and W. H. Prescott, Preseismic and coseismic deformation associated with the Coyote Lake, California earthquake, J. Geophys. Res., 86, 892-898, 1981.

King, P.B., The Evolution of North America (revised edition) Princeton University Press, Princeton, NJ, 197 pp., 1977.

Klein, M.V., Optics. John Wiley and Sons, New York, 647 pp., 1970.

Lanphere, M.A. and B.L. Reed, Timing of Mesozoic and Cenozoic plutonic events in circum-Pacific North America. Geol. Soc. Amer. Bull., 84, 3773-3782, 1973.

Lanczos, C., Linear Differential Operators. Van Nostrand, London, 564 pp., 1961.

Lawson, C.L. and R.J. Hanson, Solving Least Squares Problems. Prentice-Hall, Englewood Cliffs, 340 pp, 1974.

Lee, W.H.K. and J.C. Lahr, HYPO71 (Revised), A computer program for determining hypocenter, magnitude, and first motion pattern of local earthquakes, U.S. Geol. Survey Open-File Rept. 75-311, 113 pp., 1975.

Lee, W.H.K. and S.W. Stewart, Principles and applications of microearthquake networks. Advances in Geophysics, in press, 1981.

Lee, W. H. K., D. G. Herd, V. Cagnetti, W. H. Bakun and A Rapport, A preliminary study of the Coyote Lake earthquake of August 6, 1979 and its major aftershocks, U. S. Geological Survey Open-File Report, 79-162, 42 pp.

Lentini, M. and V. Pereyra, An adaptive finite difference solver for nonlinear two-point boundary value problems with mild boundary layers, SIAM J. Numer. Anal., 14, 91-111, 1977.

Lin, W. and C.-Y. Wang, P-wave velocities in rocks at high pressure and temperature and the constitution of the central California crust. Geophys. J. R. astr. Soc., 57, 137-157, 1979.

Luk, F., R. Comer and W.H.K. Lee, Solving seismic ray-tracing problems in a heterogeneous medium by a general shooting method. In preparation, 1981.

Lunenberg, R.K., Mathematical Theory of Optics, University of California Press, Berkeley, 448 pp., 1964.

Mayer-Rosa, D., Travel-time anomalies and distribution of earthquakes along the Calaveras fault zone, California. Bull. Seis. Soc. Amer., 63, 713-729, 1973.

Mooney, W.D. and J.H. Luetgert, Seismic-refraction study of the Santa Clara Valley, west-central California, EOS-Trans. AGU (abstract) 61, 1025, 1980.

Nabelek, J. and M. N. Toksoz, Teleseismic study of the Copyote Lake earthquake: A complex multiple event, IASPEI (abstract), 1981.

Officer, C.B., Introduction to the Theory of Sound Transmission, McGraw-Hill, New York, 284 pp., 1958.

Pavlis, G.L. and J.R. Booker, The mixed discrete-continuous inverse problem: Application to the simultaneous determination of earthquake hypocenters and velocity structure. J. Geophys. Res., 85, 4801-4810, 1980.

Pereyra, V., W.H.K. Lee and H.B. Keller, Solving two-point seismic ray-tracing problems in a heterogeneous medium, Bull. Seis. Soc. Amer., 70, 79-99, 1980.

Peters, D.C., Hypocenter location and crustal structure inversion of seismic array travel-times, Ph.D. thesis, Univ. of Wash., Seattle, 1973.

Powell, M.J.D., Subroutine NSOlA, Tech. Rept. AERE-R.5947, Harwell, U.K., 1968.

Radbruch-Hall, D.H., Map showing recently active breaks along the Hayward fault zone and the southern part of the Calaveras fault zone, California. U.S. Geological Survey Map I-813, 1974.

Schweickert, R.A. and D.S. Cowan, Early Mesozoic tectonic evolution of the western Sierra Nevada, California. Geol. Soc. Amer. Bull., 86, 1329-1336, 1975.

Shampine, L.F. and M.K. Gordon, Computer Solution of Ordinary Differential Equations - The Initial Value Problem. W.H. Freeman, San Francisco, 318 pp., 1975.

Silberling, N.J., Geologic events during Permian-Triassic time along the Pacific margin of the United States, in Logan A. and L.V. Hills, eds., The Permian and Triassic Systems and their Mutual Boundary. Alberta Soc. Petroleum Geol., Calgary, Alberta, Canada, 345-362, 1973.

Snyder, W.S., W.R. Dickinson and M.L. Silberman, Tectonic implications of space-time patterns of Cenozoic magmatism in the western United States. Earth Plan. Sci. Lett., 32, 91-106, 1976.

Spencer, C. and D. Gubbins, Travel time inversion for simultaneous earthquake location and velocity structure determination in laterally varying media. Geophys. J. Roy. astra.Soc., 63, 95-116, 1980.

Steppe, J.A. and R.S. Crosson, P-velocity models of the Southern Diablo Range, California, from inversion of earthquake and explosion arrival times. Bull. Seis. Soc. Am., 68, 357-367, 1978.

Stewart, R.M. and L. Peselnick, Velocity of compressional waves in dry Franciscan rocks to 8 Kbar and 300°C. J. Geophys. Res., 82, 2027-2039, 1977.

Stewart, R.L. and L. Peselnick, Systematic behavior of compressional velocity in Franciscan rocks at high pressure and temperature. J. Geophys. Res., 83, 831-839, 1978.

Suppe, J. and R.L. Armstrong, Potassium-Argon dating of Franciscan metamorphic rocks. Amer. J. Sci., 272, 217-233, 1972.

Thurber, C.H. and W.L. Ellsworth, Rapid solution of ray tracing problems in heterogeneous media. Bull. Seis. Soc. Am., 70, 1137-11148, 1980.

Travers, W.B., A trench off central California in Late Eocene - Early Oligocene time. In Geol. Soc. Amer. Memoir, 132, 1972.

Uhrhammer, R.A., Observations of the Coyote Lake, California earthquake sequence of August 6, 1979, Bull. Seis. Soc. Amer., 70, 559-570, 1980.

Wang, C.-Y., W. Lin and F.T. Wu, Constitution of the San Andreas fault zone at depth. Geophys. Res. Lett., 5, 741-744, 1978.

Wesson, R.L., Travel-time inversion for laterally inhomogeneous crustal velocity models, Bull. Seis. Soc. Amer., 61, 729-746, 1971.

Wiggins, R.A., The general linear inversion problem: implication of surface waves and free oscillations for Earth structure., Rev. Geophys. Space Phys., 10, 251-285, 1972.

Wolfe, M.A., Numerical Methods for Unconstrained Optimization. Van Nostrand Reinhold, New York, 312 pp., 1978.

APPENDIX A

THE RAY EQUATIONS AND FERMAT'S PRINCIPLE

A.1 DERIVATION OF THE RAY EQUATIONS FROM THE EQUATION OF MOTION

The propagation of elastic waves in an inhomogeneous, isotropic elastic medium is governed by the elastodynamic equation of motion

$$\rho \frac{\partial^2 \underline{u}}{\partial t^2} = (\lambda+\mu)\ \nabla(\nabla\cdot\underline{u}) + \mu\ \nabla^2\underline{u} + \nabla\lambda\ (\nabla\cdot\underline{u}) + \nabla\mu\ \mathrm{x}\ (\nabla\ \mathrm{x}\ \underline{u}) + 2(\nabla\mu\cdot\nabla)\underline{u} \qquad (A.1)$$

where $\underline{u} = u(\underline{r},t)$ is particle displacement, $\rho = \rho(\underline{r})$ is density, $\lambda = \lambda(\underline{r})$ and $\mu = \mu(\underline{r})$ are Lame's parameters, and $\underline{r}$ is the position within the medium. Cerveny et al. (1977) show that by seeking a solution to equation A.1 in the form of a ray series

$$\underline{u}(\underline{r},t) = \sum_{k=0}^{\infty} \underline{u}_k(\underline{r})\ F_k(t-\tau(\underline{r})) \qquad (A.2)$$

where $\tau(\underline{r})$ describes a wave front (a surface of discontinuity) and the functions $F_k(t-\tau)$ satisfy $F_k' = F_{k-1}$,

the coefficients for the k=0 term of the series solution obtained by inserting equation A.2 into A.1 yield two solutions for the wave front or phase function τ:

$$|\nabla \tau|^2 = \alpha^{-2}, \qquad \alpha = (\lambda + 2\mu)^{1/2}/\rho^{1/2}$$

$$|\nabla \tau|^2 = \beta^{-2}, \qquad \beta = (\mu/\rho)^{1/2} \tag{A.3}$$

Equations A.3 are known as the eikonal equations corresponding to the compressional (P) and shear (S) waves of seismology.

Now consider the normal to the wave front τ, which is called a ray. The ray direction $d\underline{r}/ds$ (where $\underline{r} = (x,y,z)$ is the vector along the ray and s is the parameter of path length along the ray) must be parallel to the vector $\nabla\tau$ (Lunenberg, 1964) so that

$$\nabla \tau \propto d\underline{r}/ds \tag{A.4}$$

Since $|d\underline{r}/ds| = 1$, we see from equations A.3 and A.4 that

$$\nabla \tau = \frac{1}{\alpha} d\underline{r}/ds \tag{A.5}$$

Also from equation A.3 it is clear that the directional derivative of along the ray satisfies

$$\frac{d\tau}{ds} = \frac{1}{\alpha} \tag{A.6}$$

If we now differentiate equation A.5 with respect to the path length parameter s we find

$$\frac{d}{ds}(\nabla\tau) = \frac{d}{ds}\left(\frac{1}{\alpha}\ d\underline{r}/ds\right)$$

or using equation A.6

$$\nabla(1/\alpha) = \frac{d}{ds}\left(\frac{1}{\alpha}\ d\underline{r}/ds\right)$$

These are the ray equations 2.10 shown in section 2.3.1.

A.2 DERIVATION OF THE RAY EQUATIONS FROM FERMAT'S PRINCIPLE

Fermat's principle of geometrical optics can be stated as a ray path between two points P1 and P2 is the curve for which the ray travel time obtains an extreme value (Klein, 1970). The ray travel time for a P wave is expressed as

$$t = \int_{P1}^{P2} \frac{1}{\alpha(\underline{r})}\ ds \qquad (A.7)$$

where ds is the element of arc length along the path. Thus the variation δt on passing from a true ray path to an adjacent path must vanish.

Following the development of Lee and Stewart (1981), we reparameterize the integral in equation A.7 using the

arbitrary parameter q which ranges from a value q_1 at P1 to q_2 at P2. The path is given by

$$x = x(q) \quad , \quad y = y(q), \quad z = z(q) \qquad q \in]q_1, q_2]$$

and the element ds becomes

$$ds = (\dot{x}^2 + \dot{y}^2 + \dot{z}^2)^{1/2} \, dq \qquad (A.8)$$

where the dot denotes differentiation with respect to q. If we define

$$w = (\dot{x}^2 + \dot{y}^2 + \dot{z}^2)^{1/2} / \alpha(\underline{r}) \qquad (A.9)$$

then combining equations A.7 through A.9 we have

$$t = \int_{q_1}^{q_2} w \, dq$$

Now the variation δt must vanish for a true ray path:

$$\delta t = 0 = \int_{q_1}^{q_2} \delta w \, dq$$

and using the definition of w (equation A.9)

$$\delta t = \int_{q_1}^{q_2} \left[\frac{\partial w}{\partial x} \delta x + \frac{\partial w}{\partial y} \delta y + \frac{\partial w}{\partial z} \delta z + \frac{\partial w}{\partial \dot{x}} \delta \dot{x} + \frac{\partial w}{\partial \dot{y}} \delta \dot{y} + \frac{\partial w}{\partial \dot{z}} \delta \dot{z} \right] dq \qquad (A.10)$$

since $w = w(x, y, z, \dot{x}, \dot{y}, \dot{z})$. Integrating the last three terms of equation A.10 by parts results in

$$\delta t = \left[\frac{\partial w}{\partial \dot{x}} \delta x + \frac{\partial w}{\partial \dot{y}} \delta y + \frac{\partial w}{\partial \dot{z}} \delta z \right]_{q_1}^{q_2} - \int_{q_1}^{q_2} \left[\frac{d}{dq}\left(\frac{\partial w}{\partial \dot{x}}\right) - \frac{\partial w}{\partial x} \right] \delta x \, dq$$

$$- \int_{q_1}^{q_2} \left[\frac{d}{dq}\left(\frac{\partial w}{\partial \dot{y}}\right) - \frac{\partial w}{\partial y} \right] \delta y \, dq - \int_{q_1}^{q_2} \left[\frac{d}{dq}\left(\frac{\partial w}{\partial \dot{z}}\right) - \frac{\partial w}{\partial z} \right] \delta z \, dq$$

The endpoints P1 and P2 are fixed. so

$$\delta x(q_1) = \delta y(q_1) = \delta z(q_1) = \delta x(q_2) = \delta y(q_2) = \delta z(q_2) \equiv 0$$

Finally since δt must vanish we are left with Euler's equations

$$\frac{d}{dq}\left(\frac{\partial w}{\partial \dot{x}}\right) - \frac{\partial w}{\partial x} = 0$$

$$\frac{d}{dq}\left(\frac{\partial w}{\partial \dot{y}}\right) - \frac{\partial w}{\partial y} = 0 \qquad (A.11)$$

$$\frac{d}{dq}\left(\frac{\partial w}{\partial \dot{z}}\right) - \frac{\partial w}{\partial z} = 0$$

which must be satisfied if the path is a true ray path. If we now choose to define the arbitrary parameter q to be the arc length s along the true ray path, equations A.8 and A.9 become

$$ds = d\varphi$$
$$\omega = 1/\alpha(\underline{r}) \qquad (A.12)$$

Also we have

$$\frac{\partial w}{\partial \dot{x}} = \frac{\dot{x}}{\alpha(\underline{r})\left(\dot{x}^2+\dot{y}^2+\dot{z}^2\right)^{1/2}} = \frac{1}{\alpha}\frac{dx}{ds} \qquad (A.13)$$

and similarly

$$\frac{\partial w}{\partial \dot{y}} = \frac{1}{\alpha}\frac{dy}{ds}$$
$$\frac{\partial w}{\partial \dot{z}} = \frac{1}{\alpha}\frac{dz}{ds} \qquad (A.14)$$

Combining equations A.11 through A.14, and rewriting in vector notation, we arrive at the ray equations

$$\underline{\nabla}\left(\frac{1}{\alpha}\right) = \frac{d}{ds}\left(\frac{1}{\alpha}\frac{d\underline{r}}{ds}\right)$$

APPENDIX B

ORTHOGONAL TRANSFORMATIONS, MATRIX DECOMPOSITION, AND PARAMETER SEPARATION

B.1 HOUSEHOLDER TRANSFORMATION AND QR DECOMPOSITION

A general orthogonal transformation of a matrix $\underline{\underline{A}}$ has the following two properties:

1) the transforming matrix $\underline{\underline{T}}$ is orthogonal, i.e. $\underline{\underline{T}}^{T} = \underline{\underline{T}}^{-1}$

2) the transformation preserves the singular values of $\underline{\underline{A}}$

(Acton, 1970). The parameter separation method (section 2.6) requires an orthogonal transformation $\underline{\underline{\Omega}}$ such that

$$\underline{\underline{\Omega}}\ \underline{\underline{H}} = \begin{bmatrix} \underline{\underline{H}}' \\ \hline 0 \end{bmatrix}$$

where $\underline{\underline{H}}$ is the matrix of hypocentral partial derivatives and $\underline{\underline{H}}'$ is a 4 x 4 (upper triangular) matrix. One way to construct such a matrix $\underline{\underline{\Omega}}$ is by using a sequence of Householder transformations in the procedure known as QR decomposition.

B.1.1 HOUSEHOLDER TRANSFORMATION

A Householder transformation $\underline{\underline{P}}$ of a vector $\underline{x}$ has the property

$$\underline{\underline{P}}\,\underline{x} = -\sigma \|\underline{x}\|\,\underline{e}_1$$

where $\underline{e}_1$ is defined by

$$\underline{e}_1 = \begin{bmatrix} 1 \\ 0 \\ \vdots \\ 0 \end{bmatrix}$$

and

$$\sigma = \begin{cases} +1 & \text{if} \quad x_1 \geq 0 \\ -1 & \text{if} \quad x_1 < 0 \end{cases}$$

and x_1 is the first component of $\underline{x}$ (Lawson and Hanson, 1974). It is claimed that the matrix

$$\underline{\underline{P}} = \underline{\underline{I}} - 2\left[\frac{\underline{w}\,\underline{w}^T}{\underline{w}^T\,\underline{w}}\right]$$

has this property, where $\underline{w}$ is given by

$$\underline{w} = \underline{x} + \sigma \|\underline{x}\|\,\underline{e}_1$$

To see that $\underline{\underline{P}}$ is orthogonal, check that

$$\underline{\underline{P}}^T \underline{\underline{P}} = \left(\underline{\underline{I}} - 2\frac{\underline{w}\,\underline{w}^T}{\underline{w}^T\underline{w}}\right)\left(\underline{\underline{I}} - 2\frac{\underline{w}\,\underline{w}^T}{\underline{w}^T\underline{w}}\right)$$

$$\underline{\underline{P}}^T\underline{\underline{P}} = \underline{\underline{I}} - 4\frac{\underline{w}\,\underline{w}^T}{\underline{w}^T\underline{w}} + 4\frac{\underline{w}\,\underline{w}^T\underline{w}\,\underline{w}^T}{\underline{w}^T\underline{w}\;\underline{w}^T\underline{w}}$$

and finally

$$\underline{\underline{P}}^T\,\underline{\underline{P}} = \underline{\underline{I}}$$

since $\underline{w}^T\underline{w} = \|\underline{w}\|^2$.

B.1.2 QR DECOMPOSITION

QR decomposition is accomplished using a sequence of Householder transformations. Starting with the N x 4 matrix H, construct the transformation $\underline{\underline{P}}_1$ such that

$$\underline{\underline{P}}_1\,\underline{h}_1 = -\sigma\,\|\underline{h}_1\|\,\underline{e}_1$$

where $\underline{h}_1$ is the vector containing the first column of $\underline{\underline{H}}$ and $\underline{e}_1$ is N x 1. Applying $\underline{\underline{P}}_1$ to $\underline{\underline{H}}$ yields

$$\underline{\underline{P}}_1\,\underline{\underline{H}} = \underline{\underline{H}}' = \begin{bmatrix} h_{11}' & h_{12}' & h_{13}' & h_{14}' \\ 0 & & & \\ \vdots & & H_2' & \\ 0 & & & \end{bmatrix} \equiv \underline{\underline{Q}}_1\,\underline{\underline{H}}$$

Now construct the transformation $\underline{\underline{P}}_2$ such that

$$\underline{\underline{P}}_2 \, \underline{h}_2' = -\sigma \, \| \underline{h}_2' \| \, \underline{e}_1$$

where $\underline{h}_2'$ is the first column of the submatrix $\underline{\underline{H}}_2'$ and $\underline{e}_1$ is (N-1) x 1. Applying $\underline{\underline{P}}_2$ augmented by a row and column as shown to $\underline{\underline{H}}'$ yields

$$\begin{bmatrix} 1 & 0 & 0 & \cdots & 0 \\ 0 & & & & \\ \vdots & & \underline{\underline{P}}_2 & & \\ 0 & & & & \end{bmatrix} \underline{\underline{H}}' = \underline{\underline{H}}'' = \begin{bmatrix} h_{11}' & h_{12}' & h_{13}' & h_{14}' \\ 0 & h_{22}' & h_{23}' & h_{24}' \\ 0 & 0 & & \\ \vdots & \vdots & & H_3'' \\ 0 & 0 & & \end{bmatrix} \equiv \underline{\underline{Q}}_2 \, \underline{\underline{H}}'$$

Note that $\underline{\underline{Q}}_2$ is also an orthogonal matrix.

Continuing in this manner we similarly construct the matrices $\underline{\underline{Q}}_3$ and $\underline{\underline{Q}}_4$. Now define $\underline{\underline{Q}}$ as

$$\underline{\underline{Q}} = \underline{\underline{Q}}_4 \, \underline{\underline{Q}}_3 \, \underline{\underline{Q}}_2 \, \underline{\underline{Q}}_1 \qquad (B.1)$$

Thus it is evident that $\underline{\underline{Q}}$ will have the property

$$\underline{\underline{Q}} \, \underline{\underline{H}} = \begin{bmatrix} h_{11}' & h_{12}' & -h_{13}' & h_{14}' \\ 0 & h_{22}' & h_{23}' & h_{24}' \\ 0 & 0 & h_{33}' & h_{34}' \\ 0 & 0 & 0 & h_{44}' \\ - & - & - & - \\ & & 0 & \end{bmatrix} \equiv \underline{\underline{R}}$$

as desired. See Acton (1970), Lawson and Hanson (1974), or Wolfe (1978) for further discussion.

B.2 SINGULAR VALUE DECOMPOSITION

Singular value decomposition (SVD) is a method which can be used to provide a great deal of information about the stability and the effects of errors on the solution of a given matrix equation. It can be shown that any matrix $\underline{\underline{A}}$ (m by n) can be expressed as the product of three matrices

$$\underline{\underline{A}} = \underline{\underline{U}}\ \underline{\underline{S}}\ \underline{\underline{V}}^T \qquad (B.2)$$

where $\underline{\underline{U}}$ (m by m) and $\underline{\underline{V}}$ (n by n) are orthogonal matrices and $\underline{\underline{S}}$ (m by n) is a diagonal matrix augmented by m-n zero rows (Lawson and Hanson, 1974). The diagonal elements of $\underline{\underline{S}}$ are known as the singular values of $\underline{\underline{A}}$. Lawson and Hanson (1974) point out that although the singular values of $\underline{\underline{S}}$ are uniquely determined, the vectors composing $\underline{\underline{U}}$ and $\underline{\underline{V}}$ are not. The matrix $\underline{\underline{Q}}$ in equation B.1 is an example of the matrix $\underline{\underline{U}}$ in equation B.2. In fact the QR decomposition is used in some computer routines as one step in the SVD procedure.

To solve a linear system for the unknown vector $\underline{x}$,

$$\underline{\underline{A}}\ \underline{x} = \underline{b} \qquad (B.3)$$

a singular value decomposition is performed on the matrix $\underline{\underline{A}}$:

$$\underline{\underline{U}}\ \underline{\underline{S}}\ \underline{\underline{V}}^T\ \underline{x} = \underline{b} \qquad (B.4)$$

$\underline{\underline{U}}$ is orthogonal, so $\underline{\underline{U}}^T\underline{\underline{U}} = \underline{\underline{I}}$, and operating on equation B.4 with $\underline{\underline{U}}^T$ yields

$$\underline{\underline{S}}\ \underline{\underline{V}}^T\ \underline{x} = \underline{\underline{U}}^T\ \underline{b} \qquad (B.5)$$

Since $\underline{\underline{S}}$ is an augmented diagonal matrix, equation B.5 can be rewritten as

$$\underline{\underline{V}}^T\ \underline{x} = \underline{\underline{S}}^{-1}\ \underline{\underline{U}}^T\ \underline{b}$$

where $\underline{\underline{S}}^{-1}$ is a diagonal matrix augmented by m-n zero columns whose diagonal elements are the reciprocals of the corresponding diagonal elements of $\underline{\underline{S}}$ (assuming $\underline{\underline{S}}$ is full rank, i.e. no zero singular values). Finally, $\underline{\underline{V}}$ is orthogonal also. so

$$\underline{x} = \underline{\underline{V}}\ \underline{\underline{S}}^{-1}\ \underline{\underline{U}}^T\ \underline{b}$$

is the SVD solution to equation B.3.

B.3 PROPERTIES OF THE PARAMETER SEPARATION METHOD

B.3.1 PRESERVATION OF THE ORIGINAL SOLUTION

Suppose there is a system of equations for a simultaneous inversion problem whose solution is desired. The claim is

that solving this system using the (modified) method of Pavlis and Booker for parameter separation, followed by QR decomposition of the separated velocity matrix (and back-substitution) results in the same answer as using straighforward QR decomposition.

First consider the normal QR decomposition approach. The system has the form

$$\underline{\underline{A}}\,\underline{x} = \begin{bmatrix} H_1 & & & & \\ & H_2 & & & \\ & & H_3 & & \\ & & & \ddots & \\ & & & & H_k \end{bmatrix} \begin{bmatrix} & \\ & M \\ & \end{bmatrix} \begin{bmatrix} \Delta h \\ \Delta m \end{bmatrix} = \underline{r} \qquad (B.6)$$

where each submatrix $\underline{\underline{H}}_i$ is of size number of observations (n_i) by 4, $\underline{\underline{M}}$ is of size total number of observations (n_{tot}) by number of velocity parameters (m), $\underline{x}$ is the parameter adjustment vector composed of Δh, the hypocenter adjustments, and Δm, the velocity model adjustments, $\underline{r}$ is the vector of residuals, and k is the number of events. A sensible scheme for decomposing the matrix $\underline{\underline{A}}$ using QR decomposition might proceed as follows. First construct the matrix $\underline{\underline{Q}}_1$ which satisfies

$$\underline{\underline{Q}}_1 \; \underline{\underline{H}}_1 = \begin{bmatrix} \underline{\underline{U}}_1 \\ 0 \end{bmatrix} \qquad (B.7)$$

where $\underline{\underline{U}}_1$ (4 x 4) is upper triangular. $\underline{\underline{Q}}_1$ will consist of a sequence of four Householder transformations (see Appendix

B.1). Operating on equation B.6 results in

$$\underline{\underline{Q}}_1 \underline{\underline{A}}\underline{x} = \begin{bmatrix} u_1 & & & | & M_1' \\ 0 & H_2 & & | & M_2 \\ & & H_3 & | & M_3 \\ & & \ddots & | & \vdots \\ & & & | & \vdots \\ & & H_K & | & M_K \end{bmatrix} \underline{x} = \begin{bmatrix} r_1' \\ r_2 \\ r_3 \\ \vdots \\ r_K \end{bmatrix} \qquad (B.8)$$

Now define

$$M_1' = \begin{bmatrix} \mathcal{M}_1 \\ m_1' \end{bmatrix}$$

and

$$r_1' = \begin{bmatrix} \rho_1 \\ \rho_1' \end{bmatrix}$$

where $\mathcal{M}_1$ and ρ_1 contain the first four rows of M_1' and r_1' respectively. Equation B.8 can be rearranged to the form

$$\begin{bmatrix} u_1 & & & | & \mathcal{M}_1 \\ & H_2 & & | & M_2 \\ & & H_3 & | & M_3 \\ & & \ddots & | & \vdots \\ & & & | & \vdots \\ & & H_K & | & M_K \\ & & 0 & | & m_1' \end{bmatrix} \underline{x} = \begin{bmatrix} \rho_1 \\ r_2 \\ r_3 \\ \vdots \\ r_K \\ \rho_1' \end{bmatrix}$$

This process of partial decomposition and rearrangement can be repeated k times to yield

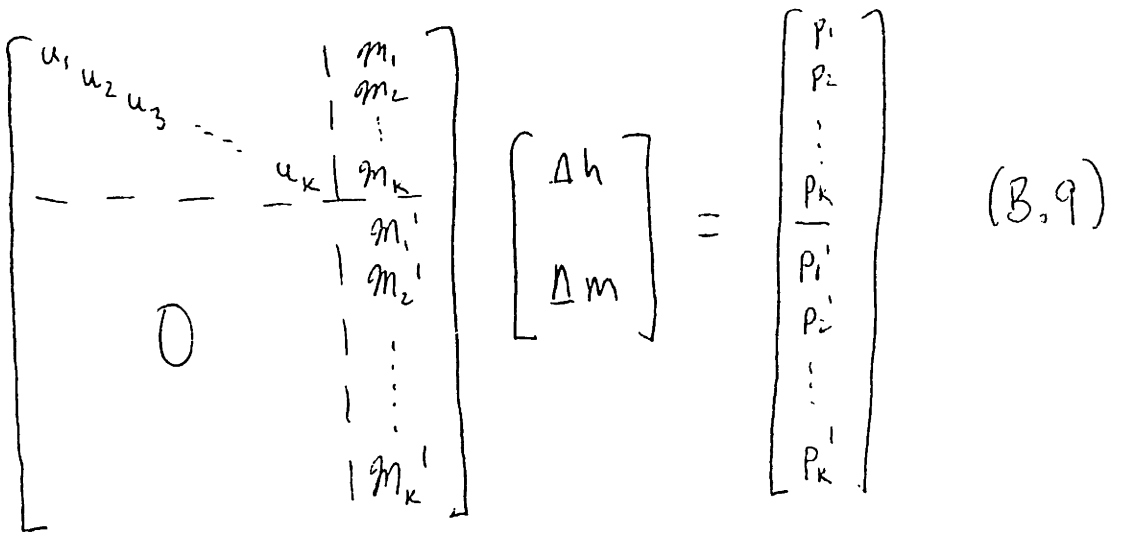

(B.9)

The first 4k equations in B.9 contain both hypocenter and velocity parameters, but the remainder do not. Continuing with QR decomposition, the application of at most m additional Householder transformations will produce

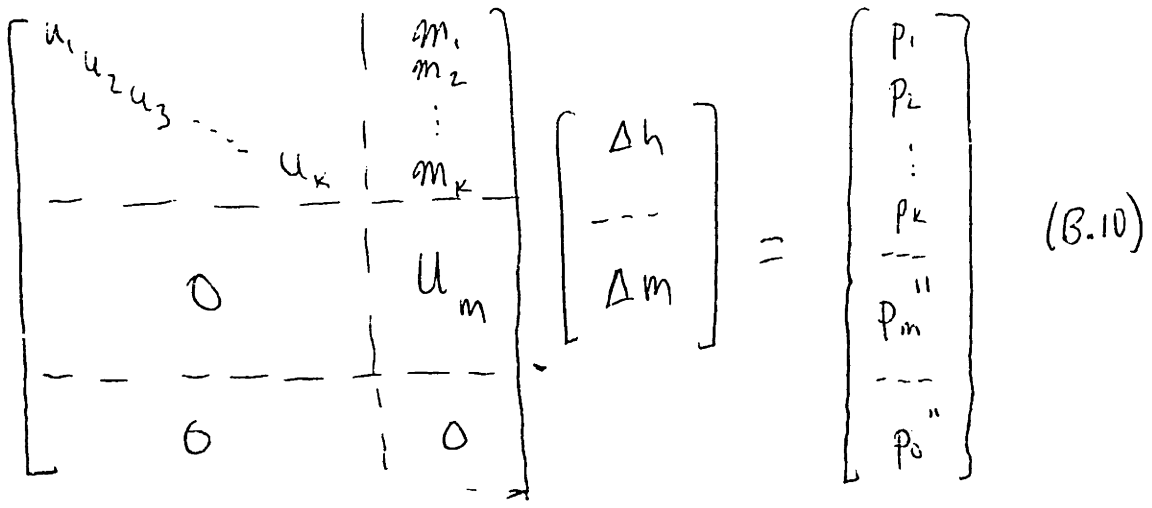

(B.10)

where $\underline{\underline{U}}_m$ is an m x m upper triangular matrix. The top 4k+m equations of B.10 can easily be solved by back-substitution, starting from the bottom up, and leaving an overall residual

of size $\sqrt{(\rho_c'')^T(\rho_c'')}$.

The modified Pavlis and Booker parameter separation scheme is simply a way of directly constructing the matrix

$$\underline{\underline{m}}' = \begin{bmatrix} m_1' \\ m_2' \\ \vdots \\ m_K' \end{bmatrix}$$

and the vector

$$\underline{p}' = \begin{bmatrix} p_1' \\ p_2' \\ \vdots \\ p_K' \end{bmatrix}$$

Returning to equation B.7, if we partition the matrix $\underline{\underline{Q}}_1$ into

$$\underline{\underline{Q}}_1 = \begin{bmatrix} \underline{\underline{2}}_1 \\ \underline{\underline{2}}_1' \end{bmatrix}$$

where $\underline{\underline{2}}_1$ is 4 x n and $\underline{\underline{2}}_1'$ is n -4 x n such that

$$\underline{\underline{2}}_1 \, \underline{\underline{H}}_1 = \underline{\underline{U}}_1$$

and

$$\underline{\underline{2}}_1' \, \underline{\underline{H}}_1 = 0$$

we see that $\underline{\underline{2}}_1'$ is simply the matrix $\underline{\underline{U}}_0^T$ defined in section 2.6.1! By constructing and applying a series of $\underline{\underline{U}}_0^T$ matrices (one for each earthquake) we are building the

matrix $\underline{\underline{m}}'$ and the vector $\underline{p}'$ directly. Solving the system of equations

$$\underline{\underline{m}}' \left[\Delta m \right] = \underline{p}'$$

by QR decomposition would then result in

$$\left[u_m \right] \left[\Delta m \right] = \begin{bmatrix} p_m'' \\ \hline p_0'' \end{bmatrix}$$

producing the same solution for the velocity parameter adjustments as equation B.10. Thus in principle the parameter separation method preserves the original solution to the simultaneous inversion problem.

B.3.2 COMPARISON OF THE METHODS OF SPENCER AND GUBBINS VERSUS PAVLIS AND BOOKER (MODIFIED)

The Spencer and Gubbins (1980) solution for the velocity model perturbations is given by

$$\underline{\Delta m} = \left(\underline{\underline{O}}^T \underline{\underline{M}} \right)^{-1} \underline{\underline{O}}^T \underline{r} \qquad (B.11)$$

where

$$\underline{\underline{O}}^T = \underline{\underline{M}}^T \left[\underline{\underline{I}} - \underline{\underline{H}} \left(\underline{\underline{H}}^T \underline{\underline{H}} \right)^{-1} \underline{\underline{H}}^T \right]$$

(see section 2.6). But using the singular value decomposition of $\underline{\underline{H}}$ we find

$$\underline{\underline{H}} \left(\underline{\underline{H}}^T \underline{\underline{H}}\right)^{-1} \underline{\underline{H}}^T = \underline{\underline{U}}_p \underline{\underline{S}}_p \underline{\underline{V}}_p^T \underline{\underline{V}}_p \underline{\underline{S}}_p^{-2} \underline{\underline{V}}_p^T \underline{\underline{V}}_p \underline{\underline{S}}_p \underline{\underline{U}}_p^T$$

$$= \underline{\underline{U}}_p \underline{\underline{U}}_p^T$$

and since

$$\underline{\underline{U}}_p \underline{\underline{U}}_p^T + \underline{\underline{U}}_o \underline{\underline{U}}_o^T = \underline{\underline{I}}$$

we have

$$\underline{\underline{O}}^T = \underline{\underline{M}}^T \underline{\underline{U}}_o \underline{\underline{U}}_o^T \qquad (B.12)$$

For the modified Pavlis and Booker (1980) method the equation to be solved is

$$\underline{\underline{U}}_o^T \underline{\underline{M}} \, \underline{\Delta m} = \underline{\underline{U}}_o^T \underline{r}$$

which we treat by forming the normal equations

$$\left(\underline{\underline{U}}_o^T \underline{\underline{M}}\right)^T \underline{\underline{U}}_o^T \underline{\underline{M}} \, \underline{\Delta m} = \left(\underline{\underline{U}}_o^T \underline{\underline{M}}\right)^T \underline{\underline{U}}_o^T \underline{r}$$

When solved for $\underline{\Delta m}$ this yields

$$\underline{\Delta m} = \left[\underline{\underline{M}}^T \underline{\underline{U}}_o \underline{\underline{U}}_o^T \underline{\underline{M}}\right]^{-1} \underline{\underline{M}}^T \underline{\underline{U}}_o \underline{\underline{U}}_o^T \underline{r} \qquad (B.13)$$

Comparing equations B.11 and B.12 with B.13 it is seen that the modified Pavlis and Booker approach is identical to the Spencer and Gubbins method.

APPENDIX C

SUMMARY OF THE RECENT TECTONIC HISTORY OF CALIFORNIA

The Klamath-Sierran island arc terrain was accreted to the North American continent in the late Permian or early Triassic during the Antler and Sonoma orogenies (Silberling, 1973; Burchfiel and Davis, 1975; see Figure C.1), resulting in a large westward shift of the continental margin. In this same time period another large change in the paleogeography occurred. As stated by Burchfiel and Davis (1975), "in Permo-Triassic time..., the southwestern part of the North American plate was truncated - either by rifting across a spreading center or by transform faulting." The mechanism of truncation and location of the rifted fragment are subjects of controversy.

The accretion of the arc was also accompanied by a change in the character of subduction to Andean-style in the early Mesozoic. This east-dipping subduction zone followed the newly truncated margin in the south and was along the western margin of the accreted arc in the north (Burchfiel and Davis, 1975). This stage was marked by a long period (throughout most of Mesozoic time) of granitic intrusion along the margin, possibly including two or three episodes of peak activity (Lanphere and Reed, 1973). In addition a wide intracontinental area was subjected to east-directed thrusting along with basement uplift, reflecting the

two-sided nature of this orogenic period (Burchfiel and Davis, 1972).

This stage was interrupted in the late Jurassic by the Nevadan orogeny. According to Schweickert and Cowan (1975) this event involved the collision of an east-facing island arc complex with the North American margin. King (1977) describes the geologic evidence for this event. In the northwestern Sierra Nevada, sequences of volcanic rocks apparently lying on ophiolitic crust are interpreted as island arc remnants; their location is west of the Jurassic Andean-type suduction zone. Farther west the Great Valley sequence (floored by ophiolitic crust) includes rocks of both Jurassic and Cretaceous age, indicating a period of accumulation which overlapped the Nevadan orogeny. Schweickert and Cowan (1975) account for these features by hypothesizing a collision between North America and a volcanic arc complex of unknown origin which included the arc, a remnant arc, and a back-arc basin (see Figure C.2). Following the collision (about 150 million years ago) the arc complex was accreted to the continent and Andean-style east-dipping subduction was reinitiated at the new western margin. The former back-arc basin provided the ophiolitic basement for the Great Valley sequence according to this model.

The Cretceous and earliest Tertiary were times of continued two-sided orogeny. To the east, thrusting (and some folding) progressed further eastward. The Sevier and

Laramide orogenies were phases of this constant development which stretched from Alaska through Mexico (Drewes, 1978). To the west, plutonism and metamorphism in the marginal arc (the Sierra Nevada; Lanphere and Reed, 1973; Armstrong and Suppe, 1973) and Franciscan metamorphism and accretion along the continental margin at the subduction zone (Suppe and Armstrong, 1972) took place throughout this period. The Great Valley sequence was also deposited (Cowan, 1974; Bailey and Blake, 1969a,b; Hamilton, 1969; see Figure C.3).

The Franciscan/Great Valley complex is an excellent example of the accretion of oceanic material to a continent. Hamilton (1969) describes the development of these features: "[The Franciscan] formation was deposited at abyssal depths during the same Late Jurassic to Late Cretaceous interval that saw the deposition of the continental-shelf and continental-slope [i.e. arc-trench gap] sediments of the Great Valley sequence...", and "the Franciscan was skimmed off oceanic basement that moved more smoothly under the continent." Thus the Great Valley sequence to the east was continually underthrust by successive pieces of the Franciscan formation. The highly deformed assemblage which resulted from the underthrusting is termed a tectonic melange (Cowan, 1974). In contrast, the Great Valley sequence is well ordered and regularly layered (King, 1977); deformation is mainly restricted to its western edge.

A long-standing controversy surrounds the determination of the basement rocks for both the Franciscan and Great

Valley formations. It was once assumed that the Franciscan rocks were floored by Salinian crystalline basement. However Salinian rocks are generally of Cretaceous age, making this assumption untenable (King, 1977). Now the general belief is that the Franciscan is underlain by oceanic crust; according to Hamilton (1969), oceanic rocks which are apparently basement are also exposed in places.

The case for the Great Valley is less clear. To the east, these rocks rest on Sierran granitic rock. To the west, mafic and ultramafic rocks along the Coast Range Thrust, which is the contact between the Great Valley sequence above and the Franciscan below, have been identified as ophiolites (Bailey et al., 1970). There are several possible interpretations, popular ones being that the entire Great Valley is underlain by Franciscan rock, or that the eastern third is floored by Sierran basement and the western two-thirds by oceanic crust of the old North American plate. If the tectonic model of Schweickert and Cowan (1975) is correct, the basement is almost entirely oceanic and of exotic origin.

Further significant changes in the nature of the interaction between the North American plate and neighboring oceanic plates to the west occurred during Cenozoic time. Motion along this boundary has gradually changed from the subductive style of the Mesozoic to primarily strike-slip movement of recent times. Clues to the history of this period are available not only in the continental geology but

also from evidence on the ocean floor.

Widespread changes in the orogenic patterns occurred during the earliest Paleocene (or perhaps latest Cretaceous, 65 to 75 million years ago). In the eastern thrust belt, thrusting terminated in much of what is now the U.S., although it continued to the north and south. Along the latitude of this gap, the style of deformation shifted to uplift of Precambrian basement in a region well to the east of the previous thrusting. Plutonic intrusion accompanied the uplift throughout this region (see Figure C.4). This period is known as the Laramide orogeny (Burchfiel and Davis, 1975). The pattern of igneous activity in the western arc also reflected this change. The gap in thrusting to the east was matched by a cessation of plutonism along the arc (i.e. the Sierra Nevada) at the same latitudes (Armstrong and Suppe, 1973). This "null region" persisted for some 25 million years (Snyder et al., 1976). Deposition of the Franciscan formation also ended at this time (Hamilton, 1969).

These alterations in tectonic style are commonly attributed to a change in relative motion between the North American plate and its neighboring oceanic plate(s) to the west (the Kula plate according to the model of Atwater, 1970). Coney (1972) suggests that the opening of the North Atlantic between North America and Europe was responsible. In any case, the result of this change in direction of relative motion was apparently the termination of subduction

and initiation of primarily strike-slip motion along the plate boundary at the latitudes of the gap. Subduction still occurred both south and north of the gap (Armstrong and Suppe, 1973). A study by Travers (1972) concludes that subduction was not occurring off the central California coast in Paleocene time. In addition marine data and the plate model of Atwater (1970) are consistent with this interpretation. This scenario would also have permitted an early Tertiary episode of right-lateral strike-slip movement along a "proto-San Andreas" fault.

By late Eocene subduction seems to have been reestablished off much of the California coast as indicated by renewed volcanism in the Sierra Nevada (Snyder et al., 1976), thrust faulting, and chaotic deformation of contemporary sediments (Travers, 1972). Subduction continued at least through early Oligocene. Considering the plate motion model of Atwater (1970), this transition might reflect the passage of the Kula plate northwards and the inception of subduction of the Farallon plate beneath that portion of the North American plate.

The next major changes occurred in middle to late Oligocene, as the Farallon/Pacific ridge neared the North American trench. Atwater and Molnar (1973) developed a detailed reconstruction of the history of relative motion between the Pacific and North American plates from the Oligocene to the present "by calculating the North America-Africa-India-Antarctica-Pacific motion." Their work

and the earlier paper of Atwater (1970) are the primary sources of information used for the following summary of the most recent tectonic history.

About 32 million years ago the Farallon plate deformed between the Mendocino and Murray fracture zones. At that time the ridge between these fracture zones was rather close to the trench, so that two large chunks of the Farallon plate were connected only by a very narrow strip of lithosphere (see Figure C.5) - hence the local deformation. Around 29 million years ago, the Pacific plate contacted the North American plate off the coast of Baja California. The thin hot young lithosphere of the edge of the Pacific plate must have been a weak point initially, so the boundary was most likely the site of strike-slip faulting at first. As the size of the zone of contact grew, the Pacific plate edge cooled, thickened and strengthened to the point that part of the continental lithosphere became the point of weakness. Initiation of intra-continental strike-slip faulting produced the beginnings of the San Andreas fault system (see Figure C.6). This occurred approximately 23 million years ago according to the geologic arguments presented by Crowell (1973) and others. This transform motion has resulted in the displacement of the Salinian block from its original location as part of the Sierra Nevada plutonic belt to its current position west of the Franciscan terrain in central California.

In the period between 21 and 10 million years ago,

relative motion between the Pacific and North American plates was rather slow, about 1.3 cm per year (Atwater and Molnar, 1973). It was at this time that the Basin and Range structure began to develop in the interior of the North American plate (King, 1977) suggesting some change in the stress regime within the plate. A change to extensional (normal faulting) intraplate tectonics is consistent with the change to strike-slip faulting along the plate boundary. The gradual northwest-trending switchoff of magmatism along the margin also reflects the northward migration of the Mendocino triple junction (Snyder et al., 1976); the switchoff apparently has about a 5 million year lag behind the passage of the triple junction (see Figure C.7).

By about 10 million years ago, subduction of the Farallon plate was complete from north of San Francisco to the tip of Baja California, the length of the entire present-day San Andreas system (Atwater, 1970). The rate of relative motion increased to 4 cm per year at this time. About 4.5 million years ago, the Gulf of California began to open and the rate increased to the present 5.5 cm per year (Atwater and Molnar, 1973). The southern tip of the Cascades chain is the current switchoff boundary of active volcanism (Snyder et al., 1976).

In summary we expect the study area to be dominated by two types of basement rock, Salinian granites and Franciscan melange. The former are identified as originating far to the south as part of the Sierra Nevada plutonic belt, and

subsequently having been displaced northwards hundreds of kilometers to their current position. The Franciscan rocks are metamorphosed oceanic trench sediments presumably floored by oceanic crust. The geology is complicated by the presence of other rock types, notably volcanic, ultrabasic, Great Valley sequence rocks, and recent sediments.

FIGURE CAPTIONS

Figure C.1 Accretion of the Klamath-Sierran island arc terrain.

Figure C.2 Late Jurassic collision of island arc complex (adapted from Schweickert and Cowan, 1975); the Nevadan orogeny.

Figure C.3 Two-sided orogeny in the Late Mesozoic.

Figure C.4 The Laramide orogeny.

Figure C.5 Deformation of the Farallon plate.

Figure C.6 Initiation of strike-slip movement along the western margin of North America.

Figure C.7 Switch-off of magmatism following the passage of the Mendocino triple junction. Numbers are in millions of years before present, and indicate the position of the triple junction (at the left) and the switch-off point (on the right).

a) DEVELOPING KLAMATH ARC AND MARGINAL BASIN

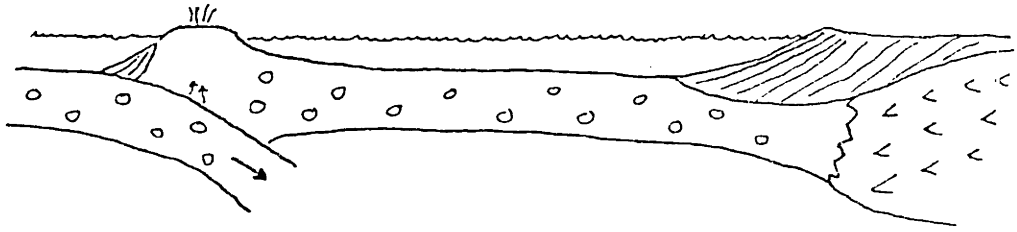

b) ANTLER OROGENY - ROBERTS MOUNTAINS THRUST

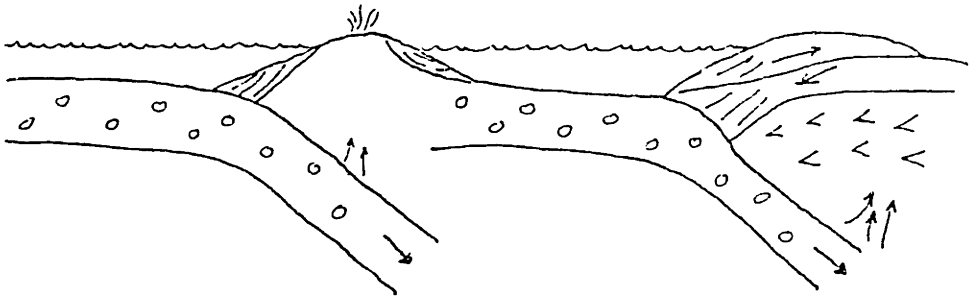

c) SONOMA OROGENY - GOLCONDA THRUST

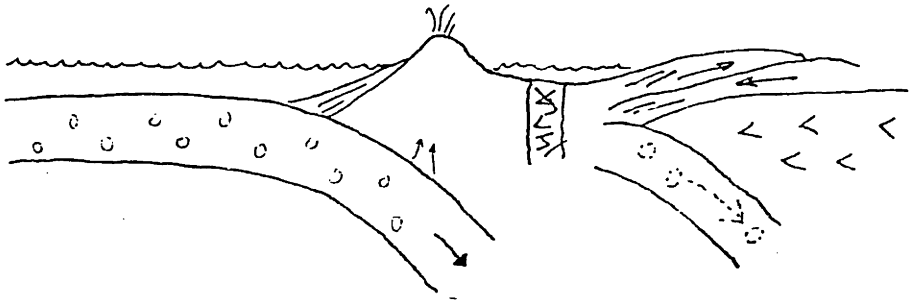

Figure C.1

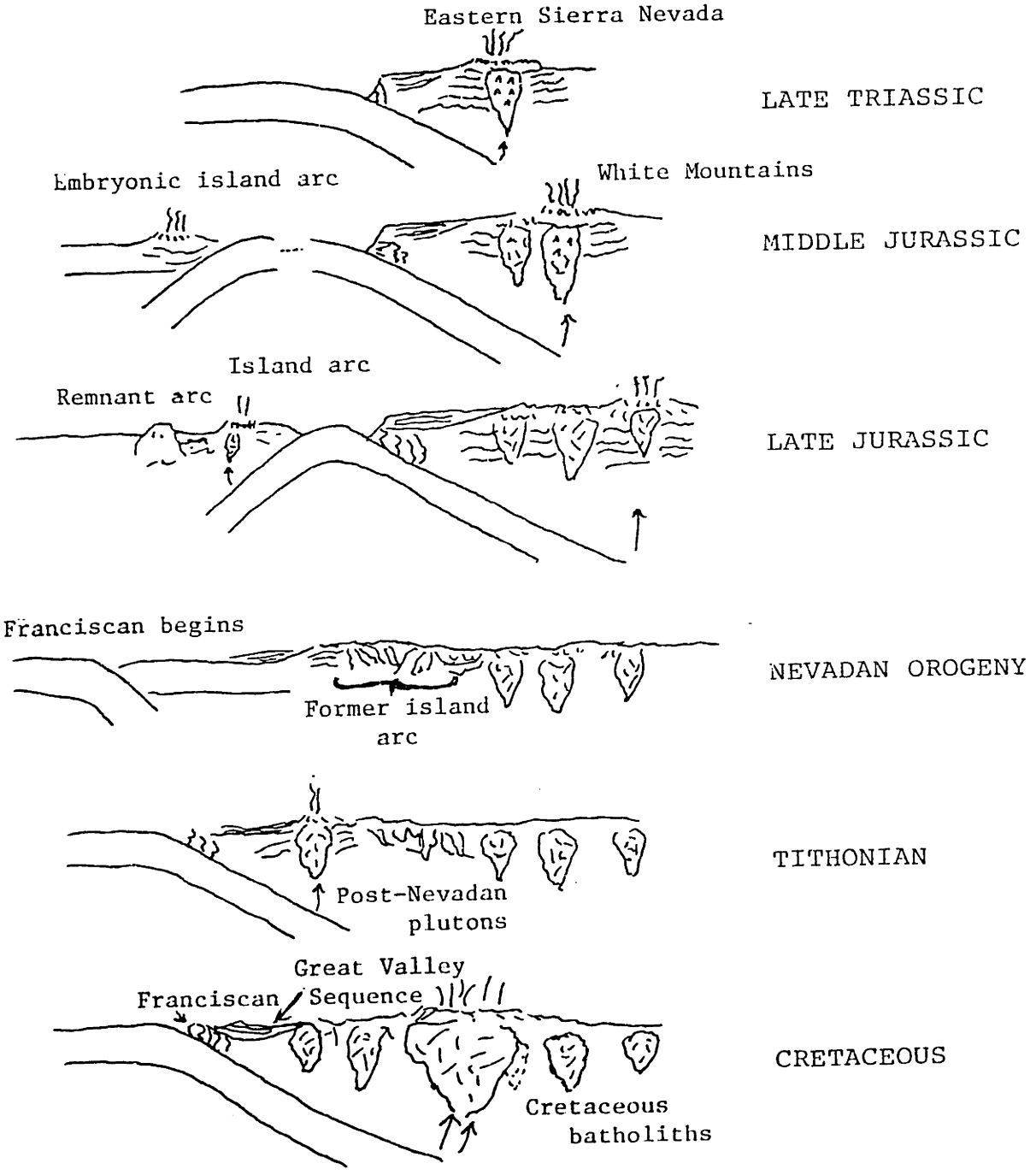
Eastern Sierra Nevada
LATE TRIASSIC
Embryonic island arc
White Mountains
MIDDLE JURASSIC
Island arc
Remnant arc
LATE JURASSIC
Franciscan begins
Former island arc
NEVADAN OROGENY
Post-Nevadan plutons
TITHONIAN
Great Valley Sequence
Franciscan
Cretaceous batholiths
CRETACEOUS

Figure C.2

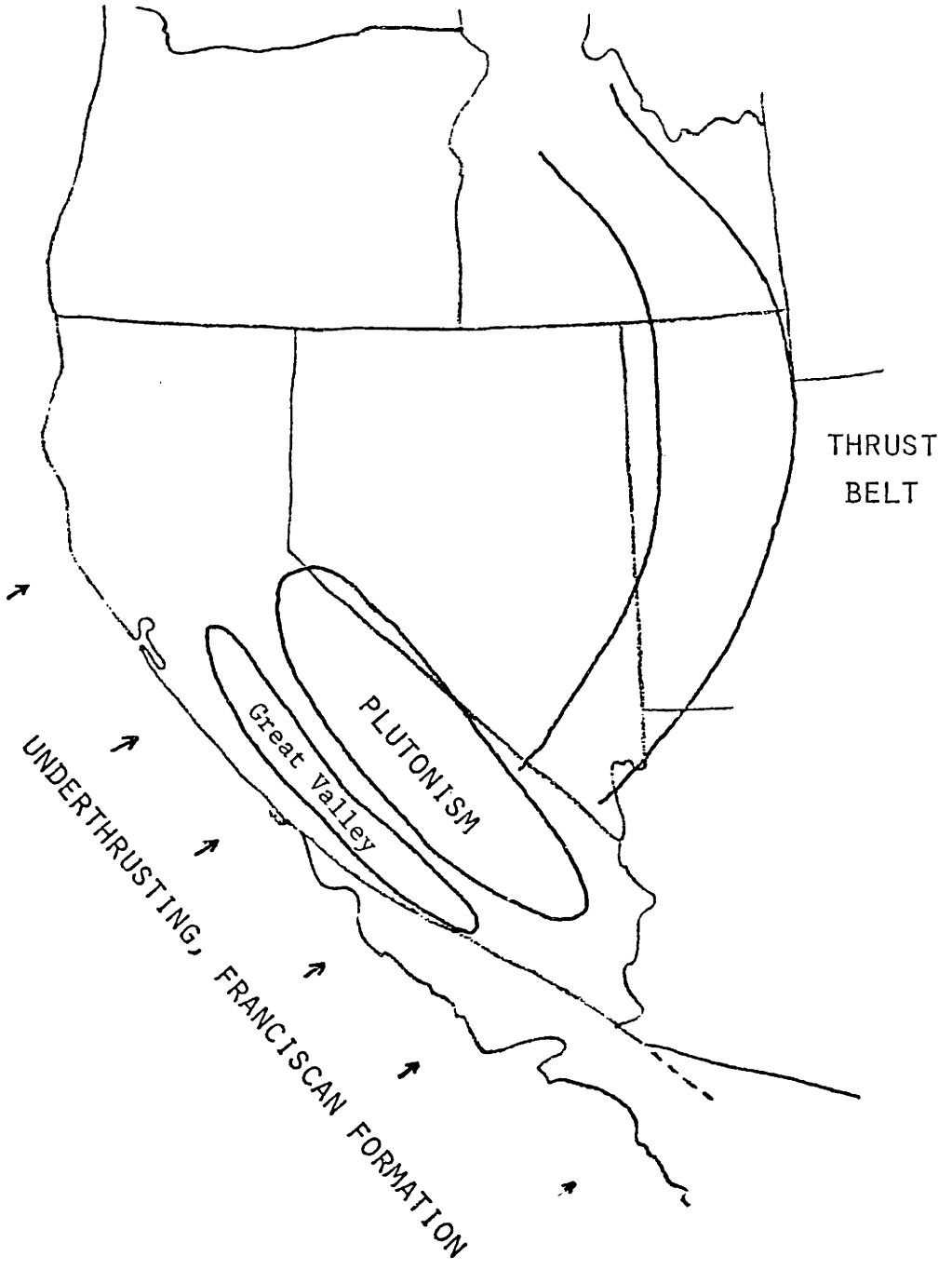
THRUST
BELT
PLUTONISM
Great Valley
UNDERTHRUSTING, FRANCISCAN FORMATION

Figure C.3

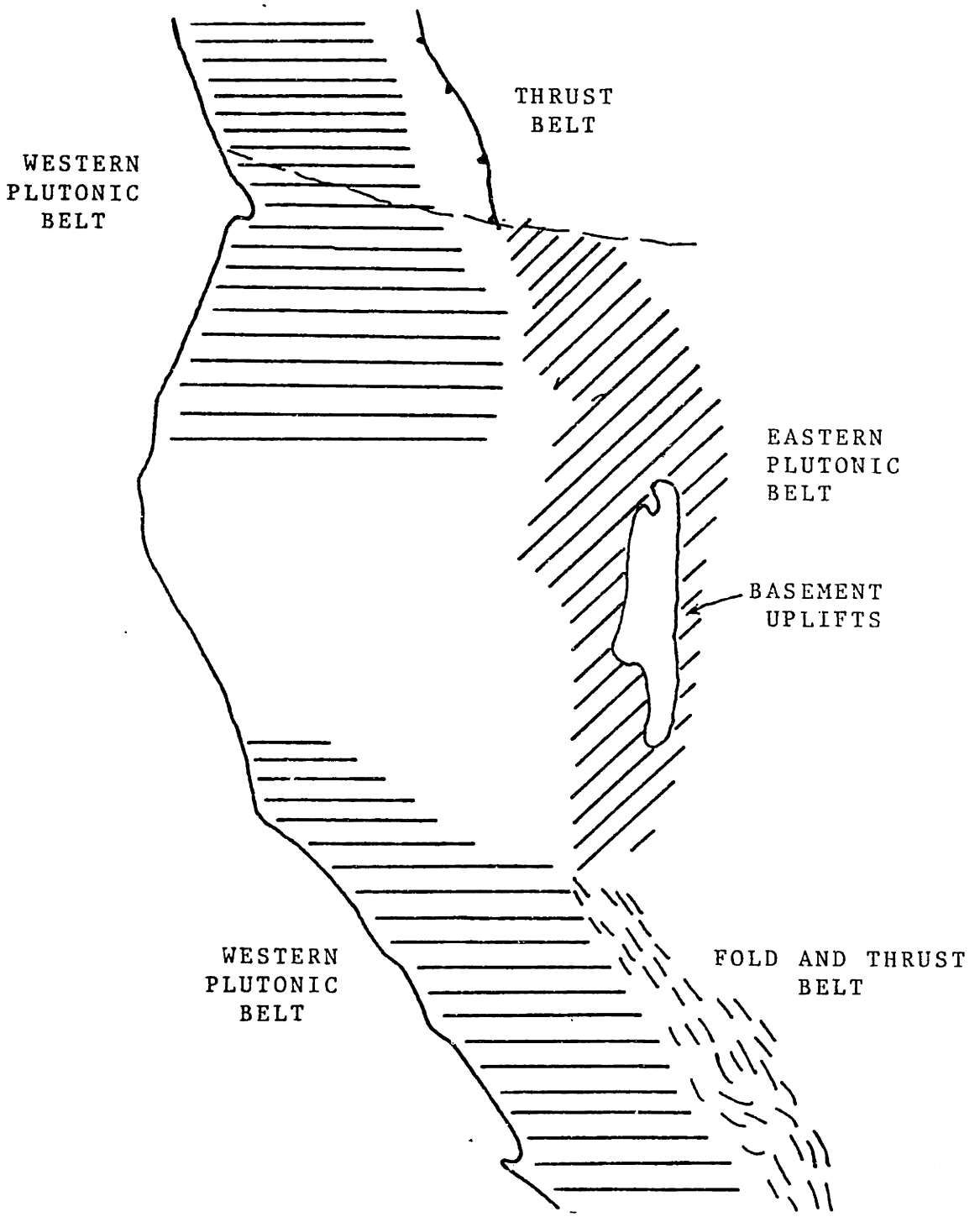
THRUST
BELT
WESTERN
PLUTONIC
BELT
EASTERN
PLUTONIC
BELT
BASEMENT
UPLIFTS
WESTERN
PLUTONIC
BELT
FOLD AND THRUST
BELT

Figure C.4

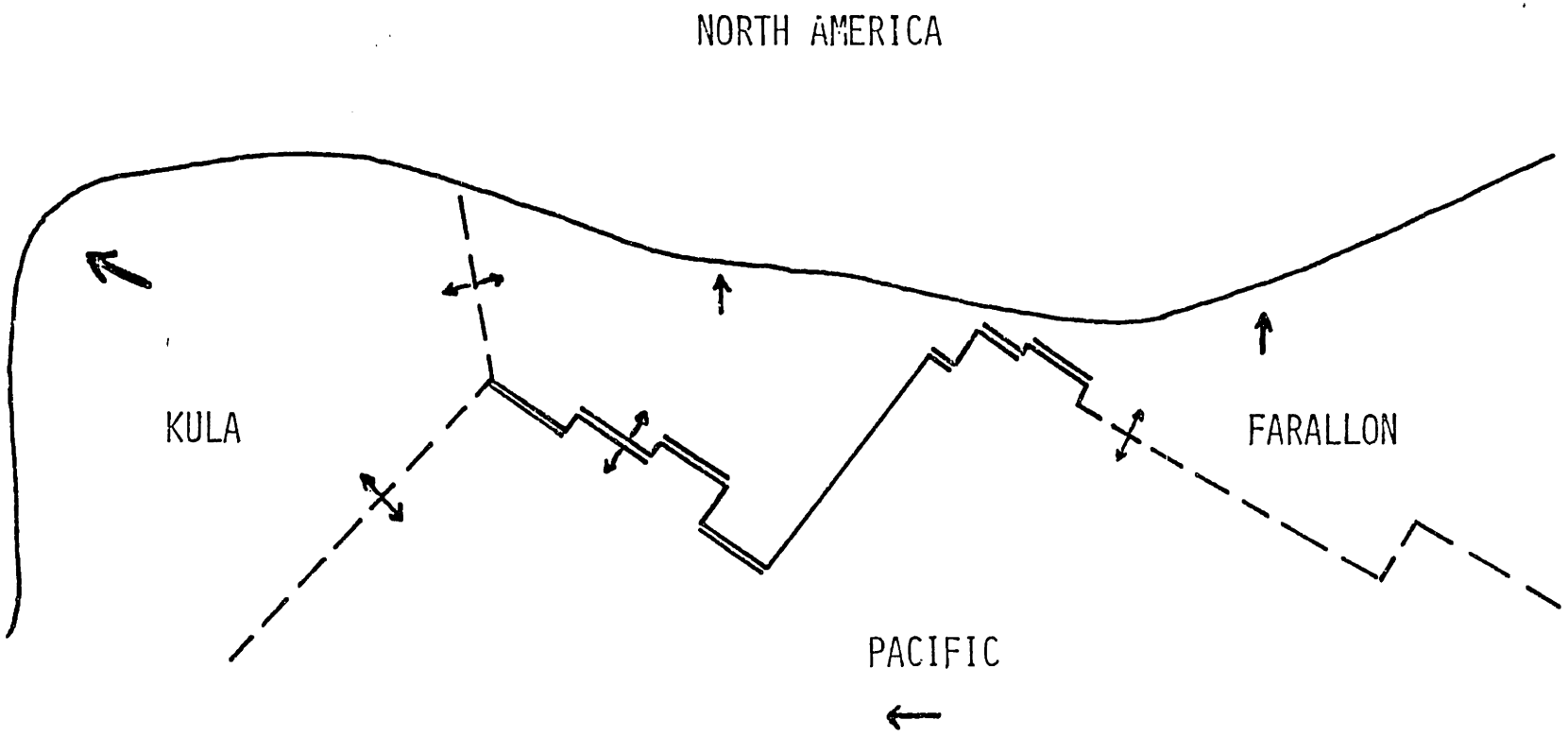

Figure C.5

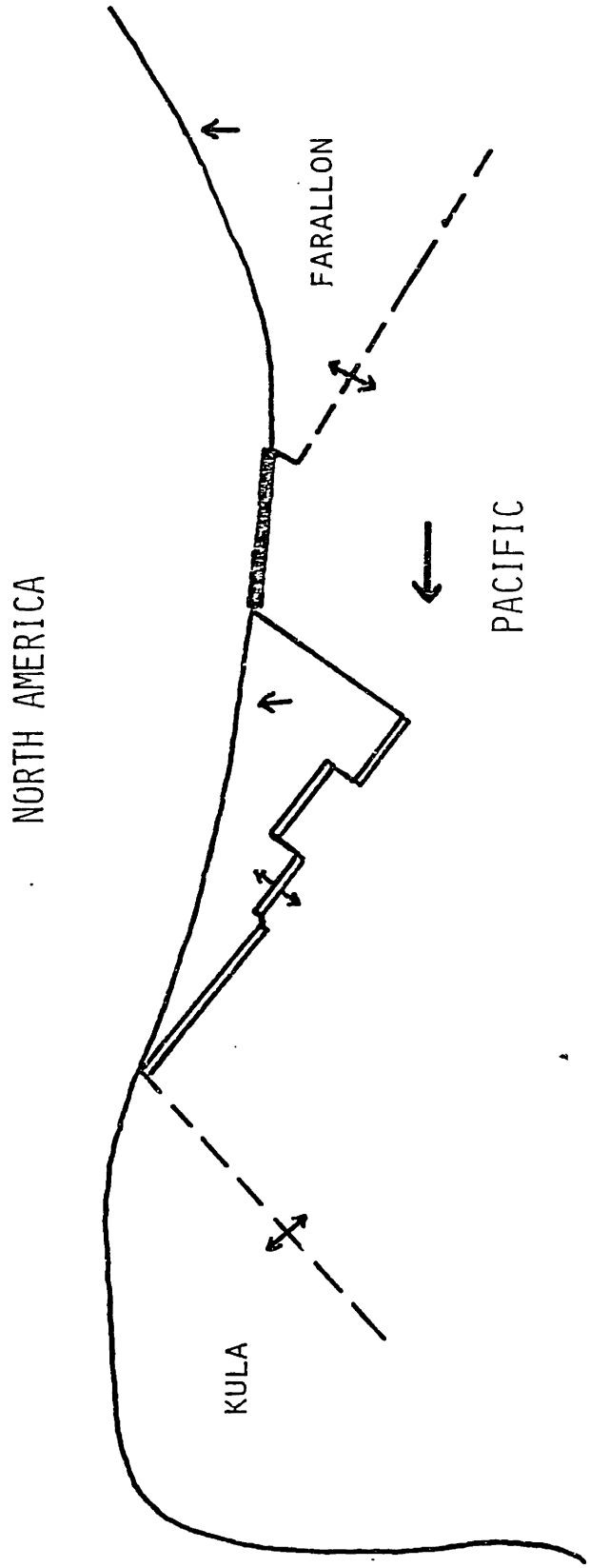

Figure C.6

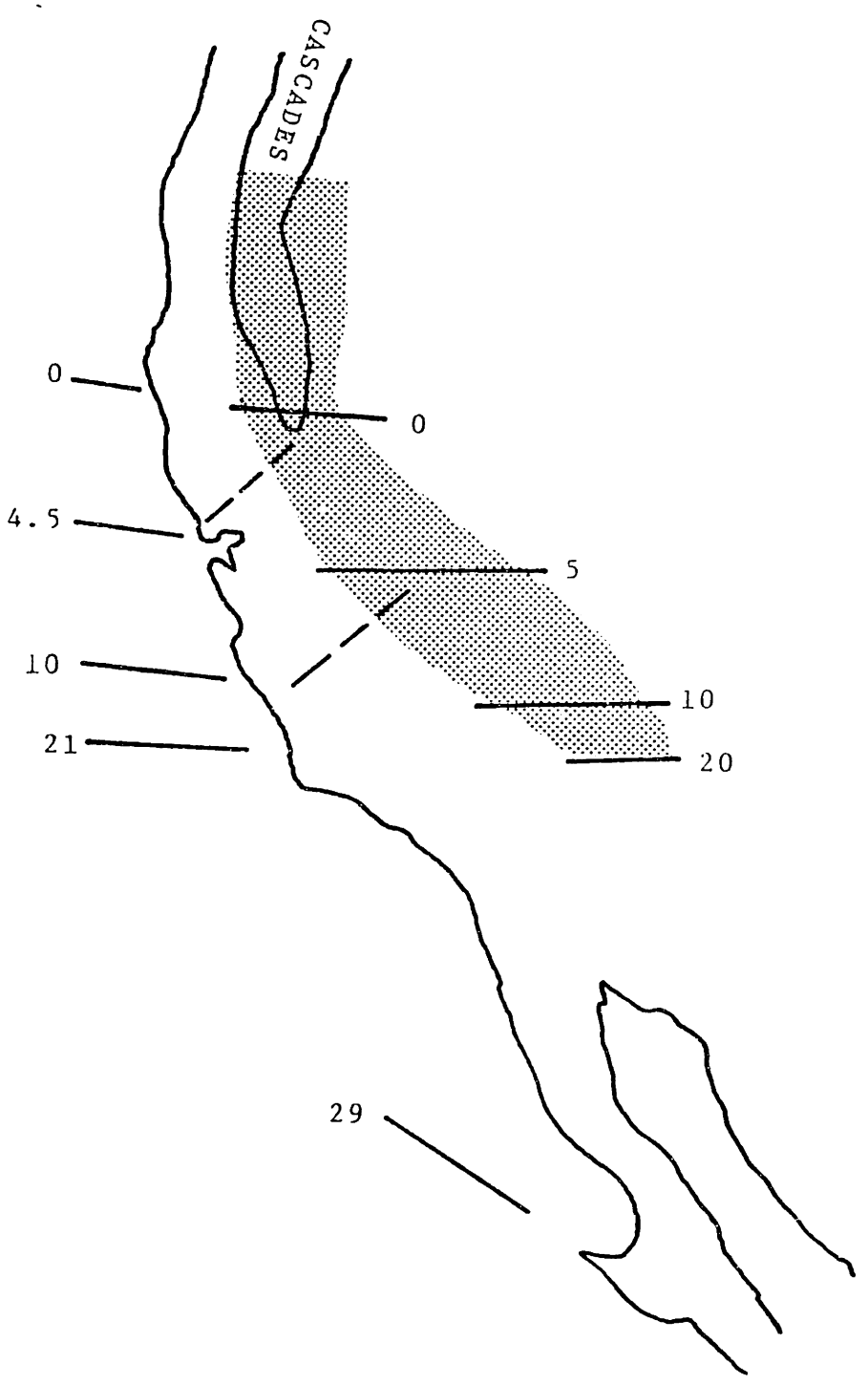

Figure C.7